BRNO UNIVERSITY OF TECHNOLOGY
VYSOKÉ UČENÍ TECHNICKÉ V BRNĚ

CENTRAL EUROPEAN INSTITUTE OF TECHNOLOGY BUT
STŘEDOEVROPSKÝ TECHNOLOGICKÝ INSTITUT VUT

MAGNETO-OPTICAL STUDY OF THE DYNAMIC PROPERTIES OF MAGNETIC NANOSTRUCTURES AND NANOSTRUCTURED METAMATERIALS

STUDIUM DYNAMICKÝCH VLASTNOSTÍ MAGNETICKÝCH NANOSTRUKTUR A NANOSTRUKTUROVANÝCH METAMATERIÁLŮ POMOCÍ MAGNETO-OPTICKÝCH METOD

DOCTORAL THESIS
DIZERTAČNÍ PRÁCE

AUTHOR AUTOR PRÁCE	Ing. Lukáš Flajšman
SUPERVISOR VEDOUCÍ PRÁCE	prof. RNDr. Jiří Spousta, Ph.D.
CO-SUPERVISOR ŠKOLITEL SPECIALISTA	Ing. Michal Urbánek, Ph.D.

BRNO 2019

Summary

The magnonics is the novel research topic in magnetism concerned with the physics of spin waves. The magnonics has the potential to introduce novel devices for wave-based computing with low power consumption. During the fabrication process of the magnonic devices using common materials and fabrication techniques, we are left only with a minimum means of how to alter the inherent properties of the magnetic materials. This highly limits the usability or versatility of the structures. This work introduces a novel material to the magnonics. The unique and highly deterministic properties of the structures prepared by focused ion beam direct writing into the metastable iron layer are presented and partially exploited in a set of prototypical structures prepared in the system. The important parameters of the system are extracted from the measurement of the spin-wave dispersion by the means of the phase-resolved Brillouin light scattering method. The findings are supported by the micromagnetic simulations and by using the analytical models. Three sets of novel magnonic devices that exploit the unique properties of the system are presented and tested.

Abstrakt

Magnonika je novým odvětvím výzkumu, který se zabývá fyzikou spinových vln. Magnonika jako vědní obor nabízí nové možnosti například v nediskrétních výpočtech na základě vlnového charakteru spinových vln. Při výrobě magnonických prvků klasickými metodami není možné příliš měnit charakter materiálů, ze kterých jsou jednotlivé prvky vyrobeny. Tento fakt silně omezuje univerzálnost vyrobených struktur. Cílem této práce je aplikovat nový typ materiálu do oboru magnoniky. Specifikum daného materiálu je možnost zápisu magnetických struktur pomocí iontového svazku. Ukazuje se, že tyto struktury mají velice zajímavé magnetické vlastnosti, které lze velice přesně řídit právě strategií ozařování iontovým svazkem. Na základě fázově rozlišené Brillouinovy spektroskopie jsme získali disperzní relaci spinových vln v tomto systému a tím i důležité parametry systému. Pozorování podkládáme mikromagnetickými simulacemi a analytickými modely. Vlastnosti systému pro magnonické aplikace prezentujeme na třech prototypických sadách struktur, které nelze vyrobit pomocí klasických materiálů.

Keywords

metastable iron, metamaterials, spin waves, magnonics, Kerr effect, magnetism

Klíčová slova

metastabilní železo, metamateriály, spinové vlny, magnonika, Kerrův jev, magnetismus

FLAJŠMAN, Lukáš. *Magneto-optical study of the dynamic properties of magnetic nanostructures and nanostructured metamaterials.* Brno, 2019. 152 s. Doctoral thesis. Brno University of Technology. Central European Institute of Technology BUT. Supervisor Jiří SPOUSTA.

I hereby declare that I have written my treatise on the theme of *Magneto-optical study of the dynamic properties of magnetic nanostructures and nanostructured metamaterials* independently, under the guidance of the supervisor, prof. RNDr. Jiří Spousta, Ph.D., and using the technical literature and other sources of information which are all properly quoted in the thesis and detailed in the list of literature at the end of the thesis.

Ing. Lukáš Flajšman

My admiration and gratitude go to many people that have surrounded me during my years at the IPE FME BUT and lately also at the CEITEC BUT. My deepest admiration goes to the key person of both institutions: prof. Tomáš Šikola. He is as selfless as he is humble. These qualities have luckily translated to both institutes that he helped to establish and guide. His qualities are greatly shared by my supervisor: prof. Jiří Spousta, to whom I owe a lot. He has walked me through all my years at the university, and luckily his guidance has a great outreach even beyond the walls of the university. He taught me not only how to enjoy windsurfing, but unknowingly he also gave me a great life-lecture how to deal with ease with certain aspects of day-to-day life. I will never forget the lessons given to me by prof. Peter Varga (†27. 10. 2018). His simple "Are you working hard enough?" still resonates in my thoughts when I feel a need to complain. He was my greatest senior scientific mentor. There was much more that I needed to learn from him that I will probably need to learn the hard way (and he would like me to learn it the hard way). His way of dealing with people and with scientific problems was a great motivation for me to further pursue my career in science. My deepest thanks go to Michal Urbánek. His outstanding diligence and skillful guidance have paved my way in daily life as a scientist. I simply owe him a lot. Many thanks go to my fellow Ph.D. students. Marek Vaňatka was always around when there was anything needed. Igor was always there when a mood needed to be lifted in the office and Tomáš Musálek and Lukáš Kormoš were always there when there was a time for a foosball match. I would also like to thank my fellow scientist Kai Wagner. He has introduced me to the BLS method. He spent many harsh evenings with me when measuring the spin-wave propagation in our metastable system. My acknowledgment also goes to my colleagues from TU Wien. Jonáš Gloss was steadily providing the samples and has taught the crucial parts of the metastable iron-nickel growth to many students. His supervisor prof. Michael Schmidt was always behind the whole project and as a co-author, he taught me (even though he might not be aware of it) much about scientific writing and critical thinking. I deeply admire prof. Ulrike Diebold as the head of the group in TU Wien for her sensitive but decisive way of dealing with world-class science. Yet the biggest thanks goes to my family and especially to my wife Jana. In the end, her love has defined me more than I have thought it ever could.

CzechNanoLab project LM2018110 funded by MEYS CR is gratefully acknowledged for the financial support of the measurements sample fabrication at CEITEC Nano Research Infrastructure.

Ing. Lukáš Flajšman

Contents

Introduction

> *"Knowledge and error flow from the same mental sources; only success can tell one from the other."*
>
> – Ernst Mach

The magnetism is amazing. It has never ceased to amaze people from the first observations of magical iron attracting stones up to the modern era of magnetism with vast research topics as e.g. spintronics and magnonics. The spintronics has already brought humanity a great advancement, mainly in the tremendous increase in the data storage density enabled with the discovery of giant magnetoresistance (GMR) [1–3] and tunelling magnetoresistance (TMR) [4–6] effects. In the last decade, the interest has been also shifted to the non-volatile magnetic random access memories (MRAM). The conceptual devices as a field-MRAM, vortex-MRAM, spin-transfer torque-MRAM (STT-MRAM), and spin-orbit torque-MRAM (SOT-MRAM), have been presented [7], and some of them are already available at the market. Despite those great advances achieved in the field of magnetism, the demands placed on future information technology generates the need for devices with higher data-transfer speeds and lower power consumption. One of the possible approaches relies on the field of magnonics, where the information is transferred without the need for moving an electric charge. This is a big advantage since it avoids Joule losses and associated heating, which is one of the limiting factors of modern transistor-based devices [8]. Magnonics is a particular branch of magnetization dynamics dealing with spin waves and their particle-like analog, magnons [9]. The spin waves represent temporally and spatially resolved coherent angular momentum waves in solid-state materials. Spin waves can travel over relatively large distances, are enormously tunable with wavelengths ranging from centimeters to nanometers, and still possess the compatibility with a current electric charge based technology via spin pumping phenomena [10]. Due to recent advances in nanofabrication and advanced deposition techniques, spin-wave based nanodevices acting as efficient and fast logic elements, frequency filters, or multiplexing ports have been recently demonstrated [8, 11–16]. Great effort has been already dedicated to the magnonics, yet it still stays rather unclear whether the magnonics will yield a solution to the approaching physical limit of CMOS based technology. The modern technology relies on patterning at a nanoscale. This more and more plays a central role in the development of novel electronic, optical, and magnetic devices, systems, and materials. Nanostructuring can lead to effects unattainable in bulk materials. In the field of magnonics, the true workhorse in the nanostructuring is the electron beam lithography with subsequent lift-off or ion beam etching processes. These techniques add or remove material in a very binary fashion. The resulting structures are planar with very defined edges or thickness steps. In the case of in-plane magnetized structures, these step-like transitions create an inherent demagnetizing field strongly affecting the magnetic ordering or spin-wave response of the system. This can be used as an advantage for sub-λ

channeling of spin waves in the very narrow domain walls [17]. But in general, it is very hard to control this demagnetizing field in structures prepared by conventional means. During the years more and more unconventional systems have been presented, always overcoming some of the limits of the conventional technology (yet naturally coming with certain specific downsides of the specific system) [18–25].

Some approaches offer the possibility to control the magnetic ordering locally, e.g. by modification of the exchange bias in the magnetic double-layer [18, 19]. This allows to deterministically write very complex magnetic patterns that cannot be stabilized in any conventional system. Other approaches use the ion beam to slightly modulate the magnetization of the irradiated areas [20, 23]. The achievable depth of modulation is rather small, and it comes with the deterioration of the magnetic layers that is generally undesirable. Continuing with the ion beam based approaches, a very promising system of $Fe_{60}Al_{40}$ has been presented. It does not show any ferromagnetic behavior in the ordered B2 structure [21, 24]. When irradiated slightly by the ion beam, the introduced disordered A2 structure shows ferromagnetic ordering. The saturation magnetization of the resulting structures can be continuously tailored through the selection of the ion beam dose used in the irradiation processes. When using the focused ion beam (FIB), very small magnetic elements can be written to the nonmagnetic material where each structure can, in theory, have very different saturation magnetization. This readily offers a huge advantage over conventional technologies as it allows the researchers to change spatially (and even in single magnetic structure) the saturation magnetization. The downside of this approach is high spin-wave damping ruling out the spin-wave propagation.

In this work, we present the possibilities of novel ion beam phase transition material based on $Fe_{78}Ni_{22}$ [26] that offers the combination of the approaches presented by [18] and [24]. In a similar fashion, as was presented by [24] we can, by specific ion beam irradiation procedure, control the saturation magnetization of the material all the way from the nonmagnetic state up to the fully ferromagnetic state with high saturation magnetization. Additionally to saturation magnetization control, as in the before mentioned approaches, we can locally control the orientation of the uniaxial magnetic anisotropy axis. This mimics to some extent what has been presented by [18]. Above all, we can combine the two approaches in a single magnetic structure, giving us the unprecedented possibilities for tailoring magnetization landscapes unattainable in any other system.

We have used the unique features of the material to prepare and study sets of magnonic waveguides, where we studied the spin-wave propagation. For the first time ever, the spin-wave propagation was experimental observed in the system with an ion beam induced nonmagnetic/magnetic phase transition. Not only we will show that the spin waves can propagate in the system, but we will also show that the spin waves propagate in our waveguides even at zero external magnetic field in the geometry with the highest group velocity. By using a suitable model, we will be able to elaborate on the magneto-dynamic parameters of our system by fitting the measured dispersion of the spin waves. From the knowledge of the waveguides, as basic building blocks of magnonic circuitry, we afterward propose and test more complex devices that use the unique possibilities of our system.

The organization of the thesis is as follows: Chapter 1 is concerned with the theoretical background needed for understanding the presented experimental work. We first introduce the basic concepts of magnetostatics. The origin and the role of the demagnetizing field in the magnetic system is described thoroughly. Then the driving forces of the magnetic ordering are presented in the form of micromagnetic energies. Very simple yet very useful Stoner-Wohlfarth model of hysteresis is presented. The section that follows the magnetostatic part is devoted to the magnetization dynamics. The concept of spin waves is introduced. The dispersion of the spin waves in a thin film is presented with a focus on the effect of the uniaxial magnetic anisotropy on the spin-wave dispersion. We end the chapter with a small overview of the spin-wave excitation means with a particular focus on the microwave antennas that are used in the experimental part for the spin-wave excitation experiments.

Chapter 2 is devoted to the experimental methods employed in the thesis. Magneto-optical Kerr effect and its manifestation in the form of Brillouin light scattering are presented. Both methods are the main workhorses of the presented thesis, and thus we put a focus on the experimental limits of the techniques and also on the actual implementation in the experiments.

Rather extensive chapter 3 presents the experimental work on the unique $\mathrm{Fe}_{78}\mathrm{Ni}_{22}$ system. We show the effect of the ion dose on the resulting magnetic properties of the transformed material. With an aim for nanostructuring, we also present a possible approach on how to lower the size of the growth initiation region with success. We present the fabrication of nanostructures with sizes down to 50 nm. By dose-testing of the material, we reveal two mechanisms of the ion beam induced transformation. One that allows for continuous tuning of the saturation magnetization and the other one that allows for changing the uniaxial magnetic anisotropy direction. The effect of the focused ion beam scanning direction used during the writing process is recognized directly in the SEM in the changes of the crystallographic contrast. We show how the crystallography (unambiguously connected to the magnetic anisotropy) can be controlled only by the means of changing the scanning direction of the FIB. An extensive part of the chapter is devoted to the description of the effect of the FIB scanning direction on the magnetic anisotropy of the material.

The experimental findings of the chapter 3, are translated to chapter 4 devoted to the spin-wave propagation in the waveguides prepared by FIB direct writing. We first introduce the micromagnetic model of the system, and we extract the relevant parameters for the subsequent experimental work. From the Kerr microscopy/magnetometry, we experimentally verify the micromagnetic state of the waveguides. The phase-resolved Brillouin light scattering analysis has allowed us to obtain the unknown magnetic parameters of the system. Knowledge of this character is needed for the design of more advanced spin-wave based devices.

In chapter 5, we employ the tunability in the direction of the uniaxial magnetic anisotropy in the fabrication of the spin-wave turns. We show that even if the magnetization in both arms of the 90° turn is stabilized in the desired direction, the bending element between the arms causes a huge distortion of the wave-front hindering the spin-wave propagation.

In the last experimental chapter 6, we use another unique property of the system. We exploit the possibility to spatially change the saturation magnetization of the system by fabricating the prototypes of graded-index magnonic waveguides. For the positive and negative profiles of the gradient, we study the thermal spin-wave spectra as well as the spin-wave propagation properties. Very low effect of the gradient on the spin-wave propagation is found.

Last chapter 7 summarizes the work. Points out the major results and suggests the orientation of future studies.

1. Theoretical background

The presented chapter introduces the background needed for understanding the topics covered by the thesis with more emphasis on the micromagnetic theory and magnetization dynamics. We follow the texts on magnetism by Coey [27], Blundell [28], Bland [29], and Aharoni [30], where for magnetization dynamics, the textbooks by Stancil and Prabhakar [31], Demokritov [32, 33] and Hillebrands [34–36], cover most of the theory needed for the sake of understanding the presented thesis. For more specialized topics concerned with e.g. spin-wave eigenmodes in confined structures, see the book of Demokritov and Slavin [37].

1.1. Magnetic field of a magnet

Magnetism, as seen by Maxwell's equations, originates from the moving charge (i.e. electric current). When looking at a regular piece of a permanent magnet, where no self-heating is observed, one states that no currents are flowing through the material, and thus there should be no magnetism. But when observed from distance small enough, the electrons orbiting around the nucleus (with orbital momentum $\boldsymbol{l}$) will resemble more the elementary current loops that are known to generate a magnetic field. This property is called orbital magnetism and the magnetic dipole moment originating from the orbital motion is defined as

$$\boldsymbol{m}_l = g\frac{|e|}{2m_\mathrm{e}}\boldsymbol{l}. \tag{1.1}$$

Here the g is a Landé factor (for orbital motion $g = 1$), e is a charge of an electron, and m_e is the mass of the electron. The prefactor in (1.1) is often rewritten with the gyromagnetic ratio $\gamma = ge/2m_\mathrm{e}$. In addition to the angular momentum, the electron itself carries a small intrinsic magnetic moment originating in its spin $\boldsymbol{s}$. From the quantum mechanical principle, Heisenberg's uncertainty principle, only one component along arbitrary quantization axis (e.g. z) of both angular and spin momentum is observable. To get a total magnetic moment we need to perform the addition of observable eigenvalues of the angular and spin momentum operators $\langle \boldsymbol{l}_z \rangle$ and $\langle \boldsymbol{s}_z \rangle$ leading to the total magnetic moment along the quantization axis

$$\langle \boldsymbol{m}_z \rangle = -\frac{\mu_\mathrm{B}}{\hbar}\left(g_l \langle \boldsymbol{l}_z \rangle + g_s \langle \boldsymbol{s}_z \rangle\right), \tag{1.2}$$

where $\mu_\mathrm{B} = \frac{|e|\hbar}{2m_\mathrm{e}}$ is called Bohr magneton. Orbital Landé factor of the electron $g_l = 1$, the value is approximately twice lower than the spin Landé $g_s \sim 2$. The resulting magnetic moment of an atom is the result of various competing magnetic moments of all electrons in the atom. Moments can add up or cancel each other leading to non-zero or zero net magnetic moment. The driving force of this selection is the energy minimalization principle of the mutual electron-electron interactions of nearby atoms. Solely the fact that the atom carries a magnetic moment does not simply result in the net magnetic moment of the material comprising of the individual atoms. For magnetic ordering and net magnetic moment (for ferromagnetic materials), a coupling of nearby atoms through short (e.g. interatomic exchange) and long-range (dipole-dipole) interactions is necessary. One of the purely spin-related interactions appearing in an atom is the so-called Exchange interaction. The origin of this interaction can be traced to the Coulomb interaction and Pauli exclusion principle. For ferromagnetic materials studied in this thesis (Fe, Ni), the interaction leads the atoms to parallel orientation of spins resulting in non-zero net magnetic dipole density $\boldsymbol{M}$ observed below Curie ordering temperature. The $\boldsymbol{M}$ is simply called magnetization and is defined as

$$\boldsymbol{M} = \frac{1}{V} \sum_{n=0}^{m} \boldsymbol{m}_n, \tag{1.3}$$

where volume V is chosen to be large enough to average the effect of individual atoms, yet small enough to account for local changes of spin orientations. The elementary current loops in a material (magnetic moments) can be viewed as magnetic dipoles producing so-called demagnetizing $\boldsymbol{H}_\mathrm{d}$ and stray $\boldsymbol{H}_\mathrm{s}$ field depending on whether we observe the field inside or outside of the material. The macroscopic relation interconnecting the fundamental field $\boldsymbol{B}$, auxiliary field $\boldsymbol{H}$ and magnetization $\boldsymbol{M}$ is following

$$\boldsymbol{B} = \mu_0 \left(\boldsymbol{H} + \boldsymbol{M}\right), \tag{1.4}$$

where μ_0 is vacuum permeability. When we apply the divergence operator to equation (1.4), and we employ the Gauss law (from Maxwell's equation), we arrive at the expression

$$\nabla \cdot \boldsymbol{H}_\mathrm{d} = -\nabla \cdot \boldsymbol{M}, \tag{1.5}$$

connecting the stray field and demagnetizing field $\boldsymbol{H}_\mathrm{d}$ to the divergence of magnetization and to hypothetical magnetic charges with volume density defined as $\rho_\mathrm{M} \equiv -\nabla \cdot \boldsymbol{M}$. Whenever there is a divergence in magnetization, the magnetic field is also present. This can be nicely seen in an equivalent view when we envision the magnetic system as a sea of discrete dipoles instead of the continuum of the magnetization vector. For infinite system, when we sum the magnetic fields from all dipoles in one place, we see that for each field contribution from the individual dipole, we find an equivalent counterpart effectively screening the respective contribution. This is a direct consequence of the high symmetry of the infinite system. Only when we break the symmetry and e.g. instead of the infinite system we consider only the semi-infinite system (in simplest case we consider the dipoles to point perpendicular to the system boundary) we see that closer we get to the edge of the plane, the less is the magnetic field from the individual dipoles compensated. At the system boundary, there is no source of field compensation, and thus the demagnetizing field here is the strongest. The connection of the stray/demagnetizing field and the divergence of magnetization is depicted in Fig. 1.1.

It might not be apparent from the first view, yet the divergence of the magnetization also comes with an energy cost to the system. The demagnetizing field created by the divergence of magnetization acts back on the magnetization itself and adds an energy contribution called the demagnetizing energy:

$$E_\mathrm{dem} = -\int \boldsymbol{M} \cdot \boldsymbol{H}_\mathrm{d} \, \mathrm{d}V. \tag{1.6}$$

This has a direct consequence in the so-called *Charge avoidance principle* which states that the magnetic charges have to be avoided as they increase the energy of the system.

In the following text, we will see that the demagnetizing energy is a driving force for creating complex domain structures. Fig. 1.1 shows that expectantly the largest demagnetizing magnetic field is observed where the magnetization points outside of the magnetic volume. This creates a large divergence in magnetization $\nabla \cdot \boldsymbol{M}$ where for a case where $\boldsymbol{M} \perp \boldsymbol{n}$ (for $\boldsymbol{n}$ being the surface normal) we find

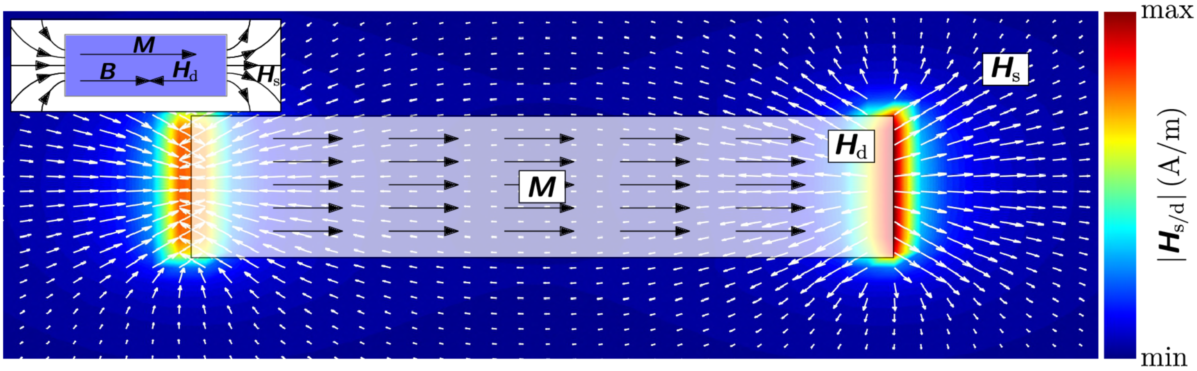

Fig. 1.1: Simulation of a demagnetizing field created by a bar magnet with magnetization pointing to the right (done in mumax^3 micromagnetic package). White arrows correspond to demagnetizing/stray field and black arrows represent the magnetization direction. Background color represents the magnitude of the demagnetizing/stray field $|\boldsymbol{H}_{\mathrm{s/d}}|$, where red (blue) color represents the highest (lowest) amplitude of the magnetic field. The top-left inset shows the orientation of magnetization $\boldsymbol{M}$, total field $\boldsymbol{B}$ and $\boldsymbol{H}_{\mathrm{d}}$ inside of the structure.

$$|\nabla \cdot \boldsymbol{M}| = \delta_{\mathrm{Dirac}} M_{\mathrm{S}} = -|\nabla \cdot \boldsymbol{H}_{\mathrm{d}}|, \tag{1.7}$$

where δ_{Dirac} is Dirac delta. If we integrate the above equation, we obtain $|\boldsymbol{H}_{\mathrm{d}}| = M_{\mathrm{S}}$.

In case of semi-infinite magnetic plane magnetized out-off-plane (or long magnet with longitudinal magnetization as in Fig. 1.1), one can estimate the magnetization of the material solely from the strength of the stray field on the surface. These arguments also illustrate why there is no magnetic field outside of the infinite thin magnetic film with out-of-plane (OOP) magnetization. When we take into account both divergences of $\boldsymbol{M}$ on both surfaces, we see that both interfaces contribute to the total magnetic field by the same amount only with reversed polarity. Such a trivial analysis depicts illustratively the trend, but when dealing with real-world problems as calculating the demagnetizing field, a more complex approach is required.

The calculation of the demagnetizing field is of importance when we need to consider confined magnetic structures. To introduce one of the possible approaches to how the demagnetizing field can be derived for uniformly magnetized bodies, we again use the effective magnetic charge density

$$\rho_{\mathrm{M}} \equiv -\nabla \cdot \boldsymbol{M}, \tag{1.8}$$

and in case there is no free charge current density, we define the scalar potential of the magnetic field (the approach closely follows the electrostatic case, where we assume real and monopolar sources of an electric field):

$$\boldsymbol{H}_{\mathrm{d}} = -\nabla \Phi, \tag{1.9}$$

whereby employing the (1.8) we arrive to Poisson equation:

$$\nabla^2 \Phi = -\rho_{\mathrm{M}}. \tag{1.10}$$

This can be readily solved for three dimensions through the Green's function

$$G(\boldsymbol{r}) = \frac{1}{4\pi|\boldsymbol{r}|}, \tag{1.11}$$

giving the following integral

$$\Phi(\boldsymbol{r}) = \int d\boldsymbol{r}' G(\boldsymbol{r} - \boldsymbol{r}')\, \rho_{\mathrm{M}}(\boldsymbol{r}) = \int d\boldsymbol{r}' \frac{-\nabla' \cdot \boldsymbol{M}(\boldsymbol{r}')}{4\pi(\boldsymbol{r} - \boldsymbol{r}')}. \tag{1.12}$$

This gives us the tool of how the potential can be derived for any general geometry. In some cases, it is more convenient to work directly with the magnetization, instead of its divergence. Equation (1.12) can be integrated by parts. When we consider the surface outside of the magnet, we get to alternative form with gradient in-place of divergence operator:

$$\Phi(\boldsymbol{r}) = \int d\boldsymbol{r}' \nabla' \left(\frac{1}{4\pi(\boldsymbol{r} - \boldsymbol{r}')} \right) \boldsymbol{M}(\boldsymbol{r}) = \int d\boldsymbol{r}' \nabla' \left(\frac{\boldsymbol{r} - \boldsymbol{r}'}{4\pi|\boldsymbol{r} - \boldsymbol{r}'|^3} \right) \boldsymbol{M}(\boldsymbol{r}). \tag{1.13}$$

One can realize that the right form of the equation (1.13) is simply the integration of elementary magnetostatic potentials originating in magnetic dipoles.

When solving the demagnetizing field problem, we can use two approaches: We find only the parts of our geometry, where $\nabla \cdot \boldsymbol{M}$ occurs and we integrate using the (1.12) or we integrate over the whole volume with the help of (1.13). Once we solve one of the integrals, we have to find the gradient of the scalar potential to obtain the demagnetizing field [with the help of an equation (1.9)]. This field is highly local and depends on the geometry of the problem and also on the position where the field is evaluated. In most cases, we are interested in the spatial average of the demagnetizing field throughout the whole volume. Doing so, one can usually (generally the solution is always valid for uniformly magnetized ellipsoids) find direct relation of the magnetization to the demagnetizing field through simple linear relation:

$$\boldsymbol{H}_{\mathrm{d}} = -\overset{\leftrightarrow}{\boldsymbol{N}} \boldsymbol{M}, \tag{1.14}$$

where $\overset{\leftrightarrow}{\boldsymbol{N}}$ is the demagnetizing tensor. It is noteworthy that the trace $\mathrm{Tr}\,\overset{\leftrightarrow}{\boldsymbol{N}} = N_x + N_y + N_z = 1$. The following Fig. 1.2 summarizes three shapes of high symmetry and its demagnetizing tensors.

One can easily see the symmetries in each object and also that e.g. to fully overcome the demagnetizing field of thin-film, one has to apply external magnetic field with strength equal to the saturation magnetization of the material.

Represented shapes in Fig. 1.2 are easily solved by the apparatus presented in (1.9) and (1.13). When we try to obtain the solution for a waveguide with rectangular cross-section, the respective integrations become hard to carry out. Not only we have to integrate the (1.13) on the faces of the waveguide (here $\nabla \cdot \boldsymbol{M} \neq \boldsymbol{0}$) but afterward second integration is needed to get the spatial average over the whole volume. Both steps are needed in order to calculate the demagnetizing tensor $\overset{\leftrightarrow}{\boldsymbol{N}}$. The approach seems to be quite straight forward yet not easy to work out. Fortunately, the process has been carried out by Aharoni [38].

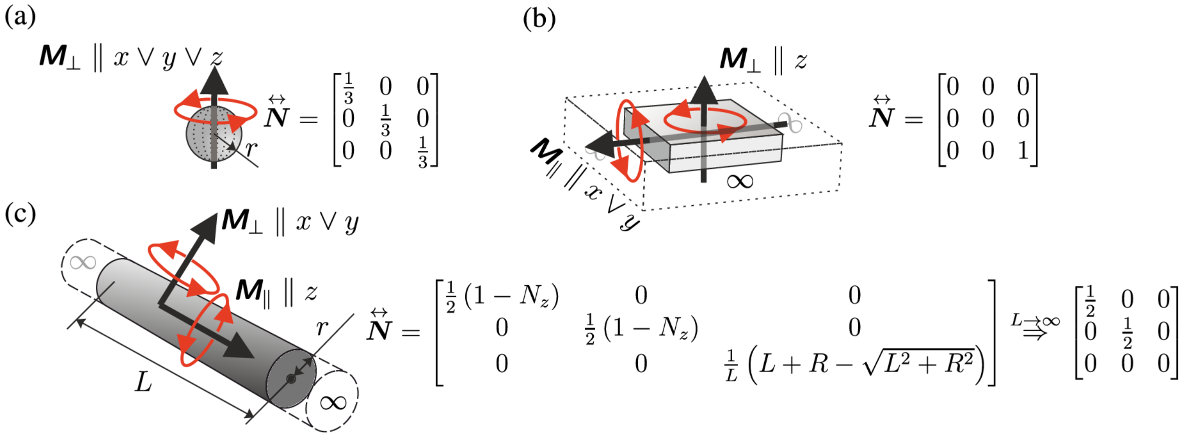

Fig. 1.2: Three representations of demagnetizing tensors for homogeneously magnetized bodies with high symmetry. (a) sphere, (b) thin infinite film, and (c) cylindrical magnet with the long-length limit.

As in many cases, the thickness t of the layer is way smaller than other dimensions, we derived the simplified form of a rather long equation (7.1) presented in the Appendix 1. We expanded the equation by the Taylor series of a parameter t to the first order around $t = 0$. After some algebra, we obtained

$$H_\mathrm{d} = \mu_0 M_\mathrm{S} \frac{7t\left(2\sqrt{l^2+w^2} + l\log\left(\frac{4l^2\left(2l\left(l-\sqrt{l^2+w^2}\right)+w^2\right)}{w^2}\right) - 2l\log(t) + l - 2w\right)}{25\pi l w}, \tag{1.15}$$

which can be again simplified by assuming $w \ll l$. Such an assumption is rather strong, so we leave it out. The calculation using the full universal approach for the magnetized rectangular prism is presented in Fig. 1.3, where we also show the approximate solution (1.15) of the thin waveguide. The agreement between the full approach and the thin-film limit is satisfying. For the following calculations, we will employ the approximate solution.

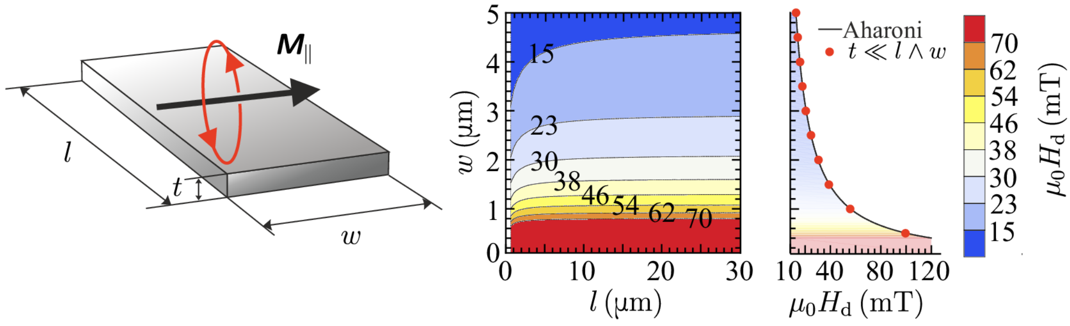

Fig. 1.3: Calculated demagnetizing field of the rectangular prism while varying both the length and the width of the prism for fixed thickness 9.5 nm and $M_\mathrm{S} = 1.4\,\mathrm{MA/m}$ calculated by the model of Aharoni from (7.1). The right plot shows a vertical cut of calculated dependence for $l = 30\,\mu\mathrm{m}$, where we also compare the full approach with the approximate solution presented by the equation (1.15).

In the later text, we will show the discrepancy between the demagnetizing field found by the analytical approach and the demagnetizing fields found from the numerical simulations. We will find that the assumption of a homogeneously magnetized body is simply too strong, and the results of the analytic theory have to be employed with care. Despite its limitations, the analytically model shows educatively the overall trend and can serve as a good sanity check of the micromagnetic simulations.

1.2. Magnetostatic energies

The theory of demagnetizing fields presented in the previous section follows only the simplest cases of homogeneously magnetized bodies. Overall it is not sufficient to explain many of the phenomena found in the magnetism as e.g. formation of magnetic domains. To describe the magnetic system, we need to employ the thermodynamic potentials. In magnetism, we usually use the free energy. When we find the minimum of the energy, we consider the system to be in equilibrium. To calculate the energy of the system, we consider a couple of energy contributions where some of them are intrinsic to the material, and some are extrinsic.

1.2.1. Exchange energy

The quantum-mechanical direct exchange interaction has its origin both in the Pauli exclusion principle and Coulomb interaction. The Pauli exclusion principle forbids two electrons (fermions) to enter the same quantum state, and thus there is energy difference of two spin-up electrons and one spin-down and one spin-up electron. In other words, there has to be a joint wave function that is antisymmetric in particle permutation [27]. Rigorously it can be described as an overlap of wave functions of neighboring atoms (spins). There are two major groups of materials with magnetic properties where the difference in both groups lie in the orbitals responsible for the magnetism. We mainly distinguish two classes: 3d metals (Fe, Ni, Co, ...) and 4f rare earth magnets (Nd, Gd, Tb, ...).

In the model presented by Heisenberg [27, 28], the exchange Hamiltonian of a many-electron system consisting of N spins is equal to

$$\mathcal{H}_{\mathrm{ex}} = -2 \sum_{i}^{N} \sum_{j}^{N} J_{ij} \boldsymbol{S}_i \cdot \boldsymbol{S}_j, \tag{1.16}$$

where J_{ij} is the exchange integral and $\boldsymbol{S}_i$ and $\boldsymbol{S}_j$ are neighboring spins. It can be easily seen that when constant $J_{ij} < 0$, the lowest energy state is found for antiparallel alignment of the spins. This is the case of antiferromagnetic substances. For $J_{ij} > 0$ the system prefers parallel alignment of spins and the ferromagnetic order arises. The sign and amplitude of J_{ij} depend highly on the inter-atomic distances of individual atoms, as can be determined by the Bethe-Slater curve [39]. In the field of magnetism, we use more often so-called exchange constant A_{ex} (a material property), where the connection to the exchange integral depends on the lattice type and lattice constant a. For cubic lattice, A_{ex} can be expressed as $A_{\mathrm{ex}}^{\mathrm{bcc}} = 2J_{ij}S^2/a$ (for bcc lattice $S = 1$) [40, p. 105]. The exchange energy, as it arises simply from the overlap of the electron wave functions, is highly local and thus when calculating the total energy of the system as in (1.16), we calculate the energy only for the closest neighbors. The energy difference for ferromagnetic spins between parallel and antiparallel states is of the order of 1 eV. It is the largest contribution from all magnetic energies. When we calculate the eigenfrequency of the system with $1 \sim$eV energy, we find that it is in the order of 100 THz. When we consider only exchange interaction in the system the ground state will be homogeneously magnetized body.

The expression (1.16) allows to describe the discrete spin systems. Often we are more interested in continuum approximation (which allows us to connect single spins to the continuous value of magnetization $\boldsymbol{M}$). In continuum picture, the exchange Hamiltonian is rewritten to the integral of exchange energy density:

$$E_{\mathrm{ex}} = \int A_{\mathrm{ex}} \left(\nabla \frac{\boldsymbol{M}}{M_{\mathrm{S}}} \right)^2 \mathrm{d}^3 r \tag{1.17}$$

having a similar consequence as (1.16). We present the (1.16) as it gives more direct insight into the phenomena than the continuum approximation. All other micromagnetic energies will be given in the approximation of the continuum.

1.2.2. Zeeman energy

Zeeman energy expresses the interaction of magnetization with the external magnetic field. It states that the magnetization is in the lowest energy state (when considering only the Zeeman energy) when it is aligned to the external magnetic field direction:

$$E_{\mathrm{Z}} = -\int \boldsymbol{M} \cdot \boldsymbol{B} \, \mathrm{d}^3 r. \tag{1.18}$$

1.2.3. Dipolar energy

Whereas the exchange energy in the ferromagnetic system preferred parallel alignment of the spins, the dipolar energy prefers antiparallel alignment. In the introductory section, we have already shown that systems, in general, tries to avoid the magnetic charges [(1.5) and (1.8)] as it leads to the creation of the demagnetizing field acting back on the magnetization. Knowing the energy of the external magnetic field from (1.18) we can simply deduce demagnetizing selfenergy of the system as

$$E_{\mathrm{d}} = -\frac{1}{2} \int \mu_0 \boldsymbol{M} \cdot \boldsymbol{H}_{\mathrm{d}} \, \mathrm{d}^3 r. \tag{1.19}$$

Since each magnetic dipole is immersed in the magnetic field created by all other dipoles in the system, we get to the prefactor $\frac{1}{2}$. In this way, we avoid counting the interaction energy twice when we sum (integrate) over the magnetic body. The existence of the demagnetizing energy hinders the possibilities for the analytical treatment of most magnetic systems as one arrives at the auto-consistent problem. Yet for some cases of uniformly magnetized bodies, one can utilize the previously introduced concept of demagnetizing tensor and arrive rather simply to the energy of the system. To do so, we substitute (1.14) to (1.6). Since we already performed the integration over the body (demagnetizing tensor components are spatial averages), we arrive directly to:

$$E_{\mathrm{d}} = \frac{1}{2} V \left(N_x M_x^2 + N_y M_y^2 + N_z M_z^2 \right), \tag{1.20}$$

where V is the volume of the system. We see that depending on the demagnetizing factors, some directions of the magnetization will be preferred simply from the geometry of the problem. This leads to an effective anisotropy of the system discussed more in detail in the following section.

1.2.4. Anisotropy energy

In first-order approximation, the Heisenberg Hamiltonian is isotropic, and thus the system does not prefer any direction for the magnetization to align with. In real systems, this is not true: if we consider the crystalline structure of the material, the spin-orbit interaction will link the electronic structure (electron orbits) to certain crystallographic directions of the material. In other words, some directions of magnetization in the crystal will be energetically more favorable than the others. The difference of the most energy-efficient and least energy-efficient directions can be described by the angular dependence of the energy on the magnetization declination from some crystallographic axis. This energy contribution is called magnetocrystalline anisotropy, and it is one of the major driving factors defining the actual real-world orientation of the magnetization (exchange interaction is isotropic, thus any other energy contribution is the leading factor for the actual alignment of the magnetization). The mathematical form of the anisotropy energy is rather phenomenological as the calculation of spin-orbit interaction is not very accurate. We usually describe the anisotropy as a power series expansion, with respect to some crystallographic directions of the crystal. Naturally, we need to respect the symmetry of the problem.

Uniaxial anisotropy
Uniaxial anisotropy is the most trivial case as it depends only on one parameter: angle κ. This angle represents the angle between the magnetization and the uniaxial axis. The uniaxial anisotropy energy contribution can be written as

$$E_{\mathrm{u}} = \int \left(-K_1 \cos^2 \kappa + K_2 \cos^4 \kappa\right) \mathrm{d}^3 r, \tag{1.21}$$

with a K_1 and a K_2 beeing experimentally found anisotropy constants. In most cases, the K_2 constant is negligible and thus does not have to be taken into account. Then we are left with only one anisotropy constant K_1, which we quite often denote as K_{u}. The parameter K_1 can be both positive and negative, where for positive values of K_1, we get an easy axis, and for the negative value, we get an easy plane solution. Both K_1 and K_2 have a temperature dependence that can differ from the temperature dependence of the saturation magnetization.

Cubic anisotropy
In cubic crystals (Fe, Ni, ...), the anisotropy follows the lattice symmetries and can be described again as an expansion of directional cosines of the angle between the magnetization and the crystallographic axis. We utilize spherical coordinates (defined with angles θ and Φ) to do so:

$$\begin{aligned} m_x &= \cos\theta \sin\Phi, \\ m_y &= \sin\theta \sin\Phi, \\ m_z &= \cos\Phi. \end{aligned} \tag{1.22}$$

And in a similar fashion as in (1.21) we write the series as

$$E_{\mathrm{c}} = \int \left[K_1^{\mathrm{c}} \left(m_x^2 m_y^2 + m_y^2 m_z^2 + m_x^2 m_z^2\right) + K_2^{\mathrm{c}} m_x^2 m_y^2 m_z^2\right] \mathrm{d}^3 r, \tag{1.23}$$

and again, the higher-order terms are neglected. Very often also the K_2^{c} term is low and we consider the only case with K_1^{c}. Then, depending on the sign of the K_1^{c} term, we

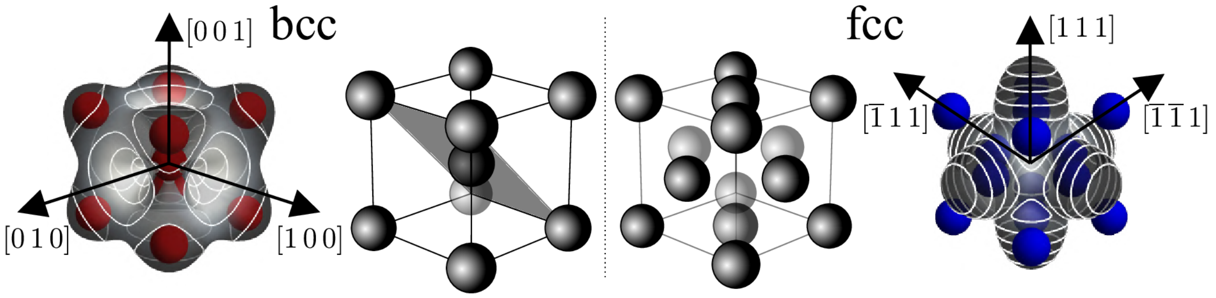

Fig. 1.4: Comparison of the energy profiles of bcc (red atoms) and fcc (blue atoms) structures defined by positive (bcc) and negative (fcc) parameter K_1^{c}. The grayscale in the left and right figures represents the energy of the system for different orientations of the magnetization. White lines are isoenergy curves. The arrows with crystallographic directions denote few exemplary easy axes of the system. Middle sketches show the sketch of bcc and fcc lattice. In the case of the bcc structure, the (1 1 0) plane is denoted as this particular crystallographic plane will be of interest for the experimental part of the thesis.

distinguish two types of cubic anisotropies (see Fig. 1.4). First is of the iron type often found in compounds with body-centered-cubic lattice (bcc), where the easy axes are of the set of direction denoted by $\langle 1\,0\,0 \rangle$ (e.g. [1 0 0] [0 1 0], . . .). It can be seen that these directions are the least occupied direction in the crystal lattice. The second type, nickel type, is usually formed for face-centered-cubic lattice materials, where the easy axes are in the set of directions denoted $\langle 1\,1\,1 \rangle$ (e.g. [1 1 1] $[1\,\bar{1}\,1]$, . . .). In bcc lattice, we see that the easy axes follow the principal axes of the crystal, yet in the case of fcc lattice the easy axes are formed on the body diagonals of the cubic lattice.

Shape anisotropy

The (1.20) clearly shows that the energy will differ between various magnetization orientations in a magnet of a certain shape. It is straightforward to see that similar form of (1.21) can be derived for example for a thin film, where the demagnetizing tensor is trivial [see Fig. 1.2 (b)]. When we assume again the magnetization in its polar form (ignoring its magnitude) as in (1.22) and we multiply it by the tensor form, we arrive at following demagnetizing field vector $\boldsymbol{H}_{\mathrm{d}} = (0, 0, \cos\kappa)$. When we multiply this form by $\boldsymbol{M}$, we obtain the $\cos^2\kappa$ dependence as in case of uniaxial anisotropy. In a similar manner, we can derive various energy contributions stemming simply from the shape of the structure. The role of the shape anisotropy starts to play a crucial role when designing basic blocks of magnonic circuitry. Elementary structures as waveguides will simply from the shape of the structure prefer the magnetization to lie in the longest direction of the waveguide, which might not be the most suitable geometry from the spin-wave propagation arguments.

1.3. Magnetic order

All energy contributions presented in the previous sections will contribute to the total energy of the system

$$E_{\mathrm{total}} = E_{\mathrm{ex}} + E_{\mathrm{Z}} + E_{\mathrm{d}} + E_{\mathrm{ani}} + E_{\mathrm{other}}. \tag{1.24}$$

E_{ani} is the sum of the all magnetocrystalline energy contributions. E_{other} stands for other (often effective) energy terms as Dzyaloshinskii–Moriya interaction [41, 42], magnetostrictive energy [30, p. 87] and other possible energy contributions. In equilibrium, the physical system will find the energy minima by changing the local orientation of magnetization. All relevant energy contributions will compete until the magnetization landscape with the smallest energy is found (or local minima). This is rather nontrivial optimization problem for which Brown [43] presented the concept of an effective magnetic field, which takes all the energy contribution and translates them to the local magnetic field. The effective field can be calculated as

$$\boldsymbol{B}_{\mathrm{eff}} = \frac{\partial E_{\mathrm{total}}}{\partial \boldsymbol{M}}. \tag{1.25}$$

In the equilibrium, of course, any torques have to vanish, and thus we get the second equation presented by Brown

$$\boldsymbol{M} \times \boldsymbol{B}_{\mathrm{eff}} = \boldsymbol{0}. \tag{1.26}$$

By utilizing (1.25) and (1.26), one can use the variational principle and try to analytically solve a rather complex problem of energy functional minimalization. The most cumbersome contribution will originate in the demagnetizing field as it directly depends on the orientation of the whole magnetization in the system. As a result of this, only a few cases can be solved analytically. For a comprehensive overview of the theory and examples of magnetization ordering see the book of Hubert and Schäfer [44]. In Fig. 1.5 we schematically show the effects of the driving forces of the magnetic ordering: exchange energy, dipolar energy, uniaxial magnetic anisotropy energy, and Zeeman energy. We one by one add energy contributions to the magnetic system and we study how the total magnetization landscape evolves.

The Fig. 1.5 captures how isotropic exchange energy forms a trivial magnetization configuration [Fig. 1.5 (a)], which results in high demagnetizing energy from the demagnetizing field having its origin in the magnetization pointing directly to the right/left edge of the structure. In the case, when we also consider the demagnetizing energy in the magnetic ordering [Fig. 1.5 (b)] four distinct regions where the magnetization has a parallel orientation are formed. We call the regions with uniform magnetization as magnetic domains. Such a close-flux structure highly decreases the demagnetizing field as no magnetization points to the edge of the structure. Contrary to that, we see an increase in the exchange energy density in the regions that separate the individual domains - domain walls. Since the exchange energy is one of the highest contributions, the system will find the magnetic configuration by (effectively) lowering the domain wall lengths. In the middle of the structure, the neighboring spins would be in the highest energy state of antiparallel spin configuration, and thus the magnetization (in the excess of the demagnetizing energy) will be pulled out-of-plane, and so-called vortex core is formed (black dot). In Fig. 1.5 (c) we added also the magnetocrystalline anisotropy with the horizontal easy axis, and thus all the domains with the horizontal orientation of magnetization will expand. With the external magnetic field [Fig. 1.5 (d)] we shrink the domain with the antiparallel orientation of magnetization and we enlarge the parallel one. The whole structure seems to move to the side. For the external magnetic field large enough, a single domain state emerges.

The situation depicted in Fig. 1.5 is valid for samples large enough to allow domain walls separating individual domains in the system yet small enough, so no random domain structure is formed. For thin Permalloy layers, typical material employed in micromagnetic studies due to its very low anisotropy, the lower bound for single domain states

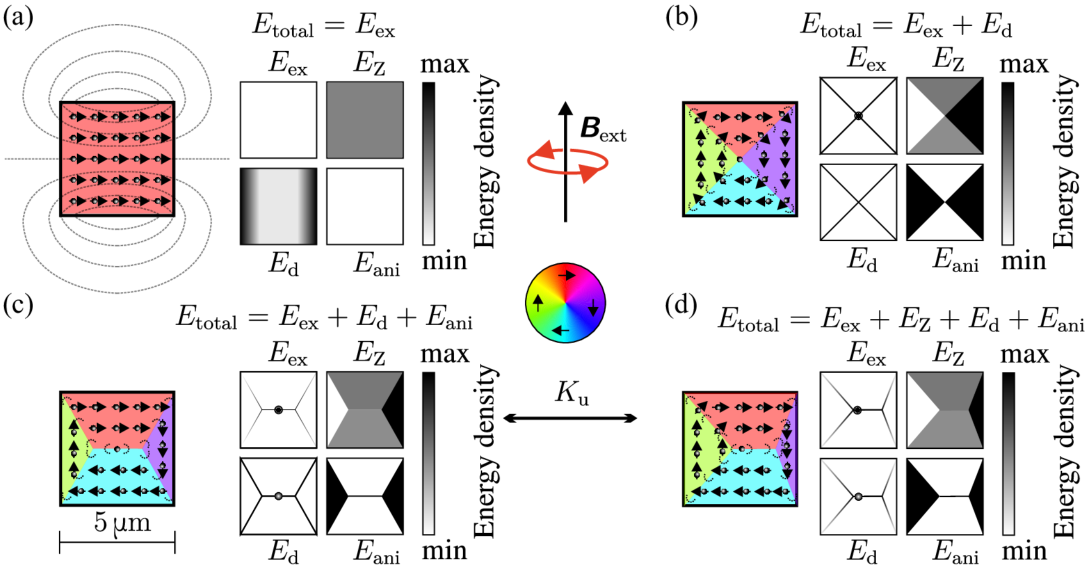

Fig. 1.5: *Gedankenexperiment* of the micromagnetic ordering if we only considered certain interactions to contribute to the total energy yet if we could visualize all remaining contributions. In the middle row the orientation of the external magnetic field, the magnetization directional color-wheel, and the orientation of the uniaxial magnetic anisotropy axis are shown. In each figure(a)-(d), the 2D map of magnetization is shown on the left with arrows denoting the in-plane vector of the magnetization and color representing the orientation of the magnetization. The stray field is represented by the dashed gray lines. On the right side of the magnetization landscapes, the maps of energy density for all considered interactions are shown. In (a), only the exchange interaction is considered, with the resulting state leading to single-domain orientation. (b) is the result of implementing also the demagnetizing energy, which results in the formation of the chiral magnetic structure - Landau pattern. (c) denotes the case where also the uniaxial anisotropy is considered and in (d) we also consider the energy arising from the applied external magnetic field.

is approximately 100 nm where upper bound for multi-domain states is in the range of approx. 10 µm.

1.3.1. Characteristic lengths in magnetism

When we perform some elementary calculations of (1.24) in 1D we can arrive to certain scaling parameters of the micromagnetic system [45]. By considering only the contribution arising from the exchange interaction (characterized by A_{ex} parameter), the dipolar self-energy ($\propto M_{\text{S}}^2$) and anisotropy energy (constant K_1), we can extract two main length parameters of the system. First parameter is

$$\delta_0 = \sqrt{\frac{A_{\text{ex}}}{K_1}}, \tag{1.27}$$

and is called a domain wall-width parameter. This material parameter determines the width of the domain wall separating two regions with the opposite orientation of magnetization. Depending on the material, it can span from nanometer range (for hard materials with high K_1 values) to hundreds of nanometers in case of soft magnetic materials.

The second parameter is also very important

$$l_0 = \sqrt{\frac{A_{\mathrm{ex}}}{\mu_0 M_{\mathrm{S}}^2}}, \tag{1.28}$$

and represents the exchange length parameter. It can be understood as a competition between the exchange interaction and the dipolar interaction. It represents the effective range of exchange interaction and also a typical grain-size, under which the material comprising from more magnetic phases behaves as an isotropic material.

1.3.2. Magnet memory - Hysteresis

When studying the response of the magnetic system to some external stimuli as e.g. external magnetic field, we often see highly nonlinear response of the magnetic system to the external stimulus. A typical example is well known $M(B_{\mathrm{ext}})$ hysteresis curve. The shape of the hysteresis loop indirectly discloses the state of the magnetic system. The shape of the loop and also the understanding of its formation is one of the crucial tasks that are addressed in the research of magnetic materials. In most cases we are interested only in the magnetization in the direction of the applied external magnetic field, so we measure the quantity $M_{\|} = \boldsymbol{M} \cdot \boldsymbol{B}_{\mathrm{ext}}/|\boldsymbol{B}_{\mathrm{ext}}|$. Fig. 1.6 shows the sketch of the hysteresis loop and typical behavior of a large magnetic sample with multiple magnetic domains and random distribution of the directions of the magnetic uniaxial anisotropy.

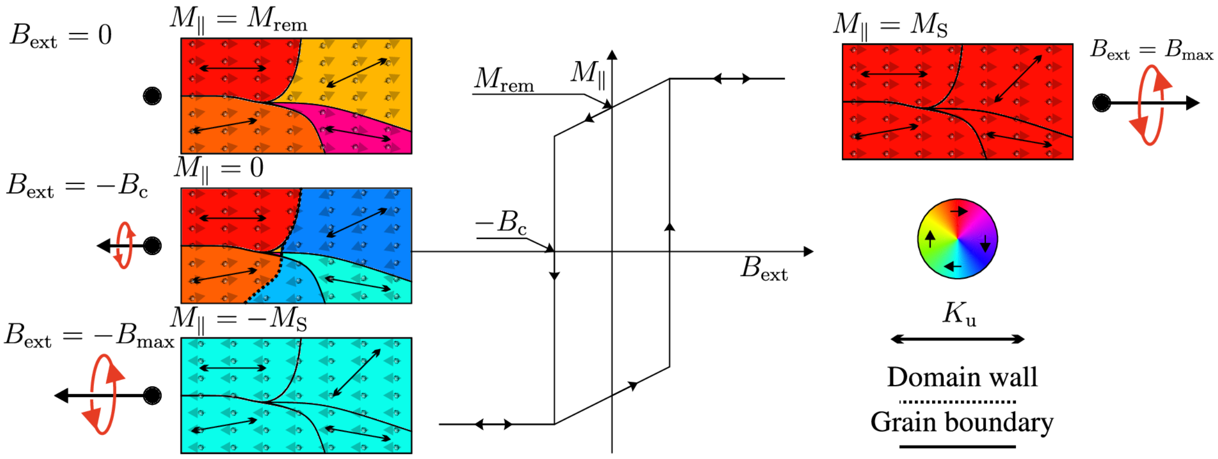

Fig. 1.6: Figure shows the hysteresis curve (net magnetization as a function of the external magnetic field) together with representative schematic maps of magnetic material with grains, where the orientation of uniaxial magnetic anisotropy spatially varies. Double-headed arrows mark the orientation of the anisotropy and small arrows denote the local orientation of the magnetization. The black dashed line shows the domain wall position and the color-wheel again represents the orientation of the magnetization. The overlaid arrows on the hysteresis curve mark the direction of the field sweep. Important parameters of the hysteresis as remanent magnetization M_{rem}, and the coercive field B_{c} are also marked in the hysteresis plot.

When going from the highest external magnetic field (magnetization map on the right side of Fig. 1.6), we start with the saturated sample where the net magnetization of the system is equal to the saturation magnetization. When we gradually decrease the field, we get to the regime of coherent rotation of the magnetization, where individual magnetic moments realign to the local anisotropy directions. In zero external magnetic field, the net magnetization value is called remanent magnetization. Fig. 1.6 shows a case, where the system still keeps a rather high remanence after the magnetic field is set to zero. Further decreasing of the magnetic field will cause the magnetization in the regions with the lowest activation energy for the switching to flip, and the domain walls will propagate through the sample. The domain wall will cause rather abrupt switching of the whole coupled system. For large negative field the sample saturates again. The most important parameters for the scope of the presented thesis are both the remanent magnetization M_{rem}, and the coercive field B_{c}. For practical reasons, we redefine the remanent magnetization to its normalized value $M_{\mathrm{rem}}/M_{\mathrm{S}}$.

1.3.3. Models of hysteresis - Stoner-Wohlfarth

Modeling of the hysteretic behavior is not an easy task as the model must capture both the saturation of the system and also the hysteretic behavior. There are several ways of modeling the hysteresis, where some are more physical than the others. One can use a mechanical model of hysteresis, where the magnetization is modeled as a damped mechanical system, or there is a famous approach by Preisach. By modeling the hysteresis as a linear superposition of elementary square loops, the model allows almost any type of hysteresis curve to be modeled. There is a very comprehensive textbook dealing solely with the models of hysteresis written by Mayergoyz [46]. In our case, we employ the coherent rotation model presented by Stoner and Wohlfarth. It is based on the micromagnetic energies [47, 48]. A nice introduction to the model, together with few examples, can be found in the book [45]. The model supposes a homogeneously magnetized body, so there is no exchange energy contribution as all the magnetic moments point in the same direction[1]. This is, in general, a very strict assumption that can be fulfilled only in very small magnetic particles yet the model can be overstretched and still provide very valuable information when only the coherent rotation of the magnetization is considered. The predictions of the coercive field usually overestimate the value by a lot. In order to model the in-plane hysteresis of the infinite thin film with uniaxial magnetic anisotropy, we first write down relevant energies of the system in a suitable coordinate system (for the definition of the coordinate system see Fig. 1.7)

$$E_{\mathrm{total}} = E_{\mathrm{Z}} + E_{\mathrm{ani}} = -B_{\mathrm{ext}} M_{\mathrm{S}} \cos(\alpha - \kappa) - K_1 \cos^2 \kappa. \tag{1.29}$$

The energy landscape $E_{\mathrm{total}}(\kappa)$ given by the equation (1.29) gives us quite a straightforward way how we can find the $M_{\|}(B_{\mathrm{ext}})$ loop. The system will always settle to the minimum in the energy by changing the angle of the magnetization κ in the 2π space. As there can be multiple minima in the system, the magnetization will always stay in the local minimum given by its previous state. As the model does not assume any activation energy, the system cannot escape this local extreme. The hysteresis can be easily found by means of numeric methods for greatly more complex energy landscapes then what we present in (1.29). The rather trivial case presented here can be solved also analytically for two unique angles $\alpha = 0$ and $\alpha = \pi/2$. By finding the first and the second derivative of the function E_{total} in the parameter κ, we can identify certain critical values of B_{ext}.

For the $\alpha = 0$ case we find that there can exist only two angles for which E_{total} has a minimum. Changing the external field from positive values towards negative (for

---

[1] It would be fairly wrong to assume that exchange interaction does not play a role in the system. The model actually assumes the exchange interaction strong enough to maintain the parallel orientation of all the magnetic moments.

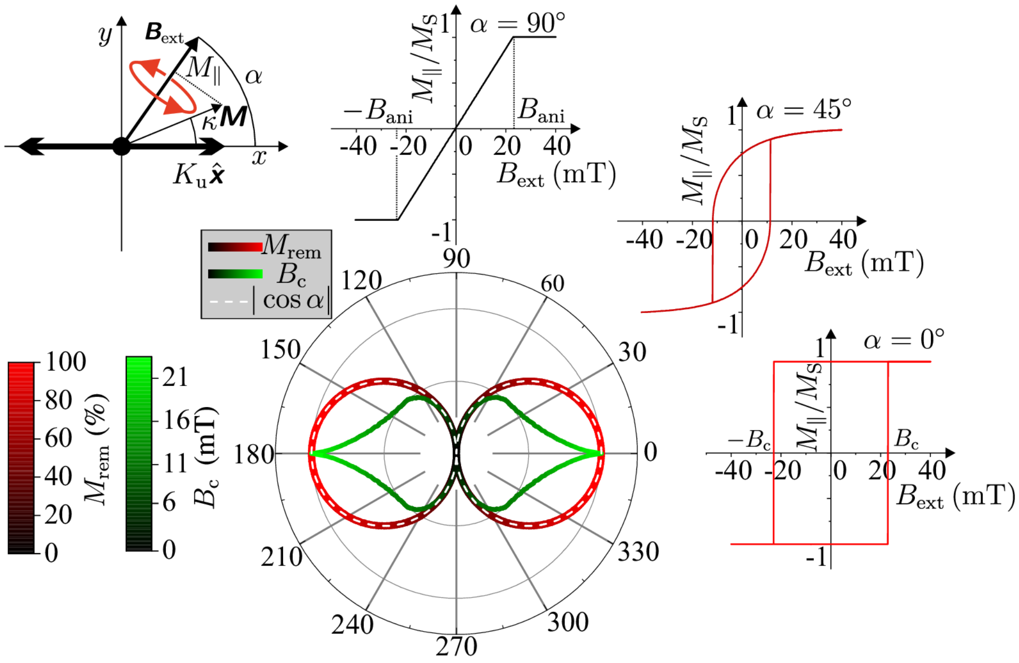

Fig. 1.7: The results of a numeric treatment of the Stoner-Wohlfarth model for a simple case of a uniaxial magnetic system in the external magnetic field. The definition of the angles can be found in the top-left corner. The polar plot shows normalized angular dependencies of the remanent magnetization and the coercive field (represented also by a color scale bar). Three representative curves for the magnetic field oriented at $0°, 45°$ and $90°$ are shown, where the important parameters as anisotropy field B_{ani} and coercive field B_{c} are denoted.

magnetization lying originally in positive direction defined by $\kappa_{\text{i}} = 0$) will cause the magnetization to maintain the angle of the magnetization fixed, until the critical (in this case called coercive) field

$$B_{\text{ext}} = -B_{\text{c}} = -\frac{2K_1}{M_{\text{S}}} \tag{1.30}$$

is reached and the magnetization flips to second stable minimum of energy at $\kappa_{\text{f}} = \pi$. Going backward will again cause a sudden switch of the magnetization now for value $B_{\text{ext}} = B_{\text{c}}$. The resulting loop is a perfect square loop (see Fig. 1.7 for $\alpha = 0$ case) and is called an easy axis loop.

The $\alpha = \pi/2$ case shows a completely different trend. For fields smaller than $\frac{2K_1}{M_{\text{S}}}$ it can be shown that the $M_{\parallel}$ will be a linear function in B_{ext} having a form

$$M_{\parallel} = \frac{M_{\text{S}}^2}{2K_1} B_{\text{ext}}. \tag{1.31}$$

For fields larger than $\frac{2K_1}{M_{\text{S}}}$ we reach the saturation. The loop can be modeled analytically as a piecewise linear function, where the saturation field is called the anisotropy field $B_{\text{ani}} = \frac{2K_1}{M_{\text{S}}}$ (see Fig. 1.7 for $\alpha = \pi/2$ case). This case is called a hard axis loop.

Both solutions for $\alpha = 0$ and $\alpha = \pi/2$ show a certain value of the magnetic field where the system either switches or reaches the saturation. The Stoner-Wohlfarth model suggests that the anisotropy and coercive fields in the same system are equal. This does not follow experimental findings for larger samples. This discrepancy can be explained by the first assumption we implemented in the model and that there is no exchange energy contribution. In the sufficiently large samples, the switching process is pronounced through nucleation and subsequent domain wall motion. The nucleation is often realized at a certain defect, allowing the system to lower the energy barrier between the two states. The coercive field is a rather extrinsic parameter and is hard to model in real systems. For the case $\alpha = \pi/2$, the model nicely predicts the shape of the loop as the magnetization is in the beginning oriented in one of the easy axis directions and the magnetic field is gradually pulling the magnetization from this direction towards the direction of the external magnetic field. The magnetization rotates as a whole with no changes in the exchange energy. When the system stays in this coherent rotation regime, the predictions of the anisotropy field are reliable and this procedure paves the way towards the quantification of the K_1 constant from the measurement as we only need to measure the anisotropy field and M_S. In contrast to the coercive field, the anisotropy field is an intrinsic parameter.

For the magnetic field oriented in between 0 and $\pi/2$ the shape of the loop gradually changes between the easy axis loop and hard axis loop. Fig. 1.7 shows the trend and also presents a calculation of the Stoner-Wohlfarth model for different angles α in a 2π interval. The figure also shows, how the remanence is simply given by the projection of the $M_\parallel$ to the external magnetic field direction. For zero external magnetic field, the magnetization will always align to one of the easy axes of the system and thus by changing the angle α, we also change the zero-field magnetization projection. For the uniaxial system, the remanence can be thus easily modeled by the $M_\mathrm{rem} = M_\mathrm{S}|\cos\alpha|$. For cases when the anisotropy does not lie in the 0 rad direction, the remanent magnetization profile changes to

$$M_\mathrm{rem} = M_\mathrm{S}|\cos(\alpha - \alpha_0)|, \tag{1.32}$$

where the α_0 parameter is the easy axis direction. It can be found from the measurement by fitting the $M_\mathrm{rem}(\alpha)$ function. The coercive field is a more complex function of α as can also be seen from the figure.

1.4. Magnetization dynamics

This section is devoted to the dynamics of magnetization in the infinite thin film and also in confined structures. We will introduce the Landau-Lifschitz-Gilbert torque equation allowing us to further address the spin excitations in magnetic samples. Consequently, the spin-wave dispersion will be introduced, with a focus on magnonic waveguides.

In equilibrium, the magnetic moments of the magnetic system will align in a way effectively lowering the total energy of the system introduced in (1.24). In the equilibrium, all torques acting on magnetization have to vanish. When a magnetic moment is tilted from its stable orientation, it will gain potential energy and start to feel external torque $\boldsymbol{M} \times \boldsymbol{B}_\mathrm{eff}$ realigning the magnetic moment again to the equilibrium orientation. The time derivative of a magnetic moment is given by the sum of the external torques. As in our case we now deal solely with an equilibrium recovering torque we write [27, 34]

$$\frac{\mathrm{d}\boldsymbol{M}}{\mathrm{d}t} = -\gamma \boldsymbol{M} \times \boldsymbol{B}_\mathrm{eff}, \tag{1.33}$$

with a gyromagnetic ratio γ. This equation directly leads to Larmor precession of magnetization with angular frequency $\omega = \gamma|\boldsymbol{B}_\mathrm{eff}|$. In physical systems, the dissipation of energy occurs, and the damping of the magnetization precession is observed by adding a phenomenological damping term with a damping parameter α. The equation describing the dynamics of the magnetic moment $\boldsymbol{M}$ is governed by the Landau-Lifschitz-Gilbert (LLG) torque equation [27, 34]

$$(1+\alpha^2)\frac{\mathrm{d}\boldsymbol{M}}{\mathrm{d}t} = -\gamma\left(\boldsymbol{M}\times\boldsymbol{B}_{\mathrm{eff}}\right) - \frac{\gamma\alpha}{|\boldsymbol{M}|}\left(\boldsymbol{M}\times\left(\boldsymbol{M}\times\boldsymbol{B}_{\mathrm{eff}}\right)\right). \tag{1.34}$$

For damping parameter $\alpha = 0$, the magnetic moment will indefinitely rotate around the effective field with the Larmor frequency. For reasonably small α it is possible to neglect α^2 term in (1.34). For the case of materials employed in this thesis, with $\alpha \sim 0.01$, this approximation is plausible, and it further simplifies the very complex torque equation, as the damping is introduced with linear scaling of the dissipation with the angular velocity. The form of the damping also ensures constant amplitude of the magnetization as only the deflection angle of the magnetization is evolving in time. For more comprehensive literature dealing with the damping of the magnetization dynamics see refs. [49–51]. Quite interestingly, the (1.34) lacks the inertia of the magnetic system (second time-derivative), and thus the system is expected to react at the same time with the cause. There is no retardance in the system even though it is expected that the spin of the conduction electron cannot simply react immediately to the changes in the local magnetic field or to a realignment of the neighboring spins. There has to exist a certain interaction speed that is simply not considered by the LLG equation. This can be taken into account when the time-independent constants in the LLG equation are substituted by time-dependent ones or by the introduction of additional torques to the equation [52]. The time-retardance effects of the spin-spin interaction start to play a role when reaching the terahertz frequencies. The magnetization dynamics of a single magnetic moment in the effective magnetic field is captured in Fig. 1.8.

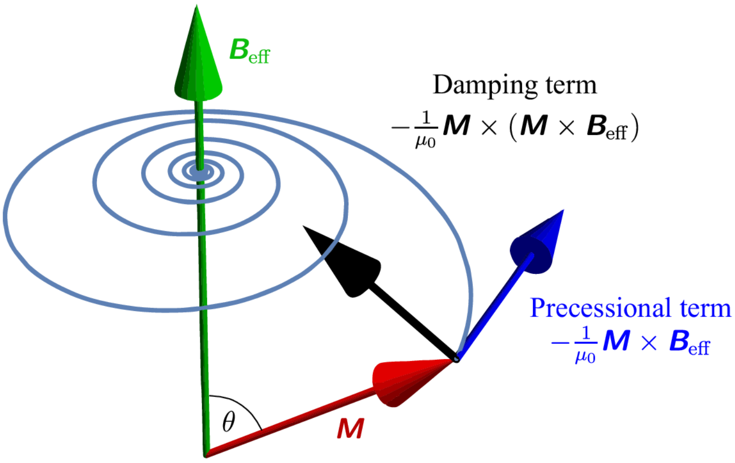

Fig. 1.8: Precession of the magnetic moment $\boldsymbol{M}$ in local effective field $\boldsymbol{B}_{\mathrm{eff}}$. The damping torque and the precessional torque are denoted in the figure. Originally deflected magnetic moment (by angle θ) follows a spiral path towards the equilibrium orientation.

Fig. 1.8 captures the situation when the isolated magnetic moment is driven from the equilibrium in the external magnetic field characterized by $\boldsymbol{B}_{\mathrm{eff}}$. In such a configuration, the trajectory is circular (spiral due to the damping). Generally, in confined structures, the trajectories take a rather elliptical form. In thin films, the strong demagnetizing field in the out-of-plane direction acts against the dynamic magnetization component $M_{\perp}(t)$. This means that also the demagnetizing field from (1.14) will have its dynamic part. This makes the problem rather complex as it leads to an auto-consistent problem. Certain approximation allowing us to at least partially solve the LLG equation (1.34) assumes the dynamic part of the magnetization to be only a minor perturbation to the ordered magnetic system. In other words

$$\boldsymbol{M}(t) = \boldsymbol{M}_{\mathrm{static}} + \boldsymbol{m}(t). \tag{1.35}$$

In the linear regime, with the sample saturated by the external magnetic field $\boldsymbol{B}_{\mathrm{ext}}$, the static part $\boldsymbol{M}_{\mathrm{static}}$ usually simplifies to $\hat{\boldsymbol{M}}_{\mathrm{static}} M_{\mathrm{sat}}$, where $\hat{\boldsymbol{M}}_{\mathrm{static}}$ is a unit vector in static magnetization direction. Term $\boldsymbol{m}(t)$ is considered small, allowing us to assume the $\boldsymbol{M}_{\mathrm{static}}$ to be constant during the magnetization precession.

1.4.1. Spin waves

When we investigate the dynamic behavior of not only a single spin (magnetic moment), but e.g. of continuous magnetic film, we find that the spins are coupled, and thus the system allows for coherent and non-coherent excitations. Coherent excitations in linear regime (i.e. small amplitude of dynamic behavior relative to static conditions) are called spin waves. The strength of the coupling of the individual spins depends on the governing interaction. In practice, we distinguish two major driving forces for the spin-wave propagation. For very small wavelengths ranging to inter-atom distance, the exchange interaction (1.16) is the driving force of oscillations. This strong inter-atomic interaction gives rise to eigenfrequencies in the order of terahertz. Whereas a large wavelength regime is governed by a dipolar interaction, arising from the dynamic demagnetizing field. The $\boldsymbol{m}(t)$ term introduced in the previous section can be decomposed in the Fourier components or diagonalized in order to obtain the eigenfrequencies and eigenmodes of the system. To each mode we can assign both the angular frequency ω and wave propagation vector $\boldsymbol{k}$. The particle-like analog of spin-wave is magnon with energy given by its frequency as $E_{\mathrm{magnon}} = \hbar\omega$.

The spin-wave propagation is realized through the spatial (Φ_r) and temporal (Φ_t) evolution of the oscillatory phase. In the case of the propagating wave both the temporal and spatial phase evolve linearly, where the spatial evolution can be expressed by the wave propagation vector $\boldsymbol{k}$ and directional vector $\boldsymbol{r}$ as $\Phi_r = \boldsymbol{k} \cdot \boldsymbol{r}$. The directional vector $\boldsymbol{r}$ defines the direction in which we probe the phase.

By suitable reorientation of the coordinate system, we can assure that $\boldsymbol{r} \parallel \boldsymbol{k}$ without any loss in generality. For the wave propagating in the x-direction, we rewrite the phase to $\Phi_r = kx$ ($k = |\boldsymbol{k}|$). The $\boldsymbol{k}$-vector unambiguously defines the wavelength of the wave by a simple relation $k = 2\pi/\lambda$. The spatial evolution of the phase can be then rewritten as $\Phi_r = (2\pi/\lambda)\, x$. A wave propagating in one direction is schematically shown in Fig. 1.9.

The temporal evolution of the magnetization precession is realized through the change of the phase in the temporal axis as $\Phi_t = \omega t$ with the angular frequency ω.

Fig. 1.9 also shows an interesting and general feature of the spin waves arising from the chiral form of the precessional torque found in the LLG equation ($\sim -\boldsymbol{M} \times \boldsymbol{B}_{\mathrm{eff}}$). The LLG does not permit any left-handed polarized modes in ferromagnetic substances, and thus there is no reason for the definition of the spin-wave polarization. *Au contraire*, the antiferromagnetic systems, and even the artificially antiferromagnetic systems offer also left-handed modes (and all the possible linear combinations with the right-handed modes) due to the coupling of multiple spin lattices [53–57]. This readily offers rich coupled spin

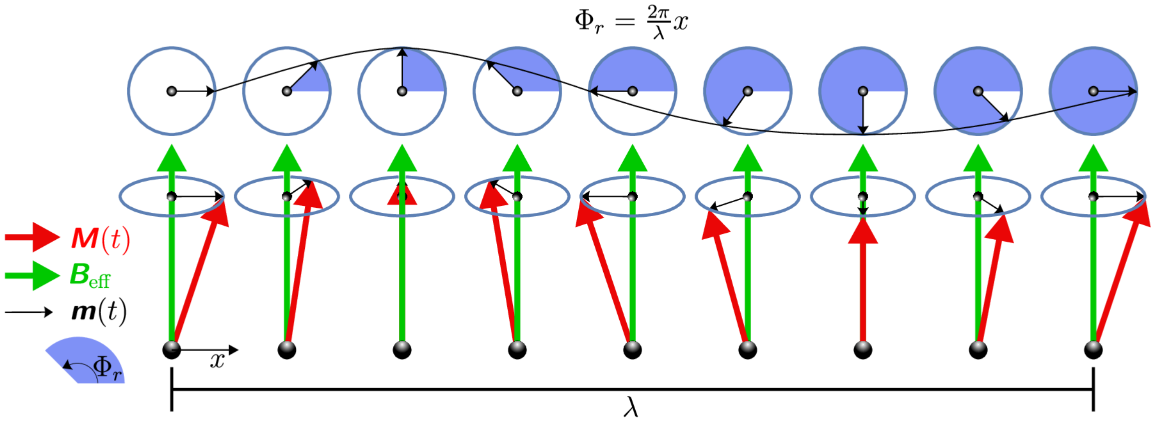

Fig. 1.9: A 1D spin wave propagating from the left to the right. The figure represents the spatial evolution of the magnetization precession. The precession is realized only by a small dynamic component $\boldsymbol{m}(t)$ of the magnetization vector $\boldsymbol{M}(t)$ around an effective magnetic field $\boldsymbol{B}_{\text{eff}}$. The top row shows the top view of the precession showing the evolution of the phase when the wave propagates in the x-direction (the phase is represented by colored circular sector). The bottom row shows the individual vectors in a tilted view. In a point where the wave accumulates a phase shift of 2π we recognize the wavelength λ.

dynamics unattainable in such a simple system as a ferromagnetic body covered in this thesis.

The theoretical insight into the problematics of spin-waves can again be found in the LLG equation (1.34). The LLG equation allows for a wave-like solution when suitably linearized (1.35) [58]. The first theoretical prediction of spin waves was done by Walker [59]. He found a solution for spheroids in the magnetic field. For thin films, the solution was given by Damon and Eshbach [60], where they distinguished two types of spin waves depending on the mutual orientation of $\boldsymbol{k}$ and $\boldsymbol{B}_{\text{ext}}$ and the plane of the sample. For the first mode, called magneto-static-surface waves (MSSW), the magnetization lies in-plane of the sample and the $\boldsymbol{k}$ is oriented perpendicular to the saturation magnetization. This mode is often called DE (Damon-Eshbach) mode. The DE mode exhibits exponential decay in the direction perpendicularly to the surface (in the material). The second mode is called magneto-static-backward-volume wave (MSBVW or simply BV) with propagation $\boldsymbol{k}$-vector oriented along the magnetization direction. This mode features negative group velocity for small $\boldsymbol{k}$-vectors. Contrary to the DE wave, the BV mode amplitude goes beyond the surface. Usually, also the third mode is distinguished, called magneto-static-forward-volume wave (MSFVW) found in out-of-plane magnetized systems with perpendicular propagation vector to the external magnetic field.

From the geometric arguments, the dispersion of the DE and BV modes has to coincide for $k = 0$. In this case, the ferromagnetic resonance (FMR) occurs. The derivation is rather straightforward. First, we again employ the assumption of small angles of the oscillations (1.35), and we assume that two major contributions are present in our system: the external magnetic field and the demagnetizing field. We assume magnetic element magnetized in the y-direction ($M_y = M_{\text{S}}$) by the external magnetic field $|\boldsymbol{B}_{\text{ext}}| = B_y$. The time varying driving (exciting) field will take similar form to magnetization: $\boldsymbol{B}_{\text{ext}} = \boldsymbol{B}_{\text{Static}} + \boldsymbol{b}(t)$. We assume linear response of the system to the driving field, and thus the magnetization dynamic components will follow the one of the external magnetic field:

$$\boldsymbol{B}_{\mathrm{ext}} = \begin{pmatrix} b_x(t) \\ B_y \\ b_z(t) \end{pmatrix} \to \boldsymbol{M} = \begin{pmatrix} m_x(t) \\ M_y \\ m_z(t) \end{pmatrix}. \tag{1.36}$$

The dynamic component of $\boldsymbol{M}$ will create the dynamic component of B_{eff} as the total field experienced by the magnetic moment will be the sum of the external field with the demagnetizing field $\boldsymbol{B}_{\mathrm{eff}} = \boldsymbol{B}_{\mathrm{ext}} + \boldsymbol{B}_{\mathrm{d}}$. From (1.14) it follows that $\boldsymbol{B}_{\mathrm{d}} = -\mu_0 \overset{\leftrightarrow}{\boldsymbol{N}} \boldsymbol{M}$. This leads to the following equation

$$\boldsymbol{B}_{\mathrm{eff}} = \begin{pmatrix} b_x(t) - \mu_0 N_x m_x(t) \\ B_{\mathrm{ext}} - \mu_0 N_y M_{\mathrm{S}} \\ b_z(t) - \mu_0 N_z m_z(t) \end{pmatrix}. \tag{1.37}$$

Now we take both equations (1.36) and (1.37) and insert them to the LLG equation (1.34). We assume the harmonic time dependence of individual dynamic components as e.g. $m_x(t) = m_x \mathrm{e}^{(\mathrm{i}\omega t + \phi)}$, with m_x representing the amplitude of the oscillations, and ϕ representing the oscillation phase shift with respect to the driving field. Doing so results in (after omitting higher orders of dynamic components)

$$\begin{pmatrix} \gamma \left[B_{\mathrm{ext}} + \mu_0 M_{\mathrm{S}} \left(N_x - N_y\right)\right] + \mathrm{i}\alpha\omega & \mathrm{i}\omega \\ \mathrm{i}\omega & \gamma \left[B_{\mathrm{ext}} + \mu_0 M_{\mathrm{S}} \left(N_z - N_y\right)\right] \end{pmatrix} \cdot \begin{pmatrix} m_x(t) \\ m_y(t) \end{pmatrix} = \mu_0 \gamma M_{\mathrm{S}} \begin{pmatrix} b_x(t) \\ b_y(t) \end{pmatrix}. \tag{1.38}$$

This well-known form of the equation reveals a nontrivial solution if the determinant of 2 × 2 matrix is zero. This leads to resonance frequency condition

$$\begin{aligned} \omega_{\mathrm{r}} = & \frac{\mathrm{i}\gamma\alpha}{2\left(1+\alpha^2\right)} \left[2B_{\mathrm{ext}} + \mu_0 M_{\mathrm{S}} \left(N_x + N_z - 2N_y\right)\right] \\ \pm & \frac{\gamma}{2\left(1+\alpha^2\right)} \sqrt{4\left[B_{\mathrm{ext}} + \mu_0 M_{\mathrm{S}} \left(N_x - N_y\right)\right]\left[B_{\mathrm{ext}} + \mu_0^2 M_{\mathrm{S}} \left(N_z - N_y\right)\right] - M_{\mathrm{S}}^2 \left(N_x - N_z\right)^2 \alpha^2}. \end{aligned} \tag{1.39}$$

Rather crude equation (1.39) transforms to the famous Kittel's formula of FMR for $\alpha \to 0$ case

$$\omega_{\mathrm{r}} = \gamma \sqrt{\left[B_{\mathrm{ext}} + \mu_0 M_{\mathrm{S}} \left(N_x - N_y\right)\right]\left[B_{\mathrm{ext}} + \mu_0 M_{\mathrm{S}} \left(N_z - N_y\right)\right]}. \tag{1.40}$$

The equation directly shows that for confined magnetic structures, the zero external field does not result in zero resonance frequency as the magnetization dynamic restoring force is supplied by the shape of the structure itself. When we perform further simplification of the infinite thin layer where $N_x = N_y = 0$, $N_z = 1$ we get elegant equation

$$\omega_{\mathrm{r}} = \gamma \sqrt{B_{\mathrm{ext}} \left(B_{\mathrm{ext}} + \mu_0 M_{\mathrm{S}}\right)}, \tag{1.41}$$

where the only restoring force for the magnetization is given by the external magnetic field. In zero external magnetic field the resonance frequency is equal to zero.

1.4.2. Effect of anisotropy on the spin precession

The anisotropy, as introduced in section 1.2.4, will cause the magnetic moments to feel different effective magnetic field for different orientations of the magnetization. Consequently, the dynamic component of magnetization will experience additional torques coming from the fact that during the realignment from the equilibrium direction, the dynamic components will align towards the anisotropy axis. The shape can be understood also as a certain manifestation of anisotropy. In thin magnetic films, we qualitatively see that for in-plane magnetization, the resulting magnetization precession is elliptical instead of circular [61] resulting in different amplitudes of the dynamic components m_x and m_y in (1.36). When the magnetocrystalline anisotropy is taken into account, similar features are expected. The derivation of the effect of anisotropy on the spin-wave precession is elaborated in chapter 2 in the book [61].

In the first step, we rewrite the uniaxial energy from equation (1.21) (leaving higher-order term out) to the energy density with normalized coordinates

$$\epsilon_{\mathrm{u}} = -K_{\mathrm{u}} \cos^2(\kappa) = -K_{\mathrm{u}} \left(\frac{M_i}{M_{\mathrm{S}}}\right)^2, \tag{1.42}$$

where the component M_i is the magnetization component along the uniaxial direction. Afterward, we find the effective anisotropy field coming from the anisotropy energy by (1.25), thus

$$\boldsymbol{B}_{\mathrm{ani}} = -\frac{\partial \epsilon_{\mathrm{u}}}{\partial \boldsymbol{M}}, \tag{1.43}$$

which results for the uniaxial crystal with the anisotropy easy axis in $\boldsymbol{e}_{\mathrm{a}}$ direction in

$$\boldsymbol{B}_{\mathrm{ani}} = \frac{2K_{\mathrm{u}} M_i}{M_{\mathrm{S}}^2} \boldsymbol{e}_{\mathrm{a}}. \tag{1.44}$$

This equation allows us in a quite straightforward manner to derive a similar form of (1.14) for the anisotropy as

$$\boldsymbol{B}_{\mathrm{ani}} = -\mu_0 \overset{\leftrightarrow}{\boldsymbol{N}}_{\mathrm{ani}} \boldsymbol{M}, \tag{1.45}$$

with $\overset{\leftrightarrow}{\boldsymbol{N}}_{\mathrm{ani}}$ representing the anisotropy tensor. At this point, we can again perform the procedure leading to (1.37), whereas now we have three fields accounting to the effective field: $\boldsymbol{B}_{\mathrm{eff}} = \boldsymbol{B}_{\mathrm{ext}} + \boldsymbol{B}_{\mathrm{d}} + \boldsymbol{B}_{\mathrm{ani}}$. We define the geometry of the problem by Fig. 1.10.

The anisotropy is in the global crystal frame pointing in y-direction. Magnetization lies in the y' direction, which is diverted from the y-direction by the angle κ (see the right panel of Fig. 1.10). The magnetic field lies in the plane defined by the y and y' axis and has inclination angle from the anisotropy axis given by α. The resulting angle in between the magnetization and the magnetic field is $\sphericalangle \boldsymbol{B}_{\mathrm{ext}} \boldsymbol{M} = \alpha - \kappa$. The anisotropy field from (1.44) is now directly in the y-direction. We now need to transform the field to the $x'y'z'$ frame:

$$\begin{aligned} B_{\mathrm{a}}^{x'} &= \frac{2K_{\mathrm{u}}}{M_{\mathrm{S}}^2} \left(M_{y'} \cos\kappa - M_{x'} \sin\kappa\right) \sin\kappa, \\ B_{\mathrm{a}}^{y'} &= \frac{2K_{\mathrm{u}}}{M_{\mathrm{S}}^2} \left(M_{y'} \cos\kappa - M_{x'} \sin\kappa\right) \cos\kappa, \\ B_{\mathrm{a}}^{z'} &= 0. \end{aligned} \tag{1.46}$$

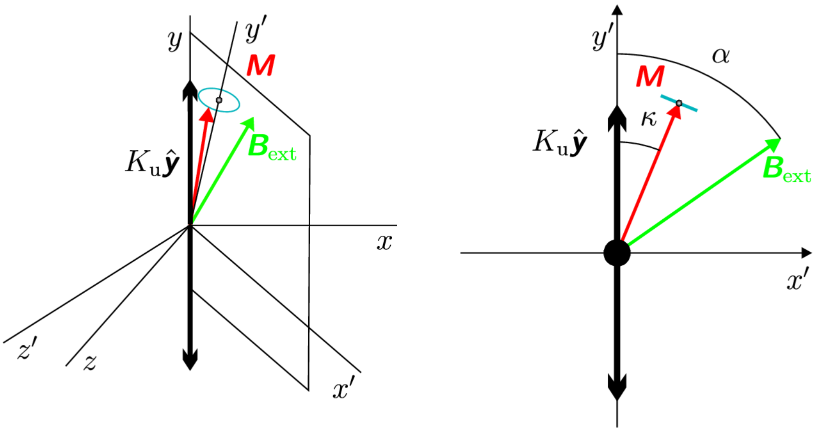

Fig. 1.10: The magnetic moment precession in the magnetic material with the magneto-crystalline uniaxial anisotropy pointing in the y-direction. The global coordinate system is given by the anisotropy axis, while the local coordinate system x', y', z' is given by the equilibrium direction of the magnetization. The magnetization precesses in the $x'z'$ plane. The right panel shows the $x'y'$ cut plane with the definition of the important angles. At this point, we do not consider any particular shape of the structure, and thus we do not define any direction of the demagnetizing field. After [61].

The external magnetic field has to be also transformed into the new coordinates by $B'_\mathrm{ext} = B_\mathrm{ext}\cos(\kappa - \alpha)$. Now it is reasonable to assume that $M_{x'} < M_{y'} \sim M_\mathrm{S}$ and then we can employ (1.45) to write

$$\begin{aligned} N_\mathrm{ani}^{x'} &= -\frac{2K_\mathrm{u}}{M_\mathrm{S}^2}\sin^2\kappa, \\ N_\mathrm{ani}^{y'} &= -\frac{2K_\mathrm{u}}{M_\mathrm{S}^2}\cos^2\kappa, \\ N_\mathrm{ani}^{z'} &= 0. \end{aligned} \tag{1.47}$$

Now by redoing the whole math leading to (1.41) we arrive to the following expression

$$\omega_\mathrm{r} = \gamma\sqrt{\left[B_\mathrm{ext}\cos(\kappa-\alpha) + \frac{2K_\mathrm{u}}{M_\mathrm{S}}\cos^2\kappa + \mu_0 M_\mathrm{S}(N_x - N_y)\right]} \times \sqrt{\left[B_\mathrm{ext}\cos(\kappa-\alpha) + \frac{2K_\mathrm{u}}{M_\mathrm{S}}\cos 2\kappa + \mu_0 M_\mathrm{S}(N_z - N_y)\right]}. \tag{1.48}$$

The angular parameter α is chosen from the experiment but the angle κ is a result of competing interactions of demagnetizing, Zeeman and anisotropy interaction. For the isotropic case, we can easily find the minimum of the function $E_\mathrm{total} = E_\mathrm{ext} + E_\mathrm{a}$ in the parameter space of κ. Performing $\partial E_\mathrm{total}/\partial\kappa = 0$ we obtain the equilibrium condition:

$$\frac{2K_\mathrm{u}}{M_\mathrm{S}}\sin 2\kappa = B_\mathrm{ext}\sin 2(\alpha - \kappa). \tag{1.49}$$

Such an equation can be solved to get the orientation of the magnetization. For simplicity, it is convenient to show two limiting cases. When the anisotropy is much smaller than the external magnetic field, we assume the magnetization to lie in the direction of the field. For the magnetic field perpendicular to the anisotropy axis ($\alpha = \pi/2 = \kappa$) and by assuming the demagnetizing factors of the thin film as in the previous case ($N_x = N_y = 0$, $N_z = 1$,) we arrive at

$$\omega_\mathrm{r} = \gamma\sqrt{B_\mathrm{ext}\left(B_\mathrm{ext} - \frac{2K_\mathrm{u}}{M_\mathrm{S}} + \mu_0 M_\mathrm{S}\right)}. \tag{1.50}$$

The anisotropy lowers the resonance frequency as the magnetization lies in the hard axis of the anisotropy. The effect can be understood as the lowering of the N_z demagnetizing factor. The equation also suggests a non-physical complex solution if the magnetic field is low enough. In such a case the equilibrium condition from (1.49) would not be fulfilled and magnetization would realign itself near/to the direction of the anisotropy axis. For the magnetic field oriented to the anisotropy axis direction ($\alpha = 0 = \kappa$) we obtain

$$\omega_\mathrm{r} = \gamma\sqrt{\left(B_\mathrm{ext} + \frac{2K_\mathrm{u}}{M_\mathrm{S}}\right)\left(B_\mathrm{ext} + \frac{2K_\mathrm{u}}{M_\mathrm{S}} + \mu_0 M_\mathrm{S}\right)}. \tag{1.51}$$

And we see that in both brackets, there is the term representing the effect of the anisotropy. This can be understood simply by adding the effective anisotropy field to the external magnetic field and thus increasing the resonance frequency. The existence of the anisotropy field has a direct consequence. At zero external magnetic field, we already obtain certain resonance frequency since the anisotropy acts as a restoring force to the oscillations of the magnetization. The magnetic field dependence of the FMR frequency is depicted in Fig. 1.11.

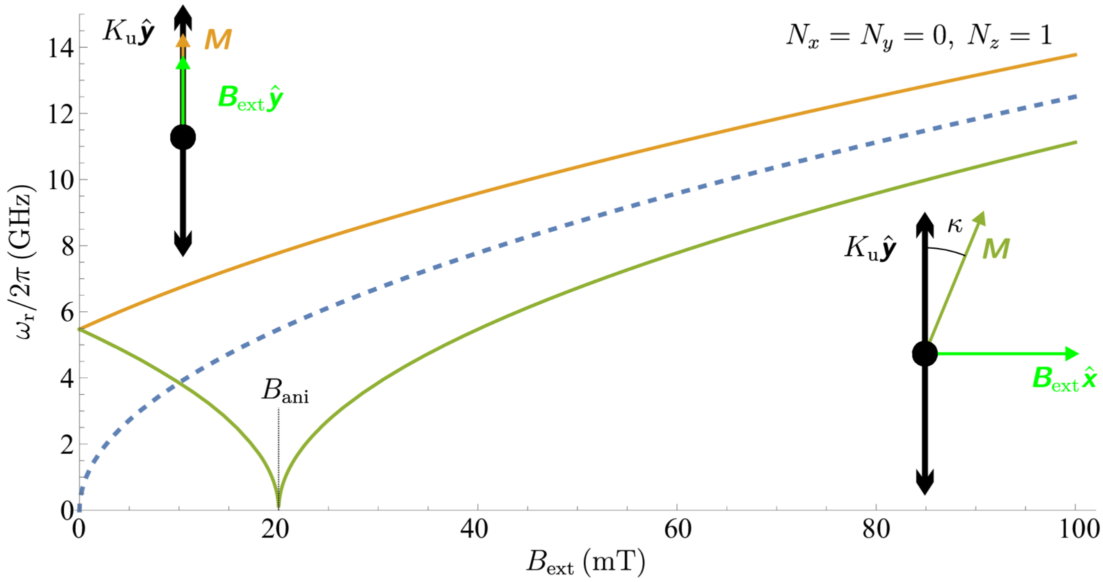

Fig. 1.11: Magnetic field dependence of the FMR frequency ω_r for three cases. The dashed curve is the FMR of the isotropic thin-film following (1.41). The orange continuous line represents the case when the external magnetic field (and thus magnetization) coincide with the uniaxial anisotropy axis as in (1.51). The green continuous line shows the result of the case where the magnetic field is oriented perpendicular to the anisotropy axis. This line was calculated by taking (1.48), where the angle of the magnetization for each external magnetic field value was calculated by the equilibrium condition (1.49). The calculations were performed for parameters $M_\mathrm{S} = 1.4\,\mathrm{MA/m}$, $K_\mathrm{u} = 17\,\mathrm{kJ/m^3}$ and $\gamma/2\pi = 29.4\,\mathrm{GHz/T}$.

The three cases represented by Fig. 1.11 show the FMR evolution in the external magnetic field for a magnetic thin film with no anisotropy and for two cases of an anisotropic magnet. The two anisotropic cases differ in the respective orientation of the uniaxial magnetic anisotropy and the external magnetic field. When the field is oriented along the uniaxial anisotropy direction the most significant difference when compared to the isotropic case is the non-zero FMR frequency for zero external magnetic field. When the magnetic field is oriented perpendicular to the uniaxial axis, the zero-field case coincides with the parallel case. Yet as seen from the green curve in Fig. 1.11 the resonance frequency initially goes down, as the magnetization realigns from the direction of the uniaxial anisotropy towards the external magnetic field direction (refer also to the hard axis hysteresis curve shown in Fig. 1.7). For the field B_{ani}, the magnetization is fully aligned to the external magnetic field. Since the external field is equal to the anisotropy field, the FMR frequency goes to zero. For the field higher than B_{ani}, the frequency again rises.

The rather elementary yet often misinterpreted case is when the system has two fundamental (not effective) anisotropy contributions to the total energy. When there are two differently oriented axes of anisotropy in a single magnetic system (e.g. the system with two uniaxial magnetocrystalline anisotropies), then as the system follows only the total energy, we can make a sum of the individual contributions to form a new effective anisotropy. This anisotropy will lie in the direction of the strongest anisotropy. The two uniaxial anisotropies never form e.g. cubic anisotropy or the anisotropy with its axis lying in between the principal direction of the two fundamental anisotropies.

1.4.3. Spin-wave dispersion in thin film

Previous text introduced the magnetic field dependence of the ferromagnetic resonance as a spatially uniform mode. In the following text, we introduce the harmonic spatial dependence of the dynamic magnetization to extract the spin-wave dispersion. We start by assuming the thickness of the magnetic film to be small enough, so no spin-waves propagate in the out-of-plane z-direction and that the film is uniformly magnetized (saturated) by the external magnetic field or by the magnetic anisotropy. We assume the spin-wave propagation vector $\boldsymbol{k}$ in the form

$$\boldsymbol{k} = \begin{pmatrix} k_{x'} \\ k_{y'} \end{pmatrix}. \tag{1.52}$$

Now we follow the approach introduced by Walker [59]. He assumes the magnetostatic regime (curl of the field is equal to zero), where the magnetic field again points in the y-direction. The small perturbation field components $\boldsymbol{b}$ and $\boldsymbol{h}$ have both the temporal and spatial evolution:

$$\boldsymbol{B}(\boldsymbol{r},t) = B_y\hat{\boldsymbol{y}} + \boldsymbol{b}(\boldsymbol{r},t), \tag{1.53}$$
$$\nabla \times \boldsymbol{b} = \boldsymbol{0}, \tag{1.54}$$
$$\boldsymbol{H}(\boldsymbol{r},t) = H_y\hat{\boldsymbol{y}} + \boldsymbol{h}(\boldsymbol{r},t), \tag{1.55}$$
$$\nabla \times \boldsymbol{h} = \boldsymbol{0}. \tag{1.56}$$

Fields $\boldsymbol{b}$ and $\boldsymbol{h}$ are connected through the material relations as $\boldsymbol{b} = \overset{\leftrightarrow}{\boldsymbol{\mu}}\boldsymbol{h}$ [62]. Now we will find the scalar magnetic potential (1.9) $\Phi(\boldsymbol{r},t)$ leading to generalized Walker equation

$$\nabla\left(\overset{\leftrightarrow}{\boldsymbol{\mu}} \cdot \nabla\Phi\right) = 0, \tag{1.57}$$

that is the fundamental equation describing the magnetostatic modes in the homogeneous media. We will look for the solution in the form $\Phi = \Phi_0 \mathrm{e}^{\mathrm{i}(\omega - \boldsymbol{k}\cdot\boldsymbol{r})}$. The solution is also expected to depend on the respective orientation of the magnetization $\boldsymbol{M}$ and the propagation vector $\boldsymbol{k}$.

In general, for in-plane magnetized films, obviously, two geometric configurations are possible. One for $\boldsymbol{M} \perp \boldsymbol{k}$ and one for $\boldsymbol{M} \parallel \boldsymbol{k}$. This would allow us to solve the above equations and get the two respective dispersions of the continuous film. The more general approach was elaborated by Kalinikos and Slavin [63] and also equivalent (yet different from the first look) derivation was performed later by Arias and Mills [64]. To begin with, we follow the coordinate system from Fig. 1.10. We assume the continuous magnetic thin film magnetized in y' direction. Now we define the propagation angle of the spin-waves with respect to the x' direction as $\sphericalangle\boldsymbol{k} = \operatorname{atan}\left(k_{x'}/k_{y'}\right)$. Following the result presented by Kalinikos and Slavin, we write

$$\omega_{\mathrm{r}} = \gamma\sqrt{\left[B_{\mathrm{ext}}\cos\left(\kappa-\alpha\right) + \frac{2K_{\mathrm{u}}}{M_{\mathrm{S}}}\cos^{2}\kappa + \mu_0 M_{\mathrm{S}} P \sin^{2}\sphericalangle\boldsymbol{k} + \frac{2A_{\mathrm{ex}}}{M_{\mathrm{S}}}k^{2}\right]} \times\sqrt{\left[B_{\mathrm{ext}}\cos\left(\kappa-\alpha\right) + \frac{2K_{\mathrm{u}}}{M_{\mathrm{S}}}\cos 2\kappa + \mu_0 M_{\mathrm{S}}\left(1-P\right) + \frac{2A_{\mathrm{ex}}}{M_{\mathrm{S}}}k^{2}\right]}. \tag{1.58}$$

Where the propagation vector magnitude is $k = \sqrt{k_{x'}^2 + k_{y'}^2}$ and the parameter P is found from the following equation

$$P = 1 - \left(\frac{1-\mathrm{e}^{-kt}}{kt}\right), \tag{1.59}$$

with t representing the thickness of the magnetic layer. The (1.58) allows calculating the spin-wave frequencies for the general orientation of the propagation vector. For $k \to 0$ and $\boldsymbol{k} \perp \boldsymbol{M}$ case, one can analytically derive the group velocity of the mode from (1.58) as

$$v_{\mathrm{g}} = \frac{\partial\omega_{\mathrm{r}}}{\partial k} = t\frac{\left(\gamma\mu_0 M_{\mathrm{S}}\right)^2}{4\omega_{\mathrm{r}}}, \tag{1.60}$$

so it can be seen that the group velocity implicitly depends on the frequency. For higher frequency, the group velocity is lower, whereas for higher M_{S} the group velocity is increasing. From a first look at (1.58), the dispersion is highly anisotropic as the frequency highly depends on the propagation direction of the spin wave. This anisotropy, nicely seen e.g. in Fig. 1.12, leads to interesting phenomena as caustic beam formation [65], spin-wave excitation from an anti-dot lattice or waveguide open-end [11], or magnonic beam-splitters [66]. The anisotropic nature of the spin-wave dispersion is rather ambiguous. When considering only the simple turning of the spin-waves by 90 degrees, we immediately realize that it becomes problematic. In uniformly magnetized magnetic turns, both arms will possess different dispersion. This leads to mode-mismatch [67]. For high k values, the isotropic $\frac{2A_{\mathrm{ex}}}{M_{\mathrm{S}}}k^2$ term will govern both sides of the equation leading to isotropic spin-wave dispersion. When the dispersion is mainly governed by the exchange term, we call the modes as the exchange spin waves. For lower k values, we call the modes as dipole spin waves (or magnetostatic spin waves).

The $\boldsymbol{k} \perp \boldsymbol{M}$ mode exhibits high group velocity (high slope of the dispersion), the $\boldsymbol{k} \parallel \boldsymbol{M}$ case shows a rather small group velocity. For modes close to the FMR ($k \to 0$), the group velocity is even negative. The isofrequency curves reveal the concave shape of the dispersion in the vicinity of the $k_{y'} \sim 0$ point leading to interesting phenomena of self-focusing of spin waves [68]. In practice, the spin-wave dispersion is usually presented only for two principal orientations of $\boldsymbol{k}$ and $\boldsymbol{M}$.

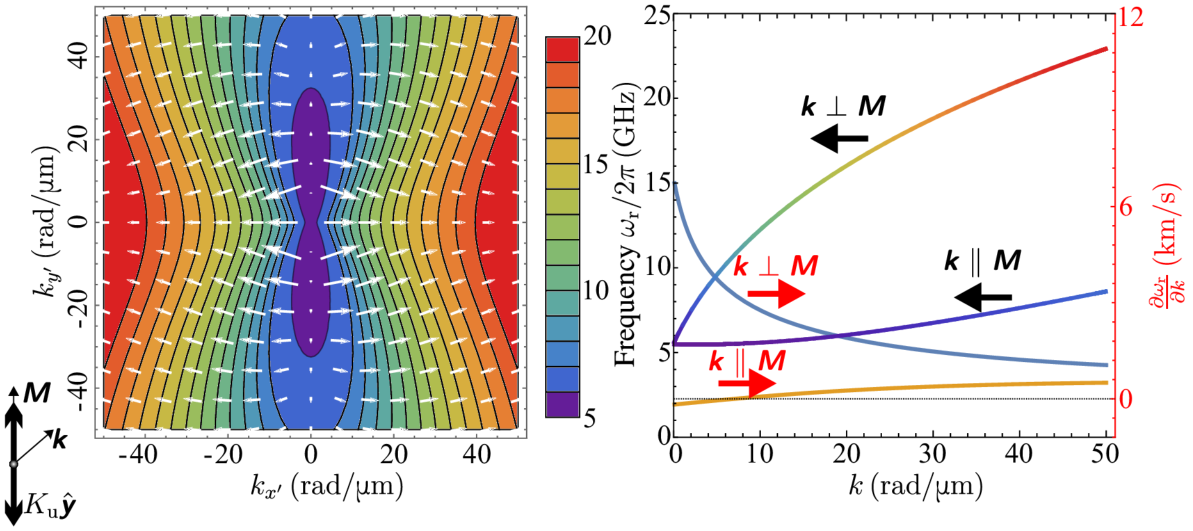

Fig. 1.12: The spin-wave dispersion relations for a range of possible in-plane propagation vectors $k_{x'}$ and $k_{y'}$. The color bar represents the spin-wave frequency and the arrows represent the group velocity. The right panel shows 1D cuts of the 2D dispersion when the spin-wave propagation is perpendicular/parallel (represented by the colored continuous line) to the static magnetization direction. Blue/orange continuous lines represent the group velocity of the modes with the propagation direction perpendicular/parallel to the static magnetization direction. The anisotropy axis is considered along the y' direction. The parameters used in the calculation are following: $B_{\mathrm{ext}} = 0$, $M_{\mathrm{S}} = 1.4\,\mathrm{MA/m}$, $K_{\mathrm{u}} = 17\,\mathrm{kJ/m^3}$, $A_{\mathrm{ex}} = 10\,\mathrm{pJ/m}$, $t = 9\,\mathrm{nm}$ and $\gamma = 29.4\,\mathrm{GHz/T}$

Magnetostatic surface waves (MSSW)

Magnetostatic surface waves, being also called Damon-Eshbach (DE) waves, represents the case where the spin-wave propagation vector is perpendicular to the static magnetization direction ($\boldsymbol{k} \perp \boldsymbol{M}$). From the form of (1.58), one can see that for the increasing k-vector, the frequency of the mode always rises. The dispersion is initially rather steep resulting in high group velocity of the mode reaching kilometers per second. This mode exhibits the largest group velocity in the direction of propagation of all the spin-wave modes. The analysis in Fig. 1.12 (for $k_{y'} = 0$ line) reveals this general trend in more detail.

The DE mode amplitude in a film exponentially decays through the thickness of the film with a maximum amplitude being found on the interface of the layer. The interface, at which the maximum is found, depends on the propagation direction of the wave.

Magnetostatic backward volume waves (MSBW)

The backward volume waves (BV), as the name suggests, have their amplitude distributed through the whole volume of the magnetic film. For small k, the frequency of the mode initially goes down resulting in the small negative group velocity of the mode. For higher k values, the $\frac{2A_{\mathrm{ex}}}{M_{\mathrm{S}}}k^2$ term lifts the mode frequency to positive k dependence. The existence of the group velocity minima (the dispersion is concave upward) in the MSBW waves (see $\boldsymbol{k} \parallel \boldsymbol{M}$ case in Fig. 1.12) allowed to observe and excite e.g. Bose-Einstein condensates of magnons [69]. The concave shape of the curve also allows for two magnitudes of the k-vector to satisfy the dispersion at single frequency ω. By pumping at 2ω it is possible to excite two magnons of oposite propagation direction (having total momentum equal to zero) even by a global dynamic magnetic field [8]. Compared to DE wave, the MSBW waves have very low group velocity resulting in rather short propagation lengths. The advantage of MSBW waves is the ease of stabilizing the $\boldsymbol{k} \parallel \boldsymbol{M}$ condition in long and narrow waveguides, where the demagnetizing energy (shape anisotropy) forces the magnetization to align along the long direction of the waveguide. Such configuration directly supports the spin-wave propagation in magnonic turns as has been presented by micromagnetic simulations by [67].

1.4.4. Spin waves in confined structures

In magnetization dynamics, Maxwell's equations do not provide a rigorous approach of finding boundary conditions for dynamic magnetization (see chapter 6 of the book [61]). Usually, one has to decide, whether in his experiment the spins at the surface are free, or if the spins are totally pinned. The selection always brings certain controversy to data evaluation and modeling. Guslienko in 2002 presented a novel redefinition of the boundary conditions by proper rigorous calculation of the demagnetizing tensors in rectangular magnetic elements [70].

In confined magnetic structures, the boundary on the edges of the waveguide causes spin-wave modes to be quantized in a geometrically restricted direction. This leads to a boundary problem with only certain solutions possible. The k-vector can have only certain-valued components in the confined direction. This situation is exaggeratedly plotted in Fig. 1.13. The wave vector component in the confined direction is called the transverse component. According to [70] the possible values this $k_\perp$ vector component can carry, are

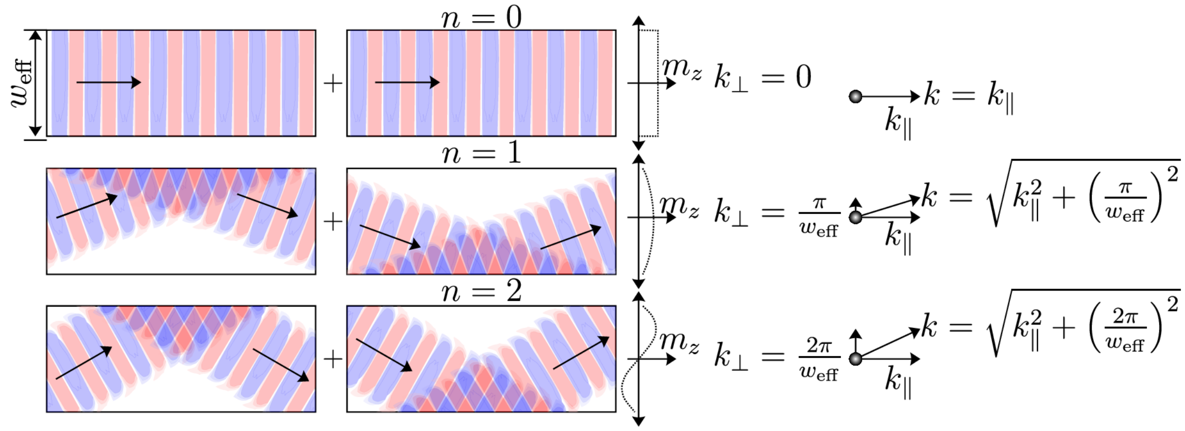

Fig. 1.13: The cartoon of spin-wave propagation in the long and narrow waveguide. The m_z component is represented by a blue-red false color bar. The confinement in the direction of the short edge (of length w_{eff}) causes the spin wave to have the propagation vector in this direction quantized to discrete values $k_\perp = \frac{n\pi}{w_{\mathrm{eff}}}$. The snapshot for cases $n = 0, 1, 2$ are schematically shown. The black arrow represents the local propagation vector direction. The propagation of single mode with a certain n number is given by the two solutions $k_\perp = \pm\frac{n\pi}{w_{\mathrm{eff}}}$. In the middle row, the transverse profile of the dynamic magnetization is schematically shown. On the right side, the total magnitude of the k-vector for individual cases is evaluated.

$$k_\perp(n) = \frac{n\pi}{w_{\mathrm{eff}}}, \text{for } n = 0,1,2,\ldots \tag{1.61}$$

where n is the integer. For $n = 0$ no confined effects are included. The w_{eff} represents the effective width of the waveguide and this parameter will be evaluated in more detail later in this section. Again, the total vector is calculated by a simple relation $k = \sqrt{k_\parallel^2 + k_\perp^2}$ and the angle of the propagation with respect to the long waveguide axis is $\sphericalangle k = \operatorname{atan}\left(k_\parallel / k_\perp\right)$. All the modes have their dynamic magnetization profile (in the transverse direction) different as schematically shown in the middle row of Fig. 1.13. The model by Guslienko [70] redefines the geometric waveguide width w to the effective width by

$$w_{\mathrm{eff}} = \frac{wd}{d-2}, \tag{1.62}$$

where d is the pinning parameter calculated by

$$d = \frac{2\pi}{p + 2\ln\left(\frac{1}{p}\right)}. \tag{1.63}$$

The parameter p is given by the geometric thickness/width ratio $p = \frac{t}{w}$. The spin-wave dispersion is then again given by the same governing equation (1.58). The quantization of the transverse propagation component causes the spin-wave dispersion to first resemble the case of BV modes (for small $k_\parallel$, the finite component of $\boldsymbol{k}$-vector governs the dispersion). For higher $k_\parallel$ values, the dispersion again converges to the DE dispersion. The effect of the finite width on the spin-wave dispersion is depicted in Fig. 1.14 for three waveguide modes (and an unconfined case for comparison). Fig. 1.14 shows that the confinement effect downshifts the dispersion for high $k_\parallel$ values and actually lowers the maximum achievable group velocity. The transition between the BV and DE character of the mode results in the peak in group velocity at $k_\parallel^{v_g\,\max}(n)$. For $k_\parallel > k_\parallel^{v_g\,\max}$ the group velocity is higher than in the unconfined case. All the effects are even more pronounced in narrower waveguides. Low width of the structures results in a rather large mode splitting (compare left and right panel in Fig. 1.14).

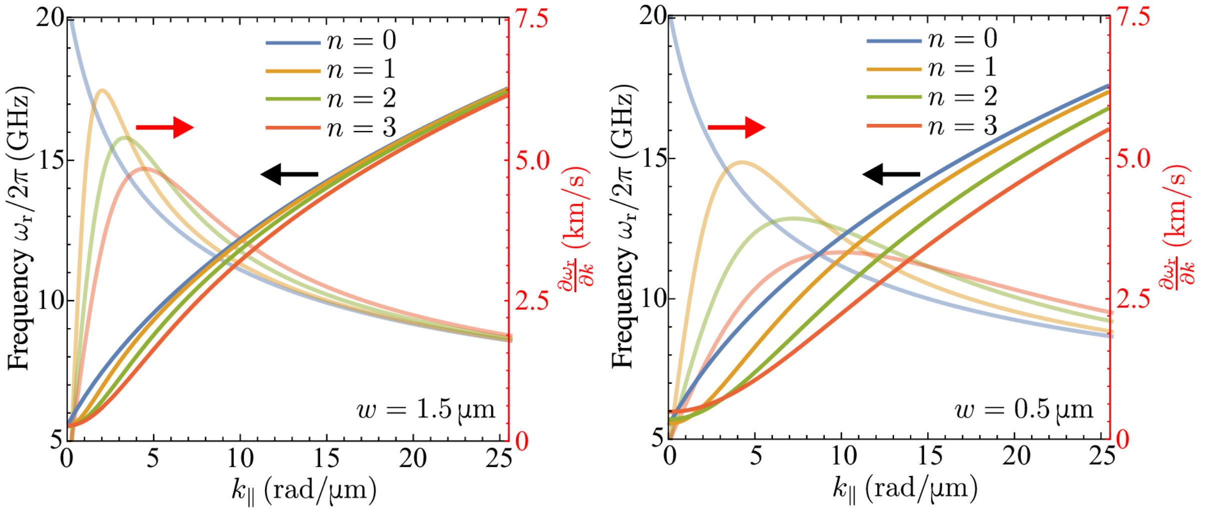

Fig. 1.14: Calculated spin-wave dispersion (continuous lines) and respective group velocity curves (continuous semi-transparent lines) for two different waveguides of various width w. The three waveguide modes are characterized by different mode number n. The reference curve of unconfined $n = 0$ dispersion is also shown. Same material parameters as in Fig. 1.12 are employed.

1.5. Spin-wave excitation

The previous section has introduced the concept of spin waves together with the spin-wave dispersion. The following text will shortly present some elementary ways of spin-wave excitation. The energy carried by the spin wave with $\omega_\mathrm{r} \sim 10\,\mathrm{GHz}$ is given by $E = \hbar\omega_\mathrm{r} \sim 50\,\mathrm{\mu eV}$. At room temperature ($T = 300\,\mathrm{K}$), the thermal energy is already $E_\mathrm{B} = k_\mathrm{B}T \sim 26\,\mathrm{meV}$. So at room temperature, the spin waves are already excited by the thermal agitation. Such excitation is rather nonspecific (noncoherent), resulting in a large ensemble of spin-wave modes in the system.

Throughout the year's selective approaches of excitation and different excitation schemes have been developed. Overall the spin-wave excitation condition is rather simple. The excitation source has to satisfy both the temporal and spatial conditions of spin-wave dispersion. In other words, the excitation source has to contain at the same time both the spatial and temporal frequencies to be able to excite the spin wave (see again the spin-wave dispersion (1.58) and also Fig. 1.14 and Fig. 1.12). In the quasi-particle view, one has to satisfy both energy and momentum condition when exciting the spin wave by external stimulus. The simplest and also most employed excitation scheme relies on the excitation by time-varying magnetic field as presented in the derivation of the FMR by (1.36). The governing mechanism is the temporal change of the Zeeman energy (1.18) [31]. As this scheme is used in this thesis, it will be covered in more detail in the following text.

In majority of experiments, the time-varying magnetic field is achieved by microwave antennas, where the microwave current (GHz frequency) creates the Oersted field acting on the magnetization [71–73]. This magnetic field couples to the magnetic system, and when the spatial profile of the magnetic field matches the one of the spin wave, the mode can be excited. The spatial profile of the magnetic field is given by the shape of the antenna, where the principal dimension of the antenna will translate to the typical spin-wave wavelengths that can be excited. At the same time, the impedance of the antenna has to be reasonably well matched to the source impedance (typically $50\,\Omega$) which again limits the bottom limit for excitation of high k spin waves.

When microwave antennas are plausible, they offer the highest degree of freedom of all other approaches for spin-wave excitation. They work in a large range of external magnetic fields, temperatures, and strain conditions offering versatile and reproducible mean of spin-wave excitation. Three typical geometries used for spin-wave excitation are shown in Fig. 1.15. The spin-wave excitation efficiency given in the last row of Fig. 1.15 is calculated from the spatial frequency spectral density of the magnetic field profile (obtained by fast Fourier transform) $P_k(\omega_k) = \sqrt{\mathfrak{F}\left(B_\mathrm{ext}^{\parallel/\perp}\right)\mathfrak{F}^{\cdot}\left(B_\mathrm{ext}^{\parallel/\perp}\right)}$. The magnetic field distribution was calculated in the FEMM software[2] by solving the magnetic vector potential under quasi-static conditions. The assumed electric current was $I_\mathrm{c} = 1\,\mathrm{mA}$.

The most trivial geometry is a simple rectangular wire (shown in the left panel of Fig. 1.15). From the symmetry, only the magnetic field components perpendicular to the current flow can exist. The in-plane and out-of-plane magnetic field components have a very different spatial profile. For an antenna with a very high width/thickness-ratio we can, under certain approximation, model the magnetic field distribution of the in-plane component by rectangular function (or by the sum of two symmetric Heaviside step functions), and the out-of-plane component as its derivative. For low width/thickness-ratio, the in-plane field resembles the Dirac distribution. The excitation efficiency plot

---

[2] Free finite element solver for magnetostatic problems. Available from `http://www.femm.info/`.

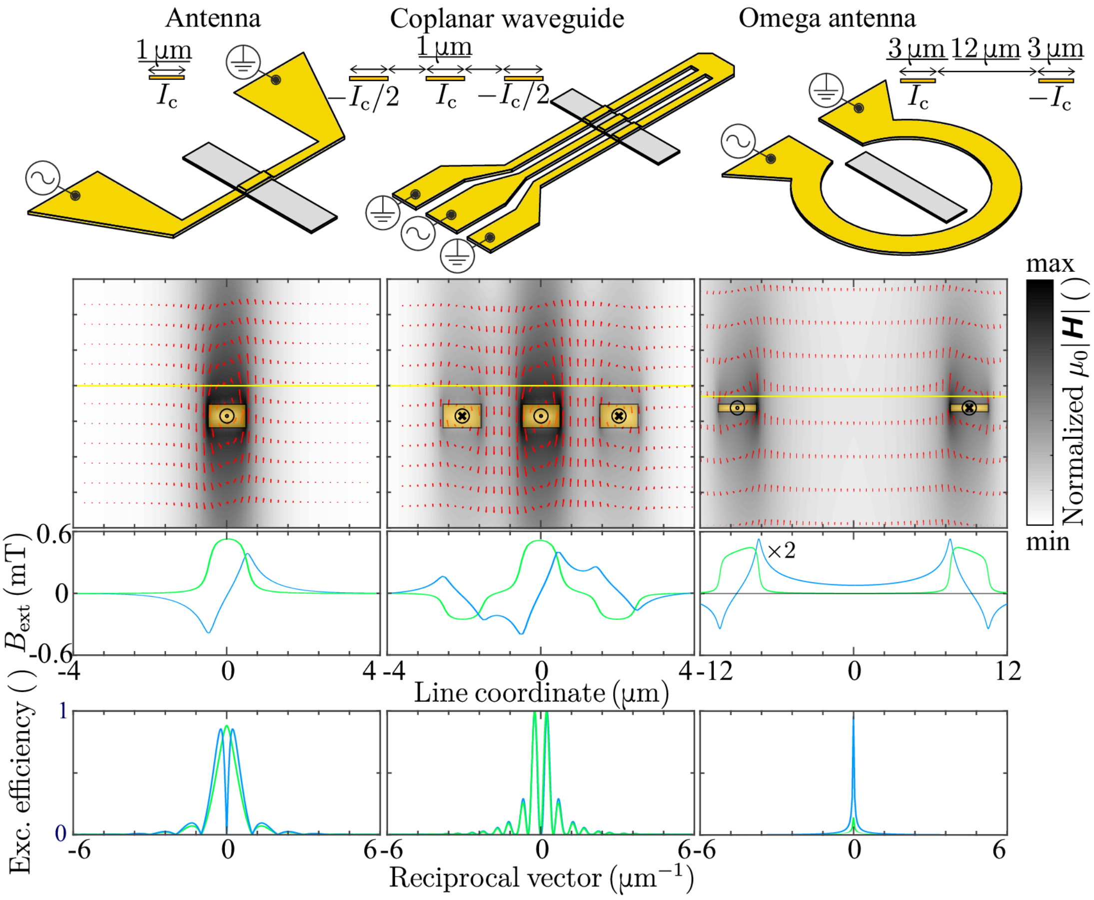

Fig. 1.15: Three main antenna geometries employed for spin-wave excitation by microwave current. The top row shows the 3D models of the antennas (yellow color). The magnonic waveguide is represented by a grey cuboid. The antennas cross-sections are also shown (thickness set to 100 nm). The finite-ground coplanar waveguide is analyzed in the left column. The middle column is designated to the antenna structure and the right column represents the omega antenna. The second row shows the 2D magnetic field distributions of individual geometries (in the plane perp. to the current flow). The magnitude and direction of the magnetic field are given by the red arrows where the magnitude is also represented by the false color scale. Each conductor with its current direction is schematically given by a transparent gold rectangle. Yellow line 100 nm above the antennas denotes the line profile for the analysis of the magnetic field of each structure. The out-of-plane/in-plane component is given in a blue/green continuous line. In the last row, the absolute value of the normalized efficiency of excitation $P_k(\omega_k)$ (the spatial-spectral distribution) is shown.

shows that whereas the in-plane component can excite even the lowest k-vectors, the out-of-plane component has two maxima close to the $k = 0\,\mu\text{m}^{-1}$. Both components have the first minimum at $k_{\min} = 1/w$, where w is the width of the antenna. The value of the k-vector of the first minimum is reciprocal in the characteristic dimension of the antenna. This directly shows that the width of the excitation window of the antenna is connected to the fabrication limits. Overall the antennas are employed to the tasks, where we do not seek the k selective excitation.

If one aims to excite a very narrow range of k-vectors, the finite ground coplanar waveguide (CPW) is a more suitable option, as it offers a very narrow and very well defined range of k-vectors it can excite. Contrary to the antenna the $k = 0$ is not excited in any component. Both components carry the very same spectral distribution. The CPW is basically composed of three individual antennas. The two antennas on the side have a twice-lower value of electric current when compared to the central conductor. The current has also reversed polarity. In our model example from Fig. 1.15 we show a calculation only for the symmetric coplanar waveguide, where all the conductors and gaps have the same dimension. It is possible to highly tune the k distribution by adjusting all the widths in the system accordingly. In general, the first maxima of excitation can be obtained as $k^1_{\mathrm{max}} = 1/(w_{\mathrm{c}} + w_{\mathrm{g}} + 2g)$, where $w_{\mathrm{c}}, w_{\mathrm{g}}, g$ are the central conductor, ground conductor and gap widths, respectively. When e.g. $g = 1/2w_{\mathrm{c}}$, the higher-order maxima are suppressed, leading to a highly k specific spin-wave excitation source. On the other hand, one should always bear in mind that the dimensions of the CPW (also of the antenna of course) highly influence the total impedance. Thus, when designing CPW, one should always consider the impedance of the structure as well as the k specificity. Overall the CPW excitation is one of the most deterministic means of excitation that allows e.g. to excite spin-wave beams simply by adjusting the individual parameters of the waveguide as presented in [73].

The last shown case is the omega antenna (Ω antenna). From the cylindrical symmetry of the problem, it produces an axisymmetric form of excitation. When looking at the out-of-plane magnetic field line profile, one can see that in the central part of the Ω, the field is almost uniform. This allows excitation of the structure placed to the central part by a quasi-global field. As it carries only the $k \to 0$-vectors, it can be easily employed to excite ferromagnetic resonance locally (to individual structures).

Quite interestingly, the spin-wave excitation of DE mode by antennas (and also from CPW) suffer from nonreciprocity [74, 75]. It can be qualitatively explained from the analysis of the magnetic field line profiles of the antenna shown in Fig. 1.15. Both the in-plane and out-of-plane components are able to excite the spin waves. In the real system, both components act on the magnetization simultaneously. When the chain of spins is overlaid on the line profile and the effect of both the in-plane and out-of-plane fields is analyzed, one can see that in one direction the excitation is partially quenched, as the joint field profiles resemble more the left-handed excitation scheme, which is not an eigenmode in a simple magnetic system. In the other direction, the excitation is resonantly enhanced supporting the right-handed modes. This effect, together with implicit spin-wave asymmetry [76], often can result in strong excitation on one side of the antenna, whereas almost zero excitation on the other. This can be switched by reversing the magnetization in the opposite direction.

The previous text analyzing various forms of microwave antennas brought a simple message and that the maximum achievable k-vector scales with the size of the excitation source [77]. As has been mentioned, for e.g. simple antenna, the first minimum of excitation is at $k_{\mathrm{min}} = 1/w$. One expects that the efficient excitation of spin waves can be considered roughly to end at $k_{\mathrm{cut-off}} = 1/2w$. This results in spin waves of the wavelength $\lambda_{\mathrm{cut-off}} = 2w$. Thus in order to excite the spin wave with a wavelength $\lambda = 200\,\mathrm{nm}$ one would need a 100 nm antenna. Such an antenna will exhibit the impedance in the range of $\sim 500\,\Omega$ (calculated by free software TXline), which would cause a huge impedance mismatch with conventional sources. The huge mismatch will translate to small microwave transmission and small microwave currents flowing through the antenna.

This motivated a vast search for other more localized excitation sources, where the narrow antennas might be at least partially avoided.

One possible approach utilizes the macroscopic excitation by homogeneous microwave fields (that can be again created by the antenna) to exploit the intrinsic irregularities (e.g. in demagnetizing fields) as a spin-wave excitation sources [65, 78]. Or the magnetization landscape itself can provide a source of spin-wave excitation by e.g. exploiting the vortex core in a magnetic disk as a spin-wave emitter [79, 80]. The technique offers a possibility to emit short-wavelength spin waves, but the applicability in real devices is rather unclear. We have to consider ultra-low excitation efficiency of presented approaches together with highly specific experimental conditions under which one can use such a scheme.

Other means of excitation rely on excitation by laser pulses [81–86], where three major mechanisms of excitation are presented. One relies on the heating of the system (nice application allowing directional control of spin-wave excitation by shaping of the exciting light pulse is presented in [85]) and its subsequent relaxation. Another approach requires femtosecond laser pulses, and the governing excitation mechanism is the terahertz magnetic field or inverse Faraday effect (see review [87]). Furthermore, as the magnetic anisotropy is closely connected to spin-orbit interaction (thus with the state of the atomic orbitals), it opens possibilities for the ultrafast switching of magnetization through non-thermal transient modification of anisotropy [88, 89]. Another method of excitation relies on the magnetoelastic coupling and the dispersion crossover of the surface acoustic waves with the spin waves [90].

Nowadays, one of the most promising ways of nanoscalling the spin-wave excitation schemes relies on spin-transfer-torque nano-oscillators (STOs), where the DC current drives high-frequency steady-state oscillations of a magnetic nano-contact [91–93]. Similarly to STO based devices, the DC-RF conversion has been presented in spin Hall nano-oscillator (SHNOs) systems. In those devices, the antidamping term stemming from the spin-Hall effect in adjacent heavy metal layer allows for stabilizing of the steady-state high-frequency oscillations of magnetization [94, 95].

2. Methods

The purpose of this chapter is to introduce the reader to the experimental methods used in the scope of this thesis. We will start with the basic underlying theory of one of the principal characterization techniques used in the thesis - the Magneto-optical Kerr effect (MOKE). We will present the physical background leading to more advanced utilization of the Kerr effect, e.g. for Kerr microscopy. We will extend the knowledge of the Kerr effect by introducing harmonic excitations leading to the Brillouin light scattering process (BLS).

2.1. Magneto-optical Kerr effect (MOKE)

Following the experimental findings of Michael Faraday [96], reverend John Kerr has observed in 1877 variation of light polarization state upon reflection on the pole piece of a magnet [97]. When originally linearly polarized light gets reflected from the magnetized matter, the reflected polarization (depending on the geometry of the experiment) will become elliptical. The polarization state after reflection can be fully described by two experimentally accessible parameters: Kerr rotation θ and Kerr ellipticity ϵ (see Fig. 2.1).

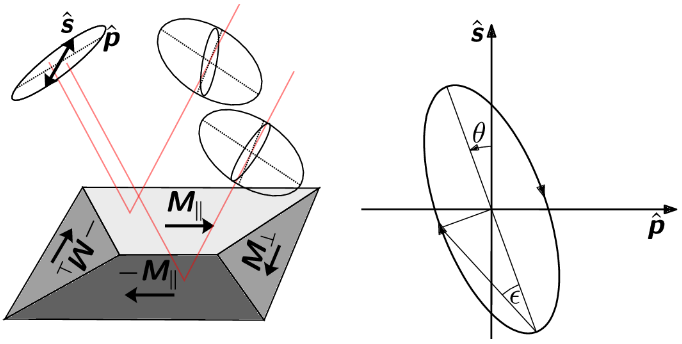

Fig. 2.1: Sketch of the originally s polarized light being reflected from the magnetic structure with four domains where the magnetization is oriented differently. After the reflection, the elliptical polarization emerges. The parameters of the elliptical polarization (denoted in the figure on the right) change between the domains with parallel and antiparallel magnetization. The transverse magnetization does not produce such an effect. Inspired by [44].

The very subtle effect was for a long time considered to be too low to be employed in sample characterization [44] until Moog and Bader in 1986 showed the monolayer sensitivity of the method [98]. As the experimental techniques developed together with more sensitive detection and better signal conditioning methods, the MOKE has become a major characterization technique in magnetic research. Because of its all-optical and non-contact character, the applicability of the method is incredibly rich. Another superior capability of MOKE is its speed, which permits the possibility for time-resolved measurements of magnetization evolution. Time resolution at the femtosecond scale has been shown [81, 99–104]. MOKE can also be depth-sensitive [105]. It can provide relatively good lateral resolution down to 0.2 µm [44, 106, 107]. Recently, a novel exotic high-resolution magneto-optical device working on the principle of SNOM (*Scanning near-field optical microscope*) has been presented, achieving a resolution below diffraction limit down to 100 nm [108, 109]. It also offers the ability to probe samples at large distances or in extreme conditions (UHV, cooled/heated samples, ...).

MOKE originates in spin-orbit interaction and can be phenomenologically understood as a form of magnetization induced circular dichroism. In the presence of the magnetic field (in simple image substituted by magnetization), the two circular paths of the electrons that are following left and/or right-handed polarized light, are not equivalent anymore. This translates to a slightly different complex index of refraction for left and right circularly polarized light waves. This second-order effect results in a variation of the light polarization state upon reflection on the magnetized material. The originally linear polarization will generally become elliptical, where the parameters of the ellipse are proportional to the magnetization.

To model this behavior, we will use a macroscopic model based on Maxwell's equations. The only effect magnetization has on the light reflection is solely given by the change of the permittivity tensor with magnetization [110]. The permittivity tensor in the presence of magnetization can be derived in various ways [110]. Probably the most accurate form is obtained by using the quantum-mechanical model, where the predictions of the magneto-optical effects even when considering interband transitions are often hindered by the unclear physical picture with not direct insight to the problem. For qualitative prediction, another model can be used considering only an electron as a particle in the potential of the positively charged nucleus. The electron feels two external forces - electric force caused by incident electromagnetic wave and also the Lorentz force of the magnetic field acting on the electron. From internal forces, we consider only a linear returning force (Coulomb interaction) and a scattering force linearly proportional to electron velocity. The derivation can be found for example in the author's master's thesis [111]. The general magnetization dependent form of the dielectric tensor $\overset{\leftrightarrow}{\boldsymbol{\varepsilon}}$ is

$$\overset{\leftrightarrow}{\boldsymbol{\varepsilon}} = \varepsilon \begin{bmatrix} 1 & \mathrm{i}Q_z & -\mathrm{i}Q_y \\ -\mathrm{i}Q_z & 1 & \mathrm{i}Q_x \\ \mathrm{i}Q_y & -\mathrm{i}Q_x & 1 \end{bmatrix}, \tag{2.1}$$

where ε is the scalar relative permittivity[1] and Q_i is the Magneto-optical Voigt constant directly proportional to magnetization [112–114]. In our model, the sample is initially isotropic and could be characterized only by the scalar permittivity ε. When the magnetization is present, the optical anisotropy appears, giving rise to magneto-optical effects.

Using the equivalency of the vector product operator (in Cartesian basis)

$$[\boldsymbol{A}\times] \equiv \begin{bmatrix} 0 & -A_z & A_y \\ A_z & 0 & -A_x \\ -A_y & A_x & 0 \end{bmatrix}, \tag{2.2}$$

---

[1] The absolute permittivity is given by $\varepsilon^{\mathrm{ABS}} = \varepsilon_0 \varepsilon$.

we rewrite the dielectric tensor from (2.1) to the vector form of a vector operator [115], [116, p. 130]

$$\overset{\leftrightarrow}{\boldsymbol{\varepsilon}} = \varepsilon \overset{\leftrightarrow}{\mathbf{1}} + \times \mathrm{i}\boldsymbol{Q}, \tag{2.3}$$

where we can recognize the antisymmetric part of the derived tensor with $A_i = -\mathrm{i}Q_i$. This particular equivalency allows us to define the so-called Voigt vector $\boldsymbol{Q} = [Q_x, Q_y, Q_z] \propto \boldsymbol{M}$. By using the dielectric tensor in material relations of vectors of the electric field $\boldsymbol{E}$ and electric displacement $\boldsymbol{D}$ [117], we find that

$$\boldsymbol{D} = \varepsilon_0 \varepsilon \left(\boldsymbol{E} + \mathrm{i}\boldsymbol{E} \times \boldsymbol{Q} \right). \tag{2.4}$$

Vector $\boldsymbol{Q}$ acts as a small perturbation to originally coinciding vectors $\boldsymbol{D}$ and $\boldsymbol{E}$. This small deviation is the only effect that the magnetization has on light propagation in the magnetized media. (2.4) also shows a very important result since it directly proves that for the s-polarized beam, the transverse magnetization (characterized by Voigt vector $\boldsymbol{Q}_\mathrm{T}$) has no effect on the light propagation at all ($\boldsymbol{Q}_\mathrm{T} \parallel \boldsymbol{E}$).

Using the result of (2.4) and inserting it to the Maxwell's equations with plane-wave solution, we can obtain the magnetization perturbed index of refraction for left and right circularly polarized light wave

$$n = \sqrt{\varepsilon} \left(1 \mp \frac{1}{2} \boldsymbol{Q} \cdot \boldsymbol{e}_\mathrm{k} \right) = n_0 \left(1 \mp \frac{1}{2} \boldsymbol{Q} \cdot \boldsymbol{e}_\mathrm{k} \right). \tag{2.5}$$

with n being index of refraction, ε scalar permittivity, n_0 unperturbed index of refraction (index of refraction when no magnetization is present) and $\boldsymbol{e}_\mathrm{k}$ is the unitary light propagation vector. This result implies that the change in the complex index of refraction is given by the dot product of the magnetization vector and the light propagation vector $\boldsymbol{e}_\mathrm{k}$.

As has been stated previously, the magnetization of the sample will introduce elliptically polarized light where the parameters of the resulting elliptical polarization will be proportional to the change of the complex index of refraction for right/left circularly polarized light. The change $\boldsymbol{Q} \cdot \boldsymbol{e}_\mathrm{k}$ is generally complex and is proportional to the so-called complex angle of Kerr rotation Φ. In small-angle approximation (valid for all the materials used within this thesis), we can write the Φ as a sum of a real and imaginary part called Kerr rotation (rotation of the ellipse) and Kerr ellipticity (azimuth of the ellipse) so that $\Phi = \theta - \mathrm{i}\epsilon$.

The fact that the magneto-optical observables θ and ϵ are proportional to $\boldsymbol{Q} \cdot \boldsymbol{e}_\mathrm{k}$ can be easily implemented for vector magnetometry [118]. The actual implementation of the $\boldsymbol{e}_\mathrm{k}$ control is done via off-axial light propagation in the microscope objective. When guiding the beam off-axis, the light beam in the sample plane will be tilted. This results in a non-zero component of the in-plane light propagation vector. The microscope objective is mounted in a 2D motorized stage allowing us to set the $\boldsymbol{e}_\mathrm{k}$ with angular precision 0.0002° for the 100× objective. The laser beam declination mechanism, together with an example of a measured signal sign with a different configuration, is shown in Fig. 2.2.

2.1.1. Kerr magnetometry

In order to get quantitative information from the measurement, one needs to be able to extract only the magneto-optical angles independent on the experimental procedure. A short summary of approaches on how to quantify the Kerr angles from measurement can be found in [119].

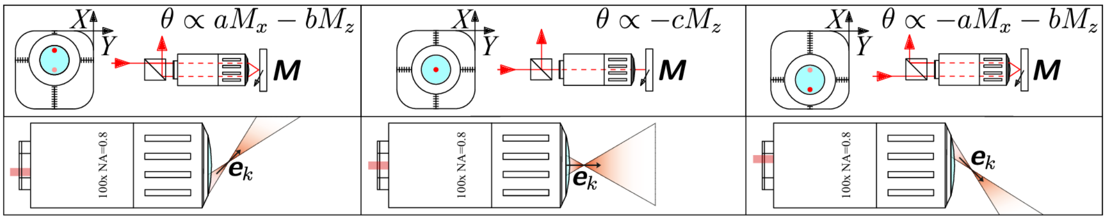

Fig. 2.2: Schematic sketch of the procedure to control the light beam declination angle by controlling the beam off-axis displacement in the entrance aperture. Schematic pictures also show what magnetization components would be detected in the different experimental geometries. The detected signal is represented by the Kerr rotation θ. The constants a, b, c represent the different contributions of individual components of magnetization to the total measured signal.

Here we model our optical setup by the means of the Jones formalism, and we derive the procedure allowing us to quantify the Kerr rotation from a measurement with our experimental setup. All the derivations are carried out for the s-polarized beam. For the s-polarized beam, the signs of the off-diagonal coefficients in the so-called sample matrix (2×2 matrix describing the effect of a sample in matrix formalism) for the polar (magnetization out-of-plane) and the longitudinal (magnetization in-plane and parallel to light propagation) Kerr effects are the same. The results obtained for the s-polarized beam and the matrix describing the polar Kerr effect will also be applicable to the longitudinal case. We start with the optical scheme presented in Fig. 2.3.

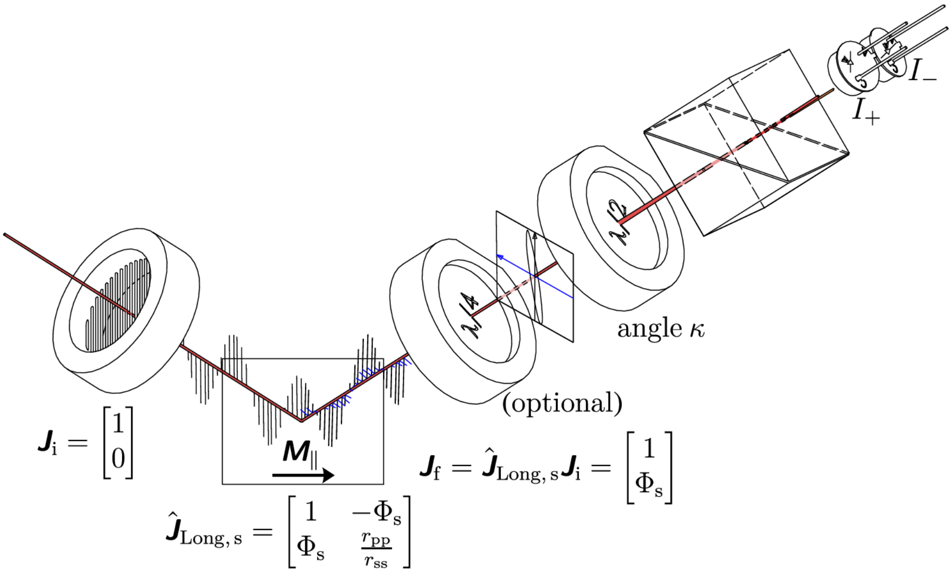

Fig. 2.3: Schematic of the reflection of the s-polarized wave on the sample with longitudinal magnetization. The magnetization introduces the p-polarized component to the originally s-polarized light wave. This altered wave then passes the quarter-wave plate (QWP). The fast axis of the QWP is in the s-direction. The Half-Wave-Plate (HWP) rotated by the angle κ serves as a simple mode coupler, allowing us to deterministically cancel (constant) polarization effects that are not caused by the magneto-optical response of the sample. The last optical element is the Wollaston prism set at 45°. With the angle of the HWP $\kappa = 0$ and for the isotropic sample ($\Phi_\mathrm{s} = 0$), it will separate the incident wave into two equivalent waves. With non-vanishing Φ_s, the intensity difference of those two waves is linear in θ_s (or in ϵ_s when the QWP is used).

Here an originally s-polarized light wave is reflected by the sample, which introduces a non-zero p component of the reflected electric field. After reflection, the altered wave passes through the Quarter-Wave-Plate (QWP, optional). This phase retarder is used as a switch between measuring Kerr rotation (no QWP) and Kerr ellipticity (with QWP). The following element, Half-Wave-Plate (HWP), serves purely as a s-p intensity converter. It allows us to balance some constant polarization effects of the apparatus. Contrary to the fixed angle of QWP, HWP is rotated by an angle of κ. After the wave is transmitted through the HWP, it continues to the Wollaston prism (rotated by 45°). This prism serves as a polarizing beam-splitter, effectively separating the s- and p-polarized beams. For the isotropic sample the measured intensities for s and p-polarized waves are the same. To start with the theoretical description, let us write down the model in the Jones formalism of the presented optical scheme in Fig. 2.3:

$$\begin{aligned}\boldsymbol{J}_{\pm} &= \hat{\boldsymbol{J}}_{\mathrm{W}} \hat{\boldsymbol{J}}_{\mathrm{HWP}}(\kappa) \hat{\boldsymbol{J}}_{\mathrm{QWP}} \hat{\boldsymbol{J}}_{\mathrm{Long,\,s}} \boldsymbol{J}_{\mathrm{s}} \\ &= \begin{bmatrix} 1 & \pm 1 \\ \pm 1 & 1 \end{bmatrix} \begin{bmatrix} 1 & 2\kappa \\ 2\kappa & -1 \end{bmatrix} \begin{bmatrix} 1 & 0 \\ 0 & \mathrm{i}^{p} \end{bmatrix} \begin{bmatrix} 1 & -\Phi_{\mathrm{s}} \\ \Phi_{\mathrm{s}} & \frac{r_{\mathrm{pp}}}{r_{\mathrm{ss}}} \end{bmatrix} \begin{bmatrix} 1 \\ 0 \end{bmatrix}.\end{aligned} \tag{2.6}$$

Term $\boldsymbol{J}_{\pm}$ stands for two Jones vectors distinguished by polarizing beam-splitter. The first matrix in (2.6) represents the polarizing beam-splitter (Wollaston prism), the second matrix stands for the HWP rotated by small-angle κ. The following matrix represents the QWP. The optionality of using the QWP is given by the superscript p. By choosing p to be 1 (or 0) we can easily model if the QWP is used (or not). The last matrix is the representation of the sample [120]. The unit vector represents the incident s-polarized light. Going through the basic algebra, we can expand (2.6) to the form of a single final vector $\boldsymbol{J}_{\pm}$

$$\boldsymbol{J}_{\pm} = \begin{bmatrix} 1 \pm 2\kappa + (2\kappa \mp 1)\mathrm{i}^{p}\Phi_{\mathrm{s}} \\ \pm 1 + 2\kappa + (\pm 2\kappa - 1)\mathrm{i}^{p}\Phi_{\mathrm{s}} \end{bmatrix}. \tag{2.7}$$

Now we get the intensity of both $+$ and $-$ beams via the following relation

$$I = \frac{\varepsilon_0 c}{2} \boldsymbol{J}^{\dagger} \cdot \boldsymbol{J}. \tag{2.8}$$

Superscript † stands for Hermitian adjoint (complex conjugate of a transposed matrix). After a few algebraic steps, we obtain

$$I_{\pm} = \boldsymbol{J}_{\pm}^{\dagger} \boldsymbol{J}_{\pm} = 8 \left[\overline{\Phi}_{\mathrm{s}} \left(\kappa \mp \frac{1}{2} \right) (-\mathrm{i})^{p} \pm \kappa + \frac{1}{2} \right] \left[\Phi_{\mathrm{s}} \left(\kappa \mp \frac{1}{2} \right) \mathrm{i}^{p} \pm \kappa + \frac{1}{2} \right]. \tag{2.9}$$

This equation still does not give much insight into the problem. In order to get a simple expression allowing us to quantify the Kerr rotation θ_{s} or Kerr ellipticity ϵ_{s}, let us do the difference I_{diff} and sum I_{sum} of the two resulting intensities given by (2.9). We also use the small-angle approximation for the complex angle of Kerr rotation. Instead of writing Φ_{s}, we use the Kerr rotation and Kerr ellipticity written as $\Phi_{\mathrm{s}} = \theta_{\mathrm{s}} - \mathrm{i}\epsilon_{\mathrm{s}}$.

We start with the case when we do not use the quarter-wave-plate in our setup ($p = 0$). Then I_{diff} divided by I_{sum} yields

$$\frac{I_{\mathrm{diff}}}{I_{\mathrm{sum}}} = \frac{2\left(4\kappa^2\theta_{\mathrm{s}} - 2\kappa\theta_{\mathrm{s}}^2 - 2\kappa\epsilon_{\mathrm{s}}^2 + 2\kappa - \theta_{\mathrm{s}}\right)}{\left(4\kappa^2 + 1\right)\left(\theta_{\mathrm{s}}^2 + \epsilon_{\mathrm{s}}^2 + 1\right)}. \tag{2.10}$$

A similar result might be obtained for $p = 1$

$$\frac{I_{\mathrm{diff}}}{I_{\mathrm{sum}}} = \frac{2\left(4\kappa^2\epsilon_{\mathrm{s}} - 2\kappa\theta_{\mathrm{s}}^2 - 2\kappa\epsilon_{\mathrm{s}}^2 + 2\kappa - \epsilon_{\mathrm{s}}\right)}{\left(4\kappa^2+1\right)\left(\theta_{\mathrm{s}}^2 + \epsilon_{\mathrm{s}}^2 + 1\right)}. \tag{2.11}$$

In the last step, we use the small-angle approximation, hence neglect all the non-linear terms in (2.10) and (2.11). By doing so, we obtain

$$p = 0 \rightarrow -\frac{I_{\mathrm{diff}}}{2I_{\mathrm{sum}}} = \theta_{\mathrm{s}} - 2\kappa, \quad p = 1 \rightarrow -\frac{I_{\mathrm{diff}}}{2I_{\mathrm{sum}}} = \epsilon_{\mathrm{s}} - 2\kappa. \tag{2.12}$$

This result allows us to quantify the Kerr rotation (or the ellipticity) only with the knowledge of the sum and differential signal on the pair of photodiodes. Angle κ of the HWP is used to cancel the (constant) polarization effects that might occur in the optical setup (e.g. strained optics [121]) or the HWP can be used to cancel some effects caused by the relative misalignment (or rotation) of the optical elements. The use of the Wollaston prism and the pair of photodiodes allows us to easily quantify the Kerr rotation and the Kerr ellipticity. This approach outperforms other methods used for measuring the magneto-optical Kerr effect in the simplicity, speed, and ease of quantification of the measured signals. The drawback is the difficulty to find the absolute zero level of the Kerr rotation. Where the signal is not symmetric in the magnetization-reversal operation (or we are not able to completely saturate the sample), it is experimentally extremely difficult to find the zero-signal level.

2.1.2. Kerr microscopy

Kerr microscopy works in a very similar manner to the Kerr magnetometry. The difference is that quite often the measured values are not quantitative as in the case of magnetometry (knowing the exact value of Kerr rotation, ellipticity). It is due to the employed method for Kerr contrast visualization. In Kerr magnetometry, the differential method and direct renormalization by the sum signal neglect many aspects of the sample and the setup (changes in the reflectivity, changes in the power of the light source). The Kerr microscopy relies on the method of nearly crossed polarizers. The light gets polarized on the polarizer, and after the reflection on the sample, it goes through the analyzer (second polarizer rotated by $\pi/2+\xi_0$) before it reaches the detector (camera). When the sample is isotropic, we find out that the intensity reaching the camera follows simply the Malus's law $I = I_0 \sin^2 \xi_0$. When we introduce e.g. Kerr ellipticity to the model, the total angle changes to $\xi = \xi_0 + \theta$. By Taylor's expansion of the Malus's law, we find out that the total intensity is proportional to $I = I_0 \left(\sin^2 \xi_0 + \theta \sin 2\xi_0\right)$. This shows that the measured signal is proportional to the angle of the analyzer, the total intensity, and in reality many other factors. Thus, it is not trivial to untangle the magneto-optical observables from the measurement. The important fact is that the intensity is linearly proportional to the Kerr rotation. This rather rudimentary analysis can be extended by adding a retarder (of the retardance δ) before the analyzer and then we can do the overall analysis as done in (2.6) again to arrive to [119]:

$$I = \frac{R}{2}\left[\sin^2 \xi_0 + \left(\theta \cos\delta + \epsilon \sin\delta\right) \sin 2\xi_0\right], \tag{2.13}$$

where R is the reflectivity of the sample. By choosing the retardance (for the $\lambda/4$ the parameter $0 \leq \delta \leq \pi/2$) we can switch inbetween the measurement of Kerr rotation θ and

Kerr ellipticity ϵ. The (2.13) can be separated to the nonmagnetic part $I_{\mathrm{NM}} = \frac{R}{2}\sin^2\xi_0$ and magnetic part $I_{\mathrm{M}} = (\theta\cos\delta + \epsilon\sin\delta)\sin 2\xi_0$. The magnetic part has the largest contribution for an angle $\xi_0 = \pi/4$, yet for such an angle the $\frac{R}{2}\sin^2\xi_0$ will also increase dramatically so that the signal to noise ratio will not be the highest for the largest I_{NM}. Usually, one has to find the maximum of the contrast function $(I_{\mathrm{M}}/I_{\mathrm{NM}})$ by adjusting the angle ξ_0 and at the same time by adjusting the retardance δ (by rotating the $\lambda/4$ plate). The $\lambda/4$ plate can be further employed to add up to the signal as both nomenclatures θ and ϵ can be used for the imaging at the same time. For samples where the Kerr rotation is low ($\theta \sim 10^{-3}$ rad) the angle of the best contrast is in the range $\xi_0 = 4° - 15°$. The angle of the $\lambda/4$ plate Δ will be in a similar range as ξ_0. Very comprehensive insight into the problematic of the Kerr microscopy can be found in review [120]. The actual implementation of the Kerr microscopy relies on classical reflecting microscope design, where a polarizer, an analyzer, and a retarder are added to the optical path. Contrary to the Kerr magnetometry, where the information is obtained from a single laser spot and for e.g. the domain pattern one has to scan with the sample/laser spot, in Kerr microscopy, we obtain the whole image of the sample at once by using a very sensitive camera. The simplified sketch of the setup is in Fig. 2.4.

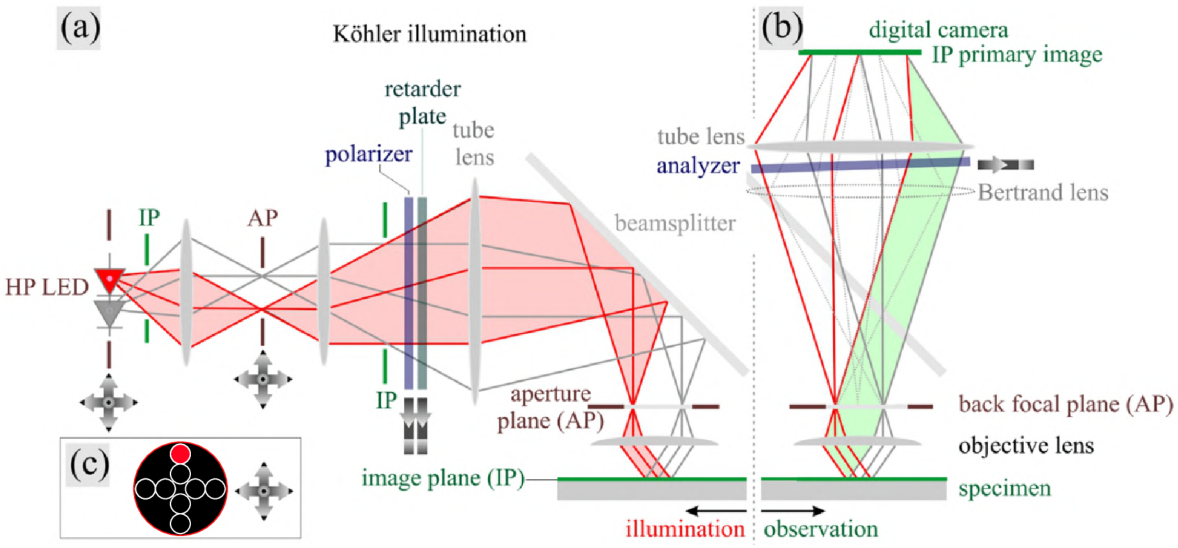

Fig. 2.4: Ray diagram for the vector Kerr microscopy. (a) The light from the LED (light is coming from left) is imaged by the condenser lens to the first aperture AP. Collimating lens images the AP to infinity. The light after the lens gets polarized on the polarizer. The next element in the way is the quarter-wave plate that adds a certain ellipticity to the light polarization. The tube lens focuses the light on the back-focal plane of the microscope objective (entrance aperture). (b) After the reflection, the light is again polarized with an analyzer and imaged by the tube lens onto the camera chip. (c) 8 LED configuration allowing Kerr magnetometry. Individual LEDs can be controlled separately. After [120].

The vectorial capability of the Kerr microscopy relies also on the off-axial light propagation in the microscope objective, as presented in Fig. 2.2. In our setup from Evico magnetics GmbH, the microscope light source consists of eight independently computer controllable high power LEDs that allow changing the angle of incidence programmatically in between two measurements (two camera images). The camera is synchronized to the LED source, and thus the individual images can be taken for different illumination conditions. Contrary to the Fig. 2.4 our setup has the retarder placed in front of the analyzer (the Jones matrix of the retarder is a diagonal matrix, thus it does not matter if the retarder is placed before or after the sample). Overall, the setup allows positioning the sample easily in 3D. Both the sample and the magnet can be rotated. This offers a great variety of experimental conditions to be probed in the measurement.

2.2. Brillouin light scattering

This section introduces the Brillouin light scattering process (BLS) with a strong emphasis on the micro-focused Brillouin light scattering (µBLS). We follow the review by [122] and the book [34]. Brillouin light scattering (BLS) is regarded as an inelastic light scattering of a light wave from space- and time-dependent potential described by inhomogeneous anisotropic dielectric tensor. Such a perturbation of optical properties can be generated by spin waves (coherent magnetization perturbation), elastic waves (coherent dynamic lattice distortion) or charge density waves (charge density distortion in a crystal). It can be understood as Bragg-like scattering on a periodical phase grating created by the change of refractive index of the material [see Fig. 2.5 (a)]. The scattered light is Doppler shifted by the frequency of the created/annihilated spin wave. When the scattering occurs on the spin wave, due to asymmetry in the off-diagonal dielectric tensor components, the photon has its polarization rotated by $\pi/2$. This allows distinguishing different contributions in the BLS spectrum simply by adding a polarizing optics.

In the photon transmission or reflection on the material with dynamic periodic perturbation of the optical properties, a fraction of the light has its momentum and energy changed as if the photon was scattered by a diffraction grating. The usual description is done in a quantum mechanical picture of quasi-particles in the process employing the scattering of the photon with quasi-particle like magnon (spin wave), phonon (lattice distortion) or polaron (charge density wave). During the scattering process, the light can lose its energy in the so-called Stokes process or gain its energy in the anti-Stokes process. Both processes have nearly the same probability at finite temperatures $\leq 5\,\mathrm{K}$. Due to the energy and momentum conservation law, we can easily connect the energy/momentum state of the spin wave to the energy of the incident and scattered photon:

$$\begin{aligned} \omega_\mathrm{f} &= \omega_\mathrm{i} \pm \omega_\mathrm{f}^\mathrm{SW}, \\ \boldsymbol{k}_\mathrm{f} &= \boldsymbol{k}_\mathrm{i} \pm \boldsymbol{k}_\mathrm{f}^\mathrm{SW}, \end{aligned} \tag{2.14}$$

where the $\omega_\mathrm{f}, \omega_\mathrm{i}$ and $\boldsymbol{k}_\mathrm{f}, \boldsymbol{k}_\mathrm{i}$ are the frequency of the scattered/incident photon, the $\boldsymbol{k}_\mathrm{f}$ and $\boldsymbol{k}_\mathrm{i}$ are the respective photon momenta and $\omega_\mathrm{f}^\mathrm{SW}$, $\boldsymbol{k}_\mathrm{f}^\mathrm{SW}$ represent the spin-wave frequency and its momentum. When the magnon is created in the process, the final frequency of the photon is lower and thus this process is represented by employing the $-$ sign in both equations (2.14). The scattering anti-Stokes process is sketched in Fig. 2.5 (b) where the expected spectrum of the light after the reflection is in Fig. 2.5 (c).

The symmetry both in the frequency and the amplitude of the Stokes/anti-Stokes peaks is true for the most cases. But for some specific cases, the asymmetries can arise. The mechanisms leading to the different amplitudes of the Stokes/anti-Stokes peak are the quadratic terms of the dielectric tensor. Another source of asymmetry is the non-reciprocity of the DE waves. The amplitude of the DE waves decays exponentially in the direction to the material. The spin waves having opposite propagation vectors propagate at different interfaces of the material. When we take into account the finite penetration

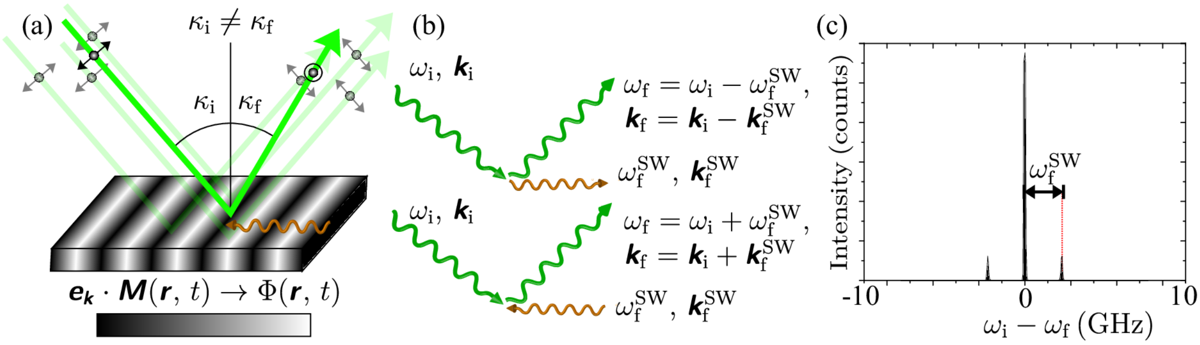

Fig. 2.5: (a) Scattering of the photon from an in-plane periodic phase grating induced by the propagating spin wave. The BLS process is rather rare and thus the majority of the photons are scattered elastically. The local complex angle of refraction is proportional to the product of the incident wave vector of the light and the magnetization. The angle of the reflection of the inelastically scattered photon is not equal to the angle of incidence. The light gains/loses part of the in-plane wave vector. Together with the change in the momentum of the light wave, the polarization of the scattered photon is rotated by π/2. (b) Quantum mechanical picture of the BLS process. Incident photon creates a magnon in the Stokes process and loses both the energy and the momentum (top row). When the incident photon annihilates the magnon, it gains both the energy and the momentum in the anti-Stokes process. (c) shows an exaggerated BLS spectrum measured relative to the elastic Rayleigh line located at 0 GHz. The Stokes and anti-Stokes peaks of low intensity are found at the frequency shift $\pm\omega_f^{SW}$.

depth of the laser light, we can conclude that the asymmetry in the spectrum is expected [123]. Quite recently, a novel approach allowing direct observation of the Dzyaloshinskii-Moriya (DMI) interaction by BLS was presented. Simply by studying the difference between the frequency shift of the Stokes and anti-Stokes peaks it is possible to directly measure the amplitude of the DMI [124].

The momentum conservation presented in (2.14) is valid only for the infinite medium. In thin films, the existence of the interfaces facilitates the broken translation invariance in the out-of-plane direction. Thus, the out-of-plane component of the wave vector is not conserved in the scattering process. The in-plane component of the wave vector of the light $k_\parallel$ can be easily calculated from the angle of incidence [see Fig. 2.5 (a)] by

$$k_\parallel = |\boldsymbol{k}_i| \sin \kappa_i, \tag{2.15}$$

the selectivity in the magnon detection can be achieved by changing the incident angle κ_i. The maximum momentum transfer is in the backward scattering geometry ($\kappa_i \to \pi/2$), where the photon is scattered opposite to the original direction. Then the total (and also maximum) momentum transfer for a green photon is equal to

$$k_\parallel^{\max} = 2|\boldsymbol{k}_i| \sin \kappa_i = 2\frac{2\pi}{\lambda_{532\,\mathrm{nm}}} \sin \kappa_i \overset{\max}{\to} \frac{4\pi}{\lambda_{532\,\mathrm{nm}}} = 23.6\,\frac{\mathrm{rad}}{\mu\mathrm{m}}, \tag{2.16}$$

which corresponds to the minimum wavelength of the detected spin waves $\lambda^{\min} = \lambda_{532\,\mathrm{nm}}/2 = 266\,\mathrm{nm}$ [122]. The detection efficiency for lower spin-wave wavelengths drops rapidly. If we compare the maximum detectable wave vector to the spin-wave dispersion in e.g. Fig. 1.12 or Fig. 1.14 one can see that the detection allows probing only the dipolar part of the DE spin-wave dispersion.

From the analysis of the Brillouin light scattering process, it can be seen that very subtle effects have to be carefully analyzed as the photon frequency shifts due to the spin-wave excitation/annihilation are $10^6\times$ smaller than the photon energy. Also, the scattering probability is extremely low, as we expect the photons to scatter from a phase grating created by the Kerr effect which is, by its nature, very low. Extreme sensitivity and extreme contrast are needed in order to distinguish the inelastically scattered photons from all the photons that went through the elastic Rayleigh scattering. For this purpose, the tandem six pass Fabry-Pérot interferometer (TFPI) was developed by John Sandercock and co-workers [125].

2.2.1. Brillouin light scattering setup

The heart of the BLS setups is the highly sensitive spectrometer TFP-2 HC from Table Stable LTD. The maximum momentum transfer is given by the experimental geometry and the wavelength of the light [(2.16)], the highest observable frequency and its resolution are given by the TFPI instrument itself. Both the frequency bandwidth and the resolution depend on the FP etalon distance d, which can be varied in TFP-2 HC from a range of hundreds of micrometers to tens of millimeters. The bandwidth of the instrument is given by the following equation

$$f_{\mathrm{BW}} = \frac{150}{d}\left(\frac{\mathrm{GHz}}{\mathrm{mm}}\right), \tag{2.17}$$

where the resolution $\Delta f = 1/\left(dF\right)$ is given both by the etalon distance and by the interferometer Finess parameter F. The resolution typically lies (for the desired bandwidths of the order of GHz to tens of GHz) in the 100 MHz range. The contrast (ratio between detected inelastically and elastically scattered photons) of the TFP-2 HC instrument is 10^{15} and higher. Such a high contrast is given both by the tandem geometry and also by using the polarizing optics inside of the interferometer. Each pass has its polarization altered so that there is no cross-talk inbetween the passes. The downside of using the polarizing optics inside of the interferometer is that the interferometer accepts only the horizontally polarized light. For more details on the interferometer, please refer to the manufacturer's specification sheet[2].

For the purpose of studying the magnetic microstructures by BLS, a suitable optical setup needs to be developed and used. The light from the powerful narrow-linewidth laser needs to be precisely guided to the high-magnification microscope objective (allowing to perform micro-focused Brillouin light scattering–µBLS). The photons scattered by the sample needs to be, with a minimum possible loss, guided to the interferometer. At the same time, the samples need to be placed in the magnetic field on a precise 3D stage for mapping purposes. The microwave excitation is achieved thermally or by the microwave antenna contacted on the substrate by a microwave probe. The sample is mounted on the 3D stage together with a pair of microwave probes for the microwave excitation. The probe is connected to a microwave generator by a SMA cable. Probes are mounted on 3D manipulators connected to the sample stage. The magnetic field is provided by the water-cooled electromagnet mounted on a rail-system. The rails allow to easily move the magnet from/to the measurement position.

The setup developed within the frame of this thesis is schematically shown in Fig. 2.6. It is based on the adjusted commercial scanning optical microscope from THATec Innovation GmbH. The commercial solution offers the microscopy module (the Cube) and the

---

[2] Available at http://tablestable.com/en/products/view/39/

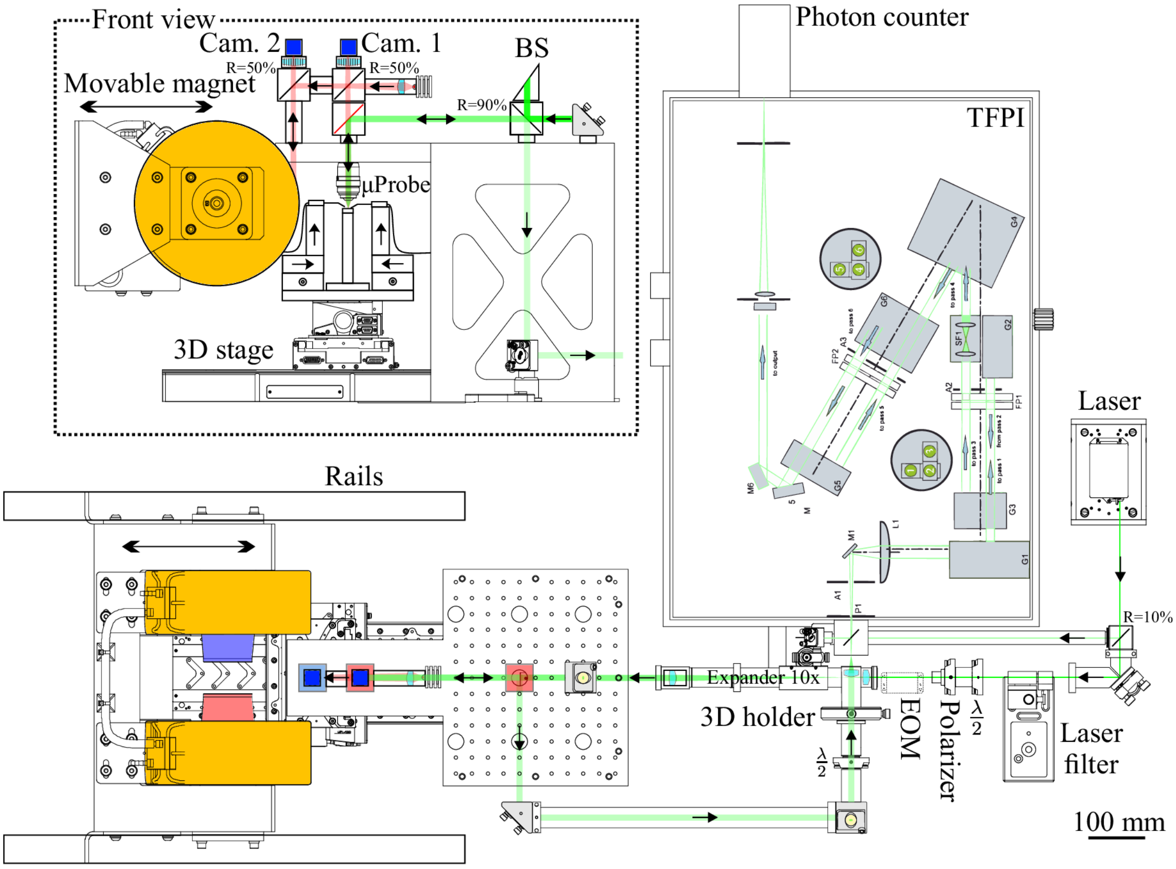

Fig. 2.6: Top view of the µBLS setup with the laser path indicated by a green line. The thickness of the line approximately reflects the width of the beam, and the black overplayed arrows mark the local beam direction. The magnetic field direction for positive current is denoted by the color of the pole pieces (magnetic field points up). Scale bar can be found in the bottom right corner. The side view of the microscopy module (the Cube) is shown in the top left corner, where also the red light for the wide-field imaging is schematically shown.

probe station (to be mounted on the 3D stage). The rest of the setup, i.e. laser, optics, electromagnet, current sources, microwave generator, and 3D stage were purchased separately.

The choice of the laser is not trivial. In our setup the laser Cobolt Samba 05.01 is used. It produces 532 nm laser light with a bandwidth below 1 MHz and very low noise at the maximum power 315 mW. The laser is dedicated to BLS measurements by the manufacturer. Extreme care of the single-mode operation has to be taken. The parasitic spurious laser modes typically lie in the window of interest of the spin-wave BLS spectra. The modes would inevitably pass the FP interferometer with the signal, and could possibly damage the sensitive detector. The spurious mode intensity needs to be at least $10^9\times$ lower than of the fundamental line so the intensity is low enough not to interfere with the expected BLS signal strength.

Following the laser path in Fig. 2.6 we will explain the individual components in the setup. The laser beam is first divided into the reference arm (10% of the intensity) and the measurement arm (90% of the intensity). The reference beam is directly guided to the reference input of the TFPI by the periscope. In the measurement arm, the laser goes through the laser filter. Its purpose in the setup is to limit the intensity of the spurious

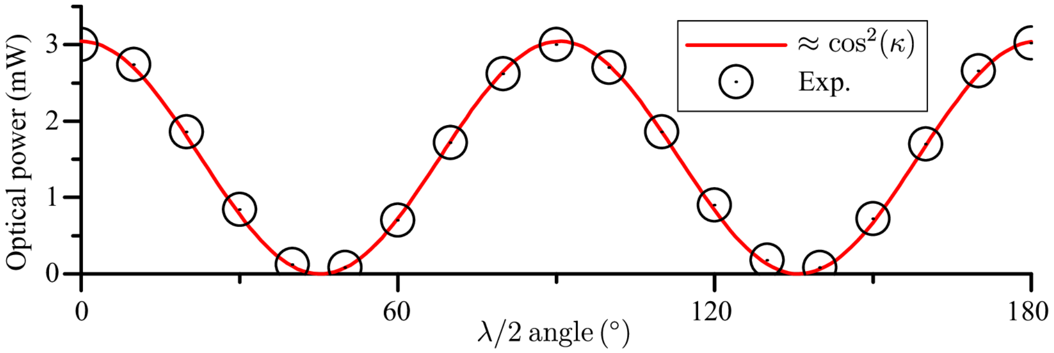

Fig. 2.7: Measured (black circles) and fitted half-wave plate angular power dependence (red continuous line). The measurement of the optical power was performed in the sample plane.

modes of the laser. It consists of a thin quartz plate with two optically flat faces coated in such a manner, so it forms a Fabry-Pérot cavity. The quartz element is mounted on the Peltier heater/cooler. By changing the temperature, the length of the cavity varies and changes the transmission band of the filter. The intensity after the filter is monitored by the photodiode. The monitored photo-current serves as feedback for the current through the Peltier. The automatic feedback analog circuit tries to maximize the intensity of the transmitted beam. As the bandwidth of the laser filter is finite, it effectively attenuates modes with the frequency shift 3 GHz and higher (around the transmission maximum).

After the filter, the power adjusting optics (half-wave plate and polarizer) is placed. By rotating the half-wave plate, it is possible to adjust the optical power going to the optics. The measurement together with the Malus law fit is shown in Fig. 2.7.

The half-wave plate angle in the rotational holder was adjusted so the maximum power of 3.1 mW is achieved for the half-wave plate angle 0°. Minimum can be reached at the angle $\pi/4$. For the maximum power, the equivalent optical power density for thought 300 nm Gaussian spot is 42 GW/m^2 which corresponds to the Laser-Induced Damage Threshold (LIDT) parameter 100 W/m. Such power can thermally damage any metallic material, and thus for measurements of the metallic ferromagnets, we employ optical power around 0.3 mW at half-wave plate angle 36°.

After the power adjustment, the laser goes through the optional electro-optic modulator (EOM) and is expanded by the pair of lenses from the original 0.8 mm to approx. 6 mm. The periscope routes the laser light to the top part of the Cube, where it goes through the beamsplitter (BS) for the backscattered light. 90% of the intensity is guided to the beam dump by the beamsplitter. The light is then directed to the coupling dichroic mirror that overlaps the laser light with the red light used for imaging. Both beams go to the microscope objective, where the beams are focused on the sample. The dichroic beam mirror allows adding the red light for the wide-field microscope (image is visible in Cam. 1). For a low magnification view, the sample can be moved to the position with Cam. 2. The backscattered beam is guided by the dichroic mirror to the beamsplitter BS. The beamsplitter also serves as a periscope guiding the light to the table level. Here it is routed towards the interferometer input. Prior to the input pinhole of the interferometer polarization angle of the beam is adjusted by the half-wave plate. After the beam passes the half-wave plate it is focused by a $f = 100$ mm lens to the input pinhole (pinhole size can be varied) of the TFPI. The lens is movable, allowing to find the best possible coupling of the backscattered beam to the optics of the interferometer. Inside of the interferometer, the beam goes six times through coupled pair of Fabry-Pérot interferometers.

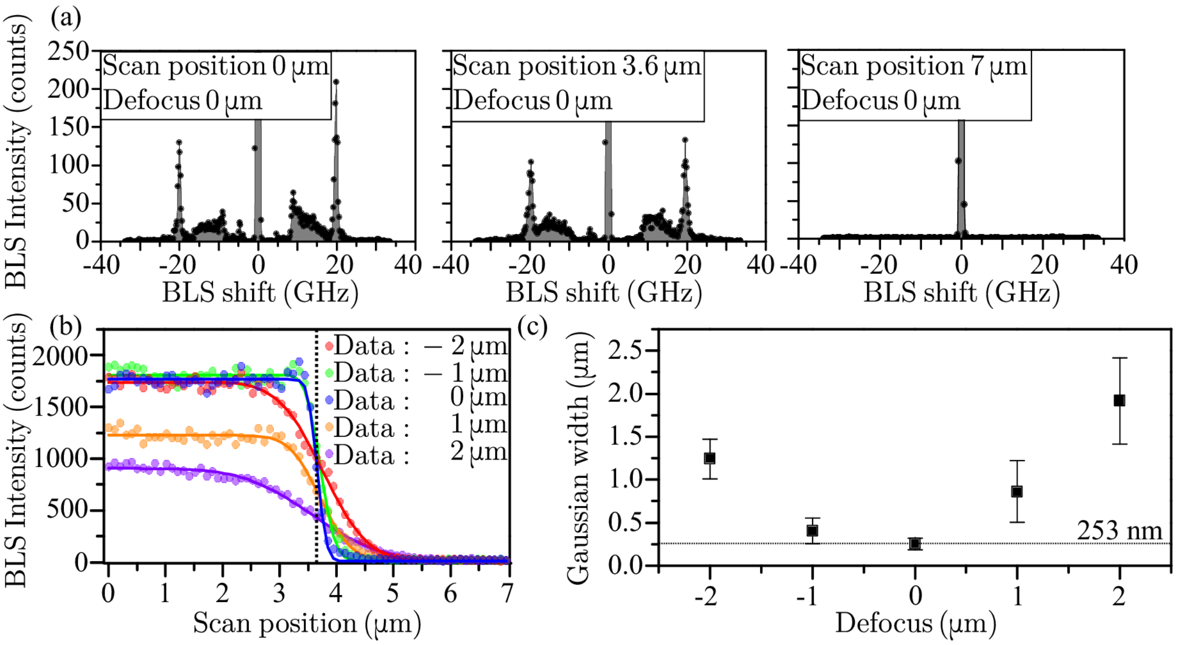

Fig. 2.8: a) Three BLS spectra obtained at different positions with respect to the edge of the structure (edge is at the position approx. 3.7 µm). (b) extracted integral intensity of the inelastically scattered light (colored circles) as a function of the scan position across the edge (the position of the edge is denoted by the dotted line) for different defocus values. (c) Extracted Gaussian widths obtained by fitting data in (b)(continuous lines) as a function of the distance from the focal point of the microscope objective. Error bars represent 95% confidence interval.

On the way, the polarization of the beam is readjusted in each path. After the beam leaves the FP pair, it is focused through the output pinhole to the highly efficient photon counter with the quantum efficiency reaching 70 % (Hamamatsu C11202-050). The interferometer automatically switches in between the reference and the backscattered beam by the double shutter system just after the input pinhole. The reference beam serves as the stabilizing reference.

The purpose of the setup is to measure spin waves with high spatial resolution. From the Rayleigh criterion, it is known that the resolution is proportional to the used wavelength (532 nm in our case) and inversely proportional to the numerical aperture of the used microscope objective. We use LD EC Epiplan-Neofluar 100x/0.75 BD microscope objective due to its suitability for polarization microscopy (NA = 0.75). The field of view of the wide-field microscope is approx. 300 µm. Rather large working distance ($w_\mathrm{d} = 4.1\,\mathrm{mm}$) of the objective allows to fit the microwave probes under the objective together with the sample and thus to excite spin waves with suitably short waveguides/antennas. We estimated the resolution of the setup by the knife-edge technique [111], where we scanned the sample (40 nm thick Permalloy sample in the field of 60 mT) under the laser spot in 100 nm steps over the edge of the structure. For each position, we recorded the BLS thermal spectra. Typically obtained spectra for a different probing position are in Fig. 2.8 (a). The thermal spectra clearly show the elastic peak (obtained from the reference input) at 0 GHz. The spin-wave band starts approx. at ±8 GHz, and the first perpendicular standing spin wave [126] is seen at ±20 GHz. For different probing positions, the spin-wave signal drops. At 7 µm, there is no sign of any inelastically backscattered photons. In the following experiment, we studied the effect of the defocus on the signal. To do so, we integrated the BLS counts from ±6 GHz to ±20 GHz for each laser position and we plot the total signal as a function of the scan position and defocus in Fig. 2.8 (b). It is easily seen that the narrowest transition from the maximum counts to the lowest counts is for the blue data points representing the data obtained in the focal point of the microscope objective. Defocus in both directions results in the broadening of the curve. Quite interestingly, a negative defocus does not cause a significant drop in the signal, whereas a positive defocus has a very negative effect on the signal strength. This might indicate a misalignment in the optical path. Afterward, we fitted the data with the complementary error function of the form

$$I = \frac{I_{\mathrm{max}}}{2}\mathrm{erfc}\left(\frac{\sqrt{2}\,(x - x_0)}{w_{\mathrm{Gauss}}}\right) - o, \tag{2.18}$$

where I_{max} is the maximum intensity, x_0 is the position of the step, w_{Gauss} is the Gaussian width (width of the Gaussian waist), and o is the spatially invariant background coming mainly from the dark counts of the detector. The Gaussian width can be thought of as an indicator of the system resolution as it marks the distance from the center of the beam, where the intensity drops to 22.8 %. In Fig. 2.8 (c) the Gaussian width w_{Gauss} as a function of the defocus is shown. It has a clear minimum for the focal point and asymmetrically rises to both sides. The minimum experimentaly achievable Gaussian width for our setup was estimated to 253±26 nm which is in agreement with similar setups, and data presented elsewhere [122]. It should be noted that the Gaussian width only does not fully describe the resolving power. In magneto-optical experiments, it is rather complex, and it also depends on the polarization of the incident light. The procedure described here is rather simple and straightforward but is a good indicator of the actual resolving power.

As direct and natural consequence of high spatial resolution, one loses the specificity in the k-space. Thus, in general, with µBLS it is not possible to distinguish the $\boldsymbol{k}$-vectors of various spin-wave modes. If there are more spin waves in the system with different $\boldsymbol{k}$-vectors, we will probe all of them at the same time without k-selectivity. This is due to the large angular distribution of the directions of the incident and scattered $\boldsymbol{k}$-vectors of the light. Not only we do not know the original $\boldsymbol{k}_{\mathrm{i}}$-vector of the incident photon interacting with the spin wave, yet we also do not know the final $\boldsymbol{k}_{\mathrm{f}}$ of the detected photon. All the incident photons and at the same time all the detected photons come from within a certain light cone with an opening angle given by the numerical aperture of the used objective. The situation is schematically shown in Fig. 2.9.

In this geometry, the maximum detectable in-plane spin-wave $\boldsymbol{k}$-vector is following the (2.16):

$$k_{\parallel}^{\mathrm{max}} = 2k_{\mathrm{max.\,IP}} = \frac{4\pi}{\lambda_{532\,\mathrm{nm}}}\mathrm{NA} = 17.8\,\mathrm{rad}/\mu\mathrm{m}, \tag{2.19}$$

with $k_{\mathrm{max.\,IP}}$ being the maximum in-plane projection of the incident photon $\boldsymbol{k}$-vector.

The effect of focusing the light is mostly apparent when measuring the thermal spin-wave spectra. The very low energy of the spin-wave excitations causes a stochastic population of all the spin-wave modes (white noise of spin-wave states). The spin-wave excitations are noncoherent and are excited at random positions. The thermal data can offer pure spin-wave behavior in the system without any convolution with the excitation scheme or other sources of spin-wave system distortions. In this case, when measuring with microscope objective, we probe the bath of spin waves of equal distribution of the states up to a certain level, where we lose the resolution due to finite probing $\boldsymbol{k}$-vector. The spectrum of thermal spin waves in the Permalloy sample in the field of 60 mT is in the

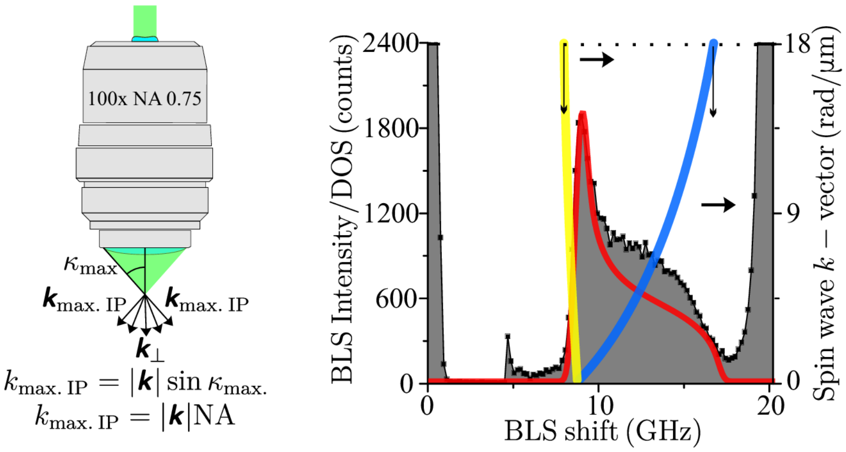

Fig. 2.9: The left figure shows a microscope objective forming a cone of light with a large distribution of $\boldsymbol{k}$-vectors. The maximum angle κ_{max} is given solely by the numerical aperture of the objective. The maximum in-plane projection is given by the formula below the sketch. The right graph shows μBLS measurement of the thermal spin waves on a 40 nm thick Permalloy layer in the magnetic field of 60 mT. The red curve is the analytically calculated density of states (renormalized to fit the measured BLS signal strength). The dispersion of the DE and BV waves is given by the blue/yellow continuous lines calculated for the sample parameters ($M_{\mathrm{S}} = 0.9\,\mathrm{MA/m}$). The horizontal dotted line marks the maximum accessible in-plane $k_{\mathrm{max.\,IP}}$-vector. The strong mode on the right side is the first perpendicular standing spin wave mode.

right panel of Fig. 2.9. The spectrum has an onset of the spin-wave band at around 7 GHz and has a peak at 8.8 GHz. Then it rapidly decays towards the final drop at 17 GHz. The drop starts to be apparent close to the cross-section of the dispersion with the maximum accessible $\boldsymbol{k}$-vector line (follow the blue line in Fig. 2.9). Looking at the position of the maximum in the measured thermal spin-wave spectrum and the dispersion relation, we see that the peak is at the position of the ferromagnetic resonance. In the vicinity of the FMR point, the highest slope of the curves causes the most spin-wave modes to fall to the individual measured frequency channels resulting in a distinct peak. The position of the peak can be further utilized for material characterization. In our case, we attempted to model the measured signal by finding a density of states of the spin-wave system for all the possible angles of the spin-waves and all the $\boldsymbol{k}$-vectors up to certain cut-off wave vector $k^{\mathrm{max}} = 17.8\,\mathrm{rad/μm}$. Conventionally, the density of states at frequency ω for a spin-wave mode at frequency ω_{r} can be defined on the basis of the delta function $\delta\left(\omega - \omega_{\mathrm{r}}\right)$ and by integrating the delta function over all the states. We use this approach and we extend it by taking into account the finite resolution of the BLS spectrometer. We assume the Gaussian sensitivity of the spectrometer with a Gaussian width $w_{\Delta} = 300\,\mathrm{MHz}$. The density of states of the system can be then found as

$$DOS(\omega) \propto \int\limits_{0}^{\pi/2} \int\limits_{0}^{k_{\parallel}^{\mathrm{max}}} \exp\left(\frac{-\delta\left(\omega - \omega_{\mathrm{r}}\left(k, \kappa\right)\right)}{w_{\Delta}}\right) \mathrm{d}k\mathrm{d}\kappa. \tag{2.20}$$

The (2.20) assumes an equal distribution of the $\boldsymbol{k}$-vectors up to a certain threshold. As can be seen in the discrepancy between the model and the data presented in Fig. 2.9, the general situation is more complex and needs to be elaborated with more care. The calculated density of states represents the detectable frequencies on the basis of detectable

k-vectors. When actively exciting the spin waves by e.g. microwave antenna (presented in Fig. 1.15), which exhibits strong variation of excitation efficiency for different ***k***-vectors, and detecting by the µBLS one expects the total signal to be given by the product of the detectable and excitable density of states from both events.

2.2.2. Phase-resolved Brillouin light scattering

The previous text has elaborated on the consequences of the laser focusing on the detection mechanism. In order to achieve high spatial resolution, one needs to sacrifice the wave vector sensitivity. The BLS process is phase-sensitive in nature, as the scattered photon carries the phase information of the excited/annihilated spin wave. This can be utilized even in experiments with µBLS. The information is extracted from a two-beam interference of the measured and reference signals in analogous configuration to Mach-Zehnder interferometer [127–129]. The reference light needs to be of a constant phase and has to be spatially invariant. It also needs to be on the very same frequency as the inelastically scattered photons on the spin waves to ensure temporal coherence of the process. The reference is generated by the electro-optical modulator (EOM) implemented to the setup. It is connected to the same RF source as the excitation antenna. The EOM consists of the electro-optic crystal made from MgO doped $\mathrm{LiNbO_3}$. By applying the voltage, the crystal changes the index of refraction, which effectively changes the phase of the transmitted light. When time-varying voltage is applied, the phase of the light is modulated in time by the factor β. For the simplest case of sinusoidal phase modulation at frequency Ω, the light obtains a time-varying phase shift in the form $\beta \sin \Omega t$. We can then write the light wave of the frequency ω and amplitude E_0 at one position in the simplest case as $E = E_0 \mathrm{e}^{\mathrm{i}(\omega + \beta \sin \Omega t)}$. As the β is usually very small, we can perform the Taylor expansion[3] of the light wave and also use the Euler's formula to arrive to

$$E = E_0 \mathrm{e}^{\mathrm{i}(\omega + \beta \sin \Omega t)} \overset{\beta \to 0}{\to} E_0 \left(\mathrm{e}^{\mathrm{i}\omega t} + \frac{\beta}{2} \mathrm{e}^{\mathrm{i}(\omega + \Omega)t} - \frac{\beta}{2} \mathrm{e}^{\mathrm{i}(\omega - \Omega)t} \right), \tag{2.21}$$

which is directly interpreted as three waves, where two low-intensity waves have its frequency shifted by frequency ±Ω (relative to the laser line). This is directly what we usually observe in the spin-wave system. Doing so, we have now the reference light at the same frequency as the spin wave, and thus we can use it in the interference experiment to entangle the phase of the scattered photons from the spin waves. The actual implementation of the phase-resolved µBLS is shown in Fig. 2.10. The temporal coherency is assured by using a single RF source (maximum frequency in our setup is 40 GHz) and by splitting the microwave signal by the power divider (bandwidth $1-18$ GHz). One part of the signal goes to the sample, whereas the other portion of the power goes to the EOM (bandwidth $0-15$ GHz). We can digitally select, whether both signals will be terminated, will go to the sample, EOM, or if we will pass the signal to both signal paths. For this purpose, we implemented two coaxial switches (bandwidth $0-18$ GHz). This allows us to distinguish the origin of the observed signal between the spin waves and the EOM. The reference light intensity needs to be controlled independently from the spin-wave excitation. The microwave power going towards the EOM is attenuated in a continuously variable coaxial attenuator (bandwidth $2-18$ GHz). The microwave signal can be attenuated up to 10 dB.

---

[3] In general, the (2.21) can be derived with the use of the Bessel function and Jacobi-Anger formula. This would also show that the EOM creates an infinite number of sidebands with quickly decaying intensity.

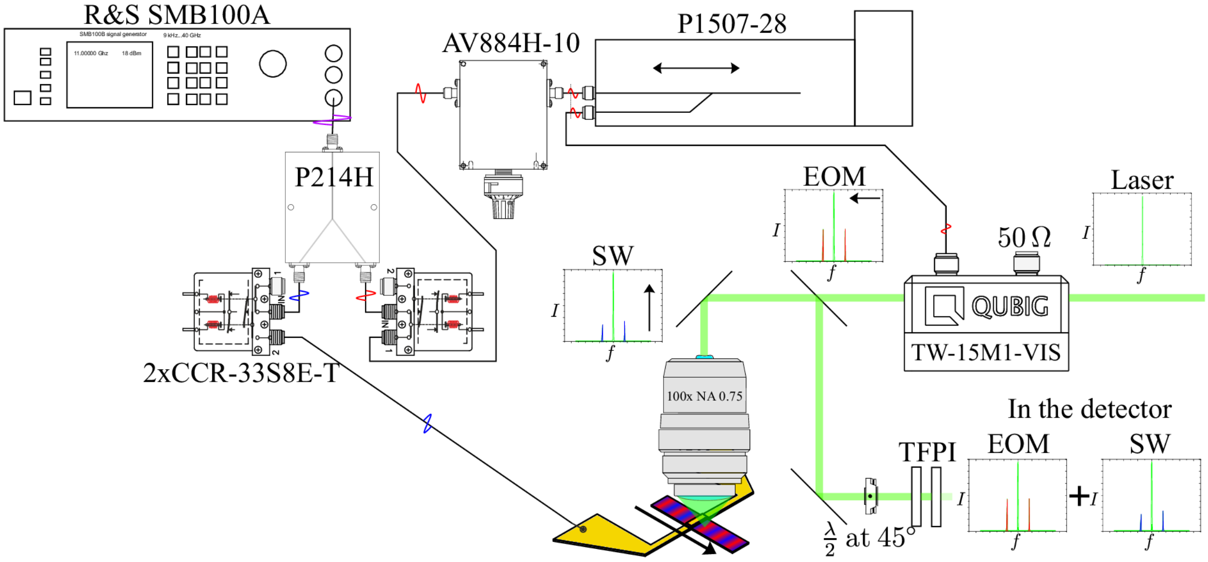

Fig. 2.10: Schematic overview of the microwave components needed for phase-resolved μBLS. The single-mode laser beam is passed through the EOM. Here, the side-bands are created by the electro-optical effect. A major part of the laser beam intensity passes the EOM unchanged. Both the unchanged and the modulated light go to the microscope objective. The light is focused on the sample where the photons interacting with the spin waves create the sidebands at the same frequency as the EOM light. The EOM light phase on the sample is constant, but the SW-scattered photons carry the phase information of the spin waves (phase is schematically shown on the sample in red/blue color). In the backscattered light path, the spin-wave signal and the EOM signal interfere in the interferometer. In the microwave path, the signal from the R&S SMB100A microwave source is split into two equivalent signals by the ATM P214H power divider. Both signals go to the Teledyne CCR-33S8E-T coaxial switches with one output terminated by 50 Ω terminator. One part of the signal is sent to the exciting antenna and the other portion is streamed to the ATM AV884H-10 microwave attenuator. The phase shift of the EOM microwave signal is added by the ATM P1507-28 phase shifter. Finally, the signal arrives at the traveling wave QUBIG TW-15M1-VIS electro-optical modulator with second input again terminated by 50 Ω terminator.

The following element is the phase shifter. By mechanically changing the signal path length, we can shift the phase of the EOM signal relative to the sample excitation. In our setup, we use motorized phase shifter with a maximum phase shift of 60°/GHz. Thus, already at 1.5 GHz, we can get the phase shift in the range $0 - \pi/2$.

At this point, the signals are still not able to interfere with each other since the spin-wave signal has the polarization rotated by $\pi/2$ and the EOM sidebands keep the original polarization. For this purpose, the polarization of the light needs to be adjusted on the half-wave plate.

After the polarization adjustment, both signals can interfere, and the interference intensity (I) is detected by the interferometer. To create a suitable model for the process, we can use the classical two-wave interference model [128]. The interference pattern is given by the photons scattered by the spin waves (intensity I_{SW}) and the sideband photons from the EOM (intensity I_{EOM}). The model reads

$$I = I_{\mathrm{SW}} + I_{\mathrm{EOM}} + 2\sqrt{I_{\mathrm{SW}} I_{\mathrm{EOM}}} \cos\theta_{\Delta}, \tag{2.22}$$

where the θ_Δ is the relative phase shift of the spin-wave signal and the EOM signal.

For the simplest case of 1D spin-wave propagation, the method can be very easily utilized to extract the wavelength information of the spin waves in the system. If we assume the same experimental geometry as presented in Fig. 2.10, we can theoretically predict the phase-resolved BLS signal. In the experiment, we will excite the spin waves by the microwave antenna and we will probe the BLS intensity locally by the µBLS while scanning the laser spot away from the microwave antenna (the distance is given by the x coordinate). We expect the spin-wave phase (omitting all the offsets) to spatially evolve as $\theta = 2\pi x/\lambda$. The intensity of the spin waves will decay exponentially with the distance from the antenna so that $I_{\mathrm{SW}} = I_0 \exp\left(-x/L_{\mathrm{att}}\right)$, where I_0 is the spin-wave maximum intensity and L_{att} is the spin-wave attenuation length[4]. Both the phase and the intensity of the EOM light are constant in the sample plane. The situation is depicted schematically in Fig. 2.11.

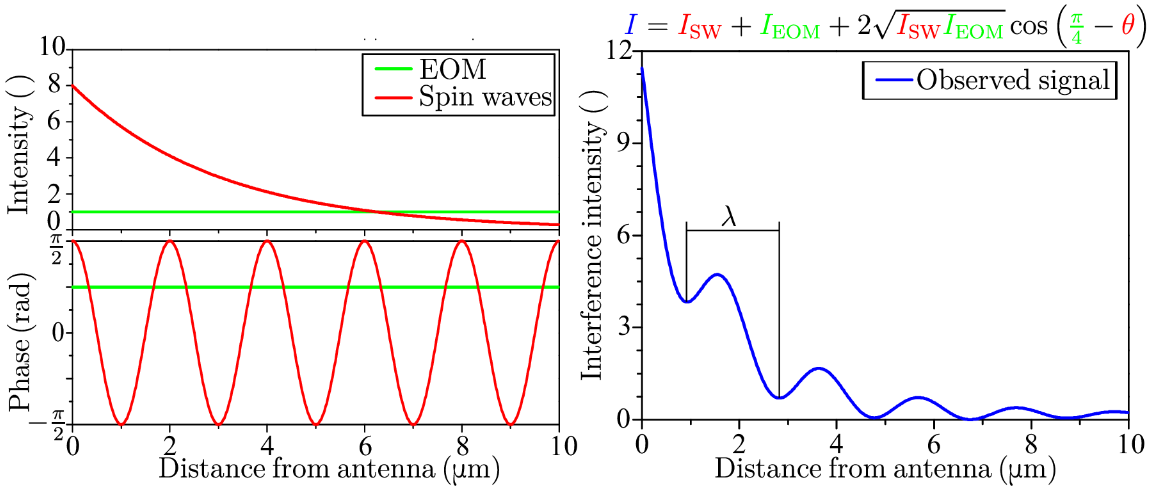

Fig. 2.11: The left column shows the spin-wave and the EOM intensities as a function of the distance from the antenna (top row). The bottom row depicts the phase evolution of both signals. The right column shows a calculated plot by using the interference formula (2.10) and the data from the left column. The spin-wave wavelength can be obtained simply by looking at the distance of the two extremes.

A rather simple experiment shown in Fig. 2.11 can serve as a workaround allowing us to again obtain the wavelength ($\boldsymbol{k}$-vector) information from the µBLS measurement. The system needs to be actively pumped by a microwave signal as in this experiment, only the coherent excitations can form an interference signal. The wavelength can be easily obtained from the measurement (presented in Fig. 2.11) either by looking for the distance between the individual extremes or by fitting the full dependence given by (2.22). Fitting of the full dependence also yields other parameters like e.g. the attenuation length of the spin waves L_{att}.

---

[4] Length at which the spin-wave intensity drops to $\frac{1}{\mathrm{e}}$ of the maximum intensity.

3. Epitaxial $Fe_{78}Ni_{22}$ system

In order to get the unique properties arising from the confined magnetism, one needs to fabricate magnetic micro and nanostructures. Classical approaches of nanostructuring of magnetic material such as optical or electron beam lithography combined with lift-off processing [130], wet [131] or dry [132] etching or ion implantation [20, 23] do not offer the same control over local material properties as these fabrication processes rely on binary selection of adding or removing the magnetic materials.

In cooperation with TU Wien, we have developed a novel system based on the $Fe_{78}Ni_{22}$ layers grown on Cu(0 0 1) substrate in the metastable nonmagnetic fcc phase. Conventionally, the iron at room temperature is stable in the α-phase, which is magnetic and has a bcc structure. The Curie temperature of iron is approx. 770 °C and for even higher temperature of 900 °C the iron recrystallizes to the fcc γ-iron phase. Later it was found that in thin films this high-temperature phase can be stabilized even at low temperatures. In order to achieve this goal, a suitable substrate with a low lattice mismatch allowing to accommodate the fcc γ-iron structure has to be found. For large lattice mismatch, the iron will not follow the substrate and will tend to again grow in the bcc phase. At the room temperature, the fcc Fe lattice has a lattice constant of 3.588 Å, and the bcc Fe has a lattice parameter of 2.68 Å. The copper has an fcc lattice with a lattice parameter of 3.615 Å. This makes the bcc Fe structure highly incompatible with the fcc Cu(0 0 1) substrate. In contrast, the lattice mismatch between the fcc Fe and fcc Cu is only 0.7 %. This renders the fcc Cu(0 0 1) substrate an almost ideal candidate for the growth of the fcc Fe in (0 0 1) orientation. It has been shown that for the small thickness of Fe (5-10 ML), the Fe grows pseudomorphically following the fcc (0 0 1) substrate. Resulting layers are fcc and paramagnetic [133]. When increasing the thickness further, the energetically favorable α-phase will take over, and the spontaneous recrystallization to the bcc (1 1 0) will occur. Structural $\gamma \rightarrow \alpha$ phase transition is linked directly to the paramagnetic→ferromagnetic phase transition. The layers will manifest the in-plane magnetic anisotropy.

The layers with the thickness in the range of 8-10 ML are on the edge of the stability between the fcc and bcc structure. Without the presence of any defects (as fcc→bcc recrystallization initiation centers), the material will keep the fcc structure even though the bcc structure would be energetically more favorable. The fcc structure is in the metastable state (local minimum of the energy), with the ground state (global minimum of the energy) being the bcc structure. It has been shown that by using the Ar^+ ion beam, this barrier can be overcome, and it is possible to deterministically drive the system from the fcc to the bcc structure. The thickness limit of 8-10 ML in pure Fe films is strict, and due to many technical and spin wave related reasons, it is more convenient to work with higher thicknesses of the material. It has been shown that CO back-pressure during the epitaxial growth has a positive effect on the stability of the fcc phase. Layer thicknesses up to 18 ML have been achieved. The potential of the material for nanostructuring has been shown by using a lithographically prepared mask [134]. Further improvement has been made by alloying pure iron with nickel [135]. Nickel is a very compatible material well embedded in the iron matrix (and vice versa). At room temperature, the nickel is found in the fcc phase. By adding approx. 20% of nickel, and by using the CO during the growth, the thickness limit is suppressed. Layers with thicknesses up to 130 ML have been successfully grown and subsequently transformed by the ion beam.

The presented thesis derives the knowledge from the analysis of three systems. The only difference between the individual systems was the thickness of the deposited $Fe_{78}Ni_{22}$ layer. We have analyzed 8 nm, 12 nm, and 24 nm thick systems. The following text will present the data on all the systems. To avoid the confusion between individual analyses, we present in Appendix 2 a complete list of samples. For each sample, we also give a list of figures, where the data obtained on the particular system are presented.

The transformation mechanism was accounted to the thermal spike model. It describes how the incident ion transfers its energy in the collision with the target atom. In case there are many incident ions, a small volume of the material is melted. This serves as a lattice defect and with a certain probability, a nucleus of the bcc structure is created. For isolated ion-collision events many bcc nuclei are created, eventually forming a continuous layer as the nuclei coalesce. This is the case when a wide-beam ion source is used.

The presented work presents the direct writing of the magnetic material by the gallium FIB instead of using the wide-beam ion source. For the sake of this thesis more relevant transformation mechanism is presented. The FIB transformation of the metastable iron was studied thoroughly and is summarized in the bachelor's and master's thesis of Viola Křižáková [136, 137], who did a very elaborate, dedicated, and systematic work on the system. The project has been initiated and guided by Michal Urbánek. The material properties are summarized in the following publication [26].

The focused ion beam writing is done in such a way that the beam of certain current I is scanned on the sample with a certain distance inbetween the two pixels. For the Tescan FIB/SEM system Lyra 3, this parameter is called simply *pitch* defined as d_s. At each spot, the beam stays for a certain dwell time T_{dw}. From the ion beam current, dwell time for each spot, and the pitch of the ion beam writing, we define the ion dose per area as:

$$D = N\frac{IT_{\mathrm{dw}}}{|e|d_s^2}, \tag{3.1}$$

with N representing a number of repeated scans of the same area. The ion beam current is always measured prior to the irradiation by deflecting the beam into the Faraday cup and measuring the electric current in the FIB system. The beam current can be controlled by changing the aperture or by changing the condenser voltage. To increase the repeatability of the irradiation conditions, we have always aimed for the same ion beam current. This was achieved by using 200 μm aperture, and by changing the condenser voltage so that we obtain a rather small ion beam current of 150 pA. From the experience, a good habit is to start the ion beam emission and wait for ~ 30 minutes. For the cold start of the FIB, the ion beam current reading usually stabilizes after this time. For selected ion beam current, the achieved spot size of the FIB was estimated by knife-edge technique (taking FIB image while detecting the SE electrons and finding the structure showing a rapid drop of contrast) to be 30 nm. This value defines the pixel size or the pitch of the ion beam. We always aim for a rather large overlap of neighboring irradiated spots. This interconnects more easily the melted material to the vicinal material and helps the material to crystallize according to the nearby lattice. We have exclusively used the experimental pitch $d_s = = 10$ nm. As will be seen later, the number of scans N has a huge influence on the growth regime and thus it is not advised to control the ion dose by changing the number of scans of the same area.

The ion dose is one of the key parameters employed during the transformation of the layers. It defines the number of collision events per unit area and time and thus can highly affect the bcc growth (by growth we mean the fcc-bcc recrystallization). From the technical reasons, it is more convenient to control the ion dose by the dwell time as the beam current is given by the actual setting of the FIB column and cannot be changed easily. The ion dose is linear in the dwell time and thus is easily and accurately controlled. The dwell time can be changed in the range between 50 ns and a couple of seconds. This assures the lowest ion dose (for the lowest measurable ion beam current of 1 pA) to be 10^{11} ions/cm^2. This dose is low enough not to cause any observable sputtering. The intermixing/sputtering usually happens for ion doses in the order of 10^{16} ions/cm^2.

Another control parameter is the ion beam energy E_I. It defines the penetration depth and the interaction cross-section of the ion with the target material. In FIB systems, it also defines the ultimate resolution of FIB. It is expected that for larger ion energy the energy that can be transferred to the target material will increase. Together with the increased energy transfer, the penetration depth of the ion in the material is expected to increase. We have performed a combined calculation of the stopping ranges and the transport of the ions in a matter in SRIM and TRIM packages [138]. The SRIM/TRIM packages allow us to calculate the ion-transport related phenomena and to address e.g. the energy deposited to the system, ion stopping ranges, impurity distribution, and many other important parameters about the ion beam interaction with the solid material. We have calculated the ion transport in a system of 8 nm $\mathrm{Fe_{78}Ni_{22}}$ on Cu substrate. Since the stopping power parameter is not known for this particular system, it was calculated as an effective value of the mass ratio given by the atomic concentration of both materials. From the calculations, we have extracted the ion penetration depth of the ions as a function of the primary ion beam energy, and for certain ion beam energies, we have also extracted the depth profile of the ion distribution [see Fig. 3.1 (a)].

The calculation shows that the projected ion range evolves linearly with the primary beam energy. For the maximum ion beam energy given by the ion beam source of the Tescan Lyra 3 microscope $E_\mathrm{I} = 30\,\mathrm{keV}$, the mean projected ion range is close to 10 nm. For $E_\mathrm{I} = 5\,\mathrm{keV}$, the mean range drops to 3 nm. The TRIM calculation shows that for $E_\mathrm{I} = 30\,\mathrm{keV}$ majority of the ions ends up in the substrate, whereas for the $E_\mathrm{I} = 5\,\mathrm{keV}$ all the ions will be implanted to the $\mathrm{Fe_{78}Ni_{22}}$ layer. Using low energy could possibly lead to a nonuniform depth profile of the material after the transformation. This would be highly undesirable. The thermal spike molten volume will have a certain size and thus it is expected that the transformation will extend further from the ion impact in the depth. To assure the transformation through the whole thickness it is desirable to use the high primary ion energies. Also, the metallic gallium embedded in the magnetic material is not desirable for a multiple of reasons. For the above reasoning, and also for the FIB writing/imaging purposes, we have fixed the energy of the primary beam always to the value of $E_\mathrm{I} = 30\,\mathrm{keV}$.

The last parameter controlled in the experiment is the scanning strategy of the FIB. Any desired shape needs to be filled by the FIB discrete writing spots in a way that the ion beam does not goes through any point twice. In our system, the two strategies are possible [see Fig. 3.1 (b) and (c)]. The first strategy is called linear scanning. The beam scans on a linear path in a zigzag manner. Two major axes can be recognized: a fast axis and a slow axis. The angle of the fast scanning direction can be selected arbitrarily

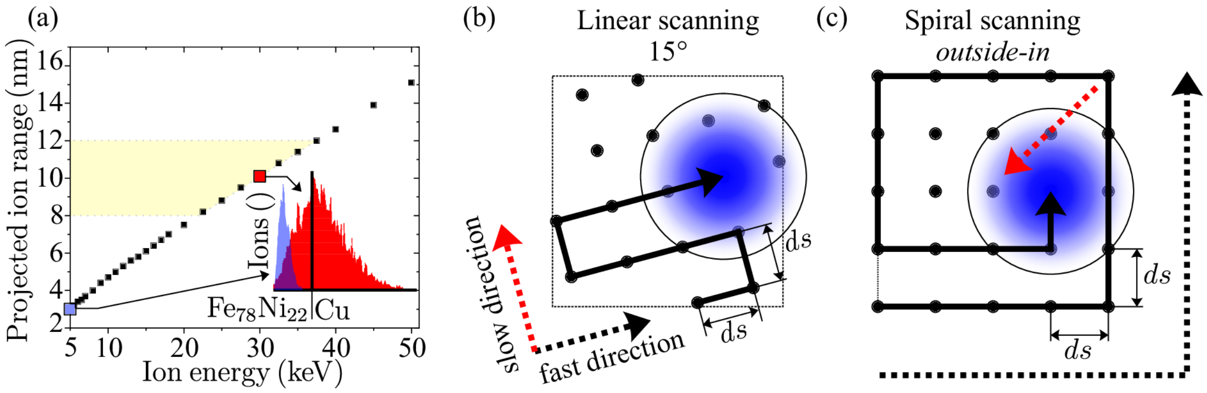

Fig. 3.1: (a) shows the SRIM calculation of the projected range of the Ga^+ ion in the 8 nm $Fe_{78}Ni_{22}$ on Cu substrate. The yellow area marks the thickness range of the $Fe_{78}Ni_{22}$ layers mainly studied in this thesis. The inset shows the TRIM calculated depth distribution of deposited Ga^+ ions to the material. The black line marks the $Fe_{78}Ni_{22}$/Cu interface. The distribution represents 30/5 keV ions marked by red/blue color respectively. (b) the definition of the linear zigzag scanning by the ion beam at a given angle 15°. Points are desired irradiated pixels separated by a pitch d_s and the thick line is the ion beam path. The ion beam spot with its approximate size relative to the selected pitch is shown by a blue gradient. The slow and fast directions of the scanning are defined in the left/bottom part. (c) shows the spiral scanning of the ion beam. The fast axis is in the azimuthal direction whereas the slow direction is the radial direction.

relative to the FIB coordinate system. For the spiral scanning, the beam follows the spiral path towards the inside of the structure for the outside-in scanning strategy or vice versa for the inside-out strategy.

Altogether, the FIB offers a huge playground of parameters that can be employed during ion beam irradiation. After many series of experiments, we have decided to fix certain parameters for the sake of understanding more the transformation process. The parameters are in the Table 3.1. Where the last three parameters are studied more in detail in the following section.

Table 3.1: Selected parameters with its ranges used in the FIB induced transformation process.

Ion beam current:	Fixed at approx. 150 pA
Ion beam energy:	Fixed at 30 keV
Ion beam pitch:	Fixed at 10 nm (1/3 of spot diameter)
Dwell time:	Adjustable: 50 ns – 500 s
Number of scans:	Fixed at 1× or 100×
Ion dose:	Adjustable by the dwell time: $10^{11} - 10^{17}$ ions/cm^2
Scanning type:	Selectable: Spiral (outside-in/inside-out) or linear (at an arbitrary angle)

3.0.1. Characterization of the transformation

Prior to the fabrication of any magnonic devices, the properties of the material need to be well characterized. The FIB writing opens many possibilities by offering an immense number of parameters/strategies of irradiation. From the pioneering experiments, it was found that the irradiated and virgin material have an observable difference in the SEM images using standard SE detector. The contrast allows us to clearly distinguish three gray levels: the intermediate gray level corresponding to the untransformed areas, bright contrast corresponds to the areas in the early stage of transformation, and dark contrast indicates the fully transformed FeNi thin film in the bcc phase. This can be easily used as feedback in the experiment, as one can directly see, whether the transformation is successful. Together with the change of the contrast, the magnetic properties also change. We illustrate this behavior by irradiating $Fe_{78}Ni_{22}$ on Cu by 30 keV Ga^+ FIB with the parameters mentioned at the end of the previous section. The thickness of the $Fe_{78}Ni_{22}$ layer was 12 nm (see Cu#14 in Appendix 2). We selected the linear scanning strategy with the horizontal fast axis scanning direction (irradiation was innitiated from the bottom). In between the structures, the ion dose was varied by the change of the dwell time. After irradiating twelve $5 \times 5\,\mu m^2$ rectangles in total, we have tilted the sample to the normal incidence of the electrons. We observed a SE signal while scanning over the irradiated structures. After the experiment, we have performed scanning Kerr magnetometry by home-build scanning Kerr magnetometer [111]. The total Kerr signal (Kerr ellipticity) is linearly proportional to the net magnetization in the measured area. This has enabled us to correlate the change of the contrast with the magnetic properties measured via the Kerr effect. The interconnection of the secondary-electron (SE) contrast and the magnetic properties is shown in Fig. 3.2.

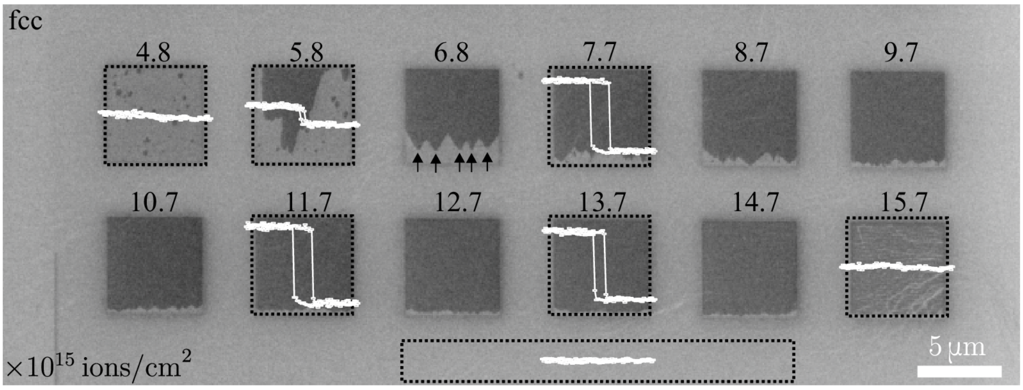

Fig. 3.2: SEM micrograph (SE contrast) of twelve $5 \times 5\,\mu m^2$ rectangles irradiated by a single scan of FIB by zigzag scanning with the angle 0° (scanning initiated from the bottom). The ion dose was varied from 4.8×10^{15} ions/cm^2 to 15.7×10^{15} ions/cm^2. The dose is increasing from the top left corner towards the bottom right corner. The hysteresis loops are overlaid to the individual structures. The regions from where we averaged the Kerr signal for individual structures are denoted by dashed black rectangles. Arrows in the rectangle irradiated by the dose of 6.8×10^{15} ions/cm^2 mark the growth initiation defects.

It is clearly seen that the change in the magnetic properties (represented by the measured maximum level of Kerr ellipticity) is closely connected to the change in the SEM contrast. For certain ion dose, we see almost no difference from the virgin fcc (compare hysteresis loop at the bottom of Fig. 3.2 and the loop obtained for the dose 4.8×10^{15} ions/cm^2). For a higher ion dose, one can see the dark area expanding from the bottom of the rectangle, where the scanning was initiated. With increasing the dose even further, we can see increasing of the maximum Kerr signal up to the maximum signal at the dose of 11.7×10^{15} ions/cm^2. Increasing the dose even further leads to sputtering and intermixing of the material which manifests itself as a decrease of the total Kerr signal. At the dose of 15.7×10^{15} ions/cm^2, all the magnetic material has vanished, and no hysteresis loop is observed. From this experiment, we can understand a little more about the growth process. It can be seen even in the first irradiated rectangle that few darker areas already appeared. From the conclusion that the darker contrast represents the appearance of the magnetic material, we can conclude that we already see small nuclei of bcc crystals that have been randomly transformed by the ions on certain defects. For the higher dose (see e.g. 6.8×10^{15} ions/cm^2 case in Fig. 3.2) the growth continues steadily after it was initiated. The bcc region is expanding in a triangular fashion from the point of initiation. This highly supports the successful desired growth regime where we aimed for the FIB melted material to follow the surrounding previously recrystallized bcc lattice. The fcc-bcc energy barrier is lowered by the existence of coalescent bcc grain and the steady-state migration of the bcc/fcc grain boundary is preferred. Such a grow regime can be understood as a threshold process. The ion dose that is sufficient for steady-state growth (we also refer to it as a critical ion dose) of the material (after the growth has been initiated by any means) is lower than the dose needed for nucleation of the bcc from the pure fcc material. It is also nicely seen that the mean length (in the slow scanning direction) needed for reaching the steady-state growth is changing between the structures. Studying this initiation length is needed for the future writing of small patterns since we need to be sure that we completely transform the whole structure. It would be rather unwise to perform writing of the 1×1 µm^2 rectangle with the ion dose 6.8×10^{15} ions/cm^2 since we see clearly from the Fig. 3.2 that the growth is starting approx. after 1.5 µm. To get more insight into this behavior, we have analyzed the average distance the FIB travels in the slow axis direction until the layers grow in steady-state growth. The length needed for the growth initiation was analyzed from horizontal SE line profiles of individual structures from Fig. 3.2. The position of the steepest contrast change (first derivative of the signal) reveals the fcc/bcc interface.

We have analyzed the line profiles from all twelve rectangles programmatically (the data from the lowest/highest doses are omitted). Afterward, we found the fcc/bcc interface by numerically differentiating the line profiles (first central derivative). The position of the peak in the first derivative from the edge of the structure marks the local initiation length. From all the vertical line profiles in a single structure, we calculate the mean initiation length. The results are shown in Fig. 3.3.

The analysis depicted in Fig. 3.3 shows that the initiation length firstly observed at the threshold ion dose 5.8×10^{15} ions/cm^2 converges quickly to a value close to 100 nm at the dose of 9.7×10^{15} ions/cm^2. Thus, by overdosing, one can push down the writing limits of the system, yet it is not the best solution as we will later show that overdosing deteriorates the magnetic properties of the layers. From the fact that the ion dose needed to initiate the growth is higher than the dose needed for sustainable growth, we can think of a couple of mechanisms exploiting this feature. In order to use a small dose to grow the whole structure, yet still limit the initiation length to the minimum, we have performed the following experiment. We have irradiated eighty 5×5 µm^2 rectangles, where prior to growing the rectangular structure, we have irradiated a very narrow 100 nm wide initiation rectangle at the position, where the growth of the whole structure is initiated. We have performed two sets of experiments. One with a single FIB scan of the initiation rectangle and second with scanning the initiation rectangle 100 times. We kept the same total dose for both experiments. The purpose of this initiation rectangle was to create an artificial number of defects allowing the growth to be sustained only by the smallest dose possible.

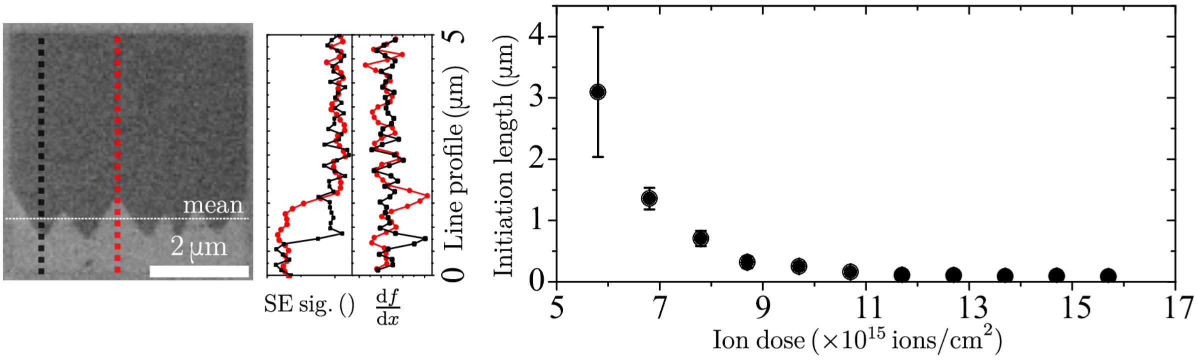

Fig. 3.3: The left panel shows the SE image of FIB transformed rectangle transformed with the ion dose 6.8×10^{15} ions/cm^2. The two vertical lines denote the position of two exemplary line profiles plotted together with its first derivative in the adjacent graphs. The dotted white line marks the mean position of the fcc/bcc interface. The right panel shows the result of the analysis from ten rectangles shown in Fig. 3.2. The error bars were calculated as 95% confidence intervals (normal distribution).

Fig. 3.4 shows the experiment outline together with the experimental results. The first row of Fig. 3.4 shows the qualitatively same behavior as presented by Fig. 3.2 and Fig. 3.3. Yet following the structures even for the smallest growth dose it is seen that the growth nucleates with more ease for increasing the initiation dose. For initiation dose high enough, we can completely get rid of the initiation region (with our finite resolution of the SEM). The same feature is observed directly from the SEM images and further supported again by analyzing the mean initiation length shown by Fig. 3.4 (c). We expect the first few tens of nanometers to be overdosed, but the rest of the structure will keep its properties as if it was grown with the smallest dose possible. For the highest doses of both the growth dose and the initiation dose the sputtering of the material occurs. Interestingly, performing the same experiment by irradiating the initiation rectangle a hundred times while keeping the same total ion dose as for single-scan irradiation, the experiment does not yield the desired result. Despite the fact that we lower the mean initiation length by increasing the dose in the initiation region, it seems that it is far less effective as if we scanned only once. It seems that the scanning type truly defines the resulting growth regime of the structure. The same less effective initiation is observed when the initiation region is scanned with a scanning oriented horizontally while the structure is scanned vertically. Also, when the initiation rectangle is exchanged by a single line again, the initiation of the growth does not proceed as for a single scan case. The performance is even worse than for single scan horizontal or multiple scans in the vertical direction. This leads to the conclusion that simply milling the material out (and forming a defect in the topography) is not sufficient enough to implement the viable type of bcc nuclei needed for the start of the growth.

The second possible mechanism we present for lowering the minimum dose needed for achieving sustained growth is using a larger seed structure. It is more probable that a large structure will, in total, contain more defects for the growth initiation. Also, as we will not be fully interested in the magnetic properties of the seed structure, we are allowed to slightly overdose the structure in order to create a good seed matrix for the structure of the interest. This type of growth initiation strategy was driven by the desire to grow long and narrow waveguides. Even when we overdosed a small region at the edge of the structures, the growth initiation was not reliable. We then added an overdosed initiation region from which the structures can grow (see Fig. 3.5).

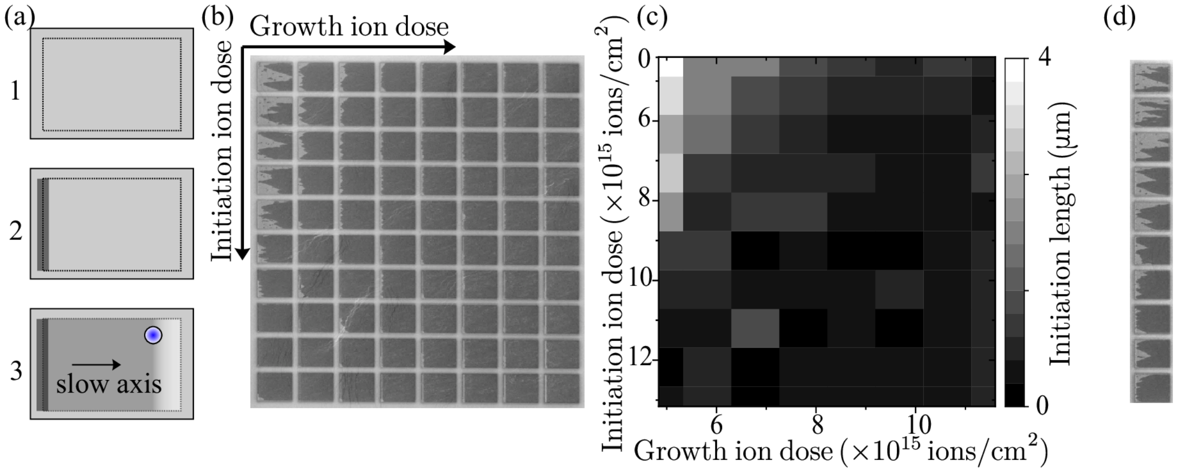

Fig. 3.4: (a)Definition of the irradiation procedure. First, we define the desired rectangle shown by the dashed line. In the second step, we irradiate a narrow rectangle on the left edge of the structure. In the last step, the structure is irradiated starting from the previously irradiated area. All irradiating steps are done with the fast scanning axis vertical. (b) shows the SEM image of the experiment for a single ion beam scan. In the 2D map, the dose for the growth is varied from 4.8×10^{15} ions/cm^2 to 11.7×10^{15} ions/cm^2 and the initiation dose is in the range 0 to 13.2×10^{15} ions/cm^2. The increasing direction is denoted by the arrow. (c) is the 2D map of the extracted initiation lengths from (b). (d) shows the first column of the experiment for the initiation area irradiated by 100 scans.

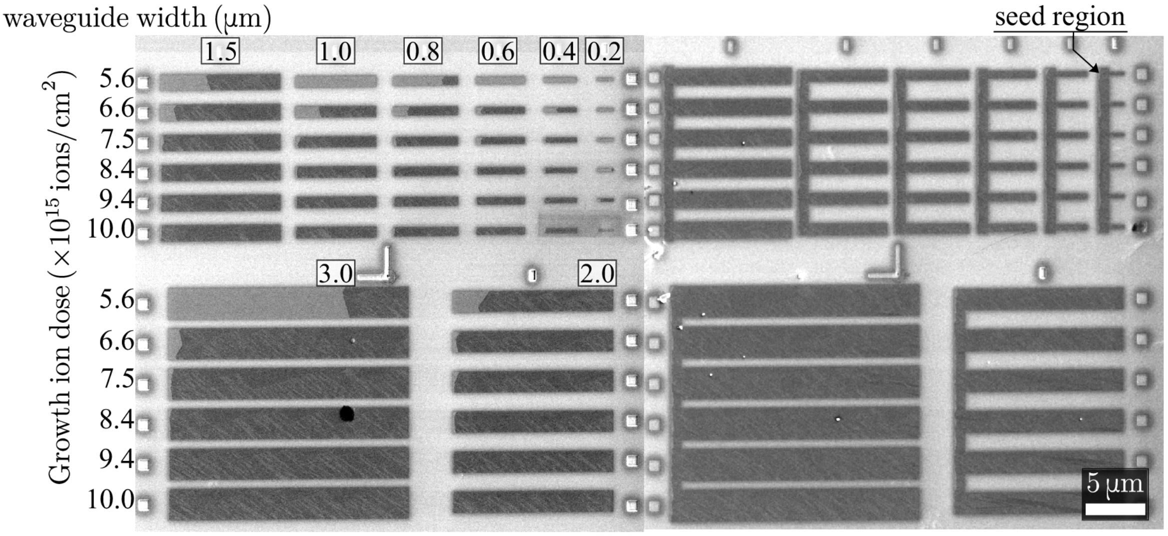

Fig. 3.5: The left panel shows an experiment probing the possibility to grow narrow magnonic waveguides by the FIB direct writing. We have varied the waveguide width (keeping the total width/length aspect ratio constant and equal to 1:8) and the overall growth ion dose. We oriented the fast scanning axis to the vertical direction. The right panel shows similar structures. The difference is that prior to the writing of the waveguides, we have irradiated large seed region with a dose of 6.6×10^{15} ions/cm^2. We initialized the growth of the structures from this region. One of the seed regions is marked in the top right corner.

In this analysis, we first attempted to grow various waveguides, where we kept the aspect ratio constant. It is clear that when lowering the waveguide width, the growth of the smallest structures becomes unreliable even when increasing the total growth dose of the structure. Except for the case with the high growth dose of 9.4×10^{15} ions/cm^2, the smallest structures were not successfully grown in any other case. The writing process relying on the intrinsic non-homogeneity of the material lowers the reproducibility of the ion beam transformation. In the right panel of Fig. 3.5 we show that by creating a slightly overdosed and sufficiently large initiation region, the growth becomes very deterministic even for lower ion beam doses. Structures of nominal widths down to 200 nm were reproducibly grown. The existence of the seed region might deteriorate some of the magnetism related phenomena, as it is e.g. expected that a higher total number of defects will lower the coercive field of the seed region. This will be translated also to the coercive field of the interconnected structure itself. This rather problematic downside of the presented approach would be also present in the approach with the small region implemented to the edge of the structure. The approach relying on the large seed region proved to be more reliable in terms of growing the narrow structures when compared to any other approach we have tested.

Following the result from Fig. 3.5, we have attempted to estimate, how long can the growth of the bcc structure be sustained, even for the extremely narrow waveguides. We followed the very same approach as in the right panel of Fig. 3.5. Instead of keeping the same aspect ratio of the waveguides, we have extended all the structures to the length of 20 μm. Fig. 3.6 presents the obtained results.

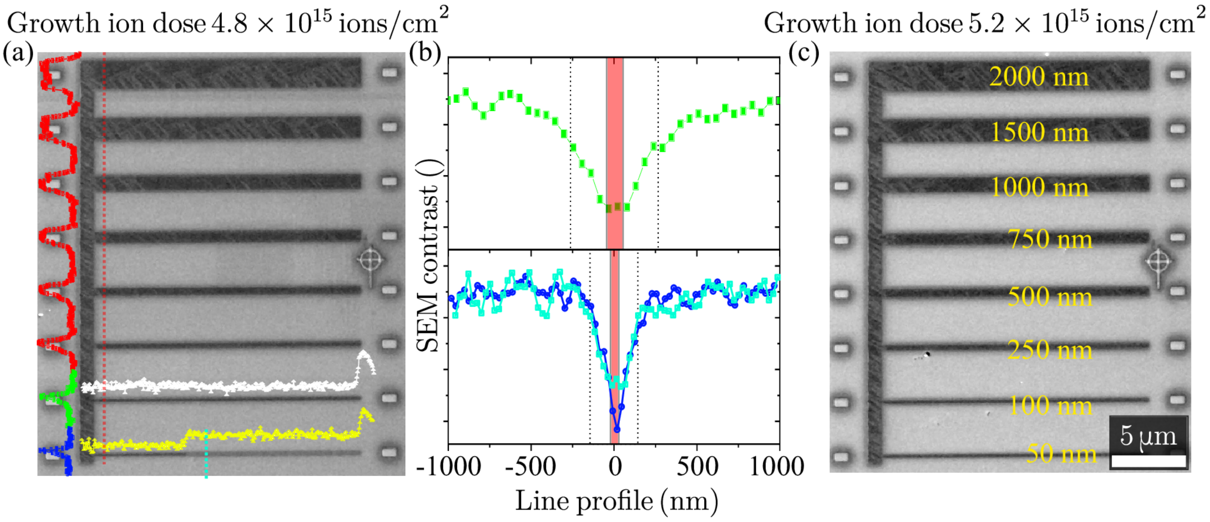

Fig. 3.6: The figure presents a complementary analysis to Fig. 3.5. It this set of experiments, the waveguide length was kept constant to 20 μm. The nominal width was varied between 50 nm and 2 μm (denoted in the right figure). (a) The waveguides written with the growth ion dose 4.8×10^{15} ions/cm^2. The red (green/blue) is the SEM vertical line profile from the red dashed line. White and yellow lines are horizontal line profiles taken from the two narrowest structures. (b) The detail of the vertical line profile with a focus on the 50 and 100 nm wide waveguides. In red, the nominal width of the structures is shown. The black dashed line shows the FWHM. For reference, a line profile (denoted by cyan dashed line in the left image) from the part of the structure where the sustained growth stopped is shown. (c) The structures grown by a slightly higher growth dose [when compared to structures in (a)] of 5.2×10^{15} ions/cm^2. In this case, we were able to completely transform even the narrowest waveguide.

Even for the lowest dose that was found from the dose testing to allow for sustainable growth, we were able to grow structures of nominal widths ranging from 2 µm to 50 nm and with the length of 20 µm [see Fig. 3.6 (a)]. The structures were grown by the single pass of the FIB. The horizontal line profile taken over the narrowest rectangle reveals that the growth stopped after ~ 7 µm. Whereas the horizontal line profile of the 100 nm wide rectangle show only one large step between the irradiated and virgin area (left side), the 50 nm wide structure exhibits two apparent steps in the contrast. One (now slightly smaller) step is again attributed to the difference between the irradiated and virgin material. The second step found approximately 7 µm from the left side represents the point, where the sustained growth stopped. There is a very apparent contrast change for both cases. Also, the transverse profile of the contrast is very different between the area that was growing in the sustainable regime and the area that was irradiated by the FIB without full fcc/bcc transformation [see the bottom row in Fig. 3.6 (b)]. For the successfully grown structure, the contrast shows a sharp peak with a width approximately equal to the nominal width of the structure. For the 100 nm wide structure [top row in Fig. 3.6 (b)] we can recognize the plateau of the signal with a width of approx. 140 nm. In a rather wide area around the nominal width of the structure, contrast continuously vanishes to the value measured at fcc material. The width of this transition is in the range of hundreds of nanometers. Multiple mechanisms are broadening the irradiation area from the nominal shape. The finite resolution of the FIB is equal approximately to the spot size 30 nm also from the TRIM calculations we see that effectively for single spot irradiation the ions in multiple scattering events reach up to 30 nm from the incident spot. One needs also to bear in mind that the FIB column used in our experiments is of the liquid-metal-ion-source (LMIS) type. This type of ion source is known to produce an ion beam tail with low intensity yet spanning further from the main ion beam spot. It has been realized by Viola Křižáková in her thesis that the dependence of the contrast on the ion dose is highly nonlinear. Thus, even small irradiation already results in a change in contrast producing a rather large width of the contrast transition as seen in Fig. 3.6 (b). Even though the growth terminated, the achieved aspect ratio of the structure is still very large. This was readily achieved for the smallest dose needed to sustain the growth. When increasing the dose by only 8%, we were able to sustainably grow even the 50 nm wide structure [shown in Fig. 3.6 (c)].

From the previous experiments, two main messages can be deduced. First is that the contrast in the SEM is already a very valuable tool that can be employed and exploited in the FIB transformation. The second important message is the crucial role of the ion dose. Thus, the following text will tackle both of the above mentioned important features of the system.

First, we have evaluated the effect of the ion dose on the transformation of the material (following publication [26]). The SEM contrast can be employed for basic pre characterization but does not bring full quantitative information about the transformation. To characterize the level of transformation from the fcc to the bcc structure, we have used the fact that also the magnetic properties are changing together with the lattice. This was already presented in Fig. 3.2. We have extended this analysis even further and we have irradiated a large number of 6×14 µm^2 rectangles where we again varied the dose between the structure from 2.5×10^9 ions/cm^2 to 4.6×10^{16} ions/cm^2. Unfortunately, the FIB system does not allow such a huge change in the dwell time to achieve this range, and thus we had to perform two sets of experiments. First for the low dose regime (2.5×10^9 ions/cm^2 to 4.6×10^{13} ions/cm^2) by changing the ion beam current to 15 pA. Afterward, we again tuned the current to 150 pA, and we continued with the experiment for higher doses. The thickness of the $Fe_{78}Ni_{22}$ layer was 8 nm (see Cu#12 in Appendix 2). We note that without the unique combination of the FIB and our home built focused Kerr magnetometer it would not be possible to perform such an experiment in a reasonable time. With our approach, we simply irradiated many rectangles and afterward we analyzed them one by one in rather fast fashion. The quantification of the degree of transformation was simply done by measuring the signal saturation value from the hysteresis loops measured on individual structures. Although the total value of saturation magnetization (in the units of A/m) cannot be quantified from such an experiment, we can easily compare the Kerr ellipticity measured on the individual structures. We also extended the approach presented in Fig. 3.2 by additionally transforming another set of structures with 100 scans of the ion beam instead of using the single-pass approach. The results of the analysis are in Fig. 3.7.

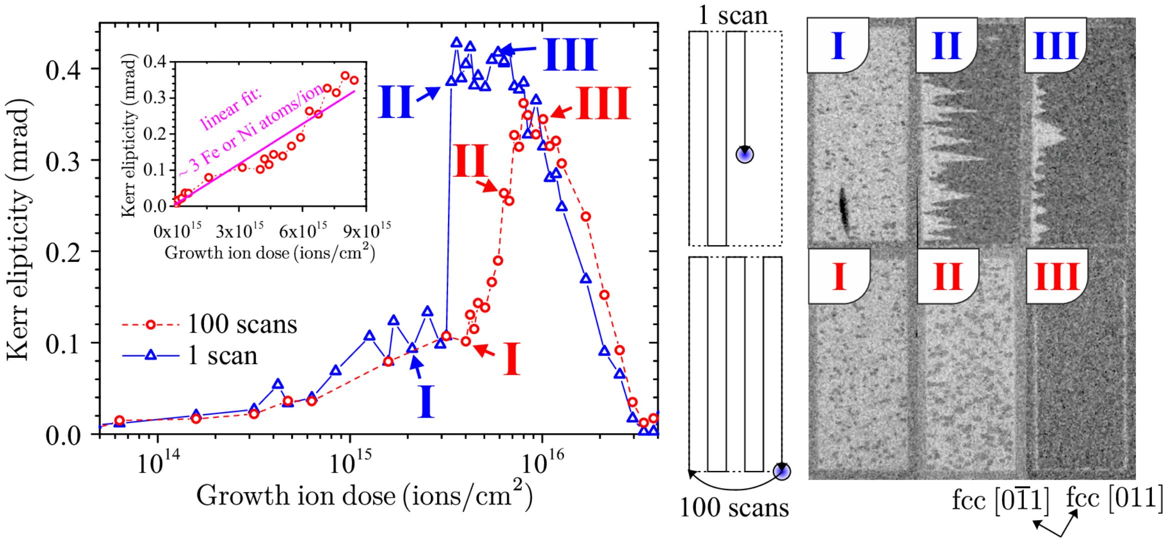

Fig. 3.7: The left graph shows the measured dependence of the Kerr ellipticity on the ion dose for the single-scan approach (blue triangles) and 100 scans (red circles). The inset shows the 100 scan curve in the linear scale with a linear fit allowing to estimate the transformation efficiency. The SEM micrographs on the right side show three representative structures for both types of irradiation. The numbers serve to interconnect the left graph with the micrographs. The top row first shows the writing schematics for the single-scan approach and the bottom represents the multi-scan approach. For future reference, we present the crystallographic orientation of the substrate in the bottom right corner. Adapted from [26].

The graph in Fig. 3.7 shows the dependence of the Kerr ellipticity (degree of transformation) on the ion dose for two approaches of FIB irradiation. The hysteresis loops were measured approximately in the middle of each rectangle. Each point in the graph is extracted from a single hysteresis loop. The results show a clear difference in the transformation process when the structures are transformed either by using multiple scans over the same area (dashed line with open circles) or by using a single scan only (solid line with open triangles). When irradiating the material by multiple passes of the ion beam, the magnetization of the structures increases linearly from the background value of 5×10^{-6} mrad to the value of 0.9×10^{-4} mrad at the ion dose of 2×10^{15} ions/cm^2. This suggests a stochastic process of transformation where incident ions create small bcc nuclei. The number of nuclei is proportional to the number of incident ions (keeping the probability of creating the bcc nuclei by incident ion constant). More details about the process of creation of the bcc nuclei can be found in [134]. Although it is not directly apparent in the logarithmic scale, the Kerr ellipticity ion dose dependence in the multi-scan approach is fairly linear up to the point, where we start to sputter the material away (see the inset in Fig. 3.7). From the linear fit of the Kerr ellipticity and assuming that maximum measured Kerr ellipticity equals to the fully transformed layer, we can estimate the transformation efficiency of approximately 3 Fe or Ni atoms per incoming Ga^+ ion. After the saturation ion dose (maximal magnetic signal) is reached, the ion-beam-induced intermixing and sputtering processes lower the magnetization down to the point where all the iron and nickel have been sputtered off, and no magnetic signal is observed anymore. In the case of the single-scan approach, the magnetization in the low-dose regime also increases linearly (suggesting the same mechanism as in the multi-scan approach), yet when the ion dose reaches the sustainable growth dose (critical ion dose) of $3 \times 10^{15}\,\mathrm{ions/cm^2}$ (slightly different ion dose from the previous set of experiments can be given by different focusing of the FIB, inhomogeneous virgin layers, and many other factors) is reached, the transformation efficiency suddenly increases to approximately 12 Fe or Ni atoms per incoming Ga^+ ion. The ion beam is now irradiating the fcc-bcc boundary with sufficient ion flux to achieve steady-state migration of the bcc structure into the fcc surroundings.

The two different regimes of transformation are also illustrated in SEM micrographs in Fig. 3.7. For low doses (rectangles marker by I and I), the transformed areas look the same for single-scan and multi-scan transformations. The irradiated rectangles for the low dose consist of a bright area with several darker fully transformed spots. For the rectangles marked by II and II irradiated with intermediate ion doses, the situation is different. For a single scan (vertical scanning direction with initiation in the bottom left corner), it is evident that once the transformation starts, it is propagating in expanding triangles from individual nuclei until the triangles connect and the film is fully transformed. The rectangle irradiated by multiple scans looks differently. The individual nuclei are becoming larger and denser, but they are homogeneously distributed over the whole irradiated area. The image of the rectangle irradiated with the single scan and a high dose (rectangle marked by III) shows a small but still apparent partially transformed bright area on the left side, while the rest of the rectangle is fully transformed. The image of the rectangle irradiated with the multiple scans and a high dose (rectangle III) shows a fully transformed area, but the resulting magnetization measured inside the rectangle is lower than in the dark area of rectangle III (compare also with the graph in Fig. 3.7). From the extrapolation of the red curve, we see that the maximum would be reached at a later stage, where sputtering and intermixing already decrease the magnetization. These results show that single-scan transformation is much more efficient than multi-scan transformation, and once the initial bcc nuclei are formed, then the transformation proceeds mainly via grain growth of the already transformed areas. Once the initial grain is transformed, it is easier to move the grain boundary via collision-induced migration of vacancies and interstitials at the boundary [139, 140]. The decrease of the Kerr ellipticity seen for doses $1 \times 10^{16}\,\mathrm{ions/cm^2}$ marks the sputtering/intermixing point. Both the single-scan and multi-scan curves almost coincide, which suggests good calibration of the ion doses for both approaches.

As we saw from the TRIM calculation in Fig. 3.1, the penetration depth of the ion beam depends highly on the acceleration voltage. For the FIB used in our work, the maximum energy of the Ga^+ ions is 30 keV. Corresponding mean ion range is then approximately 10 nm. This is fairly sufficient for 8 nm thick $Fe_{78}Ni_{22}$ layers yet will become problematic for thicker films. The majority of experiments in the experimental part of this thesis dedicated to magnonics have been performed on thicker films. The reasoning behind this selection is the higher magneto-optical signal and higher spin-wave group velocities [see again (1.60)]. Despite this fact, the majority of the data on the transformation mechanism presented in the previous text is presented on a thinner system. This discrepancy in the logical approach stems simply from the chronology of the experiment and actual needs that showed to be very important after we have thoroughly studied the 8 nm system.

To compare the systems of the $Fe_{78}Ni_{22}$ with different thicknesses, our collaborators from TU Wien have provided us with another set of samples with thicknesses 12 and 24 nm. We have repeated the analysis from Fig. 3.7 on both systems with only a minor change in the geometry of individual rectangles. Instead of previously used $6 \times 14\,\mu m^2$ we have switched to $5 \times 5\,\mu m^2$ large rectangles. The results for the two additional thicknesses, together with reference data from the 8 nm thick film, are shown in Fig. 3.8.

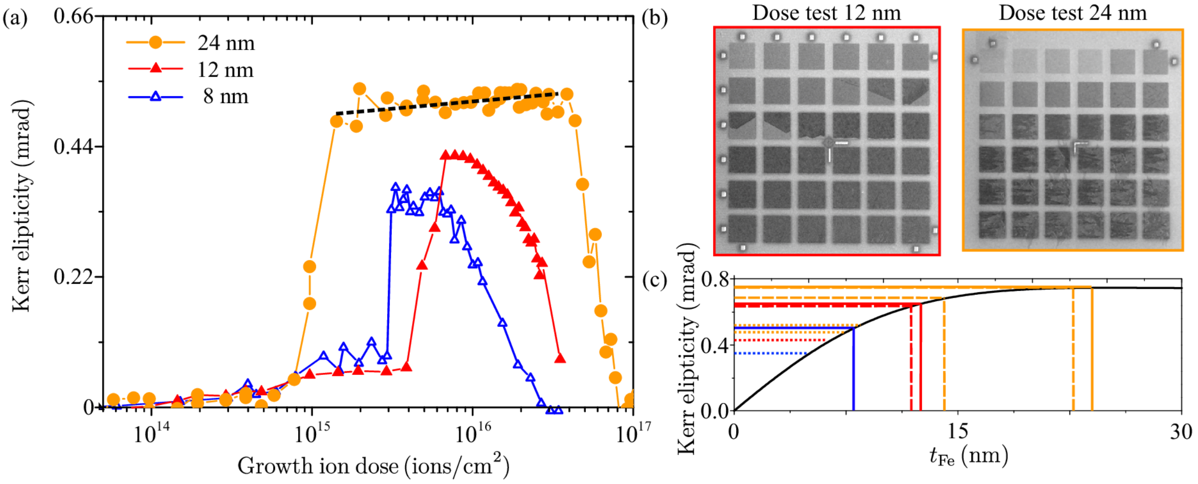

Fig. 3.8: The dose test of 8, 12 and 24 nm thick films. (a) Kerr ellipticity dependence on the ion dose measured on the structures prepared by the single scan of the FIB. For the 24 nm thick film, the slope in the plateau is highlighted by a dashed line. (b) SEM micrographs of the irradiated dose tests where we afterward measured the hysteresis loops for the data in (a). The ion dose in between the structures is increasing from left to right and from the top to the bottom. Thus, the lowest dose is in the top left corner, and the highest dose is found in the bottom right corner. Fast axis scanning direction was horizontal, and the irradiation was starting from the bottom part of the structure. (c) Calculation of the Kerr ellipticity dependence on the thickness of the iron for the magneto-optical constants taken from [141]. The dotted lines project the maximal measured values from (a). The first orange dotted line corresponds to the value at the beginning on the plateau, and the second line is the value from the end of the plateau. Continuous lines are theoretical values projected from the x-axis for the thicknesses: 8, 12, and 24 nm. Dashed lines serve for the estimation of the thickness. More details in the text.

All the curves in Fig. 3.8 (a) poses the same features. There is a sharp onset of the Kerr ellipticity at the point, where the ion dose is high enough to reach the sustainable transformation to the bcc (critical dose). The lowest critical ion dose is observed for the thickest film. This might be expected since the thicker films are less connected to the fcc stabilizing agent - the substrate. We also expect that the thicker films will contain more defects where the growth can be initiated. For the 24 nm thick film, this is supported by the SEM image of the dose test in Fig. 3.8 (b). Contrary to what we saw on the 8 nm film in Fig. 3.3 and also what is very nicely apparent on the SEM image of the 12 nm thick film from Fig. 3.8 (b), we do not see on the SEM image of the 24 nm thick film very sharp and apparent bcc transformation initiation spots. We see multiple regions where the transformation was initiated at the same time.

When comparing the ion dose dependencies of the 8 nm and 12 nm thick films, we see that the critical ion dose is increased for the thicker film. This is in contrast to the observation on the 24 nm thick film. When we compare the SEM images of ion dose tests for the two samples [compare Fig. 3.7 and Fig. 3.8 (b)] we see that for the 12 nm thick layer there are not as many transformation initiation spots as in the thinner film. This suggests that the critical dose parameter has a large extrinsic contribution given by the quality of the single-crystalline Cu substrate (or the metastable film itself). At the time when the presented experiments were performed, the 12 nm film was grown on the new crystal, whereas the 8 nm film was grown on the crystal that already went through a couple of growth and sputtering cycles (the films were grown, analyzed and afterward fully removed by the ion beam). The factors influencing the critical dose parameter are under investigation now, yet at this point, there is no common agreement on all the factors affecting the critical dose value or how this could be deterministically controlled. From the experiments we have done together with colleagues from TU Wien it seems that the critical factor is the surface quality of the Cu single crystal that is for sure degrading after sputtering cycles used for cleaning and reconstructing of the crystal surface.

After reaching the saturation, we see that all curves in Fig. 3.8 (b) have a plateau in the signal before we observe a drop of the signal from the sputtering/intermixing of the material. The widest plateau is observed for the thickest layer. Also, there is a small, but very apparent positive slope in the plateau in the thickest film. This is probably caused by the finite penetration depth of the FIB (approx. 10 nm). For higher doses, the number of ions effectively reaching the bottom layers of the fcc iron-nickel will transform the buried material to the bcc phase. Even though the Kerr effect is known as a surface-sensitive technique the bottom layers of the 24 nm thick sample will still measurably contribute to the magneto-optical signal. We have calculated the expected magneto-optical signal from the 4×4 formalism first presented by Yeh [142] and extended by Zak [141, 143, 144]. Since the optical and magneto-optical constants of our system are unknown we have employed the values known for iron [141]. This will cause a discrepancy in the magnitude of the signal, but the overall depth dependence should not be completely altered with approx. 22% of Ni. The calculated curve is in Fig. 3.8 (c). In the following text, we will try to estimate how deep the transformation spans from the surface based on a very crude estimation of the magnetic film depth from the magneto-optical signal strength.

The calculated magnitude of the magneto-optical signal is significantly higher than the one we have measured at the incident angle of approx. 40°. This is caused by the fact that the off-diagonal dielectric tensor elements of Fe are 10× higher than the one of Ni. By adding nickel, we lower the total signal significantly. Although the magnitude does not match the measured data, the shape of the curve should not significantly differ for different off-diagonal terms. This allows for the renormalization of the data. First, we started with the calibration of the expected signal strength for the 8 nm thick layer. In this case, we expect the film to be transformed through all the thickness. We rescale all the measured data [dotted lines in Fig. 3.8 (c)] so the dotted line and the continuous line (calculated value for 8 nm thick film) match in magnitude. This yields the renormalized measured magnitudes for the 12 nm film and also the values for the beginning and the end of the plateau for the 24 nm thick film. The approximate thickness of the layer can be obtained (marked by dashed lines) by the back-projection of the measured points to the x-axis. For the 12 nm thick film, the extracted value is 10.7 nm which fairly matches the expected value. For the 24 nm thick film, the beginning of the plateau corresponds to 14 nm and the end of the plateau corresponds to value 22 nm. It seems that despite some approximations, the data might yield some insight into the problem. The estimated and nominal value of thickness for the 12 nm thick film fit each other reasonably good. The transformation went through all the thickness. For the 24 nm thick film, the first value in the plateau corresponds to 14 nm, which might be accounted to the initial penetration depth for the majority of the ions. When increasing the dose, we also increase the estimated thickness of the film almost to the full nominal thickness. This shows that the energy of the ions is not directly transferred to the intermixing/sputtering, but even for higher doses, it contributes to the recrystallization of the film even further through the thickness. The sputtering/intermixing takes place almost for one order of magnitude higher ion dose than for the 8 nm and 12 nm films.

The results of the analysis shown above should serve only as a basic reference since the theoretical background for the analysis is not well defined and also the magneto-optical constants are unknown.

Another finding we might derive from the curves in Fig. 3.8 (a) is the sputtering rate. From the knowledge of the nominal thickness of the layers and also the respective ion dose at which the Kerr ellipticity reaches zero we can estimate the sputtering rate to approx. 0.3 µm/nA/s.

The previous analysis showed that the ion dose has a crucial role in the transformation process and that the SEM contrast is a great tool for the first *in-situ* check of the growth process. Purely by accident, we have found another contrast mechanism stemming from the crystallography of the layers. First, we accidentally did not change the electron acceleration voltage to commonly used 30 kV. Afterward, we have accidentally mounted the sample with a small tilt relative to the sample stage. Nonzero tilt and small acceleration voltage of the electrons resulted in the appearance of the multiple contrasts in a single structure. The rectangular structure was written by the spiral scanning of the FIB [Fig. 3.1 (c)]. After the writing process, we have tilted the sample to the normal incidence of the SEM (with a small tilt given by the wrong mounting) and we have observed four distinct domains within the structure. The domains were perfectly separated by a boundary at the diagonals of the rectangle. The contrast was changing by adjusting both the tilt and the rotation of the sample and we were able to completely cancel the contrast by a tilt of approx. 4°. We have remounted the sample and we have assured the front face of the sample to lie parallel with the stage. As usual, we did not see any contrast between the diagonal domains (see Fig. 3.9).

This contrast again reappeared at a small tilt of 10°. For this tilt, we observe four contrast levels in general. The fcc iron surrounding the structure has the lowest mean contrast value (contrary to the situation on zero tilt, where the bcc iron is darker). The next lowest contrast value is found in the left quadrant of the rectangle. Top and bottom quadrants have almost the same contrast value and the right quadrant has the brightest observable contrast. For negative tilt, we observe contrast sign change. The fcc material, the top, and the bottom quadrant are not affected, yet the left/right quadrants reverse the contrast in the tilt. The SEM imaging was done by the means of the classical Everhart-Thornley in-chamber detector. The detector, as shown in the schematics of Fig. 3.9 is placed in the plane, in which the sample is always tilted. The contrast is appearing

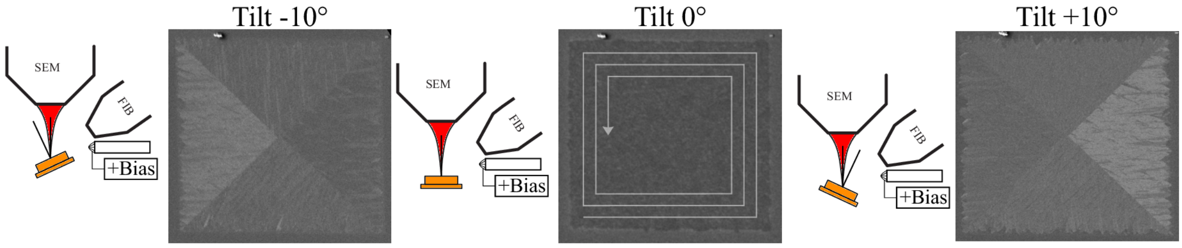

Fig. 3.9: SEM micrographs of the same $8 \times 8\,\mu\mathrm{m}^2$ rectangle irradiated by spiral scanning strategy of the FIB for three different sample tilts (relative to the normal incidence of the electrons). The schematic FIB writing path is shown in the middle image. The schematics on the right side of the SEM images show the experimental geometry. The secondary electron detector (Everhart-Thornley in-chamber detector) is schematically shown. The tilt of the sample is always towards/from the direction of the SE detector.

continuously when going from zero tilt up to $\sim 12°$, where the contrast starts to fade. This suggests the crystallographic origin of the contrast. Interestingly, one can directly connect this contrast change with the FIB writing procedure. The left/right (top/bottom) pairs have been irradiated always with the fast scanning direction of the FIB oriented vertically (horizontally). We see an abrupt change between scanning horizontally or vertically to always happen on the diagonal. This shows a very interesting feature that the FIB scanning direction (both the slow axis and the fast axis) defines this observed contrast. If we accept this premise then we might expect e.g. top and right quadrants to differ as they both have the FIB fast scanning direction rotated by $\pi/2$. Yet we see that the contrast sign reversal happens for the quadrants, where the FIB fast scanning direction was oriented in the same direction. The difference is in the direction of the slow scanning axis. For a certain rotation of the sample (at the same tilt towards the SE detector), we were able to achieve this sign reversal, not in the pairs written by FIB fast scanning axis oriented vertical, but with the horizontal fast scanning axis of the FIB.

Furthermore, we have performed additional analysis of the contrast by rotating the sample and taking the SEM images every 5°. In the post-processing phase, we have analyzed the contrast angular dependence of different regions of the sample. The images were realigned and rotated automatically by a pattern matching algorithm programmed solely for this purpose. The alignment software has allowed to automatically obtain the mean contrast in different arbitrary areas of the sample together with its evolution during the sample rotation. We have analyzed the structure from Fig. 3.9, where we focused on the difference between the virgin fcc, the quadrant written by horizontal scanning, and the quadrant written by the vertical scanning of the FIB. The analyzed areas, together with raw data obtained from the above-mentioned analysis, are shown in Fig. 3.10.

The first highly apparent feature of all the contrast curves in Fig. 3.10 (b) is the large modulation with a 2π period. This is just an artifact of a Kapton tape we have used to divide the sample to regions of interest. This has proved to be very problematic, and the tape was removed for all further experiments. The data in Fig. 3.10 (c) were spectrally cleaned by performing FFT, deleting the zeroth and first maximum, and then performing the inverse FFT. Very apparently, the data taken from the fcc show a very periodic contrast dependence. The total contrast reversal happens 8× in one 2π rotation. This is identified by a distinct 8 maxima and 8 minima in the signal. The same is observed in the FFT analysis shown in Fig. 3.10 (d) where we see a very distinct peak at the symmetry order of 8. The regions irradiated by the FIB show a more complex response.

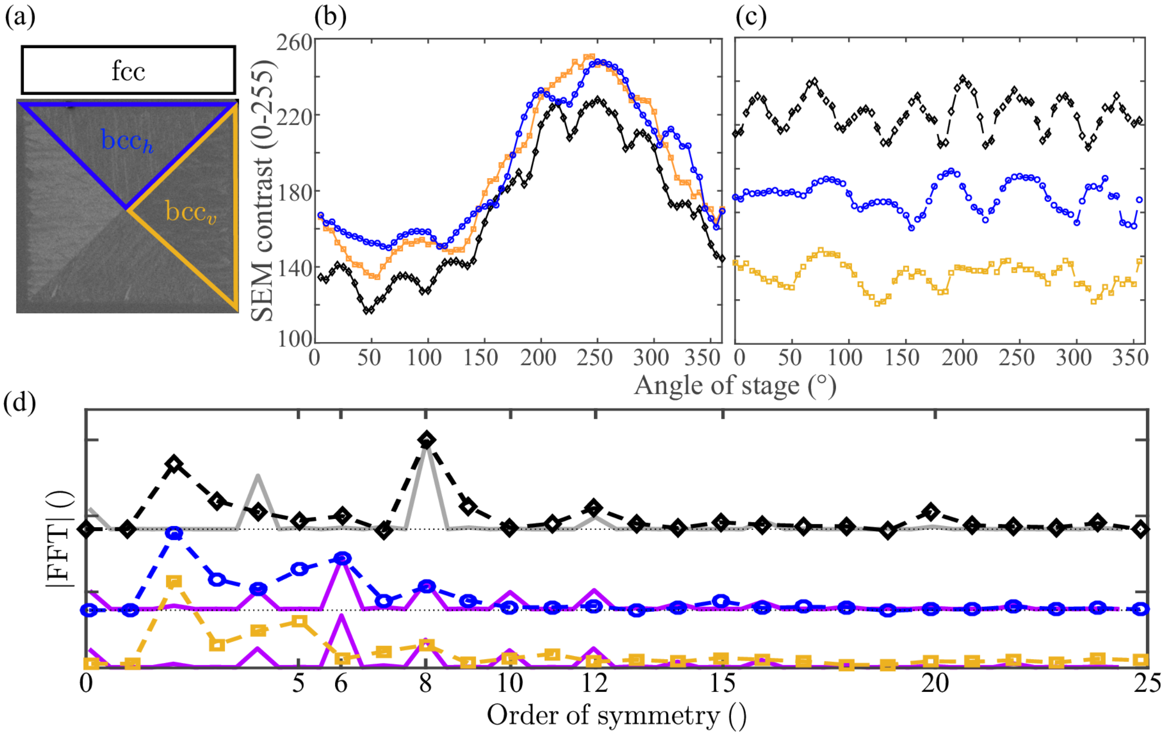

Fig. 3.10: (a) SEM micrograph of the structure from Fig. 3.9 with color designated areas where the mean contrast was analyzed during the rotation. The fcc signal was taken close to the structure from an area with the same number of pixels as used for the analysis of the quadrants. (b) The raw data that we obtained from the analysis. (c) The data where the strong first harmonic was subtracted by the means of the FFT filtering. The data are artificially shifted in the y-axis for better visualization. (d) The absolute value of the Fast Fourier Transform of the data in (c). The value on the x-axis was normalized to denote how many times the contrast completely changes its sign in one 2π rotation (it also denotes the number of maxima). Again, the FFT data are vertically shifted. Zero-level for each curve is always denoted by a dotted line. Grey continuous line is the modeled fcc signal and the violet continuous line represents the modeled bcc signal. Both modeled signals have been artificially rescaled. The curve colors in all figures (b), (c) and (d) correspond to the definition in (a).

We do not see very well defined and distinct features as on the fcc. When looking at Fig. 3.10 (d), the orange and blue curves show a lack of the peak at the symmetry order 8. The blue region exhibits a broad peak near the orders 5 and 6, yet it is not very well defined. For the orange region, the 6th order is missing. The signal of order 4 is higher than in the case of the blue curve. When we compare simply fcc and bcc region, we can state that the major difference is in the existence of the strong peak at the symmetry order equal to 8. As the signal with this symmetry is almost fully missing in the bcc regions, it can directly serve as an fcc/bcc indicator. Originally we thought that both the blue and orange regions will exhibit the same angular dependence only shifted in phase. This is not observed in the actual data presented in Fig. 3.10 (c). Quite interestingly, the blue/orange curve in Fig. 3.10 (c) does not show rotational symmetry π. This is expected from the bcc crystallography, yet the signal does not reflect this trend. It again suggests a more complex contrast formation mechanism. By shifting the blue curve relative to the orange curve, we were not able to overlap both curves reasonably well. Thus we were not able to estimate the phase shift (or the rotation of the crystal) only based on the contrast seen in the secondary electrons. We have also performed very basic modeling, where we were looking at the channeling directions for different orientations of the bcc and fcc lattices. We have done this in the simplest possible way. We have modeled the crystal lattice from individual atoms (5 layers), and then we rotated the whole crystal structure around the in-plane direction (at tilt $+10°$). We analyzed the average grey level seen from the point of an electron for different rotations of the lattice. Later we again performed the FFT analysis as in Fig. 3.10 (d). Even though we observed similar features in both the theoretical and the modeled signals, the agreement is not very strong. The model is simply too oversimplified. We have extended the idea by modeling not only the material itself but we also included the substrate underneath. In another approach, we modeled the substrate and the layers separately and we multiplied the FFT spectra of both layers. Any more advanced approaches still did not show qualitatively better agreement then what we present in Fig. 3.10 (d).

We have performed an extension of the analysis shown in Fig. 3.10. We have developed the software allowing the FFT to be performed on the pixel level. Thus instead of acquiring the rotation dependence of contrast in a certain area and subsequently performing the FFT of the signal, we follow the same procedure in each pixel. This allows us to visualize the contrast symmetry order [Fig. 3.10 (d)] spatially with a resolution given by the SEM and mainly by the quality of the software that realigns the individual images before the FFT processing. The stage in the SEM-FIB microscope suffers from many mechanical instabilities, and thus the rotation and the positioning are not precise enough. For our analysis, we need to take an image every 5°. Due to the issues with the SEM stage, we need to readjust the position between each rotation step. This still did not prove to be accurate enough. We have written a code that according to certain geometric patterns slightly readjust the image rotation (usually the error of the stage is below 1°) and mainly realigns the images so that the selected pattern is always on the same pixel position.

The above-mentioned analysis can serve as a sort of crystallography imaging mode in a simple SEM machine. The observation of the crystallographic contrast in the SEM was already resolved in literature not a long time ago in publication [145]. With the help of the electron backscattered diffraction method, they identify the dark and bright contrast and its origin in certain channeling directions of the crystal. To understand the contrast seen in the SE detector better, we have written multiple $10 \times 10\,\mu\mathrm{m}^2$ rectangles (and one circle) where between each rectangle, we change the fast axis scanning direction by 50°.

Afterward, we have also written one circle with the spiral scanning strategy (outside-in) and one rectangle with the spiral scanning strategy. The structures were then imaged at the tilt angle −10° from the SEM. The sample was afterward rotated by 5°, and for each angle, we have acquired the SEM image (fast acquisition)[1]. The SEM measurement took approx. 20 minutes. Based on the data, we performed the above-mentioned procedure and we plotted the 2D images of the FFT amplitude spectrum content in each pixel for a certain symmetry order. The results of the analysis are in Fig. 3.11.

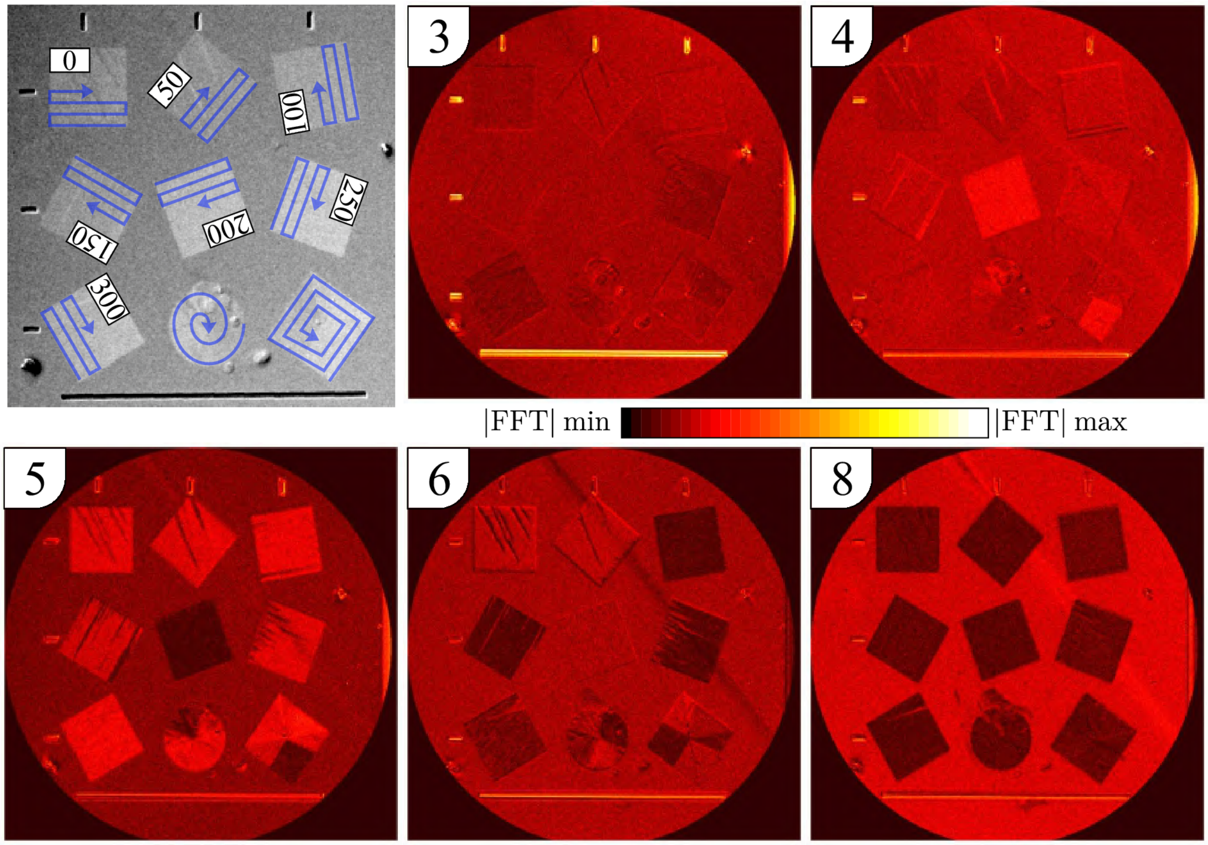

Fig. 3.11: SEM-based crystallographic analysis of the FIB written structures (rectangles are $10 \times 10\,\mu\mathrm{m}^2$, the circle has a diameter of $10\,\mu\mathrm{m}$). The top left picture is the SEM image of the written structures. Blue curves represent the FIB scanning strategy. For the structures written by the linear scanning, the number in the top left corner represents the angle of the fast scanning direction. The rest of the images (in false black-red-white color code) are the outputs of the FFT analysis. The number in the top left corner always designates the symmetry order number. The color bar scaling was kept constant for all the maps.

The analysis performed in Fig. 3.11 shows even further the complexity of the SE contrast in our system. The spatial FFT map on the symmetry order 8 shows nicely the absence of this Fourier component in the structures transformed to the bcc phase. When looking at the 5th and 6th order, huge differences between individual structures are apparent. Judging from linearly scanned rectangles from the map of the order 6, we can find four changes in total for different scanning angles. The first two structures written at 0° and 50° have a very similar level of this particular frequency content. Next structures, with the angle of scanning 100° and 150°, have lower amplitude when compared to 0° case.

---

[1] See supplementary video 1.

At 200°, we again see an increase of the FFT amplitude where just for 250° and 300° the amplitude goes again down. We can distinguish four angles where there is a distinct change in the SE emission symmetry. When looking more closely at the circle written by the spiral scanning (structure in the middle of the bottom row), we see four clear domains with four abrupt changes in the contrast when going around the circle. When writing the pattern with a spiral scanning strategy, we effectively go through all the angles of the FIB scanning. This nicely serves as a continuous angular probe of the system. Instead of writing many structures and changing the FIB angle for each structure, we can use the circular pattern and obtain all the angles at the same time. When we analyze the angles of the boundaries, where the magnitude of the FFT order 6 changes abruptly, we come to the following approximate values: $76°, 161°, 250°$ and $340°$. This perfectly matches the intervals defined by the linear scanning experiment. This symmetry order allows us to distinguish individual FIB driven crystallographic orientations of the material. For order 5 it seems that all the structures are visible except for the scanning direction at 200°. This direction is mainly apparent in order 4, where the rest of the structure does not exhibit any strong contrast. In the symmetry order 3, only slight changes are apparent.

In conclusion, the analysis from Fig. 3.10 and Fig. 3.11 shows some deterministic trends, yet the problem proved to be too complex. The original intention behind the analysis in Fig. 3.10 was to perform a study of the crystallography in the SEM microscope with a regular SE detector. The results show the viability of the method, yet we did not develop the theoretical apparatus needed for understanding the measured data to the extent that it would yield the insight to the complex process of FIB defined writing of different crystallographic orientations of the bcc iron.

In the last step, we have tried to identify the contrast creation mechanism. The signal is measured in the secondary electron detector, but the secondary electrons are usually not sensitive to the crystallography of the layers. The SE contrast conventionally originates in the chemical composition and the topography. The crystallography is in the SEM usually observed in the backscattered electrons (BSE) that can be also channeled to/from the material. Classical SE detector attracts only the low energy electrons (with energies in the order of tens of electronvolts), and the only possibility for detection of the BSE would be that the backscattered electron would be reflected from the sample to the detector directly on a straight path. This should not happen simply from the geometry of the SEM chamber.

We have performed a very simple experiment that should verify the origin of the crystallographic contrast. We have written a rather complex structure, with many parts written by the different angles of the FIB scanning. We have verified the appearance of the contrast by tilting the sample by $-10°$ (see middle panel of Fig. 3.12). Afterward, we have reconnected the sample stage touch alarm module in the SEM to the variable voltage source. This has allowed us to change the bias voltage of the sample and thus to change the secondary electron emission conditions.

When comparing the top and bottom row of Fig. 3.12 for a sample bias 0 V, we see a clear difference between individual segments (divided by the dashed red line) again resembling what we observed first in Fig. 3.9. There are multiple contrast levels. When we slowly increased the voltage, we saw that the fcc/bcc contrast is changing, yet the crystallographic contrast stays. Please note that the offset value and gain of the SE detector had to be adjusted for the case of positive and negative bias. We did not see any signal at all with bias voltage ±30 V. We have kept the dwell time of the beam constant and we only changed the gain value and the offset value. The lower total number of secondary

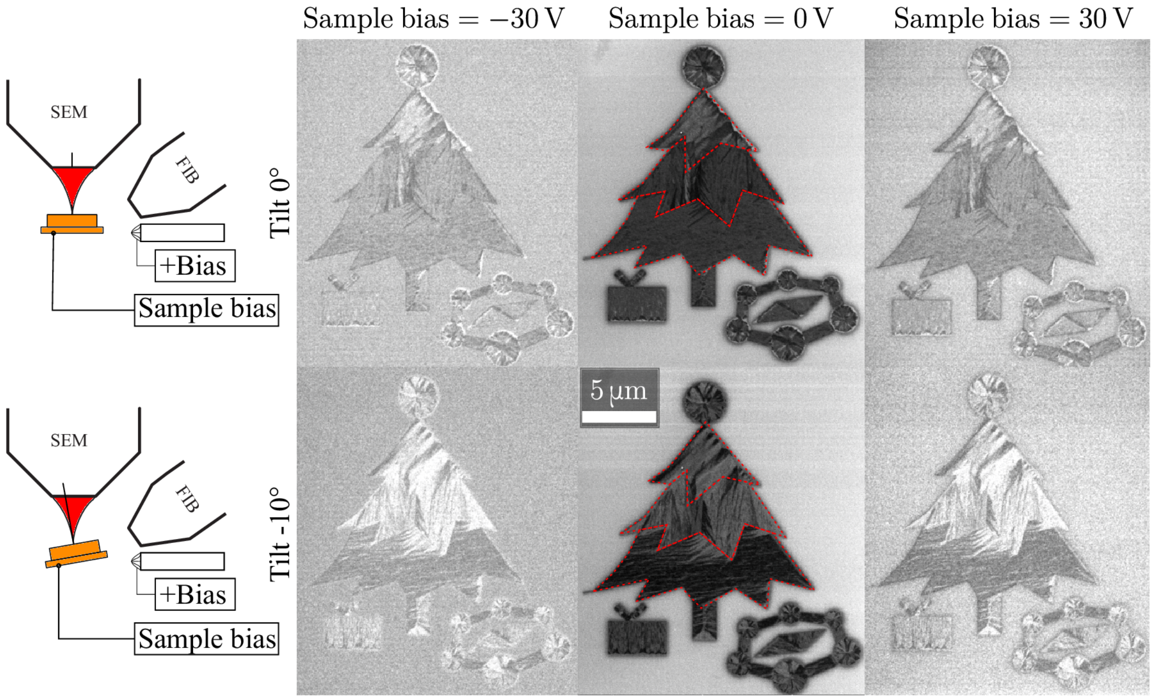

Fig. 3.12: SEM micrographs for two different tilts of the sample and three different bias voltages of the sample. In the middle column, the dashed red line shows the boundaries between individual segments with different angles of the FIB scanning. The tilt orientation, as well as the schematic position of the Everhart-Thornley in-chamber detector, are shown in the left part of the image.

electrons is reflected in the higher noise level of both pictures taken at a certain bias voltage. The persistence of the contrast suggests that the contrast mechanism is not given by the secondary electrons from the sample. After discussion with the SEM development department in the Thermo Fisher Scientific Inc., we have come to a conclusion that the contrast is given by the backscattered electrons being channeled to/from the sample in certain preferred crystallographic directions, yet the signal in the SE detector is given by the secondary electrons. The most probable mechanism is usually considered negligible. In a certain direction, we align the electron column with the certain channeling direction of the sample and thus we allow the energetic electrons to be channeled into the sample but also from the sample to the chamber. This highly energetic electron can hit the chamber of the electron microscope and cause the emission of the secondary electrons that are subsequently detected by the SE detector. According to [145], the bright contrast is seen, when we align the beam to the channeling direction of the crystal. Thus, in theory, classical tools used in electron-backscattered diffraction studies should be suitable for the description of the signal qualitatively, but as the process of the contrast creation is very complex, we still believe the quantitative description would be very problematic.

Historically, when observing the whole crystal in the SEM, we have also observed faint patterns on the crystal itself. It was only later realized that the pattern highly resembles the Kikuchi pattern [146] usually observed in the electron-backscattered diffraction studies at much higher acceleration voltages. The pattern was even more pronounced when the sample was brought very close to the electron beam column. We realized that in our microscope (Tescan Lyra 3) for small magnifications, the wide-field mode is employed. It benefits from the unique intermediate lens design in a way that instead of forming a wide beam with large numerical aperture it forms a narrow beam that is very easy to scan in a very wide angular range. As a result of that, the electron beam in this mode is changing its tilt when scanning over the sample. When we bring the sample very close to the electron column, the range of the electron beam tilting angles increases. Following the same mechanism as discussed for the contrast formation in the case of different bcc domains, we can understand that for different position of the beam on the sample the electron beam has a different tilt with respect to the normal direction of the sample and so it can align with different channeling directions of the crystal. As a general consequence, the BSE emission for different angles varies, and thus also the secondary SE[2] emission varies when scanning. This is readily observed in the overview image of the whole crystal taken in the wide-field mode at a low working distance in Fig. 3.13 (a).

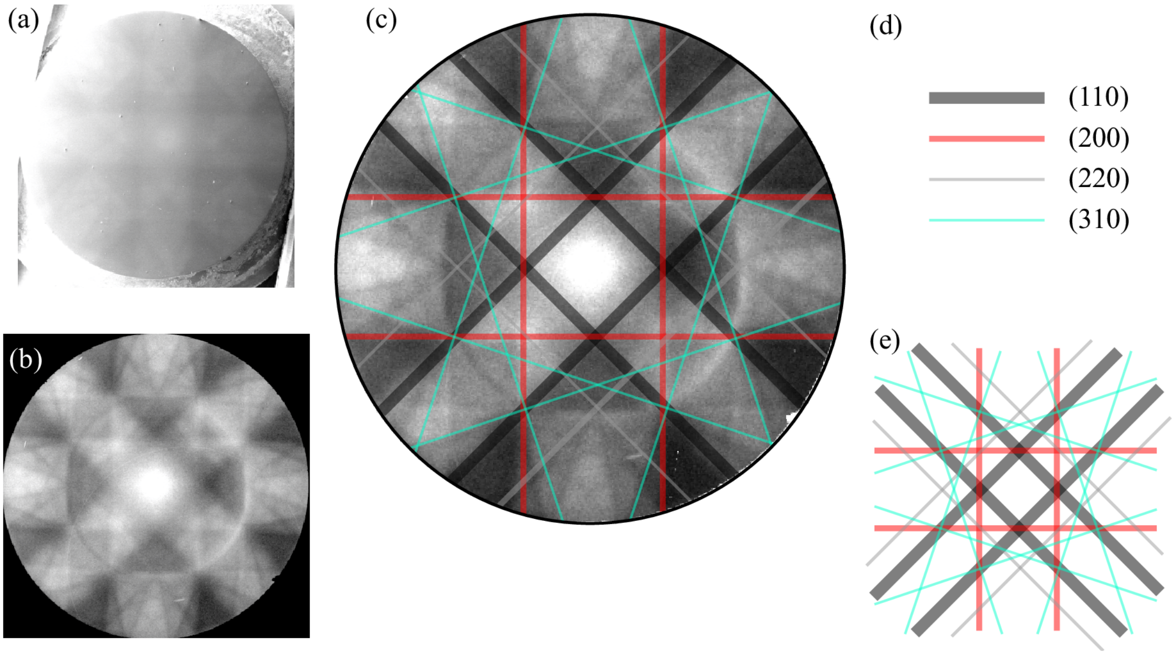

Fig. 3.13: (a) Raw data as seen in the SEM at working distance 3 mm and primary beam energy 5 keV. (b) The processed image in the ImageJ image processing software. Mainly the linear and quadratic background was subtracted from the raw image. (c) The analysis of the observed pattern in the KLine software for Cu(1 0 0). The SEM image was overlaid with four most intensive Kikuchi lines expected for the fcc lattice. (d) Definition of the individual Kikuchi lines. The width of the line is normalized to the expected intensity. (e) The Kikuchi pattern without the SEM image. To be compared with (b).

The very clear pattern seen in Fig. 3.13 (b) shows multiple minima and maxima. The Kikuchi lines up to high-order can be recognized. The pattern itself again serves as a great tool for in-situ analysis. It allows to very precisely align the sample directly in the SEM in both the rotation and the tilt. This is very valuable information since we can e.g. reexamine the findings of Fig. 3.11, where we have seen that the FIB scanning direction highly changes the SEM contrast behavior of the transformed structures. It is possible then to correlate the abrupt changes in the contrast between individual structures and to see if the changes happen at certain principal directions/planes of the crystal. The overlaid calculated Kikuchi lines (re-scaled manually to fit the most intensive lines) in Fig. 3.13 (c) match nicely the observed pattern. For higher diffraction orders, when

---

[2] The electrons are emitted from the chamber by the backscattered electrons.

approaching the edge of the view field, the correspondence is deteriorated. We believe it is due to the scanning mechanism of the SEM in the wide-field mode. Most probably, the scaling in the sample plane should not be considered to have equal spacing. It could be in theory corrected by a flat-field correction. From the geometry of the SEM, we were not able to obtain the exact angular range of the electron beam. The one given by the software does not seem to match the observed Kikuchi patterns. It is not verified whether the contrast originates more from the copper substrate or from the overlaid fcc Fe. For the clean Cu(1 0 0) crystal we have not observed any Kikuchi pattern, yet this can also be due to the cleanliness of the substrate itself. We have further verified the orientation of the crystal by the Grazing incidence X-ray diffraction (GIXD). Observed Kikuchi pattern orientation matches the X-ray analysis. Interestingly, the analysis of GIXD also showed a small amount of bcc Fe(1 1 0) oriented grains. The signal ratio with the Cu(2 0 0) was $1 : 10^5$. The X-ray analysis was performed from the whole crystal and thus this signal can correspond to already transformed areas by the FIB or also to the small level of bcc impurities expected in the system.

In conclusion, the contrast seen in the SEM is very convenient for controlling the FIB writing process, yet the exact mechanism and theoretical tools to quantify the observed image were not elaborated. The very trivial analysis allows the in-situ identification of the different bcc crystallography (e.g. Fig. 3.9) or to precisely align the sample to the SEM coordinate system with the help of the Kikuchi pattern (Fig. 3.13).

The FIB driven crystallography of the resulting bcc patterns inevitably also changes the magnetic properties of the transformed areas - mainly the magnetocrystalline anisotropy. It was already stated that the bcc patterns grow on the fcc substrate in the (1 1 1) plane. The crystal lattice is elongated in one direction and thus the energy profile of the magnetocrystalline anisotropy has no longer the four-fold symmetry yet it becomes two-fold (see the diagonal cut plane in Fig. 1.4 together with the bcc energy profile). It means that when the orientation of the crystal is driven by the scanning direction of the FIB, also the direction of the uniaxial magnetic anisotropy will change. This was realized and also more thoroughly studied by Křižáková in her bachelor's thesis [136]. At that time, we did not have enough experimental data to untangle the full dependence of the anisotropy and also the difference in the quality of the individual crystals was too high to find common features between the samples. We were able to extract several hints of the growth process. After receiving a completely new set of samples (data described in the presented thesis are only from this new set of samples), we were able to do reproducible transformations and to study the growth processes. We summarized our findings in publication [26] where we show, how the FIB can control the anisotropy of the bcc structures. The following text is derived from this particular publication.

The proof of the FIB scanning direction controlled magnetocrystalline anisotropy were seen on various structures, where we observed both the hard and easy axis loops (see again Fig. 1.7) that varied between the structures depending on the angle of the FIB scanning used for the transformation of the individual structure. For the structures transformed by e.g. 100 scans of the FIB, we did not see a significant variation of the loop shape for different scanning angles. When we performed spiral scanning, we clearly saw a spatial variation of the loop shape in a single structure.

We have decided to study the angular dependence of the loop shape on the orientation of the structure in the external magnetic field. We have transformed $15 \times 15\,\mu\text{m}^2$ large rectangle by the FIB (horizontal side of the rectangle was aligned to fcc [0 1 1] direction) in a single FIB scan. The SEM micrograph of the structure taken under small tilt of approx. 6° is shown in Fig. 3.14 (a). We have transferred the sample to our home-made magnetometer [111] and we measured the hysteresis loop angular dependence with an angular step of 10° in each quadrant (formed by the FIB spiral scanning) of the rectangle (and also in the center). Afterward, we have normalized the loops to the maximum measured signal (saturation signal) and extracted the remanent magnetization (in a similar manner as modeled in Fig. 1.7) as a function of the angle. Additionally, we have also measured the angular dependence of the remanent magnetization on the structure prepared by 100 scans of the FIB. The results of the analysis are shown in Fig. 3.14. Magnetic measurements provide further insight into the behavior of the material. The spot size of the micro-Kerr magnetometer was approx. 1 µm. In the center of the square, the plot of remanent magnetization shows clear four-fold magnetic anisotropy [Fig. 3.14 (d)], whereas inside the triangular domains the magnetic anisotropy is clearly uniaxial. Moreover, the direction of the uniaxial anisotropy changes with the FIB scanning direction [compare Fig. 3.14 (b) and (c)]. The four-fold pattern poses similar principal directions as both uniaxial plots. The plot in Fig. 3.14 (c) is very similar to Fig. 3.14 (b) only rotated by π/2. When looking at the angular dependence for the structure transformed by multiple scans of the FIB [Fig. 3.14 (e)], we see an isotropic profile with slight four-fold dependence again following the axes defined by the uniaxial plot. This is possibly due to the fact that the resulting structure of the transformed material prepared by 100 scans consists of smaller bcc grains with random orientation in both principal directions.

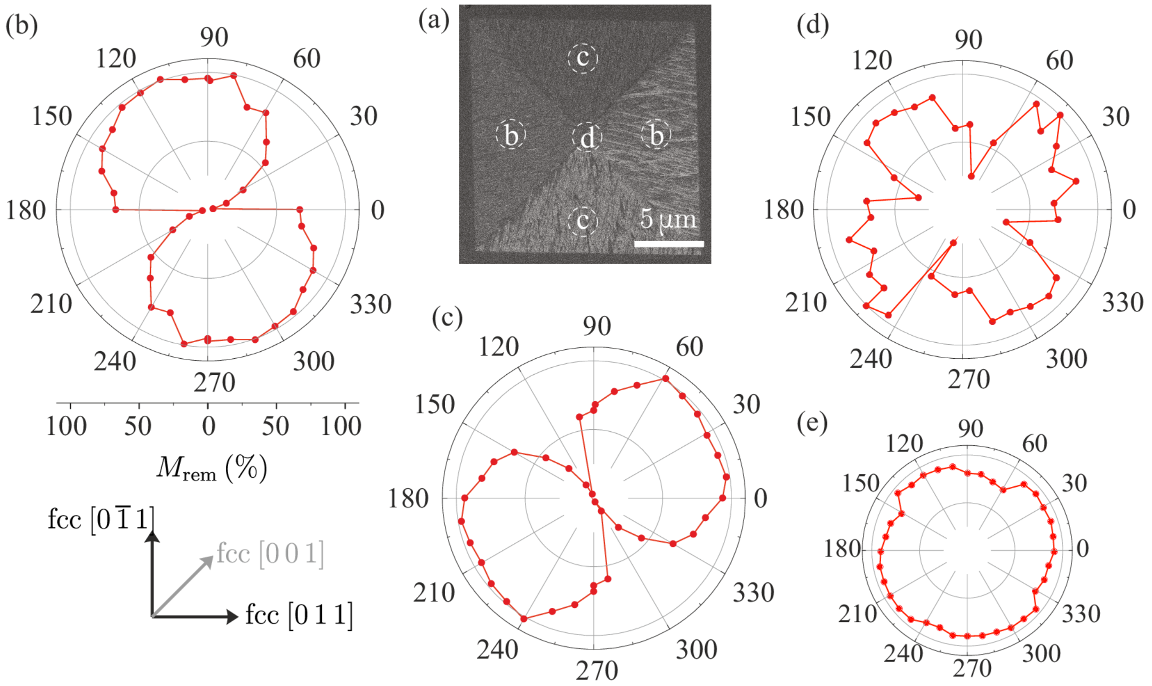

Fig. 3.14: (a) SEM micrograph of the studied structure prepared by spiral scanning of the FIB in a single pass. Letters connect the polar plots to individual spots in the rectangle. (b) and (c) Polar plots of remanent magnetization measured by micro-Kerr magnetometry show two-fold (uniaxial) anisotropy for the individual quadrants of the rectangle. (d) The four-fold magnetic anisotropy is measured in the center of the rectangle. (e) The polar plot measured on the different structure prepared by 100 scans of the FIB. The left corner shows the orientation of the measurement with respect to the principal directions of the crystal.

To study the dependence of the magnetic anisotropy direction on the scanning direction more in detail, we transformed in total 36 circles with 10 µm diameter. The circular shape is important to convincingly suppress the shape anisotropy contribution. The in-plane rotation invariant demagnetizing factor is extremely small as the thickness/diameter ratio is also very small (see Fig. 1.2). The circles were transformed by linear scanning with varying angles of FIB scanning starting from fcc [0 1 1] direction in 10° steps. After the transformation, similar analysis as in Fig. 3.14 was performed. We have measured the hysteresis loop for all structures every 10°. This resulted in $36 \times 37 = 1332$ loops that have been automatically post-processed by the prepared software. The software automatically centers the loops around 0 value, removes the linear slope in the saturation (coming from the Faraday effect in the microscope objective), normalizes the loops by the average value found in the saturation (mean value of certain points in the loop found close the maximum/minimum field), and reads the mean value from the ± remanence. Afterward, for each structure, it finds the individual remanence data for different angles of the structure in the external magnetic field. For each structure it plots the angular dependence of remanence as seen e.g. in Fig. 3.14 (a). This dependence is fitted by a similar function to (1.32) introduced in the theoretical section. The difference between theoretical function (1.32) and fitting function (3.2) is that we fit also the maximum value of the angular dependence b and we add an additional offset term c. The fitting function is then following

$$M_{\mathrm{rem}} = b|\cos(\alpha - \alpha_0)| + c. \tag{3.2}$$

We are mainly interested in the dependence of the easy axis angle α_0 on the FIB fast axis scanning angle. We have restricted the fitting parameter α_0 only for positive values in the angular range $1° - 180°$ due to the uniaxial anisotropy remanence plot shape, where the $\alpha_0 = \alpha_0 \pm n\pi$ for $n = 1, 2, \ldots$. By fitting all the angular dependencies for all the structures and then extracting the easy axis angle for each structure as a function of the FIB scanning angle, we obtained data presented in Fig. 3.15 (a) and (b). There is a very clearly visible trend of a strong dependence of the uniaxial magnetic anisotropy easy axis direction on the FIB scanning direction. We see clear two-fold symmetry of the data presented in Fig. 3.15 (a). This is the result of the data processing, where we had to limit the possible angles of the easy axis to a range equal to 180°. We cannot distinguish between the angular values in the whole 360° range. For the sake of understanding the growth process even more, we tried to transform the fitted data to the whole 360° range. We have done this by artificially adding 180° offset after the distinct jump in the data at the FIB scanning angle equal to 180°. This has allowed elaborating the whole dependence in more detail with respect to all significant direction in the fcc (0 0 1) plane.

When the direction of FIB scanning was between 0° and 90° (fcc [0 1 1] and fcc $[0\,1\,\bar{1}]$ directions) the resulting magnetic anisotropy direction, represented by the direction of the easy axis, rotated by approx. 20° between 35° and 55°. When the direction of FIB scanning passed 90° (fcc $[0\,1\,\bar{1}]$ direction) the resulting easy axis direction jumped from 55° to 125°. With further increase of the scan angle, the resulting easy axis direction further gradually changed from 125° to 145°. At 180° (fcc $[0\,1\,\bar{1}]$) the easy axis again jumped from 145° to 35° and the angular dependence continued symmetrically in third and the fourth quadrant. The anisotropy axis shows continuous rotation for FIB scanning in between the fcc low-index directions. When the FIB scanning direction is aligned with the low-index direction of the fcc, we see a jump in the easy axis direction.

To explain the behavior of the evolution of the magnetic uniaxial anisotropy with respect to the direction of the FIB scanning we need to look at the crystallographic

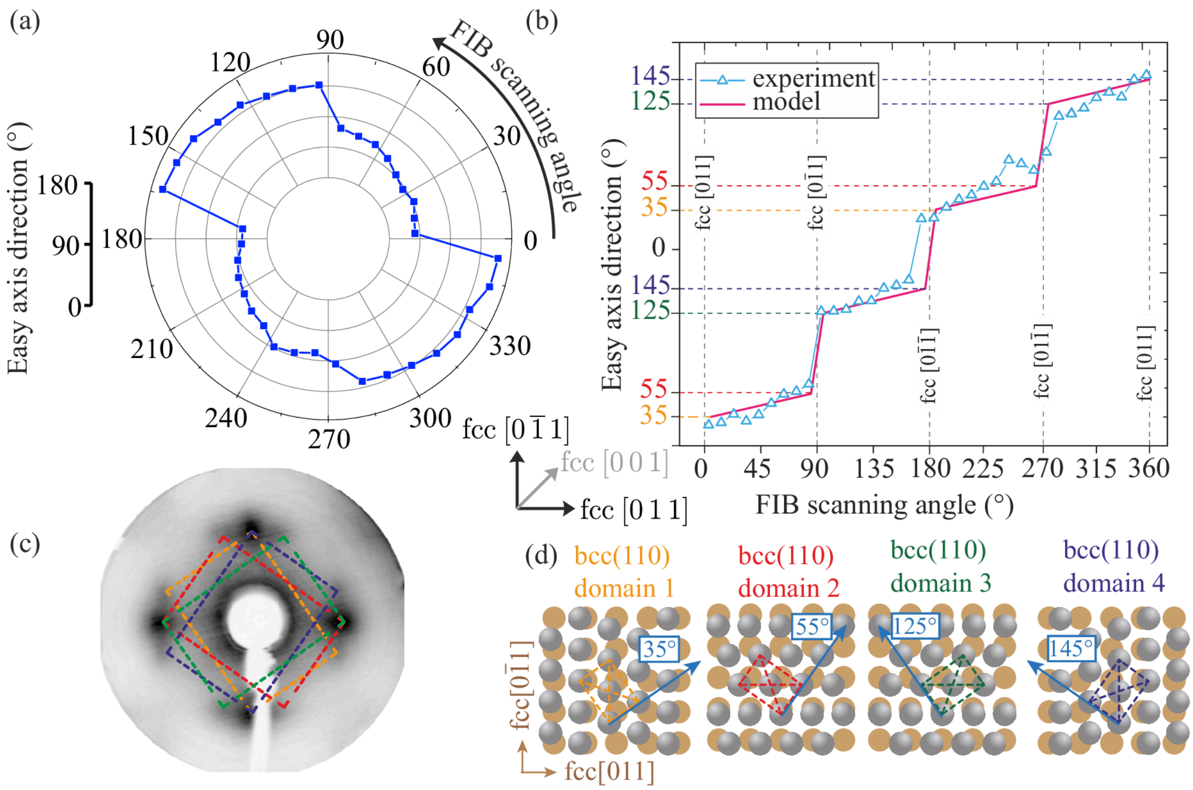

Fig. 3.15: (a) Polar plot of the fitted easy axis direction as a function of the FIB fast axis scanning direction (0° corresponds to fcc [0 1 1]). (b) Adjusted plot with corrected angles of the easy axis in the 360° range with designated principal axes of the fcc substrate. (c) Schematic of all four bcc (domains) with arrows indicating directions of the easy axes. (d) LEED pattern showing four bcc (1 1 0) domains after transformation by a broad ion beam.

structure of the bcc Fe thin films on Cu(1 0 0). The LEED pattern [see Fig. 3.15 (c)] of the 8 nm thin film transformed in UHV by broad Ar^+ ion beam shows four possible bcc (1 1 0) domains formed in a Pitsch orientational relationship [147]. The magnetic easy axis for bcc Fe is aligned with its $< 0\,0\,1 >$ directions [148]. Fig. 3.15 (d) shows all four possible bcc (1 1 0) domains, with blue arrows indicating the angles of the easy axes. For these domains, the azimuthal angles of the easy axes are 35°, 55°, 125° and 145°.

Putting together the magnetic and structural data reveals the behavior of the FIB-induced transformation. In case of transformation by the broad ion beam, spiral scanning by the FIB (and also when using multiple FIB scans) the transformed film contains all four bcc (1 1 0) domains [see Fig. 3.15 (c)] and exhibits four-fold magnetic anisotropy [see Fig. 3.14 (d) and (e)]. The linear single-scan FIB transformation results in uniaxial magnetic anisotropy [see Fig. 3.14 (b) and (c)] and the direction of the anisotropy depends on the direction of FIB scanning. The experimental data fit the model where FIB scanning in between fcc low-index directions preferentially forms bcc domains which have [0 0 1] direction parallel, or close to parallel to FIB scanning direction. For example, when the FIB is scanning between 0° and 90° then there is preferential nucleation of the domains with [0 0 1] directions at 35° and 55° [domain 1 and domain 2 in Fig. 3.15 (d)]. The FIB scanning angle can control the ratio of transformed domains and the easy axis direction can be continuously rotated between 35° and 55°. When the FIB scanning angle exceeds 90° (fcc $[0\,1\,\bar{1}]$ direction), then the other two bcc (1 1 0) domains are preferred and the magnetic easy axis jumps by 70° from 55° to 125°. Then, by a further increase of the FIB scanning angle from 90° to 180°, it is again possible to control the ratio of transformed domains [domain 3 and domain 4 in Fig. 3.15 (d)] and to rotate the easy axis between 125° and 145°. The overall tunability of the system is 40° in 180° range.

When we study Fig. 3.15 (b) little more in the detail we can realize that at the fcc directions [0 0 1], [0 1 0], $[0\,\bar{1}\,0]$ and $[0\,0\,\bar{1}]$ the easy axis direction matches the angle of the FIB scanning. As a rule of thumb, we see that when scanning with the fast axis of the FIB near any [0 0 1] (or similar direction) the easy axis will be aligned to the direction of the scanning. For the application of the knowledge gained from the angular dependence from Fig. 3.15 (b) it seems more logical to orient the sample to fcc [0 0 1] direction (i.e. 45° rotated from the coordinate system used in Fig. 3.15) prior to the FIB processing since for this orientation the easy axis direction directly follows the FIB scanning direction. This makes the use of the FIB anisotropy control much more straightforward.

For the reference, we have also elaborated on the same procedure as in Fig. 3.15 for thicker FeNi films. We have used the same samples as were studied for their dose dependencies in Fig. 3.8. To simplify the characterization process, we employ the two-fold symmetry observed in the first test and thus we limited the FIB scanning angle range to only the first two quadrants resulting in 19 structures in the FIB scanning angular range $0 - 180°$. The extracted data are in Fig. 3.16.

Quite apparently, there is a nice correspondence of the behavior between 8 nm and 12 nm thick layer. The 24 nm thick layer shows the continuous rotation of the easy axis direction, where the angle almost perfectly follows the FIB scanning angle. The initial slope of the easy axis direction angle fairly fits between all the cases. Both the 8 nm and 12 nm thick layers show a common feature at the fcc $[0\,\bar{1}\,1]$ direction. Whereas the 8 nm shows an abrupt jump of the anisotropy angle by $\sim 70°$, the transition in the 12 nm is broader, leading to more continuous rotation between mutually perpendicular uniaxial magnetic anisotropies. The abrupt jump between 130° and 140° is again caused by the data processing. When we artificially lift the data points by adding 180° [as was done

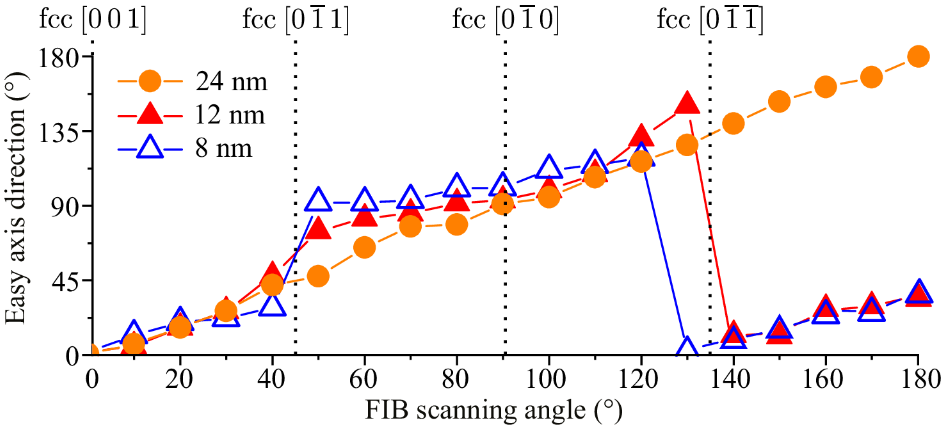

Fig. 3.16: (a) Fitted easy axis direction as a function of the FIB scanning direction (0° corresponds to fcc [0 0 1]) measured for 8, 12, 24 nm thick samples.

in Fig. 3.15 (b)], the step diminishes, and the transition is again more continuous. The 24 nm thick film exhibits very strange behavior as in theory. It shows the possibility to define any direction of the anisotropy. We believe that this is because, in this layer, the transformation does not go through all the thickness, as was previously elaborated in the discussion based on the magneto-optical measurement shown in Fig. 3.8. The theory is that the stabilizing agent for the orientation of the bcc domains is the Cu crystal. If the transformation does not go through the thickness, the melted volume of the FeNi will recrystallize on the layer of virgin fcc FeNi which possibly serves as a buffer layer allowing for the rotation of the crystal transformed on the top. This theoretical explanation could be tested in the future on e.g. 8 nm film, where we can change the acceleration voltage of the Ga^+ ions and thus limit the ion penetration range. If we will see this extended tunability, then the ion beam penetration is the limiting factor. If we will still see the distinct jump of the easy axis angle at the principal axes of the crystal, the continuous rotation will be attributed to the depth profile of the melted material. Despite the fact that it seems at the first sight that the continuous tunability of the easy axis angle in the 24 nm thick system is a huge benefit, it turns out that the control of the anisotropy is not very reliable especially for lower ion doses (slightly above the critical ion dose). For low ion doses, the anisotropy direction writing was highly stochastic. In order to reliably define the anisotropy direction, we had to overdose the structures to the ion dose 1×10^{16} ions/cm^2. Afterward in a single structure, the anisotropy writing is reliable. When we tried to e.g. write a structure where we gradually varied from one anisotropy direction to the other, the system did not follow exactly the FIB scanning angle. The crystallography of the structures was highly influenced by the orientation of the neighboring bcc structure. In theory, this could be overcome in the scanning strategy by choosing the proper initiation points. For the 8 nm and 12 nm thick film, this is not observed, and the anisotropy control works already from the lowest ion doses that allow for sustainable transformation.

To further understand the growth and the anisotropy control mechanism, we have evaluated more in detail the magnetic anisotropy strength. For the sake of the analysis of the angular dependence of the easy axis angle on the FIB scanning direction, the strength of the uniaxial magnetic anisotropy is not relevant as long as the anisotropy is strong enough to stabilize the magnetization in its direction in zero field. This leads to a hard axis loop with zero remanence at zero external magnetic field. The strength of the anisotropy can be a good indicator of the quality and the homogeneity of the film.

One of the examples is the strength of the uniaxial magnetic anisotropy and also the orientation of the anisotropy axis. When a material is inhomogeneous and consists of e.g. grains with a certain distribution of the anisotropy axes, the system behaves as if there is an effective anisotropy with a net strength and net orientation. It was stated in the theoretical introduction that when there are more sources of anisotropy in the magnetic system, the total anisotropy axis will lie in the direction of the strongest anisotropy and the strength will be given simply by the difference of the vector projections to this axis. This is true for a single magnetic system, yet when the system consists of e.g. grains, there is a fundamental difference in the behavior. The grains are separated by a grain boundary where e.g. exchange interaction is lowered, and thus every grain behaves as a separate system in the effective magnetic field given by the surrounding material. In such a system, the anisotropy direction will be given by the vector addition of individual grains with a weight function given by the grain size. In the previous text, we have elaborated on the theoretical model of four distinct magnetic domains, where two and two have its anisotropy axis very close to each other. This model worked very well for the case of the 8 nm thick film, but already 12 nm film showed less abrupt transition at the principal axis of the crystal. This could suggest mixing the two perpendicular domains (e.g. domain 2 and 3 from Fig. 3.15). To see whether this is the case, we have looked more in detail to the FIB scanning angle rotation test on this film. The SEM image under the small tilt of the test structures is in Fig. 3.17 (a). In the figure, twenty structures in total are visible in the SEM contrast. The structures written by the FIB angles between $0° - 30°$, show an additional grainy texture. In the structures written in the angular range $120° - 170°$, a clear division to two domains with different contrast is nicely visible. The boundary between the two contrast domains is always near the fcc $[0\,\bar{1}\,1]$ direction. The respective ratio of the dark/bright domain is changing: going from the mainly dark to the mainly bright case (with increasing FIB scanning angle). A similar trend, with lower contrast, is also observed between $30° - 70°$ (which is rotated by 90° from the other case written at angles $120° - 170°$). When we look at the easy axis dependence on the FIB scanning direction plot in Fig. 3.16, we see that those structures with the two contrast domains are found at the FIB scanning angles in the gradual transitions where the anisotropy axis rotates. The strength of the contrast suggests that the two domains have their anisotropy axis perpendicular to each other and what we measure in the magnetometry measurement is the effective anisotropy of the whole structure. Due to technical difficulties, we have not measured those structures by focused Kerr magnetometry, but with the Kerr microscopy. In the analysis, we have always saved the Kerr image for each external magnetic field value in the magnetic field cycle. In order to obtain the hysteresis of the individual structures, one needs to analyze the intensity [measured as a grey level proportional to magnetization (2.13)] as a function of the external magnetic field. The prepared program allows us to select multiple areas (structures) and to extract the hysteresis of all the structures at the same time. Since in the Kerr microscopy measurement it is rather hard to calibrate to magneto-optical angles (i.e. Kerr rotation, Kerr ellipticity), we always normalize the loops either to the saturation level or to the saturation level of the loop with the highest signal (in the case we measure more structures as in e.g. dose tests). One exemplary hysteresis loop measured on the highlighted structure in Fig. 3.17 (a) for a magnetic field oriented in the hard axis direction (120° from the fcc $[0\,0\,1]$ direction) is shown in Fig. 3.17 (b). The loop shows typical hard axis loop features. It exhibits the linear part, where the magnetization continuously rotates from the easy axis to the hard axis, and also the magnetic saturation found for an external magnetic field higher than the anisotropy

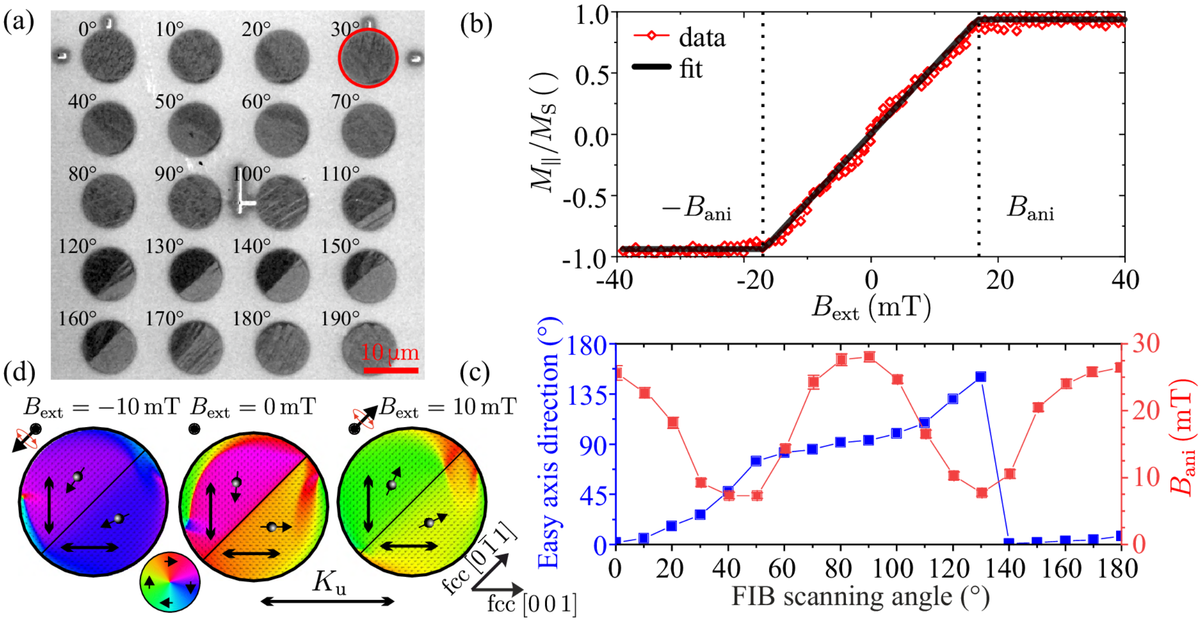

Fig. 3.17: (a) SEM image under tilt 4° of the rotational test. The number denotes the FIB fast axis scanning angle from the horizontal direction (coinciding with fcc [0 0 1] direction). (b) The example of the hard-axis loop measured on the highlighted structure (by the red circle) in (a) for the magnetic field oriented 120° from the fcc [0 0 1] direction. The black curve is the fitted function. The anisotropy field value extracted from the model B_{ani} is given by the dotted vertical lines. (c) Fitted easy axis direction and the anisotropy field strength as a function of the FIB fast axis scanning direction. (d) Numerical simulations of the structure with the two domains with perpendicular magnetic anisotropies (separate by line oriented at 45°). The double-headed arrow marks the anisotropy direction and the small arrows denote the net magnetization orientation in the half-circle. The color wheel denotes the local magnetization direction. The magnetic field strength and orientation for each simulation are shown above each vector map.

field B_{ani}. The amplitude of the anisotropy field value can give a good estimate of the crystalline quality of the film and thus we extracted it directly from the measured loops. Unfortunately when the magnetic field is not perfectly aligned with the hard axis direction, the loop will exhibit openings and other features leading to a very unreliable reading of the anisotropy field value. We have interconnected the software dedicated to the image processing directly with another software that allows us to continuously fit the measured hysteresis loops by two models of hysteresis: hard axis loop and the easy axis loop. Both loops are modeled by approximate analytic functions instead of taking the full approach as e.g. the Stoner-Wohlfarth model. For the sake of the analysis from Fig. 3.17 (b), we have used a very simple piecewise linear model for the hard axis loop:

$$M_{\parallel}/M_{\mathrm{S}} = \begin{cases} -1 & B_{\mathrm{ext}} \leq -B_{\mathrm{ani}} \\ \frac{B_{\mathrm{ext}}}{B_{\mathrm{ani}}} & -B_{\mathrm{ani}} \leq B_{\mathrm{ext}} \leq B_{\mathrm{ani}} \\ 1 & B_{\mathrm{ext}} \geq B_{\mathrm{ani}}. \end{cases} \tag{3.3}$$

This model allows extracting the anisotropy field with great repeatability. It is also rather immune to slight ($\pm \sim 15°$) misalignments of the external magnetic field from the hard axis direction. Based on the data in Fig. 3.16, we have extracted the hard axis directions for all the structures shown in Fig. 3.17 (a). Furthermore, for those directions, we have extracted the hysteresis loops measured for these particular angles at the individual structures, and we have fitted the loops by the model introduced in (3.3). This analysis yields the angular dependence of the anisotropy field as a function of the FIB scanning angle. We clearly see a strong angular dependence with a maximum aligned to the principal fcc axes $\langle 1\,0\,0 \rangle$ and to the minima at the fcc $\langle 1\,1\,0 \rangle$. The minimum value is found at the angle, where we saw, for a 8 nm thick film, the step-like transition between the different domains of the bcc. Now we see a more gradual transition. It supports the original idea that the two domains of highly different contrast have the respective anisotropies perpendicular to each other and that we see only the effective anisotropy that can be continuously rotated simply by changing the ratio of the domains 1 + 2/domains 3 + 4 [for the definition of the domains see again Fig. 3.15 (b)]. The measured hard hysteresis loop is given by the sum of the loops from both individual domains with the anisotropy oriented 45° from the domain boundary. Both domains are coupled by the demagnetizing field and thus cannot be modeled as separated objects. In order to see, how the hard axis loop is formed for such a system, even though the external field is not in the hard axis of any individual domain, we have performed the micromagnetic simulation[3] of the structure in the GPU accelerated solver mumax^3 [149]. We have divided the structure into two halves [as seen for angle 140° in Fig. 3.17 (a)] and we defined the magnetocrystalline anisotropy of both regions to be perpendicular to each other (vertical/horizontal). Afterward, we have set the external magnetic field to lie 45° from the anisotropy axis (along the boundary). Starting from saturation, we have used the mumax^3 solver to find the static equilibrium magnetization landscape for each magnetic field value with a step 1 mT. For each magnetic field step, we recorded both the net magnetization of the whole structure in the direction of the external magnetic field and also the full map of magnetization. The simulation showed that initially all the magnetic moments are aligned to the external magnetic field direction. With lowering the field, the magnetization starts to realign linearly to the local easy axis direction. For small magnetic fields, the tail-to-tail orientation of the magnetization

---

[3] $M_{\mathrm{S}} = 1.4\,\mathrm{MA/m}$, $K_{\mathrm{u}} = 22\,\mathrm{kJ/m^3}$, $A_{\mathrm{ex}} = 11\,\mathrm{pJ/m}$. Discretization was selected to 4 nm in all directions.

starts to be highly unfavorable from the charge avoidance principle. In certain parts of the structure the magnetization partially realigns to form a flux closure pattern. Close to zero field, the magnetization in one of the regions flips to the opposite direction (and the magnetization in both halves slightly rotates). This process results in a hard axis hysteresis loop. Three steps of the magnetization switching process near the zero-field are in Fig. 3.17 (d). We first see that for the negative field (above saturation), the magnetization in both halves is almost homogeneous and only slightly deviates from the external magnetic field direction. At zero field, the magnetization starts to be more infhomogeneous and one of the halves is already switched to another direction. This gives zero total projection of the magnetization to the external magnetic field direction. Going further, the magnetization forms more of the flux closure parts and then eventually also the second halve flips in the other direction. All in all, the resulting loop is a hard axis loop and as such the overall behavior of the whole structure is as if there was only one anisotropy direction. The direction is driven only by the ratio of the sizes of the individual domains. This ratio is apparently changing in our system [see structures with the angles $110^\circ - 170^\circ$ in Fig. 3.17 (a)] and thus we see a continuous rotation of the anisotropy direction. The mixture of two competing domains with mutually perpendicular anisotropy in a single structure causes four-fold modulation of the anisotropy strength in the in-plane direction. As we see in Fig. 3.17 (c), this modulation is not negligible.

The effective nature of the resulting anisotropy gives a fundamental limit to the utilization of such a behavior. The effective anisotropy is rather low and also at zero field the magnetization is highly non-homogeneous. Such a state is not very suitable for e.g. spin-wave propagation since for the spin-wave propagating between both domains, the angle between the static magnetization and the propagation vector would vary. This would inevitably result in a spin-wave mode mismatch and loss of spin-wave power due to reflections. Additionally, the process relies on the formation of two domains in one structure. For a certain size, this will be no longer possible, and the system will proceed with its transformation stochastically only in one domain. For structures smaller than $\sim 2\,\mu\mathrm{m}$ it proved to be very problematic to stabilize the effective anisotropy near e.g. fcc $[0\,\bar{1}\,1]$ direction. We have performed the size test by writing similar waveguides as were analyzed in Fig. 3.6. In this case, we oriented the fast scanning direction of the FIB to the fcc $[0\,\bar{1}\,1]$ direction. Afterward, we studied the SEM images under tilt that revealed the domains with mutually perpendicular anisotropy solely by the contrast seen in the SEM. The images are in Fig. 3.18.

Already the image taken under the normal incidence shows certain finer structure inside transformed areas. This is readily enhanced in the image taken under small tilt. Clearly, in the initiation region, the high ion dose resulted in almost equal distribution of the dark and bright domains. This translates to the rotated anisotropy direction and lower strength. This is not the case for the waveguides. For the $2\,\mu\mathrm{m}$ wide waveguide, we see that despite the very similar growth procedure, both waveguides have a highly different contrast. This is due to the stochastic growth initiation. Already for $1.5\,\mu\mathrm{m}$ wide waveguide (second from the top), we recognize only a small number of domains with opposite contrast. For narrower waveguides, we do not see any. In another experiment, we have rotated the FIB scanning direction slightly from the fcc $[0\,\bar{1}\,1]$ direction. In this condition, the majority of the waveguides grew with the domain recognized by the bright contrast (opposite to the contrast shown in the right panel of Fig. 3.18).

The analysis clearly shows the experimental limit allowing to set any direction of the anisotropy between the fcc $[0\,1\,0]$ and fcc $[0\,1\,0]$ directions.

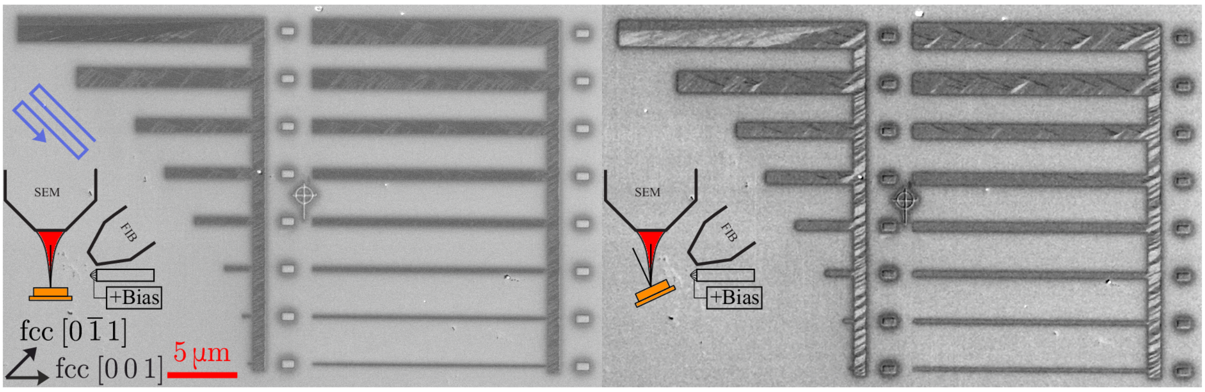

Fig. 3.18: Left panel shows the SEM image of the waveguides under normal incidence. The nominal width of the waveguides start at 2 µm and goes down to 50 nm. The initiation region (a wide narrow region on the right side of the waveguides) was overdosed to 1×10^{16} ions/cm^2. The waveguides were grown with the ion dose of 5×10^{15} ions/cm^2. The scanning direction of the FIB is given by the blue path. The right panel shows the image of the same structures taken under tilt. The sample was rotated in-plane to achieve the highest contrast between domains.

We have also performed preliminary experiments, where we tried to lower the size of the domains, and thus to allow us to grow even smaller structures with any direction of the anisotropy. We experimented with e.g. restarting the transformation every 400 nm, or by introducing the defects to the material by slight irradiation of the material prior to the FIB transformation. The results were highly nonreproducible.

The above analysis shows that again only the small angular range of easy axis tunability as found on the 8 nm [see Fig. 3.15 (b)] can be meaningfully employed in the experiments even for the 12 nm thick system.

For the reference, we have also performed a similar analysis on the 8 nm system [Fig. 3.17 (c) shows the results from the 12 nm system]. We saw a slight modulation of the anisotropy strength with the FIB scanning angle with the same periodicity as in the 12 nm system, yet the modulation depth was ~ 5 mT in contrast to ~ 25 mT in the 12 nm thick system. This suggests a slightly different behavior of both systems. The maximum value of the anisotropy constant is highly comparable in 8 nm and 12 nm thick systems. The 24 nm thick system showed the maximum anisotropy field values to be lower, around 10 mT.

In the last analysis, we have analyzed the strength of the anisotropy as a function of the ion dose. We have prepared structures with the FIB scanning angle aligned to the fcc [0 0 1] direction in order to achieve the highest possible anisotropy field. We have varied the ion dose between the structures from the doses not sufficient to sustainably grow the bcc phase up to the dose leading to sputtering of the material. The measured data are in Fig. 3.19.

The anisotropy field ion dose-dependence shows a correlation of the anisotropy field with the total measured Kerr signal. In the case of 12 nm thick film, the anisotropy field shows a more rapid decline at higher ion doses than the total signal (proportional to the magnetic moment). It opens a way for small ion dose tunability of the magnetic anisotropy field value with only a slight deterioration of the total magnetic moment. For 8 nm film, both curves closely overlap, and thus it is not possible to tune the magnetic anisotropy without deteriorating the magnetic moment of the structure.

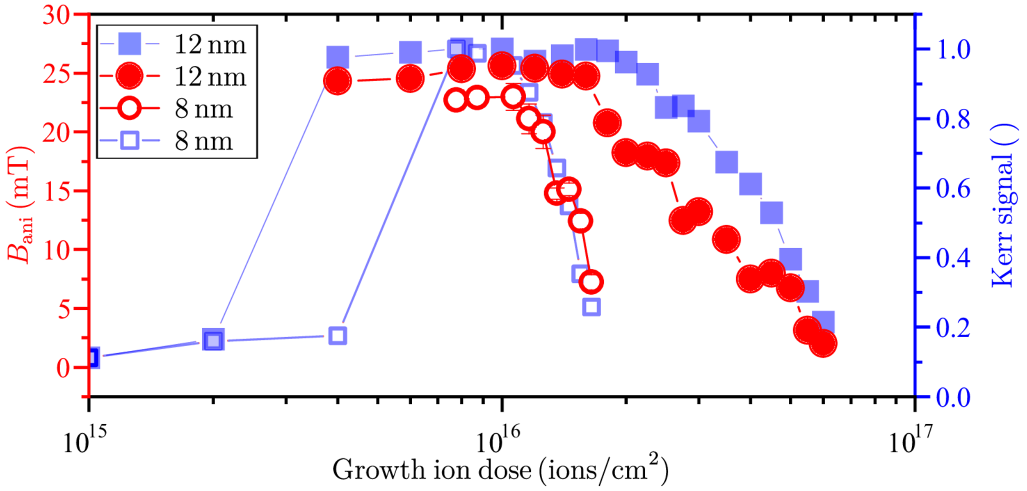

Fig. 3.19: The comparison of the ion dose dependence of the anisotropy field and the maximum Kerr signal for the 8 nm (empty symbols) and 12 nm (full symbols) thick films.

In conclusion, we have analyzed the material thoroughly. First, we have analyzed the initiation length needed for the material to continuously proceed with the fcc/bcc FIB induced recrystallization. We have proposed two means of limiting this initiation length to less than 100 nm. Subsequently, we have shown the growth of magnetic waveguides with a huge length/width ratio. For the three samples with different thicknesses, we have analyzed the dose dependence of the material, and we have found a very different growth regime to occur when the transformation is performed with single or multiple scans of the FIB. We have also found, how the FIB scanning direction modifies the crystallography of the resulting transformed layers. We have used the SEM contrast to further analyze this phenomenon. The contrast creation is attributed to channeled backscattered electrons that create secondary electrons in the SEM chamber.

- We have used this in order to obtain the Kikuchi pattern directly in the SEM.
- We have used this pattern to precisely align the sample in the SEM/FIB chamber.
- By performing Kerr magnetometry and microscopy we have found that together with the crystallography of the layers also the magnetic anisotropy can be guided by the FIB scanning strategy.
- We have shown that we can rotate the anisotropy simply by changing the scanning angle of the FIB or that we can switch the uniaxial magnetic anisotropy off by using multiple scans of the FIB.

The full angular dependence of the magnetic easy axis of the structures on the FIB scanning direction was measured and analyzed and compared to what is known about the crystallography of the bcc structures on the fcc substrate. The exact reason, why the direction of FIB scanning can control the nucleation of individual bcc domains, is not clear. The most probable explanation is uniaxial strain propagating perpendicularly to the FIB scanning direction that influences the possible bcc domain orientation that can be formed in the strained surrounding. However, this theory is not thoroughly supported by experimental data. We have only indirect indications from the growth process. We believe that using more advanced techniques as LEEM, EBSD or by using STM and in-situ UHV FIB it will be possible to entangle the mechanism of the anisotropy control in future projects.

In the last part, we have tackled the anisotropy field. First, we have shown that not all the angles in the crystal are equivalent. Even though it seems that we can gradually change the anisotropy direction by the FIB for the 12 nm thick sample, we have shown that the anisotropy for the certain angles is simply given by the existence of two crystallographic domains in a single structure. Both domains have mutualy perpendicular in-plane anisotropy and the resulting anisotropy is only an effective projection of the two contributions. We have also tried to estimate the size limit of the structure that exploits the effective anisotropy. In the last analysis, we have studied the anisotropy field dependence on the ion dose used for the transformation of the structure. The anisotropy field proved to be highly dependent on the quality of the layers that deteriorates quickly when reaching the ion dose sufficient for the sputtering of the material.

Overall, the material offers huge tunability. When the magnetic anisotropy is not of the interest, the multi-scan approach allows us to continuous tune the saturation magnetization with a spatial resolution of approx. 100 nm. When the anisotropy is needed, it allows to control rather strong uniaxial magnetic anisotropy and more interestingly, one is able to easily rotate the anisotropy only by the change of the FIB scanning angle. By fine adjustment of the ion dose, the system also allows to slightly change the anisotropy constant. All the above-mentioned features can be ultimately combined in a single structure. This paves the way towards great possibilities unattainable in any conventional system.

When considering any application of the material for spin-wave device fabrication and characterization, the material parameters are still missing. The absolute value of saturation magnetization M_S is unknown together with the absolute value of the uniaxial anisotropy constant K_u. The K_u value can be easily calculated from the measurement of the anisotropy field B_ani but the M_S parameter must be known. Extracting the material parameters from the spin-wave propagation measurement will be of interest to the following chapter.

4. Spin-wave propagation in $Fe_{78}Ni_{22}$ magnonic waveguides prepared by FIB direct writing

In the previous chapters, we have paved the guideline for the experimental application of the metastable material for the spin-wave propagation experiments. The main motivation for applying the material for the spin-wave related physics is the unmatched prototyping capability of the system. Using a FIB, the fcc->bcc transformation can be precisely controlled, which results in unprecedented local control over the local magnetic properties [26]. This approach removes the need for complicated multi-step lithography processing and provides rapid prototyping possibility. The presented properties of the material offer the additional possibility to control the magnetic properties of each structure, or even to change the magnetic properties locally in a single magnetic element [21, 24, 26, 134, 150].

The prospect of a transversely magnetized long and narrow waveguide in zero external field is ambiguously more versatile than the conventional approaches that rely on using the external magnetic fields or global magnetic anisotropy. The highly local character of the presented approach allows stabilizing the magnetization in the direction of the locally variable magnetic anisotropy. This chapter will aim to present the reader with the pioneering experiments that show the viability of this material for magnonics.

4.1. Magnonic waveguides

The previous chapter introduced the reader to the possibilities of the material. In this section, we will use the material for the fabrication of the waveguides as the basic building blocks of the magnonic circuitry. The method of choice for static characterization is the Kerr microscopy and experiments focusing on spin-wave propagation are performed by the µBLS method. The characterization was carried out partially at the home institution CEITEC BUT and also during a couple of short research stays at the HZDR Dresden in the group of Helmut Schultheiss. All the experiments presented in this chapter were performed on sample Cu#14 (see Appendix 2).

4.1.1. Thermal stability of the pristine fcc layers

Prior to the experiments on the transformed bcc iron structures, we have tested the temperature stability of the fcc material simply by adjusting the laser power of the µBLS system. First, we have recorded the BLS spectrum for optical power of approx. 0.3 mW. The initial value was chosen as a safe value from experience on different metallic material, with expectedly similar optical properties. To identify the magnetic contribution, we have always recorded two BLS spectra where the first was recorded without any applied magnetic field, and the second was recorded at the applied magnetic field of $B_{\mathrm{ext}} = = 52\,\mathrm{mT}$. We have performed the same experiment for the maximum applied laser power of approximately 1 mW. Afterward, we have decreased the laser power again to 0.3 mW. Such a procedure should reveal irreversible laser-induced damage to the material. The analysis is in Fig. 4.1. From the data, we conclude that for the highest laser power we

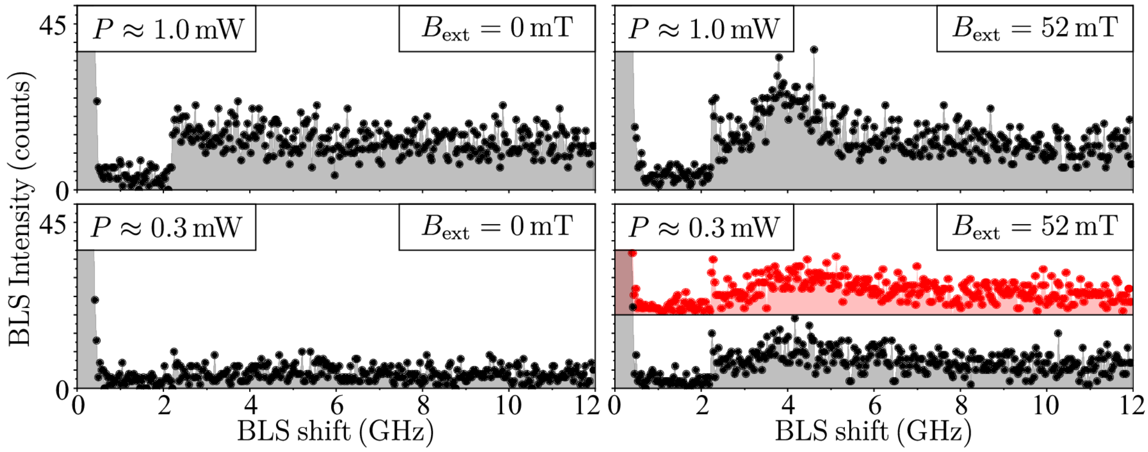

Fig. 4.1: Thermal BLS spectra for the laser-induced damage test. The top row represents the data for the maximum laser power. The bottom row shows data for lowered laser power. The red BLS spectrum was recorded before applying the highest laser power to the system.

can clearly resolve a magnetic response. It is identified by the appearance of a broad and weak peak at approx. 4 GHz at the field $B_{\mathrm{ext}} = 52\,\mathrm{mT}$. For lower laser power, when we compare the top and bottom row, we see a total level of the signal to drop. The magnetic response at 4 GHz is faintly visible. Moreover, the total signal level in the field is higher than the zero-field measurement. From the Kerr magnetometry data (see e.g. Fig. 3.7 on page 63) we see, that in the pristine fcc layers we already recognize small, yet measurable background value coming from the magnetic material. It was originally thought, that it originates in the small magnetic moment of fcc iron, but Biederman and coworkers in 2001 showed that the magnetic moment originates in small magnetic nuclei (needles) possessing the magnetic bcc structure [151]. The signal level measured by BLS is very small, yet could be attributed to the random distribution of small bcc nuclei with different sizes and orientations. When we focus solely on the strongest contribution, the peak seen at 4 GHz, we see that the shape of the thermal BLS spectra does not exhibit the same dependence as was shown in Fig. 2.9 with a very specific peak at the FMR frequency. One has to bear in mind, that the calculation in Fig. 2.9 was done for propagating waves in the infinite thin film. When we focus only on the approximate position of the peak, we can roughly estimate the effective saturation magnetization from the position of the peak at 4 GHz and the external magnetic field value. Rather crude estimation based on (1.41) yields an effective value of 150 kA/m. When we compare the BLS spectra measured at 52 mT and 0.3 mW taken before and after reaching the highest laser power, we do not recognize any evident difference.

As a short note, the overall thermal stability of the whole sample is an issue. During lithography on the whole sample Cu#12 (see Appendix 2), we have performed long term heating of one of the samples up to 200 °C (the pre-bake of the resist). After the electron beam lithography and subsequent lift-off process, we observed large contamination of the sample by the SEM. The areas of the size ∼ 100 µm appeared, exhibiting a very bright contrast covering almost half of the sample. The electron dispersive X-ray spectroscopy (EDX) performed in the SEM did not show any visible difference between the contaminated and clean areas. When performing FIB irradiation in the contaminated areas, it was possible to transform the layers into the bcc phase yet in a very different manner than what is presented in e.g. Fig. 3.2. From the magnetometry measurements, we also saw, that we are not able to modify the anisotropy of the layers by changing the FIB scanning angle. The structures transformed in the contaminated areas were isotropic. Structures transformed outside of the contaminated areas exhibited uniaxial magnetic anisotropy, yet with much lower anisotropy fields when compared to the state prior to the lithography. To distinguish the experiments performed on the sample before/after the pre-bake, we mark the experiments performed after the pre-bake by a label Cu#12d (in the Appendix 2). After a few preliminary tests, we did not come to a conclusion of the origin of the contamination. As the level of the SEM contrast was very close to the level of contrast found at the copper substrate, it might suggest the formation of the copper-rich surface areas formed by the precipitation of the copper through the iron layers. The thin film of Cu could then form Fe/Cu surface alloy resulting in deterioration of the iron crystallography. When using a pre-bake limited to 100 °C we did not observe any degradation of the layers.

4.1.2. Stability of the transverse magnetization in the magnonic waveguides

When considering the spin waves as information carriers, the merit of interest is the group velocity. The higher the group velocity, the higher the data throughput of potential devices [15]. The spin-wave dispersion (Fig. 1.12 on page 28) directly forces a need for the Damon-Eshbach geometry as it exhibits the largest group velocity of all the spin-wave modes. When forming a magnonic waveguide, the Damon-Eshbach geometry requires the magnetization to be in the transverse direction to the waveguide long axis. This is quite unfortunate as this particular magnetization configuration has the highest energy cost for a magnetic system (for in-plane magnetized structures). The resulting magnetic charges stemming from the diverging magnetization on the edges of the structure will create strong demagnetizing fields reaching almost 70 mT for 1 µm wide waveguide (see Fig. 1.3 on page 8). This becomes even more problematic when going to ultra-narrow waveguides [152]. Classically, this is overcome by applying strong enough magnetic field perpendicular to the waveguide long axis [153–155]. When considering a 2D design of a magnonic chip, there can be nothing like a global external field pointing in one direction. A simple signal turn is then a major obstacle as a huge mode mismatch for the waveguide before/after the turn will deteriorate the propagation [156]. Our material can exhibit the two perpendicular uniaxial magnetic anisotropies and thus could allow for stabilization of the magnetization in both arms in the transverse direction. The following text will be dedicated to the study of the basic building blocks of the spin-wave turns: the waveguides.

4.1.3. Micromagnetic modeling

From Fig. 3.17 (on page 82) we see the maximum anisotropy field to reach 30 mT. In order to stabilize the transverse magnetization in the long waveguide, we get directly a limit for the achievable width. The model by Aharoni (see calculation in Fig. 1.3 on page 8) gives the same value of the demagnetizing field for a waveguide width equals to 2 µm. The model was derived with an assumption of a homogeneously magnetized body. In reality, the magnetization can spatially realign in order to lower the creation of the strong demagnetizing field on the waveguide edge. We have analyzed this behavior by performing a series of micromagnetic simulations in the mumax^3 package. The step size in the finite-difference mesh used by mumax^3 was defined with respect to characteristic lengths from (1.27) and (1.28) (defined on page 15) to 4 nm in in-plane directions. In very thin films we do not expect any evolution of the magnetization in the out-of-plane direction. This allows us to approximate the thickness 9.5 nm by only one cell in the out-of-plane direction. After defining the mesh we define the magnetic constants of the layers to: $M_\mathrm{S} = 1.4\,\mathrm{MA/m}$, $K_\mathrm{u} = 22\,\mathrm{kJ/m^3}$, $A_\mathrm{ex} = 1.0 \times 10^{-12}\,\mathrm{J/m}$. The anisotropy easy axis direction is fixed in the whole structure to point in the transverse direction to the long axis of the waveguide (y direction). The selection of the parameters is not random but follows the extracted values obtained later in the text from the µBLS experiments. *A priori* to the experimental work, we have performed sets of simulations with estimated values of the magnetic constants to observe the general trends and to estimate the expected values (e.g. resonance frequency). The following text presents sets of simulations with the magnetic constants more close to the experiment.

In the simulation, we always set the initial magnetization to point in the transverse direction to the long axis of the waveguide $M_y = 0.95 M_\mathrm{S}$ with a small component also in the longitudinal direction $M_x = 0.05 M_\mathrm{S}$. The longitudinal component breaks the high symmetry of the problem, not achievable in the actual experiment. We have performed two sets of simulations. In the first simulation set, we study isolated magnetic structure with fixed length $L = 10\,\mu\mathrm{m}$ and variable-width $W = 52 - 2000\,\mathrm{nm}$. The second set of simulations mimics the long waveguide limit by applying the periodic boundary conditions (PBC) on $L = 10\,\mu\mathrm{m}$ long waveguide with the same range of waveguide widths. As such the use of PBC allows only for solutions of the magnetization with the same profile on the both edges defined by the PBC direction. Together with the periodic magnetization also the demagnetizing field is calculated to be periodic. The PBC adds terms in the demagnetizing field stemming from the virtual neighboring structures and thus allows to approximately study extended periodic systems of identical magnetic structures. In our case, we extend the waveguide in the long waveguide axis ten times.

After the problem is defined, the demagnetizing field is calculated. We save the demagnetizing field for each waveguide width. This state of magnetization fulfills the assumption of the model by Aharoni presented in the theoretical chapter by Fig. 1.3 (on page 8). It serves as a sanity check of the numerical model. After the demagnetizing field is saved, we let the solver search for the equilibrium magnetization (ground state) of the system by turning off the precessional torque in the LLG equation (1.34) (on page 19). The numerical solver then evolves the magnetization, until the torque acting on the magnetization is minimal (together with the energy). When the energy minimum of the system is found, we save the magnetization vector map and the spatial average of the magnetization vector and the demagnetizing field vector. The representative sample of the results from the micromagnetic treatment is in Fig. 4.2.

The numerical treatment shows mainly qualitative agreement between the simulated magnetization landscapes with and without the PBC. For small waveguide widths, we see that in the isolated structures the magnetization first realigns to the longitudinal direction. The magnetic charge on the left/right edge helps to stabilize the transverse magnetization on the edges of the waveguide already in 352 nm wide waveguide. Initi-

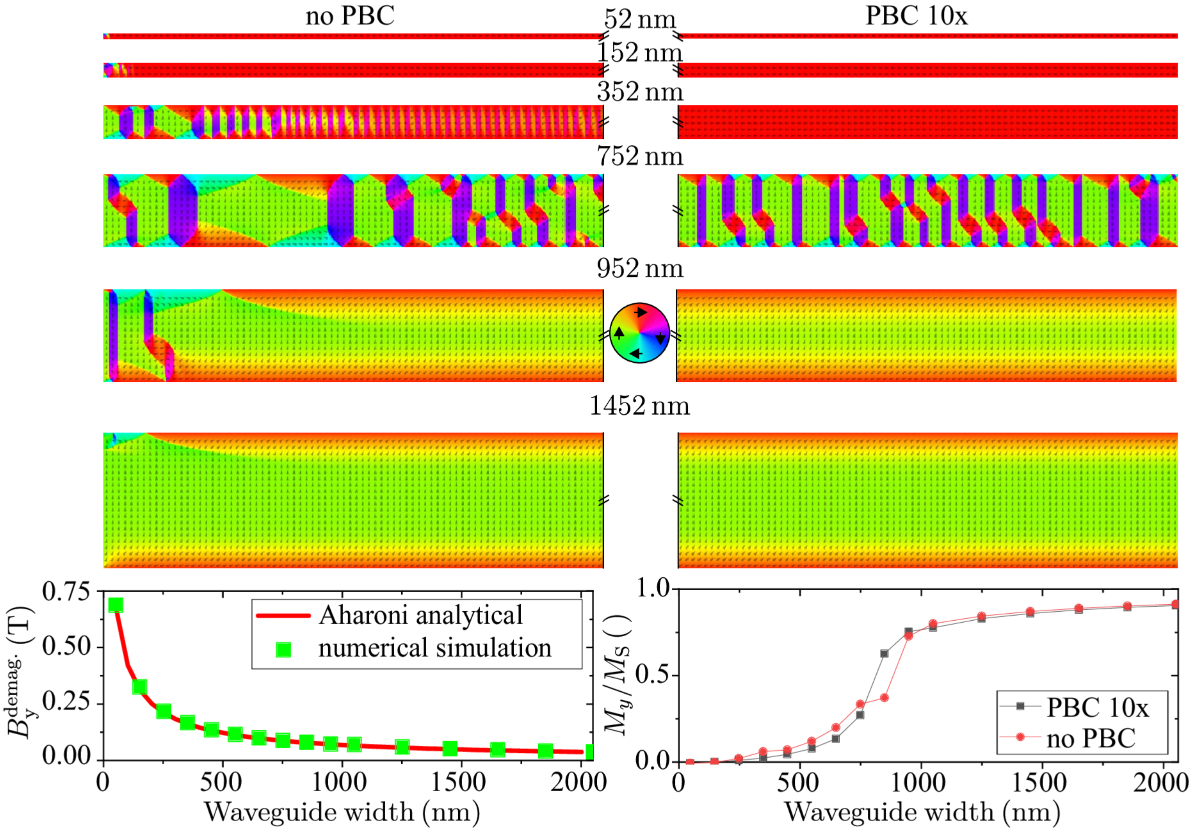

Fig. 4.2: The results of the numerical analysis of the transverse magnetization stability in long and narrow waveguides (waveguide width is denoted in the middle). The left row shows the left half of the isolated waveguides. The right row shows the right half of the waveguides calculated with an assumption of periodic boundary condition. The magnetization direction is given by the color wheel in the middle panel. The bottom left graph compares the demagnetizing field obtained from the micromagnetic model of the fully saturated waveguides with the analytical model by Aharoni [38] for the range of waveguide widths. The right graph compares the effect of the PBC on the average transverse magnetization component after we have found the ground state.

ated on the edge, the competing shape and magnetocrystalline anisotropy form together zigzag magnetization pattern. The central part has a constant longitudinal magnetization component and a ± alternating transverse magnetization component. When increasing the waveguide width, the period of the alternation gets higher. For the waveguide width $w = 752\,\mathrm{nm}$, the anisotropy energy and the shape anisotropy energy are almost equal and thus the magnetization in the waveguide breaks to larger domains. When the demagnetizing energy (shape anisotropy energy) gets lower than the anisotropy energy, the magnetization starts to lie preferentially in the transverse direction without any observable oscillations. For high waveguide widths, the magnetization in the central part of the waveguide points fully in the transverse direction, and in a small region on the edge it rotates gradually to the longitudinal direction. When the PBC is employed, the micromagnetic states with oscillating magnetization patterns are less favored as the lack of demagnetizing field on the left/right edge cannot initialize the realignment of the magnetization to the non-homogeneous state. The magnetization in narrow waveguides almost fully lies in the longitudinal direction. Around the reorientation width (approx. 800 nm), the magnetization in the central part starts to realign to the magnetocrystalline anisotropy direction. Both cases show qualitatively similar results when looking at the magnetization sufficiently far from the edge of the structure. Calculation with PBC usually converges much faster since it supports more homogeneous cases without complex magnetization patterns on the edges.

The sanity check of the simulations: the calculation of the demagnetizing field given in the bottom left graph of Fig. 4.2, extracted from the waveguide in the saturated state, shows nice agreement between the micromagnetic simulations and the analytical model. The bottom right graph of Fig. 4.2 shows the overall agreement between the simulation with/without the periodic boundary conditions. The slightly higher average transverse component is due to the effect of the left/right edge, where the magnetization realigned. From the simulations, we can also identify the waveguide width allowing for zero-field propagation of spin waves in the fast configuration of the DE geometry. Already at the waveguide width of 952 nm, the magnetization in the central part of the waveguide becomes homogeneous with only small declination from the transverse direction. This waveguide width could be used for guiding spin waves with the high group velocity. In this study, we can see the limitation of the analytical model of Aharoni calculated for the homogeneous structure. For the given anisotropy constant and saturation magnetization value, the limiting width for the transverse orientation of the magnetization in the waveguide is underestimated by more than a factor of two. This is due to the fact that in reality, the magnetization can form a localized edge region, where the magnetization can tilt to the longitudinal direction and thus to limit the creation of the strong demagnetizing field that would be created if the magnetization pointed parallel with the edge normal. The gradual rotation of the magnetization also creates the demagnetizing field, but the field is much lower when compared to the fully saturated state.

The reorientation of the magnetization and the formation of the edge region is also nicely seen from the transverse magnetization profiles shown in Fig. 4.3. The transverse profiles show again that for the waveguide widths below 500 nm, the magnetization points exclusively in the longitudinal direction. Already for $w = 852\,\mathrm{nm}$, the magnetization points mainly in the transverse direction. At waveguide width $w = 952\,\mathrm{nm}$, the magnetization in the central part reaches almost full saturation. At higher waveguide widths, the plateau of the transverse magnetization component appears. The right panel of Fig. 4.3 compares the analytic solution of the transverse demagnetizing field for homo-

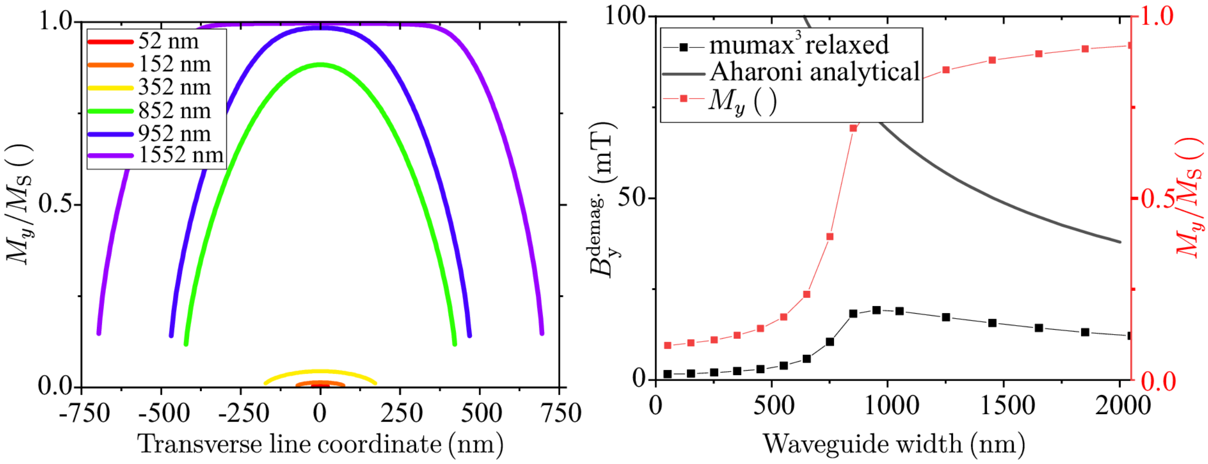

Fig. 4.3: The left graph shows the transverse profiles of the transverse magnetization component extracted from the magnetization maps shown in the right panel of Fig. 4.3. The right graph shows the comparison of the transverse demagnetizing field width dependence obtained from the analytic case of the fully saturated waveguide and also the case, where the magnetization is in the ground state. The magnetization reorientation curve is shown for reference.

geneous magnetization (black line) with the one obtained from the ground state of the magnetization (black squares). For the waveguide widths below the reorientation width, we see a very small demagnetizing field coming from a fact that the majority of the magnetization points in the longitudinal direction. For the waveguides wider than approx. 800 nm, we see an increase of the demagnetizing field strength up to the maximum value at approx. 1000 nm. Afterward, the increase of the edge region distance causes a gradual lowering of the demagnetizing field. It is directly apparent that due to the edge region with the magnetization pointing in the longitudinal direction, the demagnetizing field is a way lower than what is predicted for the homogeneous case. The maximum observable demagnetizing field obtained from the micro-magnetic treatment is 19 mT. The quantitative agreement of the demagnetizing fields for homogeneous waveguide and the waveguide with the tilted magnetization on the edges is found around the waveguide width $\sim 10\,\mu\text{m}$.

Ultimately, we are interested in the spin-wave propagation properties of the waveguides. The main important nomenclatures defining the local spin-wave dispersion are in the end the local angle of the magnetization and the local effective magnetic field [see (1.25)]. The effective field, in this case, comprises of the exchange term, uniaxial magnetic anisotropy term and also of the demagnetizing field term. To estimate the transverse profile of the spin-wave dispersion, we have taken the data from the left graph of Fig. 4.3 and we have calculated the transverse width profile of the magnetization angle. At the same time, we have extracted from the simulations the effective magnetic field (both magnitude and the angle). Having this data, we took the unconfined spin-wave dispersion[1] presented by (1.58) (on page 27) and calculated the local spin-wave dispersion width profile for each of the simulated structures. The analysis is presented in Fig. 4.4. The angle of the magnetization in Fig. 4.4 (a) was calculated from the M_x and M_y components by $\operatorname{atan2}(M_y, M_x)$ function. The calculated angle again shows the reorientation of the magnetization around the waveguide width 800 nm. For waveguide widths 500 nm and

---

[1] It is not trivial to elaborate the spin-wave dispersion in the confined structure, since the net magnetization in each structure is not homogeneous. This changes the boundary conditions and also the direction of the quantization of the spin-wave wave vector.

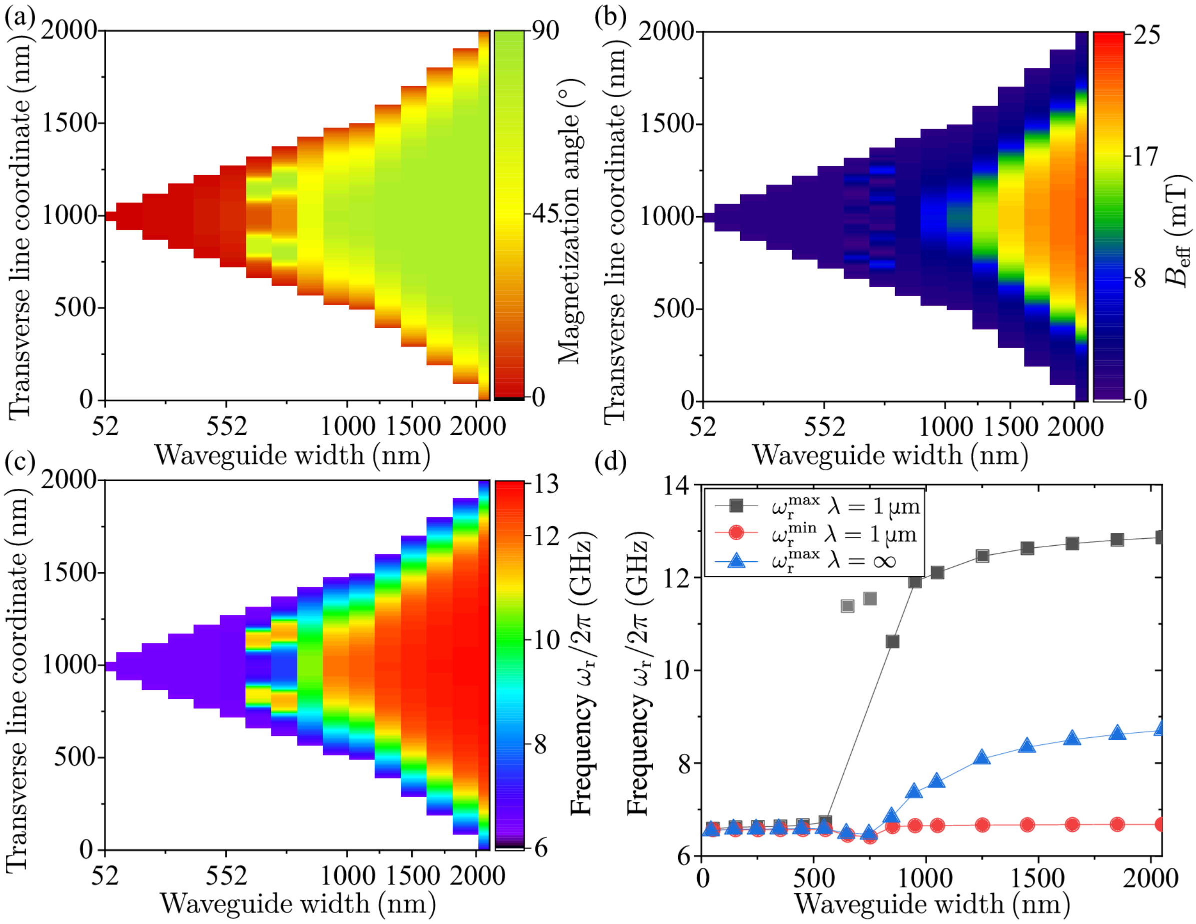

Fig. 4.4: (a) Longitudinal average of the magnetization angle calculated through the width of the waveguides with different nominal widths. (b) Longitudinal average of the calculated magnitude of the effective field extracted from the simulations. (c) Calculated local spin-wave dispersion for a spin wave with a wavelength $\lambda = 1\,\mu$m. (d) Extracted minimal (red circles) and maximal (black rectangles) frequencies from (c) as a function of the waveguide width. The grayed out points originate in waveguides with non-homogeneous magnetization. For reference, we also show the calculated FMR frequencies (blue triangles). Please note, that graphs (a), (b) and (c) have a change of the x-axis (Waveguide width) scaling at the value 1000 nm.

smaller, the magnetization lies in the longitudinal direction. For waveguide width 652 nm and 752 nm, the magnetization is nonuniform and for 852 nm wide waveguide the magnetization almost fully lies in the transverse direction. The effective field obtained from the numerical treatment is shown in Fig. 4.4 (b). Initially, for small waveguide widths, it shows only very small values for the longitudinally magnetized wires. For the waveguide width 852 nm, the demagnetizing field is almost as strong as the anisotropy field resulting in the very small effective field observed. When going further with the waveguide width, the anisotropy field (invariant in the waveguide width) will overtake the demagnetizing field.

From the knowledge of the local magnetization direction and the magnitude of the effective magnetic field [the magnetization in a static case has to follow the effective magnetic field direction and thus we omit the cosine term in the dispersion (1.58) (page 27)], we calculated the spin-wave dispersion [see Fig. 4.4 (c)]. For the spin-wave wavelength $\lambda = 1\,\mu\mathrm{m}$, the dispersion follows mainly the local magnetization angle. The maps in Fig. 4.4 (a) and Fig. (c) show qualitatively the same features. For large spin-wave wavelengths, the $\mu_0 M_\mathrm{S} P$ term from (1.58) becomes small and the spin-wave dispersion map resembles more the effective field distribution from Fig. 4.4 (b) (data not shown). We have also analyzed the maximal/minimal frequency of the waveguide by finding the maximum/minimum frequency through the width of each waveguide. Fig. 4.4 (d) clearly shows that the minimum frequency is not highly affected by the waveguide width. The maximal achievable frequency depends highly on the angle of the magnetization and thus also depends highly on the waveguide width. For waveguides wider than the reorientation width, we see only small variation of the spin-wave frequency through the waveguide widths. For the long-wavelength limit of the ferromagnetic resonance, the maximum calculated frequency varies more strongly with the waveguide width when compared to the case of spin wave with wavelength $\lambda = 1\,\mu\mathrm{m}$.

For the waveguides, where the width is sufficiently large to keep the magnetization in the transverse direction, the spin-wave reorientation region on the edge of the waveguide lowers the total waveguide width from the nominal width. This can be easily quantified. We present two means of quantification. In the first approach, we analyze the transverse magnetization profiles and we search for the distance from the edge, where the magnetization reaches $1 - 1/\mathrm{e} \sim 63\,\%$ of the maximum value in the line profile. By this distance, we can quantify the edge region width. By subtracting double of this distance from the nominal width, we can obtain the width of the waveguide region where the magnetization is quasi-uniform – the waveguide core. Same procedure we have performed for the width profile of the spin-wave dispersion (local spin-wave frequency). The results of both procedures are in Fig. 4.5.

The edge region width dependence from the Fig. 4.5 (a) shows a small variation with the waveguide width. Only close to the reorientation width 852 nm the edge region width slightly increases. The core width very closely resembles the waveguide width only with a small negative offset. The analysis of the spin-wave dispersion in the Fig. 4.5 (b) shows the opposite trend. Again, the edge region width is almost constant and only for the waveguide with the width 852 nm we observe a decrease in the edge region width. From the spin-wave frequency distribution, the waveguide with width 852 nm shows the smallest variation of the spin-wave frequency through the width. The different trends of both graphs suggest that even if the M_y component of the magnetization decreases more rapidly when approaching the edge of the waveguide in narrower structures, it is not directly translated to the spin-wave dispersion. It tends to be more homogeneous

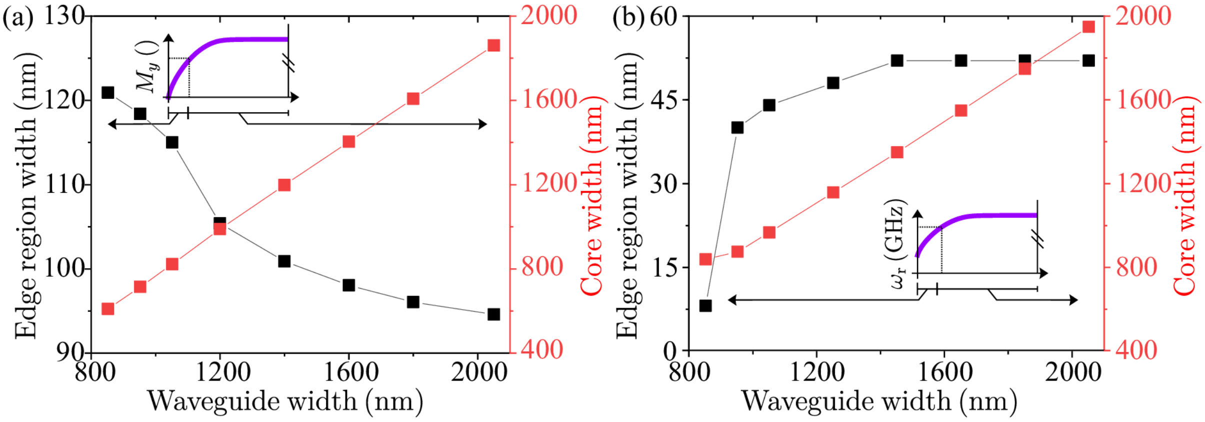

Fig. 4.5: (a) The quantified edge region and the core width as a function of the waveguide width obtained from the M_y width profiles. The edge region is defined as the region where $M_y \leq M_y^{\max}$. Sketch shows schematically the definition of the two distances. (b) Similar analysis that was obtained by analyzing the local spin-wave dispersion from Fig. 4.4 (c). The edge region is defined as the region where $\omega \leq \omega^{\max}$.

when compared only to the transverse magnetization component. This is a rather good feature of the spin-wave waveguide physics that even if the magnetization on the edges of the waveguide realigns along the waveguide edges, the effective width of the waveguide does not significantly vary from the nominal one. Since our methodology relies on the optical methods, both predicted dependencies in Fig. 4.5 cannot be simply measured due to the limited optical resolution.

As the last step of the micromagnetic modeling, we have analyzed the hysteresis loops of the simulated waveguides. For each waveguide, we have simulated two hysteresis loops. First with the longitudinal magnetic field (along the long axis), and second loop with the external magnetic field in the transverse direction. We have afterward analyzed the anisotropy field of the structures, and also the coercive fields (for definitions see Fig. 1.7 on page 17). As we follow the reorientation of the anisotropy axis, we analyze the coercive fields and the anisotropy fields always in the relevant orientations of the magnetic field concerning the anisotropy direction of each waveguide. The analysis is depicted in Fig. 4.6.

The figure Fig. 4.6 (a) clearly shows the strong dependence of the anisotropy field for the smallest structures. Above the anisotropy reorientation width, we first see a linear increase in the anisotropy field up to the saturation value $\sim 20\,\mathrm{mT}$. The results of this analysis coincide with the simulated demagnetizing field presented in the right graph of Fig. 4.3 when we consider, that the effective anisotropy field (fitted value from the simulations) in this particular case is given by the difference of the anisotropy field (coming from the magnetocrystalline anisotropy) and the demagnetizing field (in Fig. 4.3 we see a decrease in the demagnetizing field for higher waveguide widths, whereas in Fig. 4.6 (a) we see the increasing value of the effective anisotropy field value). Here we note that also the increasing spin-wave frequency with the waveguide width [Fig. 4.4 (c)] can be fully explained by increasing the effective anisotropy field value. The Fig. 4.6 (b) shows the coercive field extracted from the simulations for the magnetic field rotated by 90°. For lowest waveguide widths it swiftly diverges (following the anisotropy field from the left graph of the same figure) yet already for waveguides with width 352 nm the coercive field approaches 2 mT and stays constant. After the reorientation width, the coercive field increases up to the maximum value of 8 mT observed for the widest waveguide.

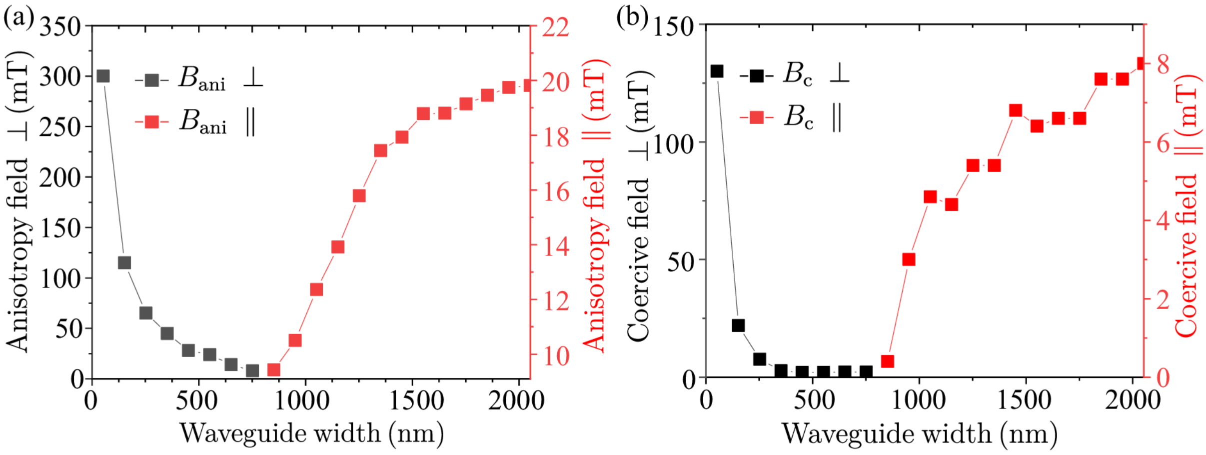

Fig. 4.6: (a) The graph of the the simulated anisotropy field obtained by fitting the hysteresis curves by the model from (3.3) (on page 83). (b) The graph showing the coercive fields obtained from the loops where the field was perpendicular to the field used in the left graph. Black data points show the data obtained for the external magnetic field parallel to the waveguide long axis. The red points show the case where we oriented the external magnetic field perpendicular to the waveguide long axis.

The results in Fig. 4.6 show the stability of the longitudinal/transverse magnetization for waveguides with a different width. The measure of the stability of the magnetization is the coercive field obtained in the relevant direction. We mentioned in the introductory part the rather extrinsic character of the coercive field which is also seen in the simulations by the non-monotonic character of the coercive field data. In theory, it should follow the anisotropy field strength. The qualitative agreement is found from the simulations, yet even for an in-theory perfect system, we observe stochastic behavior.

The purpose of this section dedicated to the micromagnetic simulations was to predict the behavior of the magnonic waveguides for relevant magnetic constants and achievable geometrical parameters. In conclusion, when the zero-field spin-wave propagation is of the interest in the Damon-Eshbach geometry, the limiting waveguide width is approx. 800 nm.

4.1.4. Magnetostatic characterization of the waveguides

In chapter 3, concerned with the material characterization, we have shown the possibility to grow long and narrow waveguides (see e.g. Fig. 3.6 on page 61). Subsequently, we have found the possibility to define the direction of strong uniaxial magnetic anisotropy. The anisotropy is strongest in four directions of the crystal reaching almost 30 mT. Previous section 4.1.3 helped us to estimate the behavior of ideal waveguides. The purpose of this section is to verify the findings of the micromagnetic treatment and to pre characterize the waveguides prior to the dynamic experiments in the GHz range.

We have irradiated number of rectangular regions (magnonic waveguides), transforming the regions into the magnetic bcc phase. All waveguides have nominal length of 30 μm and the nominal width of the waveguides is varied from 100 nm to 3 μm. We oriented the long axis of the waveguides along the fcc [0 1 0] and fcc [1 0 0] direction of the Cu substrate in order to obtain the highest possible magnetocrystalline anisotropy (see Fig. 3.17). To imprint the anisotropy direction perpendicularly to the long axis of the waveguide, we wrote the structures with a single pass of a 30 keV Ga^+ ion beam (30 nm spot, beam current 150 pA and 5 µs dwell time) with the fast scanning direction rotated by 80° from the waveguide's long axis. In the first step, we have performed the ion dose test (analogous to the one presented in Fig. 3.5) for waveguides of different widths. The nucleation of the bcc structure was facilitated by starting the growth in a triangular 5 µm wide region (seed region) with the ion dose of 8×10^{15} ions/cm^2 (in a single FIB scan). This slightly modified design of the growth initiation region, when compared to previously presented seed region design (see Fig. 3.6 on page 61)), is much smaller yet has proved itself as a reliable feature allowing initiation of the growth, even for the smallest waveguides. The dose test of different waveguide widths together with a modified seed region is shown in Fig. 4.7 (a).

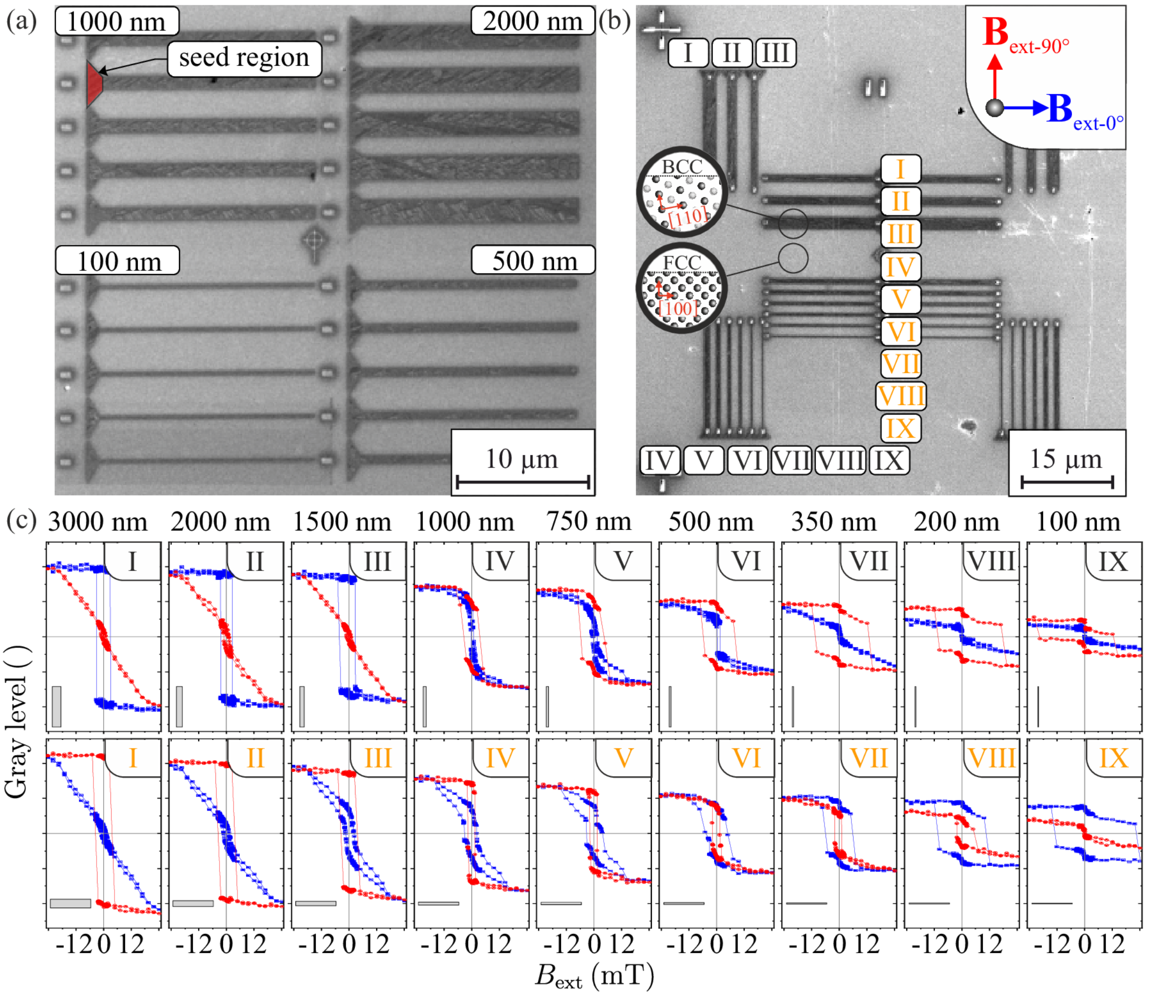

Fig. 4.7: (a) SEM image under the small tilt of the ion dose test of the waveguides with various widths. The ion dose is varied from top to bottom between $4 - 8 \times 10^{15}$ ions/cm^2 in equidistant steps. (b) SEM image (normal incidence) of the full set of waveguides. All waveguides are duplicated between the left/right half. The directions interconnecting the SEM image with the measured hysteresis loops are indicated in the top right corner. The crystallographic orientations of the fcc matrix and bcc waveguides are indicated (for the latter, inferred from the magnetic anisotropy). (c) Set of measured hysteresis loops for the vertical [black numbers in (b)]/horizontal (orange numbers) waveguides measured for two orientations of the external magnetic field. The widths of the waveguides are shown above each column. The external magnetic field was swept from −25 mT to 25 mT.

We have confirmed the reliable growth conditions for the waveguides of all widths at the ion dose 4×10^{15} ions/cm^2 and the initiation ion dose to 8×10^{15} ions/cm^2. After this elementary step, we have performed the transformation of multiple waveguides for two perpendicular orientations of the waveguides, while always keeping the imprinted magnetocrystalline anisotropy axis perpendicular to the waveguide long axis. The waveguides shown in Fig. 4.7 (b) are again clearly visible in the SE contrast. At each beginning/end of the waveguide, we milled alignment marks allowing to localize the waveguide in Kerr microscope and in µBLS. In the corners of the view field, we also see milled alignment marks for the subsequent electron beam lithography step. All waveguides seen in the left half of the image have been doubled to the right side to verify the consistency of the writing process.

After the transformation, the sample was brought ex-situ to the Kerr microscope, where we recorded Kerr images in the external magnetic field in the full field cycle from -25 mT to 25 mT and back. In the post-processing software, we have carefully defined the regions of the individual waveguides with the help of the milled alignment marks. Due to the slight magnetic field dependent drift of the whole image, we have artificially enlarged the areas in the drift direction so that the waveguide always stays in the analyzed region. By analyzing the magnetic field dependence of the mean grey level in individual areas enclosing the waveguides, we obtained the hysteresis loops of individual structures [blue curves in Fig. 4.7 (c)]. The sample was then rotated by 90° and the same analysis was performed again [red curves in Fig. 4.7 (c)].

The first evident effect of the waveguide width is the lowering of the maximum Kerr signal. The origin of this effect does not arise from the magnetic properties of the waveguides. The origin of this trend lies in the selection of the analyzed area filling factor of the magnetic structure and thus its cause can be tracked to the postprocessing of the data. We have attempted to avoid this by analyzing the maximum/minimum signal in each pixel effectively limiting the selection of the region of interest. Due to the large noise at a single-pixel level, this proved to be very problematic and unreliable.

When comparing the hysteresis loops from the vertical waveguides with their horizontal counterparts, we can directly see, by comparing the top/bottom row in Fig. 4.7 (c), the very similar behavior of the structures with the same width. This means that the horizontal set of waveguides is similar to the vertical set of waveguides only rotated by 90°.

The vertical set of waveguides [top row in Fig. 4.7 (c)] shows very nice uniaxial behavior of the 3000, 2000 and 1500 nm wide waveguides. Contradictory to the shape anisotropy requirements, we see a clear easy axis loop for the magnetic field oriented transverse to the long axis of the waveguides. The coercive fields of ~ 5 mT are observed and the loops show full remanence at zero field. When the field is oriented along the waveguide long axis, we can identify clear hard axis behavior with anisotropy fields in the range $20-25$ mT and no remanent magnetization in the applied field direction. At the waveguide width 1000 nm, we see a reorientation of the anisotropy axis. The blue curve (measured along the imprinted anisotropy direction) does not show any significant remanence of the magnetization at zero field, whereas the red loop shows remanence reaching 75 % of the saturation value. The nonequivalent ascending/descending branch of the curve with different coercive fields shows the formation of the domain structure. The blue curve resembles the hard axis behavior with a very low anisotropy field. Similar behavior is observed also for 750 nm wide waveguide, where the effects of the domain structure formation are even more pronounced (step in the blue curve at the positive field). At waveguide width of 500 nm, the blue curve shows a step near-zero field, yet we can also identify the anisotropy field at ∼ 20 mT. This shows that, most probably, we still observe a certain effect of the micromagnetic structure being induced near the zero-field, yet overall the structure follows the hard axis behavior. This is even more pronounced in 350 nm wide waveguide with the difference of smaller step-like behavior near zero-field. For 200 nm and 100 nm wide waveguides, the hard axis loop does not even reach the full saturation seen in the easy axis loop. The magnetic field was not sufficiently large to saturate the waveguide in the hard axis direction. From the slope of the curve and the level of the signal in the easy axis loop, we can still estimate the anisotropy field. Both easy axis curves show unbalanced coercive fields that are here attributed to the stochastic pinning of the magnetization during the switching process (visible in the Kerr images).

The horizontal set of waveguides show initially similar behavior. Importantly, the 1000 nm and 750 nm wide waveguides still show the full remanence even for the field oriented along the imprinted anisotropy direction. The hysteresis loops measured in the field along the long axis show the hard axis loop with a slight opening at zero field (formation of the domain structure). Narrower waveguides do not exhibit very apparent hard axis loops, yet the easy axis loops keep almost full remanence in zero external field. To relate the experimental observations to the micromagnetic simulations in Fig. 4.2 and the right panel of Fig. 4.6, we have extracted the important parameters from the measured hysteresis curves and we present them in Fig. 4.8.

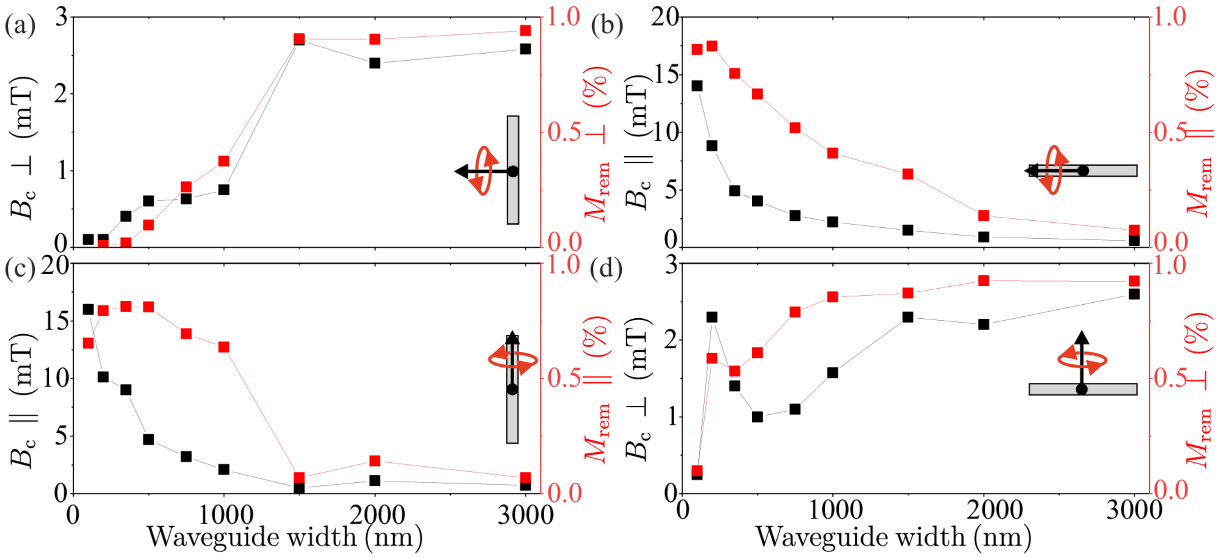

Fig. 4.8: Extracted parameters from hysteresis loops presented in Fig. 4.7. (a) Coercive field and remanent magnetization for the vertical waveguides and perpendicular magnetic field. (b) Horizontal waveguides and parallel magnetic field. (c) Vertical waveguides and parallel magnetic field. (d) Horizontal waveguides and perpendicular magnetic field.

The measured data show the expected behavior (also supported by micromagnetic simulations). When we apply the field along the imprinted anisotropy direction of the waveguides, where the width is above the reorientation width [Fig. 4.8 (a) and Fig. (d)], we see full remanence and coercive fields of approx. 3 mT. For lower waveguide widths, we see a strong decrease of the coercive field and the remanence as we apply the external magnetic field in the hard axis of the system. When the field is in the waveguide long axis direction the behavior is opposite. For the widest waveguides, the remanence and the coercive field approach zero [Fig. 4.8 (b) and Fig. (c)]. Below the reorientation width, the remanence increases to almost 100% and the coercive fields reaches 15 mT for the narrowest structures.

When comparing the absolute values obtained from the simulations to those extracted from the measurement, we see a good agreement in the remanent magnetization. In the case of the coercive field, the trend is again nicely reproduced in the simulations, yet the absolute values in the experiment are much lower to those obtained from the measurement. This is true especially for the narrowest structures. The simulations overestimate the value of the coercive field by approx. 2×. This behavior is also anticipated from the extrinsic nature of the coercive field, since the micromagnetic model assumes "perfect" rectangular waveguide without any defects, where the magnetization reversal can nucleate. We note that the magnetization reversal mechanism also highly depends on the boundary conditions of the magnetization, highly influencing the creation of the demagnetizing field. We have seen in the SEM analysis of the narrowest waveguides (see Fig. 3.6) a measurable far spanning halo (in the transverse direction). It is expected that the surrounding of the desired pattern will also be irradiated by the tail of the FIB, resulting in the partial transformation of the surrounding material. This will result in the gradient of the magnetization in the transverse direction from the nominal edge of the waveguide. This will inevitably change the distribution of the demagnetizing field and also magnetization switching properties of the waveguides. Such an effect will change the magnetic properties of the whole structure, yet is very hard to quantify as it would be extremely challenging to directly observe the gradient of the magnetization experimentally by any means available[2]. We can see only indirect effects resulting in e.g. altered switching behavior of the waveguide. Despite its importance for the stability of the magnetic order in an external magnetic field, the coercive field is again considered as a measured quantity that does not give great insight into the intrinsic magnetic properties of the waveguides.

The anisotropy field is a more reliable parameter given mainly by the intrinsic factors. Similarly to the data in Fig. 4.6, we have fitted the hysteresis curves with a hard axis hysteresis model from (3.3) (on page 83). Fig. 4.9 presents the evaluated data of the anisotropy field as a function of the waveguide width.

The experimental data show a considerable difference between the horizontal and vertical sets of waveguides. Though it was already visible in the hysteresis curves, the evaluated anisotropy field shows a factor of two difference in the anisotropy reorientation width. The horizontal set of waveguides shows a very nice resemblance to the calculated behavior shown in Fig. 4.6. In contrast to the micromagnetic model, we observe an anisotropy reorientation width at waveguide width 500 nm (the micromagnetic treatment estimated the value to 800 nm). The vertical set of waveguides also shows a similar trend with a reorientation width shifted to higher values (1000 nm). Contrary to the micromagnetic simulations, the absolute value of the anisotropy field is shifted to higher values (25 mT for the widest waveguides). The larger value of the anisotropy constant would explain the measurement of higher anisotropy field and thus would also support lower reorientation width as is seen in the horizontal set of waveguides. The vertical set of waveguides shows the same value of the maximum anisotropy field yet, the reorientation width is shifted to higher values. Below the reorientation width, the anisotropy field follows expected behavior. This discrepancy suggests a systematic error in the writing of all vertical waveguides and not a random error in the writing of a single structure in the set.

---

[2] Synchrotron based X-ray magnetic circular dichroism photoemission electron microscopy (XMCD-PEEM) would be the technique of choice for such an observation.

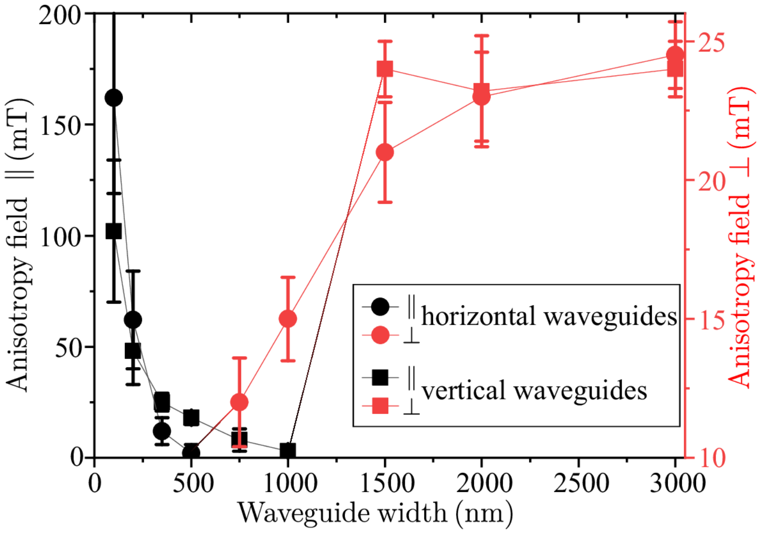

Fig. 4.9: Anisotropy field fitted from the loops presented in Fig. 4.7. The anisotropy field values obtained from the 100 nm and 200 nm wide waveguides are extrapolated from the slope of the hysteresis curve and the saturation value of the signal measured in the easy axis direction. The error bars are obtained from the confidence of the fit at the confidence interval 95 %.

When we consult the angular dependence of the uniaxial anisotropy strength from Fig. 3.17 (on page 82), we see a small yet apparent difference in the maximum anisotropy strength for two perpendicular FIB scanning direction. The vertical waveguides were written with the FIB scanning direction 10°. This direction shows lower achievable anisotropy field value (see Fig. 3.17). This might be a feasible reason for the systematic difference in two sets of waveguides.

In conclusion, the magnetometry analysis of the individual 30 µm long waveguides revealed experimentally the region of stability of the transverse magnetization configuration to waveguides with the nominal waveguide width 750 nm and higher. Those structures then exhibit full remanence when magnetized perpendicularly to the long axis of the waveguide and show the coercive fields in the range $1 - 3$ mT. The anisotropy field for this particular magnetization configuration varies between $12 - 25$ mT.

4.1.5. Spin-wave propagation in the waveguides prepared by the FIB direct writing

The purpose of this section is to show that magnonic waveguides allowing for fast spin-wave propagation at zero magnetic fields can be written directly by the FIB. As a spin-wave excitation source, we have selected a simple antenna design. At this point, we did not know the spin-wave dispersion nor the magnetic parameters of the system, and thus using a k-specific excitation as provided by e.g. coplanar waveguide would be rather risky. The antenna of suitable size can excite a vast range of spin-wave propagation vectors. We have fabricated the excitation antenna on top of the waveguides that were already presented in Fig. 4.7 (c). The FIB-written waveguides together with a microwave antenna for spin-wave excitation are shown in Fig. 4.10 (a).

The antenna is fabricated by electron-beam lithography with a subsequent liftoff process by using an electron positive resist based on poly(methyl methacrylate) (PMMA). The antenna consists of multiple layers prepared by physical vapor deposition (in the

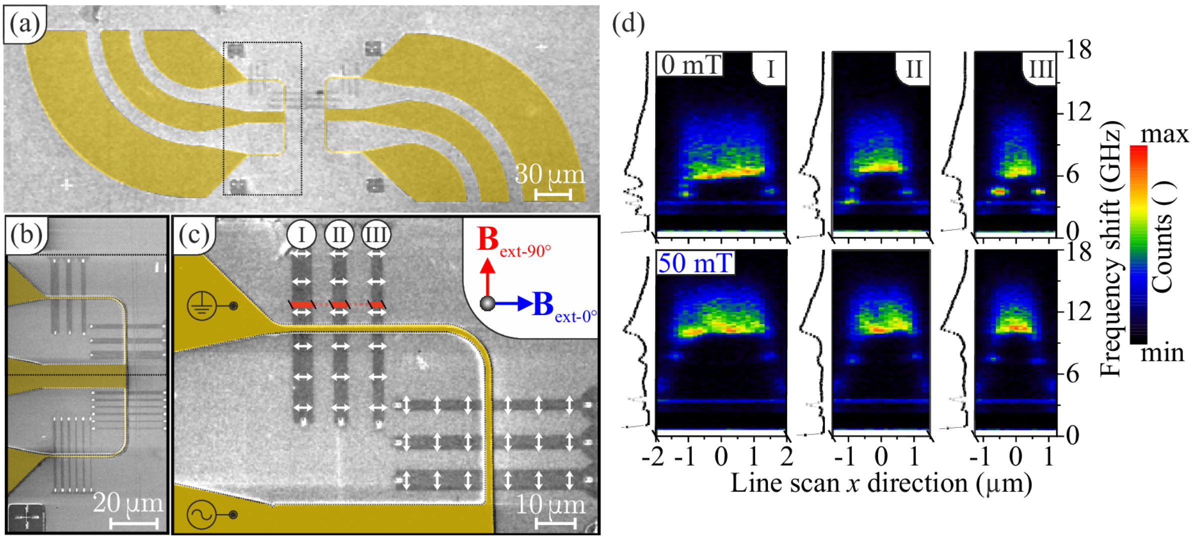

Fig. 4.10: (a) SEM overview image of the waveguides with overlaid microwave antenna (highlighted by ocher color). (b) Magnified image of the waveguides. c) Detail of the excitation antenna with the three widest waveguides. White double-headed arrows indicate the imprinted anisotropy direction. The signal and ground connections are indicated. (d) 2D frequency maps of the thermal spin-wave spectra measured by micro-focused BLS scanning over the waveguides in the transverse direction along the red lines in (c) in zero external magnetic fields (top row) and in an applied magnetic field $B_{\text{ext}-0^\circ} = 50\,\text{mT}$ (bottom row). The integrated spectra over the width of the given waveguide are presented to the left to the 2D frequency maps. The spatially and magnetic field invariant mode at approx. 3 GHz is a spurious laser mode.

electron beam evaporator). The full stack comprises of (starting from the iron layers) 5 nm Ti/ 50 nm SiO_2/ 5 nm Ti/ 85 nm Cu/ 10 nm Au. Both titanium layers increase the adhesion of the adjacent layers. The Ti layers are necessary to prevent the peeling of the deposited layers. The SiO_2 prevents the shorting of the microwave signal through the iron/copper. The main conductor is the copper layer capped with a gold layer (preventing oxidation). The shape of the coupling part of the antenna comes from the calculation assuring 50 Ω impedance. Even though we attempted to match the impedance of the coupling part to the source impedance 50 Ω, the narrow part of the antenna serving for spin-wave excitation will inevitably exhibit the impedance $\sim 100\,\Omega$. We aim for the wide k-excitation window translating to small widths of the antenna (see Fig. 1.15 on page 32). For a simple microstrip (antenna/spacer/ground) configuration, the decreasing antenna width causes the impedance to increases. This means simply that the coupling part does not have to be matched precisely to the ideal 50 Ω as the excitation part will always deteriorate the impedance of the whole system. The bent shape of the coupler allows contacting the antenna by 50 µm-pitch microwave probe in 90° span. This allows us to study spin-wave propagation in different magnetic field orientations (the magnetic field and excitation probe orientations were fixed in all used experimental setups and thus only the sample could be rotated to achieve different measurement configurations).

As a first experiment, prior to the active excitation of the spin waves by microwave antenna, we have measured the thermal spectra of the waveguides while changing the external magnetic field. In addition, we have scanned the sample under the laser spot and recorded the BLS spectrum every 200 nm (mirror distance 5 mm, 500 scans of the TFPI per step). The direction of the scanning was transverse to the long axis of the waveguides. This allows us to probe the local density of states of the spin-wave system (see again Fig. 2.9 on page 49). The density of states is expected to spatially vary due to irregular local effective field as was presented in the micromagnetic model in Fig. 4.4. Since the local magnetic field in our case comprises of the anisotropy field, the demagnetizing field and also from the external magnetic field, the density of states can be controlled by the external magnetic field. When the field is parallel to the imprinted anisotropy, we expect the frequency of the spin-wave system to rise [see again (1.58) on page 27 for the $\alpha = \kappa$ case]. This is readily seen in Fig. 4.10 (d). The signal shows pronounced spin-wave spectral intensity localized solely in the areas irradiated by the FIB. The signal level directly suggests good spin-wave properties of the material (at least for the noncoherent excitations). The band gap of the spin-wave band structure for the center of the waveguide ($x = 0\,\mu\mathrm{m}$) can be clearly seen as a sudden increase in the density of spin-wave states for frequencies higher than approx. 6 GHz in zero fields and at approx. 10 GHz in the external field of 50 mT. All three waveguides show qualitatively the same behavior. The data also reveal the local change in spin-wave spectra towards the sides of the waveguide. Here, localized low-frequency modes appear at approx. 4 GHz in zero field and at approx. 8 GHz in the external field of 50 mT. This is a clear indication of the successful transverse orientation of the magnetization and its inherent demagnetizing field, leading to lower effective fields at the waveguide edges and thus directly resulting in the localized spin-wave edge modes [157, 158]. The overall analysis is depicted for three vertically oriented waveguides only. The horizontally oriented waveguides show qualitatively the same behavior (the anisotropy is again imprinted perpendicular to the long axis of the waveguides). This also demonstrates the unique potential of our approach when compared to other less versatile approaches or materials with spatially invariant global magnetocrystalline anisotropy.

The previous experiment has proved that the system can exhibit a rich spin-wave response and also revealed a set of frequencies feasible for the spin-wave excitation. In the following experiment, we have contacted the prepared antenna by the microwave probe and assured a good contact of the microwave probe to the antenna by measuring the resistance of the antenna on a bias tee. Readings of approx. 20 Ω were observed. Due to mechanically soft Cu antenna and also the Cu substrate, it was possible to contact the antenna in one spot only once, and thus the number of recontacting trials was highly limited. The number of experiments we were able to perform was given by the need to repeatedly recontact the antennas fabricated on the structures of interest. After contacting the high-frequency probe and verifying good contact, we have started to actively pump the high frequency signal from the RF source to the antenna (see again the μBLS schematic in Fig. 2.10 on page 51). At this point, the microwave switches were in such a configuration that only the antenna was connected to the RF source and the EOM was turned off. We have focused on 1.5 μm wide waveguide, as in both the horizontal and vertical structures, the waveguides showed full remanence and high effective anisotropy fields (Fig. 4.8 and Fig. 4.9).

For the vertical waveguide (and the magnetic field $B_{\mathrm{ext}-0^\circ}$ oriented perpendicular to the waveguide long axis) we have fixed the laser spot approx. 3 μm from the excitation antenna (in the waveguide core). The positioning stability was assured by the image stabilization software. For a given RF power 0 dBm we have swept the frequency of the RF source in 100 MHz steps. For each excitation frequency, we have measured the μBLS spectra. The 2D frequency-frequency map is presented in the left panel of Fig. 4.11.

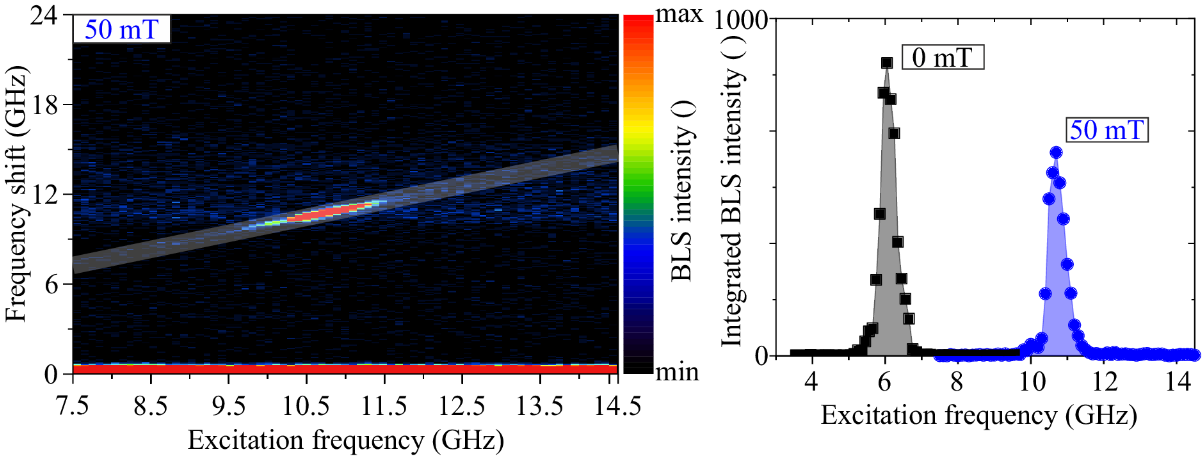

Fig. 4.11: Left panel presents the 2D map of measured μBLS spectra for different RF excitation frequency at the external field $B_{\mathrm{ext}-0^\circ} = 50\,\mathrm{mT}$. The semi-transparent line has a slope of 1 and serves as an integration region (along the horizontal axis) for the graph in the right panel. Herein we present the integrated counts in the region given by the semi-transparent line region. The right panel can be understood as a measurement of the excitation efficiency of the spin-waves at a given frequency and field.

The 2D map measured at the external field $B_{\mathrm{ext}-0^\circ} = 50\,\mathrm{mT}$ shows a distinct peak slightly below 11 GHz. A closer look at the 2D map shows an excitation frequency invariant signal with an onset at $\sim 10\,\mathrm{GHz}$. The low-intensity signal comes from the thermal spin waves [see again Fig. 4.10 (d)]. The position of the peak nicely corresponds to the thermal spin-wave spectra with a slight shift to the higher frequencies (the antenna excites mainly the modes with non-zero k). The formation of the peak in the observed spectra is a rather complex process. The observed signal is given by the spin-wave density of states, the excitation efficiency of the antenna and also by the detection efficiency of the µBLS method. Simply said, the peak in the map highlights the frequency of the highest excitation efficiency of the spin-wave system. The spectra also show that the excited spin waves are in a linear regime as no higher/lower order modes are seen in the spectra [159]. The detected frequency of the excited spin waves is very close to the excitation frequency. In reality, there can be a small offset between the measured and the frequency of excitation. In most cases, it will be given by the inertia of the TFPI piezo scanner. The inertia effects are highly influenced by the selection of the T factor parameter of the interferometer. The T factor changes the measurement time per frequency bin and thus changes the scanning speed of the TFPI stage. This is the most trivial cause of the excitation/detection offset and also of the frequency asymmetry between the Stokes and anti-Stokes peaks. In systems with Dzyaloshinskii-Moriya interaction, the Stokes/anti-Stokes asymmetry can be also caused by the chiral interaction [124].

To determine the RF frequency at which we excite the spin waves with the maximum efficiency, we integrated the BLS intensity along the line with a slope ~ 1 (adjusted so the semi-transparent line in the left panel of Fig. 4.11 is along the peak in the 2D map). We have repeated the same procedure for zero external magnetic field. Highly apparent peaks are seen in the right panel of Fig. 4.11. The zero-field case is downshifted in the frequency when compared to the external magnetic field $B_{\mathrm{ext}-0^\circ} = 50\,\mathrm{mT}$. The maximum signal in the zero field is at the RF frequency 6.1 GHz and for the 50 mT the frequency rises to 10.7 GHz. Both RF sweeps exhibit only small contribution from the higher-order modes. This is seen in the asymmetry of the peaks. The higher-order modes, in this case, arise mainly from two sources. The waveguide itself can exhibit more modes (see again Fig. 1.14) and also the microwave antenna has a higher excitation maximum (Fig. 1.15). As mentioned earlier we measured the spin-wave intensity approx. 3 µm from the excitation antenna. The resonance condition was found for a frequency higher than the FMR frequency. This rules out far-field excitation and thus confirms successful spin-wave propagation up to 3 µm and possibly further. This is observed also for the case of zero field. This elementary experiment immediately shows the possibility to propagate spin waves in our material. Additionally, the propagation is also possible even at zero external field. To our knowledge, there is no other material with FIB induced nonmagnetic-magnetic phase transition allowing spin-wave propagation.

In the following experiments, we extract the magnetic field-dependence of the spin-wave dispersion relation [160]. By fitting the measured dispersion, we are able to obtain the full set of magneto-dynamic parameters of the material. The standard µBLS method does not directly sense the phase of the detected spin waves and, thus it does not allow to determine the wavelength (or equivalently the wave propagation vector k) of the spin waves. In order to extract the wave vector information, we employed the phase-resolved µBLS technique as described in section 2.2.2. The method directly reveals the spatial profile of the spin-wave phase by letting the scattered photons interfere with a reference signal of a constant phase created by an electro-optic modulator. Before the actual experiment with the EOM is performed, it is a good practice to match the spin-wave intensity to the EOM intensity at a certain distance from the excitation antenna. This is done in a way, that the laser spot is positioned again few micrometers from the excitation antenna and first only the spin-wave systems is excited with the antenna. We monitor the BLS counts at the excitation frequency. Afterward, the microwave switches are switched to such a configuration that only the EOM is connected to the RF source. We again observe the

BLS intensity. At this stage, it is given only by the spatially invariant EOM signal. We reduce the EOM signal by the attenuator to match it to the spin-wave intensity measured in the previous configuration. After we have done so, we switch both the EOM and the microwave excitation antenna to the active status, and by changing the phase shift on the phase shifter (delay line), we can minimize or maximize the signal at a given point by introducing the constructive or destructive interference.

In the actual experiments, we have recorded the interference signal along the 1.5 µm wide waveguide (at $x = 0\,\mu\mathrm{m}$) with a step size of 120 nm. We have scanned the waveguide from the edge of the exciting antenna up to 7 µm distance. The excitation frequency was set to 10.2 GHz. Before we performed the line scan with the above-mentioned parameters, we have tested multiple excitation frequencies. Though we were able to maximize/minimize the signal by changing the phase shifter, we did not see clear beating pattern, as presented in Fig. 2.11 (on page 52). The large wavelength of the excited spin waves was higher than the measurement range, and thus we did not see beating pattern. From the relative field-induced shift seen in the excitation efficiency plot and also from the zero-field frequency (and also from the data measured with thermal spin waves), we were able at this point to roughly estimate the magnetic parameters of the material and thus to estimate the dispersion of the waveguide. From the preliminary dispersion calculation, we estimated that the spin wave with 1 µm wavelength will be excited between 9 GHz and 11 GHz at zero external field. When looking at the excitation efficiency plot in the right panel of Fig. 4.11, the selection of the frequency is far from the optimal excitation/detection frequency. At 10.2 GHz we see almost no excitation. Yet when we look at the thermal spectra in Fig. 4.10 (d), we see a nonzero signal at 10 GHz. This means that the excitation efficiency plot in Fig. 4.11 is given mainly by the excitation efficiency of the microwave antenna. The calculated excitation efficiency in Fig. 1.15 (on page 32) shows a cutoff k-vector at $1\,\mu\mathrm{m}^{-1}$. The reasoning behind choosing 10.2 GHz is that despite its low excitation efficiency, we were able to directly observe the beating pattern in the line scan. We have extended directly this experiment by acquiring the line scans for different external magnetic fields. We measured the BLS interference line scans with an applied external magnetic field (perpendicular to the waveguide long axis) from 0 to 15 mT. The phase-resolved measurements are shown in Fig. 4.12. The BLS interference intensity map in Fig. 4.12 (a) shows a gradual transition of the spin-wave wavelength from the lowest value found at zero field up to the longest wavelengths at 15 mT. This is additional evidence for the presence of the Damon-Eshbach geometry even at zero field, since otherwise a decrease in wavelength with the increasing field would be expected from the spin-wave dispersion. To extract the spin-wave wavelength, we fitted the measured data with the simple interference model presented in (2.22) (on page 51). Fig. 4.12 (b) shows a nice correspondence of the measured data with simple model. This allowed us to extract the longitudinal spin-wave wavelength (from the symmetry of the problem defined by the scanning direction only the propagation vector along the waveguide long axis can be measured) dependence on the magnetic field. Afterward, we have performed a similar experiment for different excitation frequencies (and again we changed the external magnetic field). For each frequency, the RF power going to the EOM needs to be adjusted as the EOM efficiency highly depends on the RF frequency. For the magnetic field dependence it is stable and does not have to be adjusted. By repeating the experiment multiple times in the frequency and external magnetic field space, we can point-by-point build the dispersion of the system. The spin-wave wavelength dependencies are plotted in Fig. 4.13.

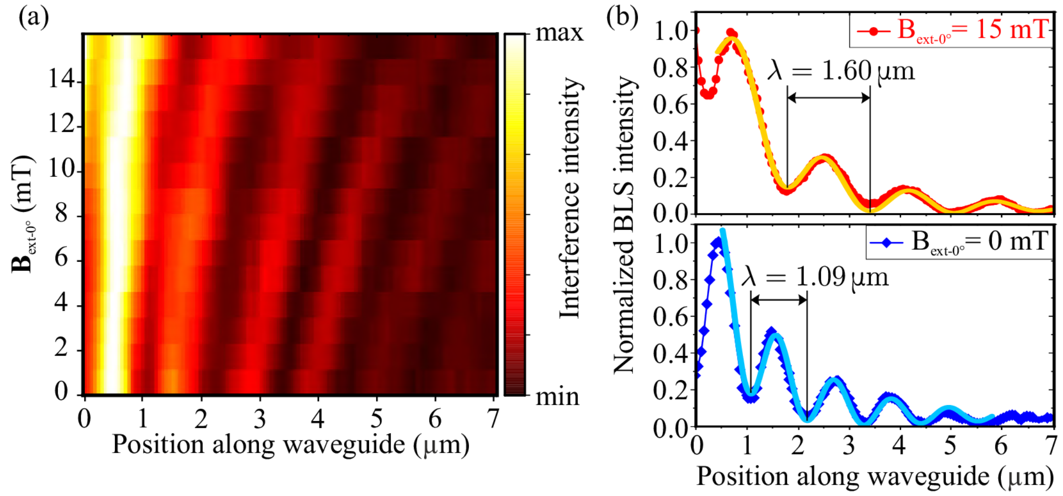

Fig. 4.12: (a) Phase-resolved μBLS microscopy interference intensity map for various external magnetic fields at the fixed excitation frequency of 10.2 GHz. Individual line scans have been normalized and a space-invariant background was subtracted. (b) Line profiles extracted from the intensity map for 15 mT (red circles) and for zero external magnetic field (blue squares). Overlaid continuous lines are fitted curves calculated with (2.22). The wavelength schematically denoted in the line scan graphs is obtained from the fit.

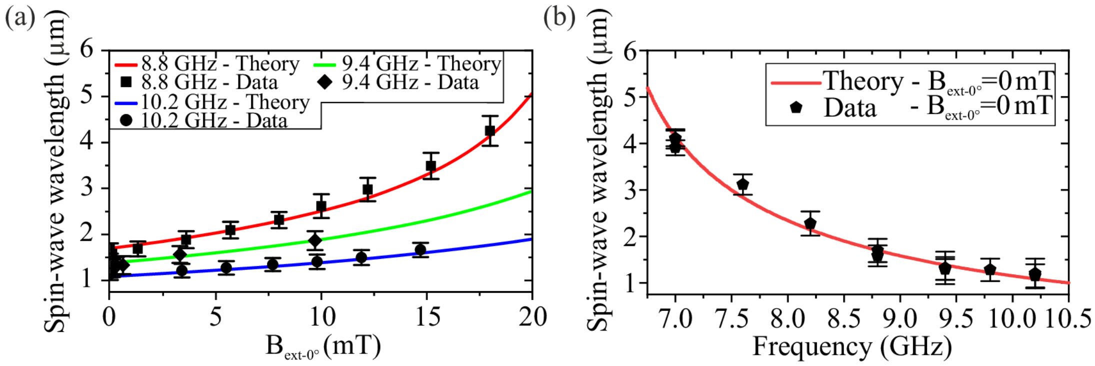

Fig. 4.13: (a) Dependence of the spin-wave wavelength λ on the external magnetic field for three different RF frequencies. (b) Extracted zero-field wavelength dependence for multiple RF excitation frequencies. Details on the fitted theoretical curves in both (a) and (b) are given in the text. The error bars have been calculated from the 95% fit confidence intervals.

Clearly with the increasing external magnetic field, the spin-wave frequency also increases as was indisputably presented in Fig. 4.12. Increasing the spin-wave frequency has the opposite trend. Fig. 4.13 (a) shows the smallest spin-wave wavelength of $\lambda \sim 1\,\mu\text{m}$ measured for the highest frequency. Apparently, we were able to tune the spin-wave wavelength both by the external magnetic field and by the RF frequency between $1\,\mu\text{m}$ measured in zero external field and at the RF frequency 10.2 GHz and $4.3\,\mu\text{m}$ at the frequency 8.8 GHz. In Fig. 4.13 (b) only the zero-field case measured in the frequency range $7 - 10.2$ GHz is presented.

The data in Fig. 4.13 offers great insight into the spin-wave system in our material, as when fitted with a suitable model, it will yield the magneto-dynamic parameters. We used the model (1.58) introduced in chapter 1. The finite width of the waveguide was considered, by assuming the effective boundary conditions as described by Guslienko et al. (1.62). For the spin-wave dispersion model, we assumed that the external magnetic field $B_{\text{ext}-0^\circ}$ points in the direction of the magnetic anisotropy [see again (1.58) for $\alpha = {}$ $= \kappa$], i.e. perpendicularly to the long edge of the waveguide. We introduced the magnetic anisotropy in a form of effective magnetic field B_{A} (that is comprised of demagnetizing field and anisotropy field).

We performed the fit using (1.58) (page 27) [considering 95% confidence intervals obtained by fitting of the (2.22) (page 51)] for various width modes (and their linear combinations [157, 161]) with a single set of universal parameters, and we minimized the total residuals of the fit. The best fit was found using a single mode [$n = 1$ in (1.61)] only (in contrast to experiments in e.g. permalloy waveguides [157, 161]), with magnetic parameters of $M_{\text{S}} = 1.41 \pm 0.03\,\text{MA/m}$, $\gamma = 29.3 \pm 0.1\,\text{GHz/T}$, $B_{\text{A}} = 24 \pm 1\,\text{mT}$, $t = 9.5 \pm 1.0\,\text{nm}$, $11 \pm 5\,\text{pJ/m}$ and $1.62 \pm 0.05\,\mu\text{m}$ (the waveguide nominal width was $1.5\,\mu\text{m}$). The obtained fit parameters lie close to the bulk values of single-crystal iron films [162]. The saturation magnetization $M_{\text{S}} = 1.41\,\text{MA/m}$ is expectantly lower than the bulk value of iron ($M_{\text{S}}^{\text{Fe}} = 1.7\,\text{MA/m}$). If we consider 22 % of nickel ($M_{\text{S}}^{\text{Ni}} = 0.51\,\text{MA/m}$) in our films and assume a linear dependence on composition, we estimate the expected saturation magnetization to be $M_{\text{S}}^{\text{FeNi}} = 1.45\,\text{MA/m}$, which is very close to the value $M_{\text{S}} = 1.41\,\text{MA/m}$ obtained from the fit. The large saturation magnetization, together with the Damon-Eshbach geometry, results in a high group velocity of the spin waves reaching almost 6 km/s (see Fig. 4.14). To visually more relate the measured data in Fig. 4.13 to the calculated dispersion in Fig. 1.14, we again plot the spin-wave dispersion in Fig. 4.14 with a horizontal axis in the units of longitudinal propagation vector $k_\parallel$.

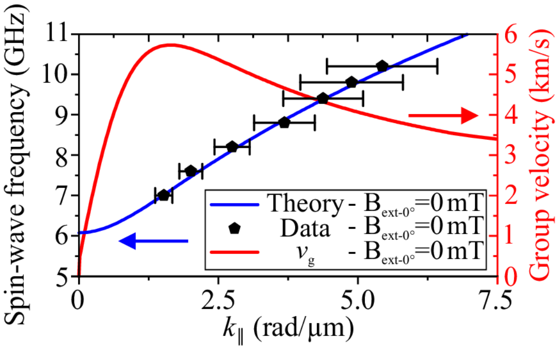

Fig. 4.14: Experimental (black pentagons) and calculated (blue line) spin-wave dispersion together with the calculated group velocity (red line) at zero external magnetic field. The error bars have been calculated from the error bars in Fig. 4.13 (b) by the propagation of uncertainty calculated from the equation $k_\parallel = 2\pi/\lambda_\parallel$.

The anisotropy field resulting from the fit reproduces the value measured by Kerr microscopy. This further supports the validity of the model. The fitted thickness is very close to the nominal thickness of 12 nm (the few topmost layers are expected to oxidize when performing ex-situ experiments), which indicates that the film is transformed to the magnetic bcc phase throughout the whole thickness (see SRIM/TRIM calculations in Fig. 3.1 presented on page 56). The width of the waveguide 1.62 µm is slightly larger than the nominal value 1.5 µm. First, and presumably, the major contribution increasing the width of the waveguide is the finite size and shape of the focused ion beam spot. Furthermore, in our previous work [163], it was shown that the bcc crystallites protrude to the fcc phase slightly further from the ion impact spot and thus they again effectively increase the width of the waveguides (the protrusion length is approx. 50 nm). Both effects effectively create a gradient in the magnetization affecting the dynamic boundary conditions of our waveguides [164], which differs from the discontinuous boundary conditions found e.g. in structures prepared by classical lithography techniques [157, 161]. Due to the gradient of the saturation magnetization, it is expected that the local spin-wave dispersion will differ from the discontinuous case where the saturation magnetization changes abruptly [164]. We performed micromagnetic simulations in mumax^3 [149] to study the effects of the magnetization gradient at the waveguide edges on the spin-wave dispersion.

In order to obtain the spin-wave dispersion of a magnonic waveguide with the continuous magnetic-nonmagnetic transition at the waveguide edges, we employed the procedure described e.g. in [165]. The solver mumax^3 allows us to define up to 256 regions, in which the material parameters can be individually defined. In our approach, the waveguide core has a constant value of the saturation magnetization M_S, whereas the edge regions have a saturation magnetization that decreases quasi-continuously from the maximum value of M_S to zero. Fig. 4.15 (a) depicts the geometry definition of the problem.

The spatial modulation of the saturation magnetization has been chosen in the form of a complementary error function because it resembles the convolution of nominal geometry with the spot of the focused ion beam (approximated by a Gaussian beam profile):

$$M_\mathrm{sat}(x) = 0.5 M_\mathrm{S} \mathrm{erfc}\left[\sqrt{2}\left(\frac{-x + x_\mathrm{edge}}{d}\right)\right], \tag{4.1}$$

with x_edge representing the offset of the error function to the edge of the waveguide and d being the Gaussian width of the transition. The width of the modulated part was selected as $4d$ in order to ensure the continuity of the magnetization on the transition inbetween the modulated part and the core part. The central core width w_core is lower than the nominal width $w_\mathrm{nominal} = 1.5\,\mu\mathrm{m}$ by $2d$ to make space for the edge region. The $x_\mathrm{edge} = 2d$ is measured from the core boundary. The total width of the simulation window is then $W = w_\mathrm{core} + 6d$. In this configuration, the magnetization at the nominal width has still 98% of the M_S [see schematic drawing in Fig. 4.15 (a)]. This definition of the problem avoids discontinuities of the saturation magnetization and does not create any unwanted artifacts in e.g. demagnetizing field. The discretization grid spacing was chosen as $\mathrm{d}x = 3.52\,\mathrm{nm}$, $\mathrm{d}y = 14.7\,\mathrm{nm}$ and $\mathrm{d}z = 9.5\,\mathrm{nm}$. The rather large value of $\mathrm{d}y$ is due to computational reasons, as for a good resolution in the reciprocal space (small step in $k_\parallel$) the simulated geometry needs to be rather large. The resolution of $k_\parallel$ is determined by $1/\left(n_y \mathrm{d}y\right)$, where n_y is the number of elements in the y direction. The resulting grid size with $d = 50\,\mathrm{nm}$ was 2048 points in y-direction and 512 points in x-direction. Thus, the simulated geometry was $30000 \times 1800 \times 9.5\,\mathrm{nm}^3$ large. For the simulations, we employed the material parameters obtained from the fit, namely M_S, and A_ex. For the sake of the simulation, we had to modify the anisotropy constant K_u derived from the measurement.

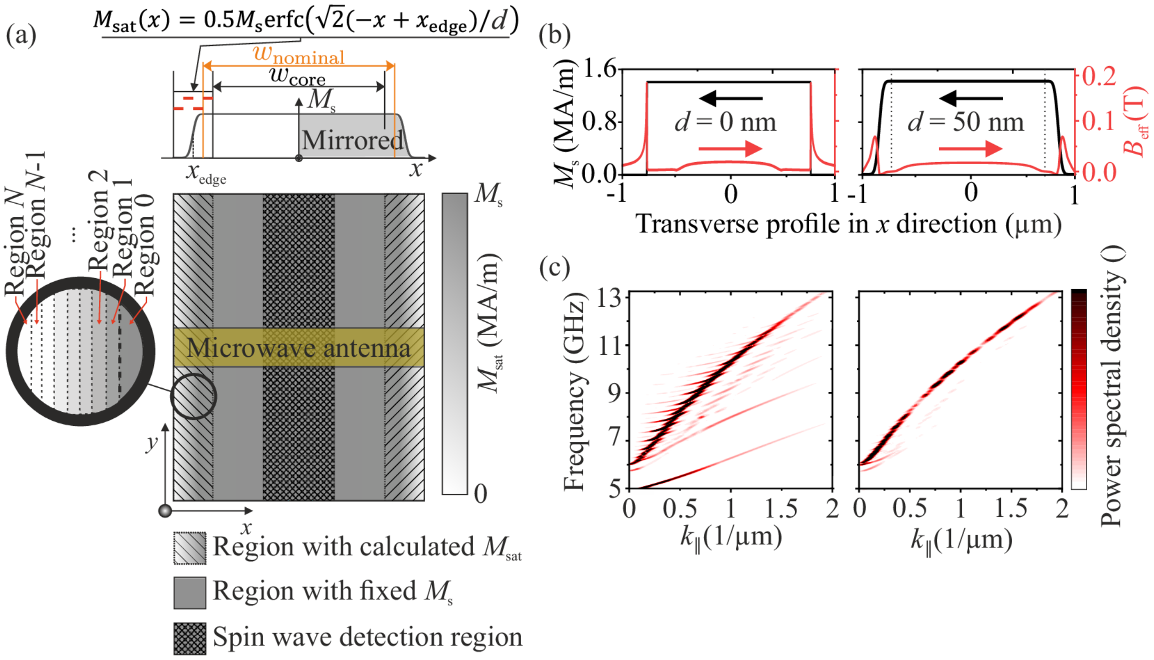

Fig. 4.15: (a) Schematic definition of the micromagnetic problem. The waveguide is divided into a discrete number of material regions, where the central part is defined as one region. The excitation antenna is overlaid in the image. The spin-wave detection region is depicted by the cross-hatched region. Above the 2D map we plot a transverse profile of the magnetization. The magnetization profile in the edges was calculated by the governing formula presented above the plot. Individual short red lines in the edge region denote the length of the Gaussian width parameter d. (b) shows the transverse profiles of the saturation magnetization (dark grey) and effective magnetic field (red) for a discontinuous (left panel) and continuous (right panel) transition of the saturation magnetization on the edges of the waveguide. The effective field was extracted in the ground state. The material parameters follow the experimentally found values. Dotted lines separate the core from the edge regions. (c) presents the simulated dispersion relations of the spin-wave modes for both magnetization profiles. The power spectral density of the modes (represented by the color scale) has been normalized to the maximum value.

The value measured in the experiment $B_\mathrm{A} = 24\,\mathrm{mT}$ would yield $K_\mathrm{u} = 17\,\mathrm{kJ/m^3}$. Again this value is an effective value of two competing anisotropies: the shape anisotropy and the magnetocrystalline uniaxial anisotropy. The absolute value of K_u is obtained by summing the experimentally found value of $K_\mathrm{u} = B_\mathrm{ani}M_\mathrm{S}/2$ with the estimation of the shape contribution based on the model by Aharoni [38]. Due to the limitations of the analytical model, we final-tuned the K_u value in the micromagnetic simulations. We changed the value of K_u and observed the frequency of the ferromagnetic resonance. For the anisotropy value $K_\mathrm{u} = 22\,\mathrm{kJ/m^3}$, the FMR frequency extracted from the simulations matched the analytical model.

After the initialization of the geometry, the static magnetic field was applied in the transverse direction of the waveguide (direction along the magnetocrystalline anisotropy) and the magnetization was relaxed to the ground state. Subsequently, the field was set to zero and again the energy minimum was found. At this point, we have extracted the transverse profile of the effective field B_eff in a similar manner as presented in Fig. 4.4. In Fig. 4.15 (b) we present the analysis performed for the step-like magnetization profile and also for the gradient with $d = 50\,\mathrm{nm}$. The micromagnetic simulations reveal that an infinite gradient in the magnetization leads to a sharp spike of the effective magnetic field just after the edges of the waveguide (outside of the structure). In the case of a finite magnetization gradient, the B_eff profile becomes smeared out. The maximum value of the B_eff is lower (and has a nonzero value also inside of the structure) and the central homogeneous region is significantly broadened, as the lower gradient of the magnetization leads to a lower and less localized demagnetizing field. The simulations also showed that for both cases in a narrow region near the edges of the waveguide, the magnetization realigns to the longitudinal direction. Afterward, we excited the waveguide by a localized in-plane magnetic field B_y with $\mathrm{sinc}\,(t)$ time dependence:

$$B_y(t) = B_\mathrm{max}\mathrm{sinc}\left[2\pi f\,(t - t_0)\right], \tag{4.2}$$

where the peak field value is $B_\mathrm{max} = 1\,\mathrm{mT}$, the offset time $t_0 = 100\,\mathrm{ps}$, and $f = 30\,\mathrm{GHz}$ is a cut-off frequency. The dynamic field is localized in a rectangular region spanning over the width of the waveguide (x direction) and having a length of $0.5\,\mathrm{\mu m}$. After the excitation, the magnetization vector map in a $0.5\,\mathrm{\mu m}$ wide region spanning over the length of the waveguide is saved every $25\,\mathrm{ps}$ for $40\,\mathrm{ns}$. For post-processing phase, we load the map of the out-of-plane component of the magnetization $m_z(x, y)$. From the 2D map we calculate the average value over the width to obtain $m_z(y)$ for each time step. This creates a 2D data set $m_z(y, t)$. The spatio-temporal matrix is then windowed by the Hann function in order to eliminate windowing artifacts in the subsequent FFT analysis. The spin-wave dispersion is then obtained directly by plotting the amplitude of the spatial and temporal frequencies obtained from a two-dimensional Fast Fourier transform of $m_z(y, t)$:

$$m_z(k_\parallel, \omega) = \mathfrak{F}\left\{m_z(y, t)\right\}. \tag{4.3}$$

These data still contain some artifacts as e. g. non-uniform excitation in the k space due to the rectangular antenna shape. Deconvolution of the obtained dispersion with the Fourier image of the antenna shape and the excitation pulse would enhance the data quality even further, yet it would not reveal any new phenomena in the presented data. For this reason, and for the sake of simplicity, we did not employ this step in our data processing.

The longitudinal spin-wave dispersion extracted from the micromagnetic simulations is plotted in Fig. 4.15 (c). There is an obvious difference in the modal structure of the dispersion when we compare the cases with $d = 0\,\text{nm}$, and $d = 50\,\text{nm}$. As the gradient is introduced to the edge region, the boundary conditions for the dynamic magnetization are altered. The quantization of the modes with higher transverse mode numbers is deteriorated. As a direct consequence, the modes with higher transverse $k_\perp$-vector get weaker (as can be seen from a lower power spectral density). The first waveguide mode does not significantly change even for $d = 200\,\text{nm}$. This is likely the main mechanism explaining the absence of any higher-order waveguide modes seen in the phase-resolved BLS data (Fig. 4.12). This statement is further supported by a careful analysis of the line scans (Fig. 4.12). To confirm the visual impression, we have extended equation (2.22) (on page 51) to allow for more overtone spatial frequencies (as expected from the model by Guslienko) to be detected, since we expect from the modal profiles of the analytical model presented by equations (1.58) (on page 27) and (1.61) (on page 29) to excite multiple odd modes [157, 166] at certain frequency by the excitation antenna. The analysis confirmed the best agreement in the absence of any higher spatial frequencies. Above all, the RF sweeps presented in the right panel of Fig. 4.11 do not show any significant lower/higher modes. From the dispersion presented in Fig. 1.14, the frequency difference between the first two odd modes (for a spin-wave wavelength $\lambda_\parallel = 2\,\mu\text{m}$) is approx. 1 GHz. Peak with such a frequency shift would be resolvable in Fig. 4.11.

To conclude the presented data, we have studied the spin-wave propagation in waveguides prepared by FIB direct writing into metastable fcc $\text{Fe}_{78}\text{Ni}_{22}$ thin films. We have shown that in these high-aspect-ratio waveguides, spin waves can propagate with attenuation length up to $3.1 \pm 0.4\,\mu\text{m}$ with high group velocities reaching almost 6 km/s without the necessity of external magnetic fields or global magnetic anisotropy. This unique feature is realized by the local uniaxial magnetic anisotropy, which is controlled by the writing procedure. The spin-wave dispersion relation has been determined by using phase-resolved BLS microscopy, and the magnetic properties of the waveguides were extracted. The relatively large saturation magnetization, together with high (controllable) magnetic anisotropy, renders the material suitable for high/frequency spin-wave circuits operational even at zero external magnetic field. Moreover, the extracted material properties of the system will allow us to design more complex spin-wave devices by utilizing the possibility to spatially control both the saturation magnetization and the direction of the uniaxial magnetic anisotropy in a single magnetic structure. Our unique approach paves the way towards many other possibilities to develop and study spin-wave propagation in magnetization landscapes that are unattainable in any conventional magnetic system.

5. Magnonic turns

The previous chapter has presented the reader with the possibility to stabilize the magnetization in the long and narrow waveguide in the transverse direction (see e.g. Fig. 4.7). Afterward, we have shown that even the spin-wave propagation in the Damon-Eshbach geometry can be achieved with zero external magnetic field applied. By doing so, the magnonic 90° turns can be readily fabricated and studied as our system allows to imprint the magnetic anisotropy with the highest strength in two perpendicular directions.

The need for the ability to turn spin waves in complex networks is obvious. The most trivial approach is to use the shape anisotropy of the waveguides and employ the backward volume geometry of the spin-wave propagation [67]. Not only this geometry exhibits the lowest group velocity, but it also shows mode conversion leading to nontrivial modal structures behind the bend due to the dynamic demagnetizing field on the edges [67, 154]. By using the external magnetic field, the mode conversion effects get even more pronounced as the individual segments (before/after the bend) of the waveguide realign its magnetization, and thus the spin-wave dispersion highly varies between the two perpendicular segments of the turn. The difference in the dispersion forms a strong mode mismatch between the regions before/after the bend, and again low bend transmission properties are seen [156].

There have been attempts to stabilize the individual regions of the spin-wave turn in DE geometry, as presented e.g. in [167]. In this study, the authors used a gold underlayer under the magnonic waveguide. When they passed an electric current through the gold underlayer, the formed Oersted field stabilized the transverse orientation of the magnetization in a spin-wave waveguide allowing propagation of spin waves in the DE geometry. This approach is not very universal, nor it is passive. Our system allows inherently the 90° turns to be fabricated without the need for an electric current to stabilize the transverse magnetization in the turn.

The following text briefly presents the outcomes of the project focused on the spin-wave turns. In our experiments, we have employed the 8 nm thick system (thus the magnetic constants extracted in the previous chapter on 12 nm system are not valid). Also, the sample went through lithography with too high temperatures, and thus e.g. the strength of the uniaxial magnetic anisotropy is lower than the maximum anisotropy strength measured on the same system before we accidentally deteriorated its properties (see sample Cu#12d in the Appendix 2).

In order to fabricate the spin-wave turns, we have used the 1.5 µm wide waveguides as basic building blocks. In the fabrication process, we always start by first writing the horizontally oriented waveguide from the left edge by scanning the FIB 80° from the waveguide long axis. The schematic picture of the writing process is visualized in Fig. 5.1 (a).

Before we write the vertically oriented waveguide, we need to make the interconnecting bend. We have selected the most trivial one, where we continuously bend the waveguide

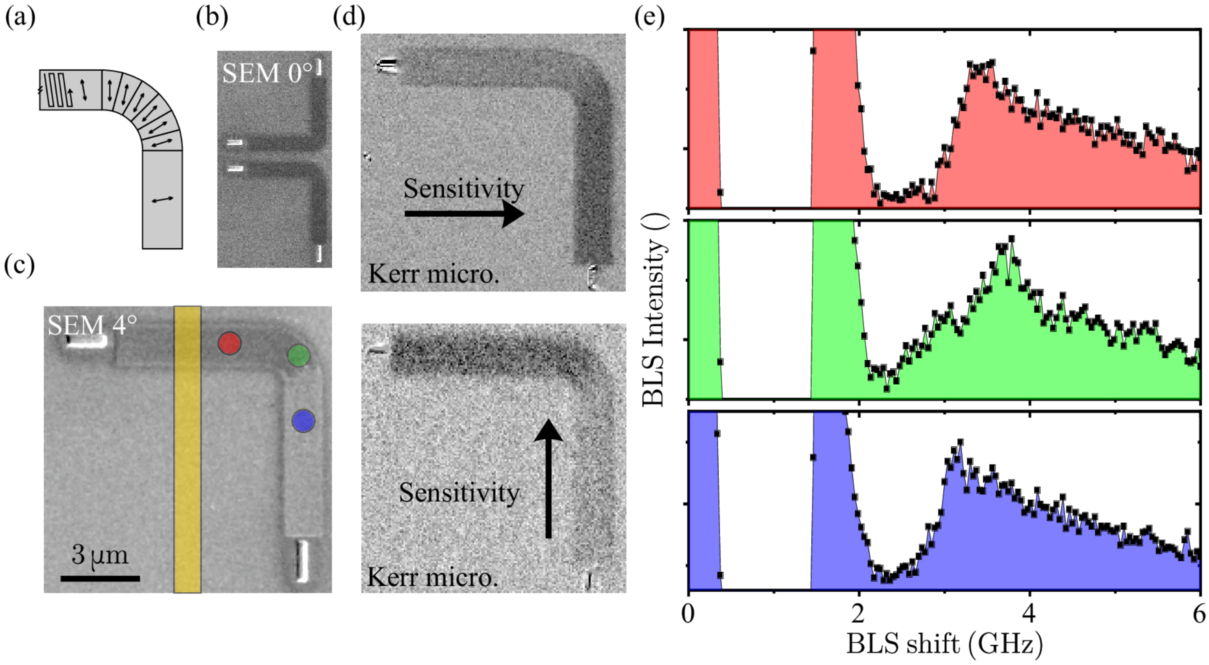

Fig. 5.1: (a) The schematics of the writing procedure of the waveguides. The double-headed arrow marks the FIB fast scanning axis direction. The zigzag pattern marks the irradiation initiation spot. (b) The zero-tilt SEM image of two magnonic turns. (c) SEM detail of one of the waveguides taken under small tilt revealing the crystallography of the structure. The ocher rectangle marks the position of the microwave antenna for microwave excitation. (d) Zero-field vector Kerr microscopy images of the structure. The background was taken in the saturation of the structures with the external field oriented 45° from the horizontal axis. (e) BLS thermal spectra measured in individual positions shown in (c).

on radius 1.5 µm (radius measured in the waveguide central line). We expect the radius to influence the spin-wave transmission as is known from e.g. microwave technology [168, 169]. In this proof-of-concept experiment, the radius was chosen rather arbitrarily. In order to write the bend, we divide it into six circular sectors with the central angle of 15°. In each subsequent sector (writing from the horizontal waveguide), we decrease the FIB scanning angle by 15°. In the last step, the vertical part of the waveguide was written. The SEM image under tilt in Fig. 5.1 (c) shows a distinct boundary between two observable contrast levels in the bend. From the contrast, we assume that there will be a discontinuity in the uniaxial anisotropy orientation. We have shown earlier that there is a certain "gap" of anisotropy orientations that are not experimentally accessible in the 8 nm thick system. To see the zero-field ground state of the structure, we have performed Kerr microscopy with the vector sensitivity. This allows us to record two perpendicular components of the magnetization at the same time (with a certain small delay between the two images). We have first applied a strong magnetic field 45° from the horizontal direction to initialize both segments. In this state, we have taken the background image. Afterward, we have ramped the field towards zero, where we recorded the two images in Fig. 5.1 (d). It is nicely seen that the vertical segment measured with the vertical sensitivity gained (darker, in this case, means stronger signal) certain contrast. The same is seen in the horizontal segment with horizontal sensitivity. This means that the anisotropy successfully realigned the magnetization from the original saturation direction at 45° to both desired directions. The magnetization is aligned in the transverse direction to both arms of the waveguide. In the bend, it seems that the magnetization rotates more continuously than what we expected from the SEM image. The thermal spectra measured by µBLS in Fig. 5.1 (e) show that in zero external field the vertical and horizontal segments have very similar magnetic properties. We judge so from the thermal spectra. The onset frequency is similarly located for both arms at approx. 3 GHz and also the signal drop rate with the frequency seems very comparable. This means that both arms have similar dispersion and should be able to propagate spin waves without a strong mode mismatch. Despite the nice equivalency of the horizontal/vertical waveguides, the interconnecting bend element show different dispersion. This already suggests a problematic spin-wave transmission through the turn.

In the second step, we have contacted the microwave antenna (1 µm wide antenna approx. 3 µm from the bend) by high-frequency probes, and we measured the frequency sweeps to locate the maximum signal after the bend. The maximum was found at 3.5 GHz.

At this frequency, we have fixed the excitation, and we measured the 2D map of the spin-wave intensity. We have scanned specifically the part of the horizontal waveguide after the excitation antenna, the bend, and partially the vertical waveguide in 60 nm steps. At each spot, we recorded the BLS spectra. Afterward, we have extracted the integral counts from 2 GHz window around the excitation frequency. This reveals the spin-wave intensity map Fig. 5.2.

First, we see very strong excitation of the part before the bend. In the bend, we see the diagonal cut at which the signal drops significantly. We see only a small portion of the power "leaking" to the vertical waveguide. The intensity profile after the bend is very complex, suggesting a very strong mode conversion to occur in the bend. As the majority of the spin-wave signal stops in the diagonal of the bend, we expect the magnetization to rotate here rather more abruptly that what is seen in the Kerr microscopy images presented in Fig. 5.1 (d). In the µBLS setup, we have used a high-magnification microscope objective that cannot be simply used in the Kerr microscope. In this configuration, the

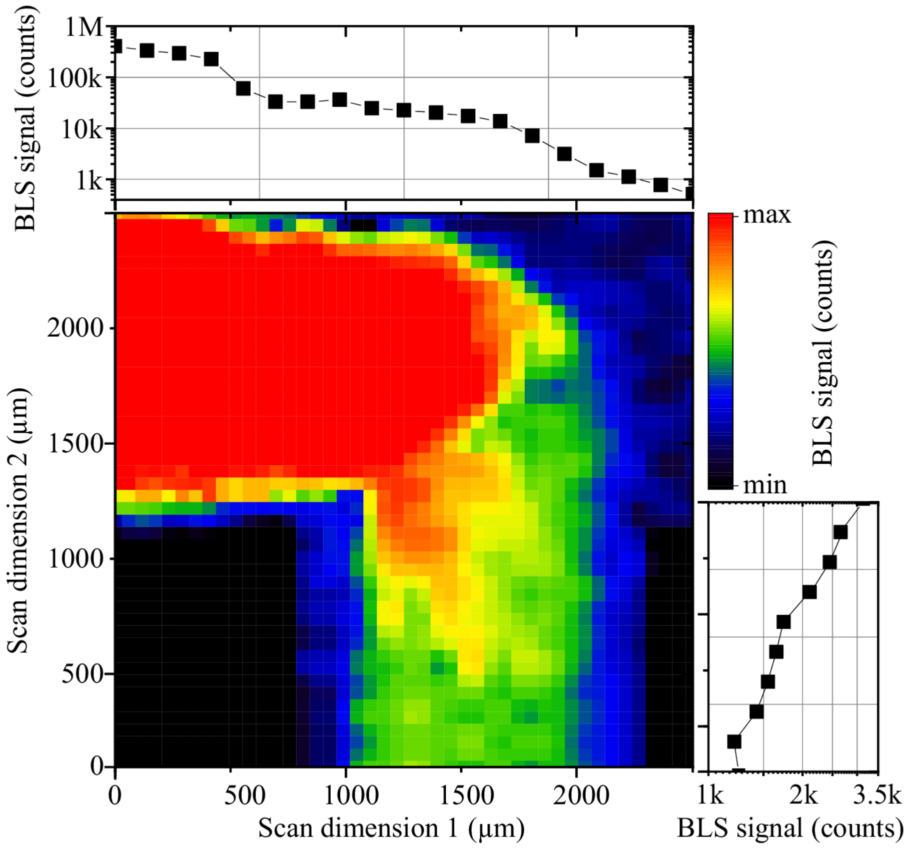

Fig. 5.2: The 2D map of the spin-wave intensity measured on the magnonic turn shown in Fig. 5.1 (c). The signal is shown in the logarithmic scale in order to show the detail of the spin-wave intensity after the bend. Above the map, we show the plot of the integrated BLS counts over the width of the horizontal waveguide and also of the bend. The graph on the right side shows integrated counts over the width of the vertical waveguide only.

µBLS has higher resolving power and thus reveals more details. The map in Fig. 5.2 suggests that the tail-to-tail domain wall is formed in the bend region blocking partially the spin-wave transmission. This behavior has been resolved in the literature [170] for slightly different spin-wave geometry. We expect the underlying mechanism to follow the same pattern. Looking at the integrated counts above the 2D maps, we see exponential decay (almost linear decay in logarithmic scale) to support the propagating spin waves towards the bend. Periodic modulation of otherwise linear function might suggest the partial formation of the standing spin waves between the antenna and the point of the reflection at the tail-to-tail domain wall. At Scan dimension 1 equal to approximately 1700 nm, we see a drop of signal related to the fact that we partially integrated the counts also in the part where there is no magnetic material.

After the bend, we see again an exponential decay of spin-wave intensity from the bend area. By comparing the decay rate in both regions, we have extracted similar values before/after the bend. When studying the transmission coefficient of the bend, we have found that only $\sim 5\,\%$ of the power passes the bend. Apparently, the magnetic configuration does not support the continuous bending of the spin-wave wavefronts. What we observe seems more like the refraction of the spin waves on the boundary between two regions [171].

From the very preliminary measurements, it seems that a very problematic part blocking the spin-wave transmission is the discontinuous step in the orientation of the uniaxial magnetic anisotropy. Such discontinuity can form a domain wall. The system employed in this study with only 8 nm of magnetic material does not allow continuous rotation of the anisotropy axis. The more viable system would be a 12 nm thick system offering more degrees of freedom in the selection of the anisotropy axis (even though in the intermediate angles we partially lose the anisotropy strength). Again, the system would have to be forced to lower the size of the individual domains with mutually perpendicular anisotropies [see again Fig. 3.17 (a) and Fig. (d)]. This might be achieved by dividing the bend to even more circular segments, and by starting the growth always from the side not adjacent to already transformed bcc material. The writing would be more stochastic, yet might achieve the desired continuous rotation of the anisotropy axis in the bend. When we have performed the experiments on the 8 nm thick system, since at the time of the experiments with the spin-wave turns the 12 nm thick systems were not available.

In the following step, we have performed the micromagnetic simulations to study the spin-wave propagation in a perfect system, where the magnetization continuously rotates along the bend, and to compare the obtained behavior with the model following more the real system. In the first step, we have defined the geometry of the problem, and in the same manner, as in the experiment, we have divided the bend to six circular segments. In each segment, we individually change the direction of the uniaxial magnetic anisotropy. In the first simulation, we fix the anisotropy direction of the first three segments to the direction of the horizontal waveguide. The other three segments have the anisotropy rotated by 90° to the direction defined also for the vertical waveguide. The second simulation has the anisotropy in the bend rotated continuously from the direction defined for the vertical waveguide to the direction defined in the horizontal waveguide. The sketch of the anisotropy direction definition for both cases can be found in Fig. 5.3. After we defined the geometry of the problem, we saturated the sample with a field pointing 45° from the vertical direction. Then the magnetic field was turned off, and the ground state was formed. The ground states for both cases are shown in the left column of Fig. 5.3. We see that in the discontinuous case, the tail-to-tail 90° domain wall is formed. In the

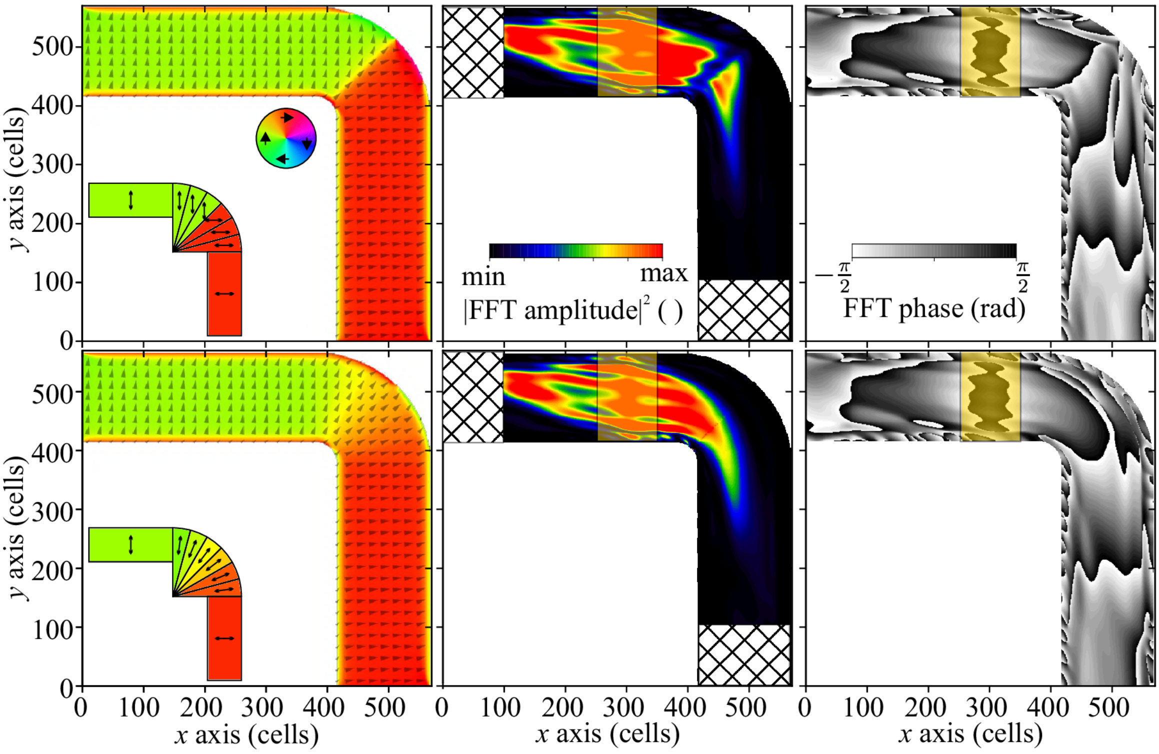

Fig. 5.3: The micromagnetic simulations of the spin-wave propagation through the bend. The top row summarizes the behavior of the spin-wave turn with a discontinuous transition between vertical/horizontal anisotropy. The bottom row shows the results for the continuous transition. The left column shows the simulated ground state of the structures (insets schematically show the definition of the anisotropy direction). The middle row shows the FFT amplitude map extracted at the frequency equal to the excitation frequency (3.5 GHz). The region of the excitation is marked by ocher color. The cross-hatched areas on the end of the waveguide mark the absorbing boundary. The right column shows the FFT phase maps.

continuous case, the magnetization nicely follows the local anisotropy direction. Afterward, we aimed to mimic the expectation spin-wave map when the structure is excited by the microwave antenna. The BLS works in the frequency domain, and what is detected (leaving out the phase-resolved BLS option) is the square of the local spin-wave intensity [132]. Obtaining directly the spin-wave spectra from the micromagnetic simulation would be rather complicated as one would have to find both the spatial and temporal waves in the system. To a certain extent, the local spin-wave amplitude can be found from the Fourier transform of the local dynamic magnetization. This allows us to translate the time-domain micromagnetic data to the frequency domain. The resulting images reveal the local frequency content of the dynamic magnetization at a given frequency. This is a very good approximation of what is measured by the BLS.

To calculate the expected BLS signal from the micromagnetic simulations, we first add the three additional regions to the previously defined geometry. The first region is the approximation of the excitation antenna in the horizontal arm of the spin-wave turn. In 1 µm wide region we add a time-dependent magnetic field with a simple $B_{\mathrm{max}}\sin(2\pi f t)$ time dependence. The dynamic field oscillates in the horizontal direction, effectively exciting spin waves. Then two regions are added to the ends of the waveguide. Here we artificially increase the damping α parameter to 0.5 (otherwise we use $\alpha = 0.008$). The regions are defined as absorbing boundaries that decrease the reflection of the spin waves from the edges of the waveguide (we simulate only the region close to the bend) and thus prevent the formation of the standing spin waves.

At this point, we have to get over the transient state when no spin waves are excited in the system. We have to find the steady-state spin-wave distribution (resembling the continuous wave excitation from the experiment). We do so by allowing the system to run for time $25T$, where $T = 1/f$ is the period of the excitation signal. After twenty-five periods, where we continuously excite the system, we see steady-state propagation of the spin waves that attenuate along the propagation direction. We save the 2D map of $m_z(x,y)$ every $T/50$ for the total time of $2T$. The achieved resolution in the frequency is then given by the total time window as $1/(2T)$. From the data set $m_z(x,y,t)$ we form a 3D matrix. Depending on the total volume of the data, we also implemented data binning (2×2, 3×3 or 4×4) allowing us to lower the resolution (and thus also the number of data points) of individual $m_z(x,y)$ maps. The maps are first convolved with a kernel, finding the mean between neighboring data points (depending on the binning rate), and then we extract a certain number of pixels from the whole map (again depending on the binning rate). This has allowed us, by the means of sacrificing the spatial resolution, to work with huge data sets without problems with overflowing computer memory.

For each x and y coordinate, we extract the time dependence of the $m_z^{x,y}(t)$, and we perform the fast Fourier transform of the signal. From the FFT data we form again the 3D matrix $\mathfrak{F}\left\{m_z(x,y,t)\right\}(x,y,\omega)$. Individual maps carry the complex-valued information about the frequency content of the dynamic magnetization at a given frequency. The 2D map resembling the BLS spin-wave intensity map (squared map of FFT amplitude) can be then found as

$$A(x,y,\omega) = \left|\mathfrak{F}\left\{m_z(x,y,t)\right\}\right|^2, \tag{5.1}$$

and the spin-wave phase can be extracted as

$$\Phi(x,y,\omega) = \mathrm{atan}\left(\frac{\mathrm{Im}\left(\mathfrak{F}\left\{m_z(x,y,t)\right\}\right)}{\mathrm{Re}\left(\mathfrak{F}\left\{m_z(x,y,t)\right\}\right)}\right). \tag{5.2}$$

We have performed the above-described procedure for the excitation frequency $f = 3.5\,\text{GHz}$. The calculated spin-wave intensity maps are shown in the middle panel of Fig. 5.3. The first very apparent feature is the lack of the magnetization dynamics (of the m_z component) at the fundamental frequency in the region of the anisotropy discontinuity. Partially the spin waves pass this region and propagate further with lowered intensity. The situation resembles more the refraction of the spin waves on the domain wall than simple propagation through a bend. The intriguing missing dynamics of the m_z component in the domain wall are not caused by the postprocessing of the data (namely by the convolution with the kernel). When studying m_x and m_y, we see non-zero dynamic components also in the domain wall.

When the anisotropy is changed gradually, the spin waves can pass the bend and get coupled to the vertical segment more easily. The phase maps in the right column of Fig. 5.3 show wavefront distortion on the anisotropy discontinuity. The phase map in case of the spin-wave turn with the gradual tilt of the anisotropy does not show such a significant wavefront distortion, yet the mode profile is far from being perfect.

When we compare the experiment from Fig. 5.2 and the simulation presented in the first row of Fig. 5.3 we can find similar features, but overall the simulation does not satisfactorily describe the real observation. The experimental data show that the spin-wave propagation is strongly terminated in the bend region. The model might be oversimplified. Fig. 5.1 (c) shows a more complex shape of the transition between the vertical and horizontal anisotropy. High-resolution Kerr microscopy should reveal the true static ground state of the structure and should allow optimizing the region of the bend. Simply judging from the BLS spectra on the vertical and horizontal arm, there should be no mode mismatch between the two, and thus the only problematic part is the bend.

We have extended the analysis presented in Fig. 5.3 by exciting the magnetization with a broadband excitation (represented by $\text{sinc}(t)$ pulse). Afterward, we have saved the $m_z(x,y)$ maps for $10\,\text{ns}$, and in a similar analysis, as presented above, we have analyzed the amplitude/phase maps extracted for different excitation frequencies. We did not find any special frequency at which the spin waves in our system (system with discontinuity in the direction of the uniaxial magnetic anisotropy direction) would pass without strong distortion of the wavefront.

In conclusion, we were able to fabricate the magnonic turns by interconnecting the vertical and horizontal segments with a bend. The structure in the zero field showed the transverse magnetization configuration in both vertical and horizontal segments (see Kerr images in Fig. 5.1). From the thermal BLS spectra, we concluded that both segments have very similar spin-wave dispersion as the thermal BLS spectra measured in zero external magnetic field presented in Fig. 5.1 showed very similar results. The bend region showed different spin-wave dispersion. The SEM image showed a rather abrupt change in the crystallography inside of the bend. This got translated to the discontinuity in the uniaxial magnetic anisotropy direction. The µBLS revealed that the spin waves almost did not propagate through bend where we observed a very strong drop of the spin-wave intensity on the bend diagonal (visible in Fig. 5.2). We have identified this as a tail-to-tail domain wall that stops the spin waves from propagation to the vertical segment. Only a small portion of the spin waves could pass the domain wall mainly in the region close to the inner radius of the bend. The line profiles revealed that the small portion of spin waves measured behind the bend has a propagating character in the direction from the bend (identified by the exponential decay of the signal in the direction from the bend). The micromagnetic modeling did not satisfactorily reproduce the measured data but has given a little more insight into the problem. It has also shown that even the perfect spin-wave turn, with the continuous transition of the uniaxial magnetic anisotropy direction, does not show distortion-free propagation behind the bend. This rather complex problem will need more modeling before the experimental investigation. The knowledge can be drawn from e.g. bends based on the metamaterials [172] or simply from the vast knowledge of the microwave technology. Very recent and preliminary results show that even with our system (showing discontinuity in the bend), the mitered bends, as are used for a long time in microwave waveguide technology, show enhanced transmission at certain frequencies.

6. Graded-index magnonic waveguides

In this rather short chapter, we briefly summarize the development and outcomes of the project focused on waveguides with an artificial gradient of the magnetization towards the edge of the structure. The motivation behind this project was to mimic and study the magnonic equivalent of graded-index optical fibers. In optics, adding a gradient to the edge of the structure lowers the leaky modes of the fiber and thus decreases the light attenuation of the fiber [173].

The concept of graded-index magnonics is not new to the spin-wave community. As the index of refraction unambiguously depends on the dispersion of the spin-wave system, it can be influenced by many means [171]. We have presented already one method of introducing the gradient of one nomenclature to the magnonic waveguide as we have identified that on the waveguide edges the magnetization continuously realigns from the transverse orientation of the magnetization in the waveguide core to the longitudinal orientation of magnetization on the waveguide edge (see Fig. 4.2 shown on page 83). This, together with continuous change in the waveguide width, has been presented also in literature by e.g. [174, 175].

Another way how the gradient can be artificially induced in the system is to imprint it directly to the saturation magnetization. In conventional non-metallic magnonic systems, this has been achieved by local heating of the magnetic material by the laser. Thermal diffusion then created a thermal gradient allowing a continuous transformation of spin-wave modes or even turning the spin waves by 90° [176, 177]. The gradient in such a system is hard to control as the profile of the magnetization gradient is not changed easily (the irradiation laser intensity profile can be changed by using e.g. spatial light modulator, but the thermal gradient will be very hard to control or miniaturize).

We have shown already that when the magnetic anisotropy is not needed, we can achieve the fcc/bcc transformation by employing multiple scanning of the FIB in the writing process. This allows us to continuously tune the saturation magnetization locally with linear dependence, as was presented by Fig. 3.7 (on page 63). In theory, this allows us to write magnetization gradients with various profiles that are imprinted passively to the magnetic system.

In the proof-of-concept experiment, we have written a set of waveguides, where we introduced two types of gradients. The positive gradient $\nabla M_\mathrm{S}\,(\perp) > 0$ is the case, where we on-purpose lowered the ion dose in the waveguide core (a central rectangular region with the width w_core) and we gradually (linear dependence) increased the ion dose towards the waveguide edges in a region of the width d. The increase of the ion dose was performed quasi-continuously by adjoining individual 50 nm wide regions of different ion dose. All the features were written by 100 scans of the FIB. Here the resulting structures have a lower magnetization of the core, and the magnetization increases towards the edge where it is maximal. After reaching the maximum ion dose, i.e. also the maximal saturation magnetization, the saturation magnetization abruptly drops to the value of non-irradiated material. The second set of waveguides has a negative gradient of the saturation magnetization $\nabla M_\mathrm{S}(\perp) < 0$. The core was written by a single-scan approach, and thus it possesses the highest possible saturation magnetization. On the edges, we gradually decreased the ion dose in 100 scan approach. The schematics of both positive and negative gradients are presented in Fig. 6.1 (a).

Contrary to the previous measurements of the waveguides on a 12 nm (nominal) thick system, the following data were measured on the 8 nm thick system that also went through the lithography steps with too high temperatures (see sample Cu#12d in the Appendix 2). This translated to low anisotropy and lower maximum achievable saturation magnetization value. All the effects achievable on a 12 nm thick system can also be performed on a 8 nm system. We have to bear in mind that due to different magnetic constants, the spin waves have different dispersion. Prior to the BLS measurements, we have estimated

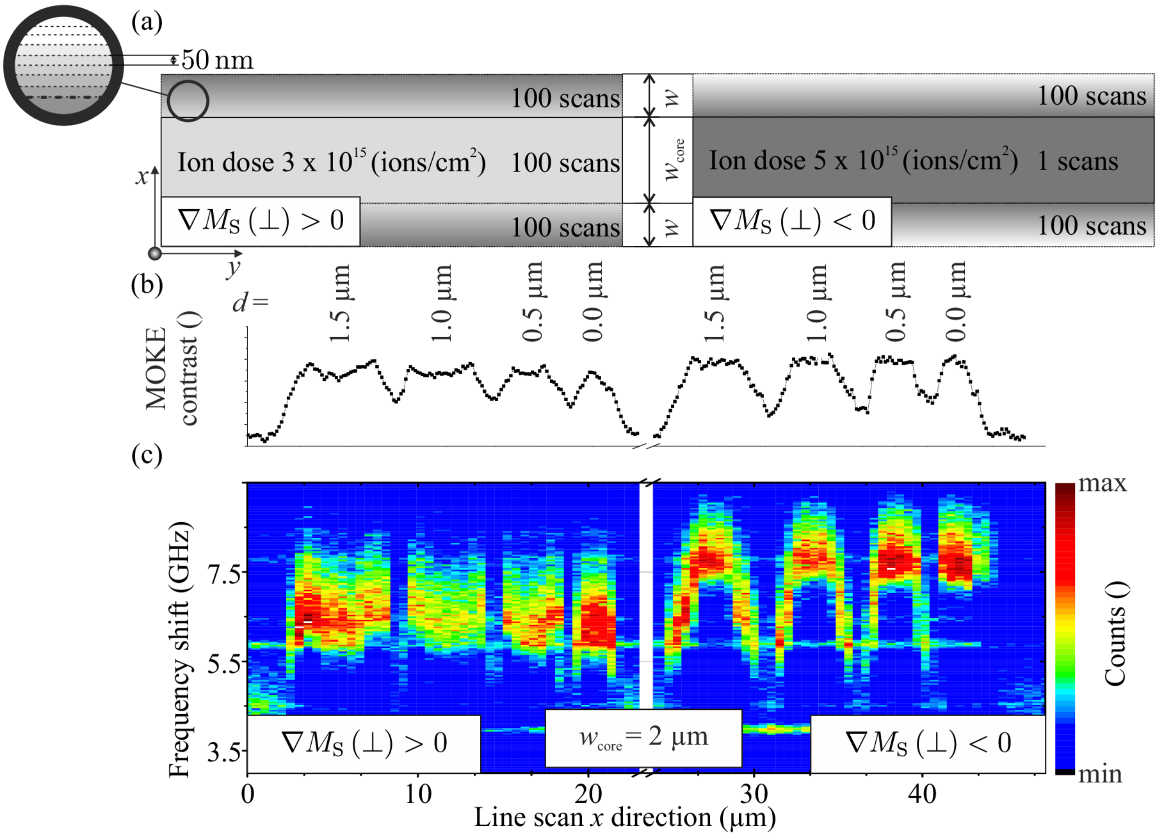

Fig. 6.1: (a) Schematics of the design of both sets of waveguides. The grey level schematically represents the ion dose (lower values have lower ion dose). (b) Saturation magnetization line profile of the waveguides with different transition width d parameter (and constant $w_\mathrm{core} = 2\,\mu\mathrm{m}$ parameter) extracted from the difference in MOKE signal in ±saturation. (c) 2D frequency maps of thermal spin-wave spectra measured in the external field $B_\mathrm{ext} = 52\,\mathrm{mT}$ in the transverse direction [x axis in (a)].

the transverse saturation magnetization profile by the MOKE. First, we have saturated the sample by the negative field, and we took the background image for subtraction. Afterward, we have applied the positive magnetic field, and we have acquired the line profile of the signal over the waveguides. The line profile of the Kerr contrast plotted in Fig. 6.1 (b) reveals the saturation magnetization line profile. Data for the waveguides with an imprinted positive gradient of the saturation magnetization show the lowest value (except for the $d = 0\,\mu\mathrm{m}$ case) of the saturation magnetization in the waveguide core. The magnetization then increases towards the edges of the waveguide, where it drops down. The data exhibit a rather large noise floor and many artifacts. For example, the waveguide with zero d does not show an expected plateau of the signal at all. This is possibly due to the stochastic process of writing the structure with a 100 scan approach. For the waveguides with the negative gradient of the magnetization, we always see a plateau of the signal in the middle of the waveguides. The signal then gradually decreases towards the edges. Expectantly, the width of the region where the magnetization decreases is increasing with higher d. The µBLS revealed the originally intended feature and that with the positive gradient, we can reverse the natural transverse profile of the spin-wave spectra in the waveguides. The waveguide core has a resonance frequency lower than the edges of the waveguide. This directly offers a mean to selectively excite only the core of the waveguides. The spin-wave gap (minimum frequency of the spin-wave system) increases with the saturation magnetization. Thus when the core has a lower magnetization than the edges of the waveguide by tuning the frequency we can find a condition, when there is no solution of the LLG equation in the high M_S edge regions yet the low M_S core can be excited (consult Fig. 1.12 shown on page 28). Such a situation does not exist (in DE geometry) for the waveguides with the negative gradient. Whenever we can excite the waveguide core also the edge regions can be excited.

From the knowledge of the transverse profiles of the BLS spectra in all waveguides, we have advanced the study by fabricating 1 µm wide antenna on the waveguides and actively pumping the system on selected frequencies. The 2D maps revealing the spin-wave propagation in waveguides with different magnetization profiles are presented in Fig. 6.2.

The BLS maps show the selectivity of excitation of individual parts of the waveguide. At excitation frequency of 6.1 GHz, we are able to selectively excite only the edge region of the waveguide with a negative gradient of magnetization. The waveguide without any artificial gradient does not show any propagation in the edge region of the waveguide. At the same frequency, we strongly excite the edge region of the waveguide with the positive gradient of the magnetization. Together with the strong excitation of the edge regions, we also excite the waveguide core. However, the excitation is weaker here. This can be understood from the dispersion together with the knowledge of the ensemble of k-vectors being excited by the microwave antenna. For the waveguide with the positive gradient of the magnetization on the edges at 5.6 GHz, we can selectively excite the waveguide core as the dispersion crosses only the low M_S curve (see right panel of Fig. 6.2). Similar effect can be seen for the waveguides with a negative gradient when we excite at 7.1 GHz. Seemingly only the waveguide core is excited. From the knowledge of the dispersion, we know that also the edge regions are excited, but lower effectivity of the excitation and detection hinders the signal from the excited spin waves in the edge regions.

In the last step, we have analyzed the propagation properties of the spin waves. We have measured the spin-wave signal strength as a function of the distance from the excitation antenna. The spin waves are expected to exhibit exponential decay from the excitation source. The governing equation is then similar to (2.22) (page 51) when we assume $I_\mathrm{EOM} = 0$. In order to correctly extract the attenuation length L_att, we first subtract the offset value (the minimum value found at the end of the waveguide), and then we Log-transform the data. The data might be fitted by the exponential decay directly, yet in the Least Squares Fitting method, the large values found near the antenna would overwhelm the still very important low intensity data points found far from the excitation source. By Log-transforming the data and fitting the linear dependence, we more

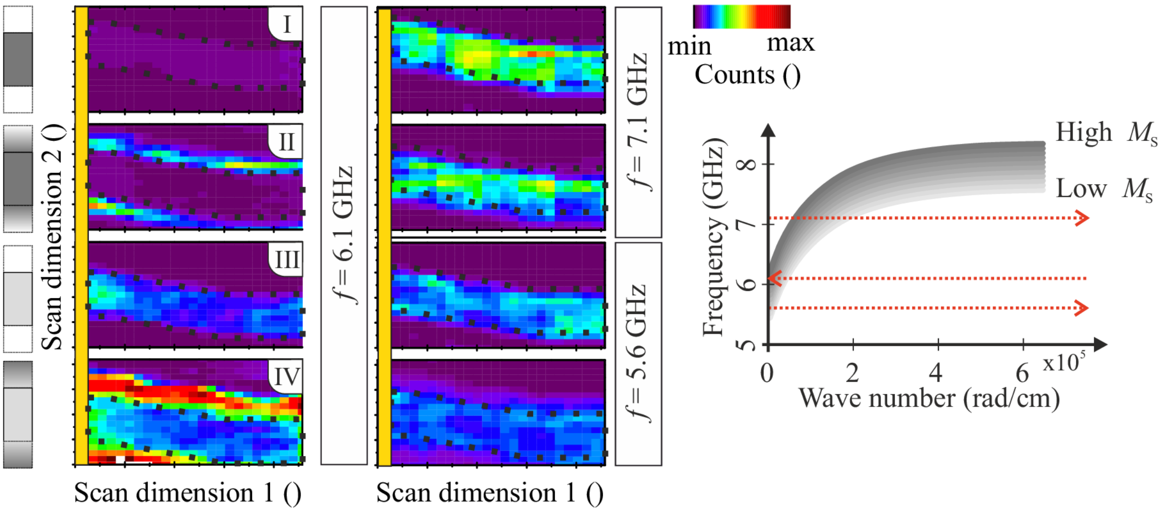

Fig. 6.2: 2D maps of the spin-wave intensity (external field $B_{\text{ext}} = 52\,\text{mT}$ in the Scan dimension 2 direction) measured on the waveguides with a negative gradient (waveguides I and II) and positive gradient (waveguides III and IV) of the saturation magnetization measured at different excitation frequencies. The edge region width d is zero in structures I and III. Both structures II and IV have the transition width fixed to $d = 1\,\mu\text{m}$. The signal decay along the Scan dimension 1 was artificially compensated. The waveguides are slightly tilted from the excitation antenna (as seen by the dashed black line marking the edge of the waveguide core). In the right panel, we present a schematic spin-wave dispersion for the high and low M_S case as expected in the waveguides with a positive gradient. The waveguides with a negative gradient have the low M_S curve shifted even further down. The horizontal lines mark the frequencies used for the excitation of the waveguides presented in the left set of 2D maps.

equivalently consider even the low-intensity data points. The slope of the curve is then equal to $-1/L_{\mathrm{att}}$.

In the experiment, we have excited the waveguides with a step profile of the magnetization and also the waveguides with a gradient of the magnetization with width $d = 1\,\mu\mathrm{m}$. The waveguides with the positive gradient were excited at the frequency of 5.6 GHz. The waveguides with the negative gradient were excited at 7.1 GHz. Then we scanned the center of the waveguides in 180 nm steps, and we recorded the measured BLS spectra (again in the external magnetic field $B_{\mathrm{ext}} = 52\,\mathrm{mT}$). We have extracted the integrated counts in a 2 GHz window around the excitation frequency. Data are plotted in Fig. 6.3.

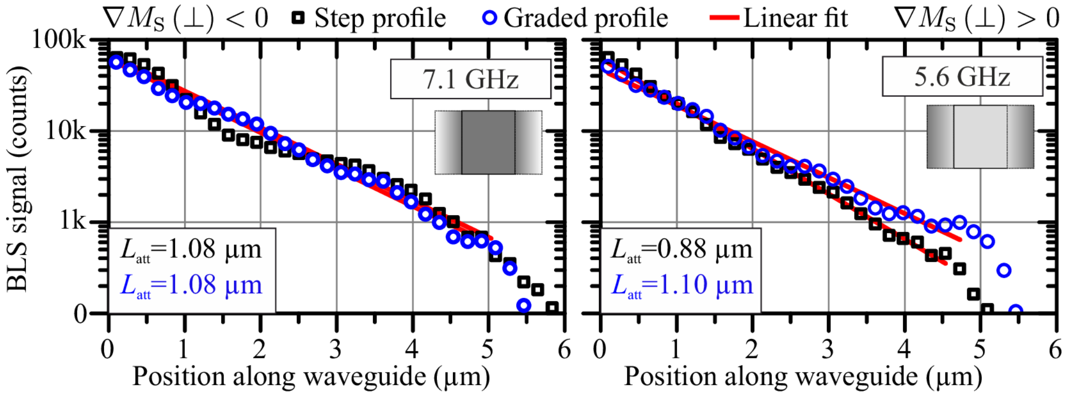

Fig. 6.3: The graphs present the spin-wave attenuation length measurement. The aim is to compare the waveguides with a step-like profile of the magnetization (black squares) and gradient profiles (blue circles). The fitted linear curves are represented by red continuous lines. Extracted respective spin-wave attenuation lengths are denoted in the bottom left corners. The left graph represents the measurement of the waveguide with the negative gradient of the magnetization, whereas the right graph represents the measurement of the waveguide with the positive gradient of the magnetization.

Data clearly show no influence of the negative gradient of the magnetization on the spin-wave propagation properties. Both curves exhibit the same attenuation length represented by the slope of the fitted linear dependence. In the case of the positive gradient of the magnetization, we see that the classical waveguide without any artificial gradient has the lowest spin-wave attenuation length of all measurements. By introducing the gradient, we increased the attenuation length to similar value as was observed in the waveguides with the negative gradient of the magnetization. From the Kerr microscopy measurement in Fig. 6.1 we see that the waveguide with the positive gradient of the magnetization and $d = 0\,\mu\mathrm{m}$ has the transverse magnetization profile somehow deformed. The lower attenuation length may be simply given by the non-homogeneous magnetization of the waveguide. All the waveguides show significantly lower attenuation length compared to the previous system with a thicker magnetic layer. This can be due to lower thickness, which translates to lower group velocity and thus lower propagation length, or simply it is given by the fact that the magnetic properties of the structures have been damaged by heating during the lithography step. The changes in the propagation length of the spin waves between all the waveguides are rather insignificant and the effects of the gradient remain inconclusive.

As an outcome of the above-mentioned analysis, we conclude that introducing a gradient of the magnetization does not significantly change the spin-wave propagation of the lowest waveguide mode. Recently similar results were also presented in publication [178], where the authors by the means of the micromagnetic simulation proved only a small effect of the magnetization gradient at the waveguide edges on the spin-wave propagation. They have observed a small decrease in the spin-wave propagation that was rather insignificant. Our data presented previously e.g. in Fig. 4.15 (on page 112) and now in Fig. 6.3 supports such findings. So even though the gradient of the magnetization does not increase the spin-wave attenuation length, the possibility to induce such an effect passively in the magnetic system opens many possibilities for e.g. continuous mode matching between the structures, multiplexing of the signals and many more.

7. Conclusion - Contribution of the thesis

The purpose of this thesis was to pioneer the applicability of the unique system of $Fe_{78}Ni_{22}$ [26] to the topic of magnonics. Quite naturally, the extended study of the system revealed very interesting phenomena connected by the writing of the magnetic patterns with the focused ion beam. The effects and possibilities we have revealed show the applicability of the system for even more advanced studies that cannot be easily performed in any other system. The work dedicated to the material properties and the FIB direct writing process has answered many questions about the system, offered many possibilities that can be further followed yet also raised a number of questions that need to be answered in the future. Gaining from the previous works performed on the system, we have successfully summarized the behavior of the material in a cookbook fashion. Through a series of experiments, we have unraveled many effects and features of the system that can be further exploited for many branches of the magnetism. Despite the vast experimental work done on the system, much of the FIB transformation-related physics is not fully understood yet. Mainly the missing point of the presented work is how the focused ion beam scanning direction defines the crystallography of the material and how it translates to the magnetic anisotropy of the system. We have correlated the magnetic measurements with the expected crystallography in very qualitative analysis. In the future, more quantitative analysis is needed to reveal the underlying mechanism that will allow us to define the crystallography simply by changing the scanning direction of the FIB.

The most direct and for the sake of this thesis most relevant effect is the possibility to define the uniaxial magnetic anisotropy by changing the FIB scanning angle. This was readily used for fabrication of long and narrow magnonic conduits, where contradictory to the shape anisotropy of the system we were able to stabilize the magnetization in the transverse direction to the long axis of the elements. The lowest width of the waveguides still showing the transverse orientation of magnetization was 750 nm. The orientation of the magnetization was further supported by the Brillouin light scattering. The fabricated antennas on the prepared waveguides have allowed us to excite the spin waves and to study the spin-wave propagation. The system, as a first of the ion beam phase transition systems, has shown satisfactory spin-wave propagation properties. Since we were able to propagate spin waves over relatively large distances (micrometers), we were able to perform the phase-resolved Brillouin light scattering measurements revealing also the dispersion of the spin waves. From the model, we have extracted the magnetic properties of the system which will allow us to design even more complex spin-wave devices.

We have designed and experimentally tested first prototypes of spin-wave turns and also graded-index magnonic waveguides. Both structure types are uniquely allowed by the properties offered by our system. Despite the fact that the first prototypes did not show spin-wave propagation through the bend in the spin-wave turns nor we have seen enhancement of the spin-wave propagation in the graded-index magnonic waveguides, the structures behave in an expected way as is seen from the micromagnetic models and is resolved in the literature. In the future, this pioneering experiments can serve as a starting point for more elaborate implementations.

The spin-wave turns show a large distortion of the wavefront when passing the bend between two perpendicular waveguides. By proper design, this behavior should be possible to suppress at least for certain spin-wave frequencies. The simplest design drawn from the microwave technology is mitered bend design. Preliminary micromagnetic simulations show the viability of such an approach. Thanks to the modern micromagnetic models and free software, testing of the complex magnetic designs is fairly easy and can be done within a short time. This effectively lowers the time needed for the design of the complex micromagnetic devices.

Another possible mean, how to perform the spin-wave turn, might lie in the possibility to combine the saturation magnetization gradient in the bend region and the two arms where both have the anisotropy imprinted transverse to the long axis. The gradient in the bend should perform a continuous mode conversion between the two arms [177].

Combining both the saturation magnetization control and the control of the uniaxial magnetic anisotropy within a simple structure offers unprecedented possibilities. The Gaussian beam emitters [73] imprinted directly to the material, periodic arrays of domain wall spin-wave emitters or graded–index 2D magnonic grin lenses are uniquely possible to be fabricated in our system. With a bit more realistic touch, the spin-wave propagation length achieved in our system is not viable for large–scale magnonic circuits, but the properties of the material offer great possibilities to test new ideas that are not possible to test in any other system. We have also shown that we can write magnonic waveguides down to width of 50 nm. This is already on the edge of what has been achieved with conventional techniques [152]. The properties of such narrow waveguides have to be tested.

Overall, the presented thesis gives an overview of the possibilities and related effects of the FIB direct writing of magnetic structures to the metastable fcc $Fe_{78}Ni_{22}$ system. Many basic concepts have been elaborated, yet more advanced studies are needed to fully understand the material and to fully employ its unique properties in magnetostatics and magnetodynamics.

Appendix 1: Demagnetizing factor of rectangular prism

The solution for the demagnetizing field of a magnetic prism as was presented in the reference [38] takes a form:

$$
\begin{aligned}
H = {} & \frac{b^2-c^2}{2bc}\ln\left(\frac{\sqrt{a^2+b^2+c^2}-a}{\sqrt{a^2+b^2+c^2}+a}\right)+\frac{a^2-c^2}{2ac}\ln\left(\frac{\sqrt{a^2+b^2+c^2}-b}{\sqrt{a^2+b^2+c^2}+b}\right)+\frac{b}{2c}\ln\left(\frac{\sqrt{a^2+b^2}+a}{\sqrt{a^2+b^2}-a}\right)\\
& +\frac{a}{2c}\ln\left(\frac{\sqrt{a^2+b^2}+b}{\sqrt{a^2+b^2}-b}\right)+\frac{c}{2a}\ln\left(\frac{\sqrt{b^2+c^2}+b}{\sqrt{b^2+c^2}-b}\right)+\frac{c}{2b}\ln\left(\frac{\sqrt{a^2+c^2}+a}{\sqrt{a^2+c^2}-a}\right)\\
& +2\arctan\left(\frac{ab}{c\sqrt{a^2+b^2+c^2}}\right)+\frac{a^3+b^3-2c^3}{3abc}+\frac{a^2+b^2-2c^2}{3abc}\sqrt{a^2+b^2+c^2}\\
& +\frac{c}{ab}\left(\sqrt{a^2+c^2}+\sqrt{b^2+c^2}\right)-\frac{(a^2+b^2)^{\frac{3}{2}}+(b^2+c^2)^{\frac{3}{2}}+(c^2+a^2)^{\frac{3}{2}}}{3abc}. \qquad (7.1)
\end{aligned}
$$

Aharoni in his text assumes the total length $2a$, total width $2c$ and total thickness $2b$. It is slightly different from what we employ in the text. We assume the magnetic element to have a total length l, total width w and total thickness t. In this configuration the structure spans between e.g. $-l/2$ to $l/2$. Thus the substitution

$$
\begin{aligned}
a &= \frac{l}{2},\\
b &= \frac{t}{2}, \qquad (7.2)\\
c &= \frac{w}{2},
\end{aligned}
$$

was employed prior to performing any approximations.

Appendix 2: List of samples

The following Table 7.1 presents the list of samples used in the scope of this thesis. We follow the sample labeling form as presented in the work of Jonáš Gloss [179]. The parameters used during the growth of the individual samples can be found in the Appendix A.

Table 7.1: List of samples used within this work. The results obtained on the sample with 8 nm thick $Fe_{78}Ni_{22}$ layer are divided into two groups. The first sample called Cu#12 collects the list experiments that were measured before performing the lithography with the resist pre-bake step. After the pre-bake (sample Cu#12d), the properties of the sample were deteriorated, resulting in different magnetic properties before and after the pre-bake.

Sample	$Fe_{78}Ni_{22}$ thickness	Analysis in chapter	Figures:	Comment
Cu#12	8 nm	3	Fig.3.7 Fig.3.8 Fig.3.9 Fig.3.10 Fig.3.11 Fig.3.12 Fig.3.13 Fig.3.14 Fig.3.15 Fig.3.19	
Cu#12d	8 nm	5, and 6	Fig.5.1 Fig.5.2 Fig.6.1 Fig.6.2 Fig.6.3	Damaged by heating
Cu#14	12 nm	4, and 6	Fig.3.2 Fig.3.3 Fig.3.4 Fig.3.5 Fig.3.6 Fig.3.8 Fig.3.16 Fig.3.17 Fig.3.18 Fig.3.19 Fig.4.1 Fig.4.7 Fig.4.8 Fig.4.9 Fig.4.10 Fig.4.11 Fig.4.12 Fig.4.13 Fig.4.14	
Cu#16	24 nm	6	Fig.3.8 Fig.3.16 Fig.3.19	

References

[1] BAIBICH, M. N., BROTO, J. M., FERT, A., VAN DAU, F. N., PETROFF, F., ETIENNE, P., CREUZET, G., FRIEDERICH, A., and CHAZELAS, J. Giant Magnetoresistance of (001)Fe/(001)Cr Magnetic Superlattices. *Physical Review Letters*. 1988, vol. 61, no. 21, pp. 2472–2475. ISSN 0031-9007. Available from: doi:10.1103/PhysRevLett.61.2472.

[2] BINASCH, G., GRÜNBERG, P., SAURENBACH, F., and ZINN, W. Enhanced magnetoresistance in layered magnetic structures with antiferromagnetic interlayer exchange. *Physical Review B*. 1989, vol. 39, no. 7, pp. 4828–4830. ISSN 0163-1829. Available from: doi:10.1103/PhysRevB.39.4828.

[3] CAMLEY, R. E., and BARNAŚ, J. Theory of giant magnetoresistance effects in magnetic layered structures with antiferromagnetic coupling. *Physical Review Letters*. 1989, vol. 63, no. 6, pp. 664–667. ISSN 0031-9007. Available from: doi:10.1103/PhysRevLett.63.664.

[4] MIYAZAKI, T., and TEZUKA, N. Giant magnetic tunneling effect in Fe/Al2O3/Fe junction. *Journal of Magnetism and Magnetic Materials*. 1995, vol. 139, no. 3, pp. L231–L234. ISSN 03048853. Available from: doi:10.1016/0304-8853(95)90001-2.

[5] MOODERA, J. S., KINDER, L. R., WONG, T. M., and MESERVEY, R. Large Magnetoresistance at Room Temperature in Ferromagnetic Thin Film Tunnel Junctions. *Physical Review Letters*. 1995, vol. 74, no. 16, pp. 3273–3276. ISSN 0031-9007. Available from: doi:10.1103/PhysRevLett.74.3273.

[6] JULLIERE, M. Tunneling between ferromagnetic films. *Physics Letters A*. 1975, vol. 54, no. 3, pp. 225–226. ISSN 03759601. Available from: doi:10.1016/0375-9601(75)90174-7.

[7] BHATTI, S., SBIAA, R., HIROHATA, A., OHNO, H., FUKAMI, S., and PIRAMANAYAGAM, S. N. Spintronics based random access memory: a review. *Materials Today*. 2017, vol. 20, no. 9, pp. 530–548. ISSN 13697021. Available from: doi:10.1016/j.mattod.2017.07.007.

[8] CHUMAK, A. V., VASYUCHKA, V. I., SERGA, A. A., and HILLEBRANDS, B. Magnon spintronics. *Nature Physics*. 2015, vol. 11, no. 6, pp. 453–461. ISSN 1745-2473. Available from: doi:10.1038/nphys3347.

[9] KRUGLYAK, V. V., DEMOKRITOV, S. O., and GRUNDLER, D. Magnonics. *Journal of Physics D: Applied Physics*. 2010, vol. 43, no. 26, pp. 264001. ISSN 0022-3727. Available from: doi:10.1088/0022-3727/43/26/264001.

[10] SANDWEG, C. W., KAJIWARA, Y., CHUMAK, A. V., SERGA, A. A., VASYUCHKA, V. I., JUNGFLEISCH, M. B., SAITOH, E., and HILLEBRANDS, B. Spin Pumping by Parametrically Excited Exchange Magnons. *Physical Review Letters*. 2011, vol. 106, no. 21, pp. 216601. ISSN 0031-9007. Available from: doi:10.1103/PhysRevLett.106.216601.

[11] HEUSSNER, F., TALMELLI, G., GEILEN, M., HEINZ, B., BRÄCHER, T., MEYER, T., CIUBOTARU, F., ADELMANN, C., YAMAMOTO, K., SERGA, A. A., HILLEBRANDS, B., and PIRRO, P. A passive GHz frequency-division multiplexer/demultiplexer based on anisotropic magnon transport in magnetic nanosheets. 2019, pp. 1–16. Available from: `http://arxiv.org/abs/1904.12744`.

[12] WU, H., HUANG, L., FANG, C., YANG, B. S., WAN, C. H., YU, G. Q., FENG, J. F., WEI, H. X., and HAN, X. F. Magnon Valve Effect between Two Magnetic Insulators. *Physical Review Letters*. 2018, vol. 120, no. 9, pp. 1–6. ISSN 10797114. Available from: doi:10.1103/PhysRevLett.120.097205.

[13] CORNELISSEN, L. J., LIU, J., VAN WEES, B. J., and DUINE, R. A. Spin-Current-Controlled Modulation of the Magnon Spin Conductance in a Three-Terminal Magnon Transistor. *Physical Review Letters*. 2018, vol. 120, no. 9, pp. 97702. ISSN 10797114. Available from: doi:10.1103/PhysRevLett.120.097702.

[14] TOPP, J., HEITMANN, D., KOSTYLEV, M. P., and GRUNDLER, D. Making a Reconfigurable Artificial Crystal by Ordering Bistable Magnetic Nanowires. *Physical Review Letters*. 2010, vol. 104, no. 20, pp. 207205. ISSN 0031-9007. Available from: doi:10.1103/PhysRevLett.104.207205.

[15] LENK, B., ULRICHS, H., GARBS, F., and MÜNZENBERG, M. The building blocks of magnonics. *Physics Reports*. 2011, vol. 507, no. 4-5, pp. 107–136. ISSN 03701573. Available from: doi:10.1016/j.physrep.2011.06.003.

[16] SERGA, A. A., CHUMAK, A. V., and HILLEBRANDS, B. YIG magnonics. *Journal of Physics D: Applied Physics*. 2010, vol. 43, no. 26, pp. 264002. ISSN 0022-3727. Available from: doi:10.1088/0022-3727/43/26/264002.

[17] WAGNER, K., KÁKAY, A., SCHULTHEISS, K., HENSCHKE, A., SEBASTIAN, T., and SCHULTHEISS, H. Magnetic domain walls as reconfigurable spin-wave nanochannels. *Nature Nanotechnology*. 2016, vol. 11, no. 5, pp. 432–436. ISSN 1748-3387. Available from: doi:10.1038/nnano.2015.339.

[18] ALBISETTI, E., PETTI, D., PANCALDI, M., MADAMI, M., TACCHI, S., CURTIS, J., KING, W. P., PAPP, A., CSABA, G., POROD, W., VAVASSORI, P., RIEDO, E., and BERTACCO, R. Nanopatterning reconfigurable magnetic landscapes via thermally assisted scanning probe lithography. *Nature Nanotechnology*. 2016, vol. 11, no. 6, pp. 545–551. ISSN 1748-3387. Available from: doi:10.1038/nnano.2016.25.

[19] ALBISETTI, E., PETTI, D., SALA, G., SILVANI, R., TACCHI, S., FINIZIO, S., WINTZ, S., CALÒ, A., ZHENG, X., RAABE, J., RIEDO, E., and BERTACCO, R. Nanoscale spin-wave circuits based on engineered reconfigurable spin-textures. *Communications Physics*. 2018, vol. 1, no. 1, pp. 56. ISSN 2399-3650. Available from: doi:10.1038/s42005-018-0056-x.

[20] OBRY, B., PIRRO, P., BRÄCHER, T., CHUMAK, A. V., OSTEN, J., CIUBOTARU, F., SERGA, A. A., FASSBENDER, J., and HILLEBRANDS, B. A microstructured ion-implanted magnonic crystal. *Applied Physics Letters*. 2013, vol. 102, no. 20, pp. 202403. ISSN 00036951. Available from: doi:10.1063/1.4807721.

[21] RÖDER, F., HLAWACEK, G., WINTZ, S., HÜBNER, R., BISCHOFF, L., LICHTE, H., POTZGER, K., LINDNER, J., FASSBENDER, J., and BALI, R. Direct Depth- and Lateral- Imaging of Nanoscale Magnets Generated by Ion Impact. *Scientific Reports*. 2015, vol. 5, no. 1, pp. 16786. ISSN 2045-2322. Available from: doi:10.1038/srep16786.

[22] DEV, B. N., BANU, N., FASSBENDER, J., GRENZER, J., SCHELL, N., BISCHOFF, L., GROETZSCHEL, R., and MCCORD, J. Ion irradiation effects on a magnetic Si/Ni/Si trilayer and lateral magnetic–nonmagnetic multistrip patterning by focused ion beam. *Indian Journal of Physics*. 2017, vol. 91, no. 10, pp. 1167–1172. ISSN 09749845. Available from: doi:10.1007/s12648-017-1025-z.

[23] FASSBENDER, J., and MCCORD, J. Control of saturation magnetization, anisotropy, and damping due to Ni implantation in thin Ni81Fe19 layers. *Applied Physics Letters*. 2006, vol. 88, no. 25, pp. 33–36. ISSN 00036951. Available from: doi:10.1063/1.2213948.

[24] BALI, R., WINTZ, S., MEUTZNER, F., HÜBNER, R., BOUCHER, R., ÜNAL, A. A., VALENCIA, S., NEUDERT, A., POTZGER, K., BAUCH, J., KRONAST, F., FACSKO, S., LINDNER, J., and FASSBENDER, J. Printing Nearly-Discrete Magnetic Patterns Using Chemical Disorder Induced Ferromagnetism. *Nano Letters*. 2014, vol. 14, no. 2, pp. 435–441. ISSN 1530-6984. Available from: doi:10.1021/nl404521c.

[25] FASSBENDER, J., RAVELOSONA, D., and SAMSON, Y. Tailoring magnetism by light-ion irradiation. *Journal of Physics D: Applied Physics*. 2004, vol. 37, no. 16. ISSN 00223727. Available from: doi:10.1088/0022-3727/37/16/R01.

[26] URBÁNEK, M., FLAJŠMAN, L., KŘIŽÁKOVÁ, V., GLOSS, J., HORKÝ, M., SCHMID, M., and VARGA, P. Research Update: Focused ion beam direct writing of magnetic patterns with controlled structural and magnetic properties. *APL Materials*. 2018, vol. 6, no. 6. ISSN 2166532X. Available from: doi:10.1063/1.5029367.

[27] COEY, J. M. D. *Magnetism and Magnetic Materials*. Cambridge University Press, 2010. ISBN 9780521016766. Available from: doi:10.1017/CBO9780511845000.

[28] BLUNDELL, S. *Magnetism in Condensed Matter*. Oxford University Press, 2001. ISBN 9780198505914.

[29] BLAND, J. A. C. Ultrathin magnetic structures—magnetism and electronic properties. In: *The Chemical Physics of Solid Surfaces*. ScienceDirect, 1997pp. 583–634. Available from: doi:10.1016/S1571-0785(97)80018-1.

[30] AHARONI, A. *Introduction to the theory of ferromagnetism*. 2. edition. Clarendon Press, 1980. ISBN 9780198508090.

[31] STANCIL, D. D., and PRABHAKAR, A. *Spin Waves*. 1. edition. Boston, MA: Springer US, 2009. ISBN 978-0-387-77864-8. Available from: doi:10.1007/978-0-387-77865-5.

[32] DEMOKRITOV, S. O. *Spin Wave Confinement*. 1. edition. 2009. ISBN 9789814241069. Available from: doi:10.1201/9781315110820.

[33] DEMOKRITOV, S. O. *Spin Wave Confinement: Propagating Waves*. 2. edition. Jenny Stanford Publishing, 2017. ISBN 9781315110820.

[34] HILLEBRANDS, B., and OUNADJELA, K. *Spin Dynamics in Confined Magnetic Structures I*. 1. edition. Berlin, Heidelberg: Springer Berlin Heidelberg, 2002. Topics in Applied Physics. ISBN 978-3-540-41191-8. Available from: doi:10.1007/3-540-40907-6.

[35] HILLEBRANDS, B., and OUNADJELA, K. *Spin Dynamics in Confined Magnetic Structures II*. 1. edition. Berlin, Heidelberg: Springer Berlin Heidelberg, 2007. Topics in Applied Physics. ISBN 978-3-540-41191-8. Available from: doi:10.1007/3-540-40907-6.

[36] HILLEBRANDS, B., and THIAVILLE, A. *Spin Dynamics in Confined Magnetic Structures III*. Springer Berlin Heidelberg, 2006. Topics in Applied Physics. ISBN 978-3-540-20108-3. Available from: doi:10.1007/b12462.

[37] DEMOKRITOV, S. O., and SLAVIN, A. N. *Magnonics*. Berlin, Heidelberg: Springer Berlin Heidelberg, 2013. Topics in Applied Physics. ISBN 978-3-642-30246-6. Available from: doi:10.1007/978-3-642-30247-3.

[38] AHARONI, A. Demagnetizing factors for rectangular ferromagnetic prisms. *Journal of Applied Physics*. 1998, vol. 83, no. 6, pp. 3432–3434. ISSN 0021-8979. Available from: doi:10.1063/1.367113.

[39] SOMMERFELD, A., and BETHE, H. Elektronentheorie der Metalle. In: *Aufbau Der Zusammenhängenden Materie*. Berlin, Heidelberg: Springer Berlin Heidelberg, 1933pp. 333–622. ISBN 978-3-642-89260-8. Available from: doi:10.1007/978-3-642-91116-3_3.

[40] SELLMYER, D. J., and SKOMSKI, R. *Advanced Magnetic Nanostructures*. 1. edition. Springer, 2006. ISBN 1441936033.

[41] HU, C. D. The Dzyaloshinskii–Moriya interaction in metals. *Journal of Physics: Condensed Matter*. 2012, vol. 24, no. 8, pp. 086001. ISSN 0953-8984. Available from: doi:10.1088/0953-8984/24/8/086001.

[42] VAŇATKA, M., ROJAS-SÁNCHEZ, J.-C., VOGEL, J., BONFIM, M., BELMEGUENAI, M., ROUSSIGNÉ, Y., STASHKEVICH, A., THIAVILLE, A., and PIZZINI, S. Velocity asymmetry of Dzyaloshinskii domain walls in the creep and flow regimes. *Journal of Physics: Condensed Matter*. 2015, vol. 27, no. 32, pp. 326002. ISSN 0953-8984. Available from: doi:10.1088/0953-8984/27/32/326002.

[43] BROWN, W. F. *Micromagnetics*. 1. edition. Interscience Publishers, 1963. ISBN 978-0-88275-665-3.

[44] HUBERT, A., and SCHÄFER, R. *Magnetic Domains*. 1. edition. Berlin, Heidelberg: Springer Berlin Heidelberg, 1998. ISBN 978-3-540-64108-7. Available from: doi:10.1007/978-3-540-85054-0.

[45] SKOMSKI, R. *Simple Models of Magnetism*. 1. edition. Oxford University Press, 2008. ISBN 9780198570752. Available from: doi:10.1093/acprof:oso/9780198570752.001.0001.

[46] MAYERGOYZ, I. D. *Mathematical Models of Hysteresis and Their Applications*. 2. edition. Elsevier, 2003. ISBN 9780124808737. Available from: doi:10.1016/B978-0-12-480873-7.X5000-2.

[47] TANNOUS, C., and GIERALTOWSKI, J. The Stoner–Wohlfarth model of ferromagnetism. *European Journal of Physics*. 2008, vol. 29, no. 3, pp. 475–487. ISSN 0143-0807. Available from: doi:10.1088/0143-0807/29/3/008.

[48] STONER, E. C., and WOHLFARTH, E. P. A Mechanism of Magnetic Hysteresis in Heterogeneous Alloys. *Philosophical Transactions of the Royal Society A: Mathematical, Physical and Engineering Sciences*. 1948, vol. 240, no. 826, pp. 599–642. ISSN 1364-503X. Available from: doi:10.1098/rsta.1948.0007.

[49] KAMBERSKÝ, V. Spin-orbital Gilbert damping in common magnetic metals. *Physical Review B*. 2007, vol. 76, no. 13, pp. 134416. ISSN 1098-0121. Available from: doi:10.1103/PhysRevB.76.134416.

[50] GILMORE, K., IDZERDA, Y. U., and STILES, M. D. Identification of the Dominant Precession-Damping Mechanism in Fe, Co, and Ni by First-Principles Calculations. *Physical Review Letters*. 2007, vol. 99, no. 2, pp. 027204. ISSN 0031-9007. Available from: doi:10.1103/PhysRevLett.99.027204.

[51] KUNEŠ, J., and KAMBERSKÝ, V. First-principles investigation of the damping of fast magnetization precession in ferromagnetic 3d metals. *Physical Review B*. 2002, vol. 65, no. 21, pp. 212411. ISSN 0163-1829. Available from: doi:10.1103/PhysRevB.65.212411.

[52] BAJPAI, U., and NIKOLIĆ, B. K. Time-retarded damping and magnetic inertia in the Landau-Lifshitz-Gilbert equation self-consistently coupled to electronic time-dependent nonequilibrium Green functions. *Physical Review B*. 2019, vol. 99, no. 13, pp. 134409. ISSN 2469-9950. Available from: doi:10.1103/PhysRevB.99.134409.

[53] DUINE, R. A., LEE, K.-J., PARKIN, S. S. P., and STILES, M. D. Synthetic antiferromagnetic spintronics. *Nature Physics*. 2018, vol. 14, no. 3, pp. 217–219. ISSN 1745-2473. Available from: doi:10.1038/s41567-018-0050-y.

[54] DI, K., FENG, S. X., PIRAMANAYAGAM, S. N., ZHANG, V. L., LIM, H. S., NG, S. C., and KUOK, M. H. Enhancement of spin-wave nonreciprocity in magnonic crystals via synthetic antiferromagnetic coupling. *Scientific Reports*. 2015, vol. 5, no. 10153, pp. 1–6. ISSN 20452322. Available from: doi:10.1038/srep10153.

[55] LAN, J., YU, W., and XIAO, J. Antiferromagnetic domain wall as spin wave polarizer and retarder. *Nature Communications*. 2017, vol. 8, no. 1, pp. 178. ISSN 2041-1723. Available from: doi:10.1038/s41467-017-00265-5.

[56] BELMEGUENAI, M., MARTIN, T., MAIER, M., and BAYREUTHER, G. Frequency- and time-domain investigation of the dynamic properties of interlayer-exchange- coupled Ni81Fe19/Ru/Ni81Fe19 thin film. *Physical Review B*. 2007, vol. 76, no. 10, pp. 104414. ISSN 1098-0121. Available from: doi:10.1103/PhysRevB.76.104414.

[57] BELMEGUENAI, M., MARTIN, T., WOLTERSDORF, G., BAYREUTHER, G., BALTZ, V., SUSZKA, A. K., and HICKEY, B. J. Microwave spectroscopy with vector network analyzer for interlayer exchange-coupled symmetrical and asymmetrical NiFe/Ru/NiFe. *Journal of Physics Condensed Matter*. 2008, vol. 20, no. 34. ISSN 09538984. Available from: doi:10.1088/0953-8984/20/34/345206.

[58] BERTOTTI, G., MAYERGOYZ, I., and SERPICO, C. *Nonlinear Magnetization Dynamics in Nanosystems*. 1. edition. Elsevier, 2009. ISBN 9780080443164. Available from: doi:10.1016/B978-0-08-044316-4.X0001-1.

[59] WALKER, L. R. Magnetostatic Modes in Ferromagnetic Resonance. *Physical Review*. 1957, vol. 105, no. 2, pp. 390–399. ISSN 0031-899X. Available from: doi:10.1103/PhysRev.105.390.

[60] DAMON, R. W., and ESHBACH, J. R. Magnetostatic modes of a ferromagnet slab. *Journal of Physics and Chemistry of Solids*. 1961, vol. 19, no. 3-4, pp. 308–320. ISSN 00223697. Available from: doi:10.1016/0022-3697(61)90041-5.

[61] GUREVICH, Alexander G., and MELKOV, Gennadii A. *Magnetization Oscillations and Waves*. CRC Press, 1996. ISBN 9780849394607.

[62] GRIFFITHS, D. J., and COLLEGE, R. *Introduction to electrodynamics*. 4. edition. Cambridge University Press, 2017. ISBN 013805326X.

[63] KALINIKOS, B. A., and SLAVIN, A. N. Theory of dipole-exchange spin wave spectrum for ferromagnetic films with mixed exchange boundary conditions. *Journal of Physics C: Solid State Physics*. 1986, vol. 19, no. 35, pp. 7013–7033. ISSN 0022-3719. Available from: doi:10.1088/0022-3719/19/35/014.

[64] ARIAS, R., and MILLS, D. L. Extrinsic contributions to the ferromagnetic resonance response of ultrathin films. *Physical Review B*. 1999, vol. 60, no. 10, pp. 7395–7409. ISSN 0163-1829. Available from: doi:10.1103/PhysRevB.60.7395.

[65] DAVIES, C. S., SADOVNIKOV, A. V., GRISHIN, S. V., SHARAEVSKII, Y. P., NIKITOV, S. A., and KRUGLYAK, V. V. Generation of propagating spin waves from regions of increased dynamic demagnetising field near magnetic antidots. *Applied Physics Letters*. 2015, vol. 107, no. 16, pp. 162401. ISSN 0003-6951. Available from: doi:10.1063/1.4933263.

[66] SADOVNIKOV, A. V., DAVIES, C. S., GRISHIN, S. V., KRUGLYAK, V. V., ROMANENKO, D. V., SHARAEVSKII, Yu P., and NIKITOV, S. A. Magnonic beam splitter: The building block of parallel magnonic circuitry. *Applied Physics Letters*. 2015, vol. 106, no. 19, pp. 192406. ISSN 0003-6951. Available from: doi:10.1063/1.4921206.

[67] XING, X., YU, Y., LI, S., and HUANG, X. How do spin waves pass through a bend? *Scientific Reports*. 2013, vol. 3, no. 1, pp. 2958. ISSN 2045-2322. Available from: doi:10.1038/srep02958.

[68] VEERAKUMAR, V., and CAMLEY, R. E. Magnon focusing in thin ferromagnetic films. *Physical Review B*. 2006, vol. 74, no. 21, pp. 214401. ISSN 1098-0121. Available from: doi:10.1103/PhysRevB.74.214401.

[69] DEMOKRITOV, S. O., DEMIDOV, V. E., DZYAPKO, O., MELKOV, G. A., SERGA, A. A., HILLEBRANDS, B., and SLAVIN, A. N. Bose–Einstein condensation of quasi-equilibrium magnons at room temperature under pumping. *Nature*. 2006, vol. 443, no. 7110, pp. 430–433. ISSN 0028-0836. Available from: doi:10.1038/nature05117.

[70] GUSLIENKO, K. Y., DEMOKRITOV, S. O., HILLEBRANDS, B., and SLAVIN, A. N. Effective dipolar boundary conditions for dynamic magnetization in thin magnetic stripes. *Physical Review B*. 2002, vol. 66, no. 13, pp. 132402. ISSN 0163-1829. Available from: doi:10.1103/PhysRevB.66.132402.

[71] BAILLEUL, M., OLLIGS, D., FERMON, C., and DEMOKRITOV, S. O. Spin waves propagation and confinement in conducting films at the micrometer scale. *Europhysics Letters*. 2001, vol. 56, no. 5, pp. 741–747. ISSN 0295-5075. Available from: doi:10.1209/epl/i2001-00583-2.

[72] DEMIDOV, V. E., KOSTYLEV, M. P., ROTT, K., KRZYSTECZKO, P., REISS, G., and DEMOKRITOV, S. O. Excitation of microwaveguide modes by a stripe antenna. *Applied Physics Letters*. 2009, vol. 95, no. 11, pp. 10–13. ISSN 00036951. Available from: doi:10.1063/1.3231875.

[73] GRUSZECKI, P., KASPRZAK, M., SEREBRYANNIKOV, A. E., KRAWCZYK, M., and ŚMIGAJ, W. Microwave excitation of spin wave beams in thin ferromagnetic films. *Scientific Reports*. 2016, vol. 6, no. 1, pp. 22367. ISSN 2045-2322. Available from: doi:10.1038/srep22367.

[74] SCHNEIDER, T., SERGA, A. A., NEUMANN, T., HILLEBRANDS, B., and KOSTYLEV, M. P. Phase reciprocity of spin-wave excitation by a microstrip antenna. *Physical Review B*. 2008, vol. 77, no. 21, pp. 214411. ISSN 1098-0121. Available from: doi:10.1103/PhysRevB.77.214411.

[75] SEKIGUCHI, K., YAMADA, K., SEO, S. M., LEE, K. J., CHIBA, D., KOBAYASHI, K., and ONO, T. Nonreciprocal emission of spin-wave packet in FeNi film. *Applied Physics Letters*. 2010, vol. 97, no. 2, pp. 022508. ISSN 0003-6951. Available from: doi:10.1063/1.3464569.

[76] KOSTYLEV, M. Non-reciprocity of dipole-exchange spin waves in thin ferromagnetic films. *Journal of Applied Physics*. 2013, vol. 113, no. 5, pp. 053907. ISSN 0021-8979. Available from: doi:10.1063/1.4789962.

[77] CIUBOTARU, F., DEVOLDER, T., MANFRINI, M., ADELMANN, C., and RADU, I. P. All electrical propagating spin wave spectroscopy with broadband wavevector capability. *Applied Physics Letters*. 2016, vol. 109, no. 1, pp. 012403. ISSN 0003-6951. Available from: doi:10.1063/1.4955030.

[78] MUSHENOK, F. B., DOST, R., DAVIES, C. S., ALLWOOD, D. A., INKSON, B. J., HRKAC, G., and KRUGLYAK, V. V. Broadband conversion of microwaves into propagating spin waves in patterned magnetic structures. *Applied Physics Letters*. 2017, vol. 111, no. 4, pp. 042404. ISSN 0003-6951. Available from: doi:10.1063/1.4995991.

[79] WINTZ, S., TIBERKEVICH, V., WEIGAND, M., RAABE, J., LINDNER, J., ERBE, A., SLAVIN, A., and FASSBENDER, J. Magnetic vortex cores as tunable spin-wave emitters. *Nature Nanotechnology*. 2016, vol. 11, no. 11, pp. 948–953. ISSN 17483395. Available from: doi:10.1038/nnano.2016.117.

[80] DIETERLE, G., FÖRSTER, J., STOLL, H., SEMISALOVA, A. S., FINIZIO, S., GANGWAR, A., WEIGAND, M., NOSKE, M., FÄHNLE, M., BYKOVA, I., GRÄFE, J., BOZHKO, D. A., MUSIIENKO-SHMAROVA, H. Yu., TIBERKEVICH, V., SLAVIN, A. N., BACK, C. H., RAABE, J., SCHÜTZ, G., and WINTZ, S. Coherent Excitation of Heterosymmetric Spin Waves with Ultrashort Wavelengths. *Physical Review Letters*. 2019, vol. 122, no. 11, pp. 117202. ISSN 0031-9007. Available from: doi:10.1103/PhysRevLett.122.117202.

[81] KOOPMANS, B., VAN KAMPEN, M., KOHLHEPP, J. T., and DE JONGE, W. J. M. Ultrafast magneto-optics in nickel: magnetism or optics? *Physical Review Letters*. 2000, vol. 85, no. 111, pp. 844–847. ISSN 00319007. Available from: doi:10.1103/PhysRevLett.85.844.

[82] KAMPEN, M., JOZSA, C., KOHLHEPP, J. T., LECLAIR, P., LAGAE, L., de JONGE, W. J. M., and KOOPMANS, B. All-Optical Probe of Coherent Spin Waves. *Physical Review Letters*. 2002, vol. 88, no. 22, pp. 227201. ISSN 0031-9007. Available from: doi:10.1103/PhysRevLett.88.227201.

[83] AFANASIEV, D., IVANOV, B. A., KIRILYUK, A., RASING, Th., PISAREV, R. V., and KIMEL, A. V. Control of the Ultrafast Photoinduced Magnetization across the Morin Transition in DyFeO3. *Physical Review Letters*. 2016, vol. 116, no. 9, pp. 097401. ISSN 0031-9007. Available from: doi:10.1103/PhysRevLett.116.097401.

[84] KIMEL, A. V., KIRILYUK, A., USACHEV, P. A., PISAREV, R. V., BALBASHOV, A. M., and RASING, T. Ultrafast non-thermal control of magnetization by instantaneous photomagnetic pulses. *Nature*. 2005, vol. 435, no. 7042, pp. 655–657. ISSN 0028-0836. Available from: doi:10.1038/nature03564.

[85] SATOH, T., TERUI, Y., MORIYA, R., IVANOV, B. A., ANDO, K., SAITOH, E., SHIMURA, T., and KURODA, K. Directional control of spin-wave emission by spatially shaped light. *Nature Photonics*. 2012, vol. 6, no. 10, pp. 662–666. ISSN 1749-4885. Available from: doi:10.1038/nphoton.2012.218.

[86] AWAD, A. A., MURALIDHAR, S., ALEMÁN, A., KHYMYN, R., DVORNIK, M., LU, D., HANSTORP, D., and ÅKERMAN, J. Stimulated k-vector selective magnon emission in NiFe films using femtosecond laser pulse trains. 2019, pp. 1–21. Available from: `http://arxiv.org/abs/1908.03388`.

[87] KIRILYUK, A., KIMEL, A. V., and RASING, T. Ultrafast optical manipulation of magnetic order. *Reviews of Modern Physics*. 2010, vol. 82, no. 3, pp. 2731–2784. ISSN 0034-6861. Available from: doi:10.1103/RevModPhys.82.2731.

[88] HANSTEEN, F., KIMEL, A., KIRILYUK, A., and RASING, T. Femtosecond Photomagnetic Switching of Spins in Ferrimagnetic Garnet Films. *Physical Review Letters*. 2005, vol. 95, no. 4, pp. 047402. ISSN 0031-9007. Available from: doi:10.1103/PhysRevLett.95.047402.

[89] STUPAKIEWICZ, A., SZERENOS, K., AFANASIEV, D., KIRILYUK, A., and KIMEL, A. V. Ultrafast nonthermal photo-magnetic recording in a transparent medium. *Nature*. 2017, vol. 542, no. 7639, pp. 71–74. ISSN 0028-0836. Available from: doi:10.1038/nature20807.

[90] HASHIMOTO, Y., BOSSINI, D., JOHANSEN, T. H., SAITOH, E., KIRILYUK, A., and RASING, T. Frequency and wavenumber selective excitation of spin waves through coherent energy transfer from elastic waves. *Physical Review B*. 2018, vol. 97, no. 14, pp. 140404. ISSN 2469-9950. Available from: doi:10.1103/PhysRevB.97.140404.

[91] SILVA, T. J., and RIPPARD, W. H. Developments in nano-oscillators based upon spin-transfer point-contact devices. *Journal of Magnetism and Magnetic Materials*. 2008, vol. 320, no. 7, pp. 1260–1271. ISSN 03048853. Available from: doi:10.1016/j.jmmm.2007.12.022.

[92] URAZHDIN, S., DEMIDOV, V. E., ULRICHS, H., KENDZIORCZYK, T., KUHN, T., LEUTHOLD, J., WILDE, G., and DEMOKRITOV, S. O. Nanomagnonic devices based on the spin-transfer torque. *Nature Nanotechnology*. 2014, vol. 9, no. 7, pp. 509–513. ISSN 1748-3387. Available from: doi:10.1038/nnano.2014.88.

[93] TAREQUZZAMAN, M., BÖHNERT, T., DECKER, M., COSTA, J. D., BORME, J., LACOSTE, B., PAZ, E., JENKINS, A. S., SERRANO-GUISAN, S., BACK, C. H., FERREIRA, R., and FREITAS, P. P. Spin torque nano-oscillator driven by combined spin injection from tunneling and spin Hall current. *Communications Physics*. 2019, vol. 2, no. 1, pp. 20. ISSN 2399-3650. Available from: doi:10.1038/s42005-019-0119-7.

[94] DEMIDOV, V. E., URAZHDIN, S., ZHOLUD, A., SADOVNIKOV, A., and DEMOKRITOV, S. O. Nanoconstriction-based spin-Hall nano-oscillator. *Applied Physics Letters*. 2014, vol. 105, no. 17, pp. 172410. ISSN 0003-6951. Available from: doi:10.1063/1.4901027.

[95] AWAD, A. A., DÜRRENFELD, P., HOUSHANG, A., DVORNIK, M., IACOCCA, E., DUMAS, R. K., and ÅKERMAN, J. Long-range mutual synchronization of spin Hall nano-oscillators. *Nature Physics*. 2017, vol. 13, no. 3, pp. 292–299. ISSN 1745-2473. Available from: doi:10.1038/nphys3927.

[96] FARADAY, M. *Faraday's Diary of Experimental Investigation*. 2. edition. HR Direct, 2008. ISBN 0981908349.

[97] KERR, J. XLIII. On rotation of the plane of polarization by reflection from the pole of a magnet. *The London, Edinburgh, and Dublin Philosophical Magazine and Journal of Science*. 1877, vol. 3, no. 19, pp. 321–343. ISSN 1941-5982. Available from: doi:10.1080/14786447708639245.

[98] BADER, S. D., MOOG, E. R., and GRÜNBERG, P. Magnetic hysteresis of epitaxially-deposited iron in the monolayer range: A Kerr effect experiment in surface magnetism. *Journal of Magnetism and Magnetic Materials*. 1986, vol. 53, no. 4, pp. L295–L298. ISSN 03048853. Available from: doi:10.1016/0304-8853(86)90172-1.

[99] HIEBERT, W. K., STANKIEWICZ, A., and FREEMAN, M. R. Direct Observation of Magnetic Relaxation in a Small Permalloy Disk by Time-Resolved Scanning Kerr Microscopy. *Physical Review Letters*. 1997, vol. 79, no. 6, pp. 1134–1137. ISSN 0031-9007. Available from: doi:10.1103/PhysRevLett.79.1134.

[100] ACREMANN, Y., BACK, C. H., BUESS, M., PORTMANN, O., VATERLAUS, A., PESCIA, D., and MELCHIOR, H. Imaging Precessional Motion of the Magnetization Vector. *Science*. 2000, vol. 290, no. 5491, pp. 492–495. ISSN 00368075. Available from: doi:10.1126/science.290.5491.492.

[101] FASSBENDER, J. Magnetization Dynamics Investigated by Time-Resolved Kerr Effect Magnetometry. In: *Spin Dynamics in Confined Magnetic Structures II*. Berlin, Heidelberg: Springer Berlin Heidelberg, 2003pp. 59–92. ISBN 9783540440840. Available from: doi:10.1007/3-540-46097-7_3.

[102] BARMAN, A., KIMURA, T., OTANI, Y., FUKUMA, Y., AKAHANE, K., and MEGURO, S. Benchtop time-resolved magneto-optical Kerr magnetometer. *Review of Scientific Instruments*. 2008, vol. 79, no. 12, pp. 123905. ISSN 0034-6748. Available from: doi:10.1063/1.3053353.

[103] LEE, K. D., KIM, J. W., JEONG, J. W., KIM, D. H., SHIN, S. C., HONG, K H, LEE, Y. S., NAM, C. H., SON, M. H., and HWANG, S. W. Femtosecond pump-probe MOKE microscopy for an ultrafast spin dynamics study. *Journal of the Korean Physical Society*. 2006, vol. 49, no. 6, pp. 2402–2407. ISSN 0374-4884. Available from: doi:10.3938/jkps.49.2402.

[104] RIZO, P. J., PUGŽLYS, A., LIU, J., REUTER, D., WIECK, D., WAL, C. H., and LOOSDRECHT, P. H. M. Compact cryogenic Kerr microscope for time-resolved studies of electron spin transport in microstructures. *Review of Scientific Instruments*. 2008, vol. 79, no. 12, pp. 123904. ISSN 0034-6748. Available from: doi:10.1063/1.3046283.

[105] FERRÉ, J., MEYER, P., NYVLT, M., VISNOVSKY, S., and RENARD, D. Magnetooptic depth sensitivity in a simple ultrathin film structure. *Journal of Magnetism and Magnetic Materials*. 1997, vol. 165, no. 1-3, pp. 92–95. ISSN 03048853. Available from: doi:10.1016/S0304-8853(96)00479-9.

[106] CORMIER, M., FERRÉ, J., MOUGIN, A., CROMIÈRES, J.-P., and KLEIN, V. High resolution polar Kerr magnetometer for nanomagnetism and nanospintronics. *Review of Scientific Instruments*. 2008, vol. 79, no. 3, pp. 033706. ISSN 0034-6748. Available from: doi:10.1063/1.2890839.

[107] SAVOINI, M., CICCACCI, F., DUÒ, L., and FINAZZI, M. Apparatus for vectorial Kerr confocal microscopy. *Review of Scientific Instruments*. 2011, vol. 82, no. 2, pp. 023709. ISSN 0034-6748. Available from: doi:10.1063/1.3555757.

[108] LODEWIJKS, K., MACCAFERRI, N., PAKIZEH, T., DUMAS, R. K., ZUBRITSKAYA, I., ÅKERMAN, J., VAVASSORI, P., and DMITRIEV, A. Magnetoplasmonic Design Rules for Active Magneto-Optics. *Nano Letters*. 2014, vol. 14, no. 12, pp. 7207–7214. ISSN 1530-6984. Available from: doi:10.1021/nl504166n.

[109] RUDGE, J., XU, H., KOLTHAMMER, J., HONG, Y. K., and CHOI, B. C. Subnanosecond time-resolved near-field scanning magneto-optical microscope. *Review of Scientific Instruments*. 2015, vol. 86, no. 2, pp. 023703. ISSN 0034-6748. Available from: doi:10.1063/1.4907712.

[110] VIŠŇOVSKÝ, Š. *Optics in Magnetic Multilayers and Nanostructures*. 1. edition. CRC Press, 2006. ISBN 0849336864.

[111] FLAJŠMAN, L. *Vectorial Kerr magnetometry*. 2015. Master's thesis. Brno University of Technology.

[112] QIU, Z. Q., and BADER, S. D. Surface magneto-optic Kerr effect. *Review of Scientific Instruments*. 2000, vol. 71, no. 3, pp. 1243. ISSN 00346748. Available from: doi:10.1063/1.1150496.

[113] VOIGT, W. *Magneto-Und Elektrooptik*. B.G. Teubner, 1908.

[114] BADER, Samuel D. Smoke. *Journal of Magnetism and Magnetic Materials*. 1991, vol. 100, pp. 440–454. ISSN 03048853. Available from: doi:10.1016/0304-8853(91)90833-V.

[115] VIŠŇOVSKÝ, Š. Matrix representations for vector differential operators in general orthogonal coordinates. *Czechoslovak Journal of Physics*. 2004, vol. 54, no. 8, pp. 793–819. ISSN 00114626. Available from: doi:10.1023/B:CJOP.0000038589.21954.81.

[116] MANSURIPUR, M. *The Physical Principles of Magneto-optical Recording*. 1. edition. Cambridge University Press, 1995. ISBN 9780521461245. Available from: doi:10.1017/CBO9780511622472.

[117] JACKSON, J. D. *Classical electrodynamics*. 3. edition. Wiley, 1998. ISBN 9780471309321.

[118] FLAJŠMAN, L., URBÁNEK, M., KŘIŽÁKOVÁ, V., VAŇATKA, M., TURČAN, I., and ŠIKOLA, T. High-resolution fully vectorial scanning Kerr magnetometer. *Review of Scientific Instruments*. 2016, vol. 87, no. 5, pp. 053704. ISSN 0034-6748. Available from: doi:10.1063/1.4948595.

[119] NÝVLT, M. *Optical interactions in ultrathin magnetic film structures*. 1996. Doctoral Thesis. Charles University.

[120] MCCORD, J. Progress in magnetic domain observation by advanced magneto-optical microscopy. *Journal of Physics D: Applied Physics*. 2015, vol. 48, no. 33, pp. 333001. ISSN 0022-3727. Available from: doi:10.1088/0022-3727/48/33/333001.

[121] HECHT, E. *Optics*. 4. edition. Addison-Wesley, 2002. ISBN 0133977226.

[122] SEBASTIAN, T., SCHULTHEISS, K., OBRY, B., HILLEBRANDS, B., and SCHULTHEISS, H. Micro-focused Brillouin light scattering: imaging spin waves at the nanoscale. *Frontiers in Physics*. 2015, vol. 3, no. 35, pp. 1–23. ISSN 2296-424X. Available from: doi:10.3389/fphy.2015.00035.

[123] CAMLEY, R. E., GRÜNBERG, P., and MAYR, C. M. Stokes-anti-Stokes asymmetry in Brillouin scattering from magnons in thin ferromagnetic films. *Physical Review B*. 1982, vol. 26, no. 5, pp. 2609–2614. ISSN 0163-1829. Available from: doi:10.1103/PhysRevB.26.2609.

[124] DI, K., ZHANG, V. L., LIM, H. S., NG, S. Ch., KUOK, M. H., YU, J., YOON, J., QIU, X., and YANG, H. Direct Observation of the Dzyaloshinskii-Moriya Interaction in a Pt/Co/Ni Film. *Physical Review Letters*. 2015, vol. 114, no. 4, pp. 047201. ISSN 0031-9007. Available from: doi:10.1103/PhysRevLett.114.047201.

[125] LINDSAY, S. M., ANDERSON, M. W., and SANDERCOCK, J. R. Construction and alignment of a high performance multipass vernier tandem Fabry–Perot interferometer. *Review of Scientific Instruments*. 1981, vol. 52, no. 10, pp. 1478–1486. ISSN 0034-6748. Available from: doi:10.1063/1.1136479.

[126] YIN, Y., PAN, F., AHLBERG, M., RANJBAR, M., DÜRRENFELD, P., HOUSHANG, A., HAIDAR, M., BERGQVIST, L., ZHAI, Y., DUMAS, R. K., DELIN, A., and ÅKERMAN, J. Tunable permalloy-based films for magnonic devices. *Physical Review B*. 2015, vol. 92, no. 2, pp. 024427. ISSN 1098-0121. Available from: doi:10.1103/PhysRevB.92.024427.

[127] SERGA, A. A., SCHNEIDER, T., HILLEBRANDS, B., DEMOKRITOV, S. O., and KOSTYLEV, M. P. Phase-sensitive Brillouin light scattering spectroscopy from spin-wave packets. *Applied Physics Letters*. 2006, vol. 89, no. 6, pp. 063506. ISSN 0003-6951. Available from: doi:10.1063/1.2335627.

[128] FOHR, F., SERGA, A. A., SCHNEIDER, T., HAMRLE, J., and HILLEBRANDS, B. Phase sensitive Brillouin scattering measurements with a novel magneto-optic modulator. *Review of Scientific Instruments*. 2009, vol. 80, no. 4, pp. 043903. ISSN 0034-6748. Available from: doi:10.1063/1.3115210.

[129] VOGT, K., SCHULTHEISS, H., HERMSDOERFER, S. J., PIRRO, P., SERGA, A. A., and HILLEBRANDS, B. All-optical detection of phase fronts of propagating spin waves in a Ni81Fe19 microstripe. *Applied Physics Letters*. 2009, vol. 95, no. 18, pp. 182508. ISSN 0003-6951. Available from: doi:10.1063/1.3262348.

[130] VOGT, K., FRADIN, F. Y., PEARSON, J. E., SEBASTIAN, T., BADER, S. D., HILLEBRANDS, B., HOFFMANN, A., and SCHULTHEISS, H. Realization of a spin-wave multiplexer. *Nature Communications*. 2014, vol. 5, no. 1, pp. 3727. ISSN 2041-1723. Available from: doi:10.1038/ncomms4727.

[131] ORDÓÑEZ-ROMERO, C. L., LAZCANO-ORTIZ, Z., DROZDOVSKII, A., KALINIKOS, B., AGUILAR-HUERTA, M., DOMÍNGUEZ-JUÁREZ, J. L., LOPEZ-MALDONADO, G., QURESHI, N., KOLOKOLTSEV, O., and MONSIVAIS, G. Mapping of spin wave propagation in a one-dimensional magnonic crystal. *Journal of Applied Physics*. 2016, vol. 120, no. 4, pp. 043901. ISSN 0021-8979. Available from: doi:10.1063/1.4958903.

[132] BAYER, C, JORZICK, J, and HILLEBRANDS, B. Spin-wave excitations in finite rectangular elements of Ni80Fe20. 2005, pp. 1–12. Available from: doi:10.1103/PhysRevB.72.064427.

[133] KATANIN, A. A., BELOZEROV, A. S., and ANISIMOV, V. I. Magnetic exchange and susceptibilities in fcc iron: A supercell dynamical mean-field theory study. *Physical Review B*. 2018, vol. 98, no. 4, pp. 045138. ISSN 2469-9950. Available from: doi:10.1103/PhysRevB.98.045138.

[134] RUPP, W., BIEDERMANN, A., KAMENIK, B., RITTER, R., KLEIN, Ch., PLATZGUMMER, E., SCHMID, M., and VARGA, P. Ion-beam induced fcc-bcc transition in ultrathin Fe films for ferromagnetic patterning. *Applied Physics Letters*. 2008, vol. 93, no. 6, pp. 1–4. ISSN 00036951. Available from: doi:10.1063/1.2969795.

[135] GLOSS, J., SHAH ZAMAN, S., JONNER, J., NOVOTNÝ, Z., SCHMID, M., VARGA, P., and URBÁNEK, M. Ion-beam-induced magnetic and structural phase transformation of Ni-stabilized face-centered-cubic Fe films on Cu(100). *Applied Physics Letters*. 2013, vol. 103, no. 26, pp. 262405. ISSN 0003-6951. Available from: doi:10.1063/1.4856775.

[136] KŘIŽÁKOVÁ, V. *Magnetické vlastnosti materiálů založených na metastabilních vrstvách Fe-Ni*. 2016. Bachelor's thesis. Brno University of Technology.

[137] KŘIŽÁKOVÁ, V. *Spin wave excitation and propagation in magnonic crystals prepared by focused ion beam direct writing*. 2018. Master's thesis. Brno University of Technology.

[138] ZIEGLER, J. F., ZIEGLER, M. D., and BIERSACK, J. P. SRIM – The stopping and range of ions in matter (2010). *Nuclear Instruments and Methods in Physics Research Section B: Beam Interactions with Materials and Atoms*. 2010, vol. 268, no. 11-12, pp. 1818–1823. ISSN 0168583X. Available from: doi:10.1016/j.nimb.2010.02.091.

[139] ATWATER, H. A., THOMPSON, C. V., and SMITH, H. I. Ion-bombardment-enhanced grain growth in germanium, silicon, and gold thin films. *Journal of Applied Physics*. 1988, vol. 64, no. 5, pp. 2337–2353. ISSN 0021-8979. Available from: doi:10.1063/1.341665.

[140] SPOLENAK, R., SAUTER, L., and EBERL, C. Reversible orientation-biased grain growth in thin metal films induced by a focused ion beam. *Scripta Materialia*. 2005, vol. 53, no. 11, pp. 1291–1296. ISSN 13596462. Available from: doi:10.1016/j.scriptamat.2005.07.030.

[141] ZAK, J., MOOG, E. R., LIU, C., and BADER, S. D. Magneto-optics of multilayers with arbitrary magnetization directions. *Physical Review B*. 1991, vol. 43, no. 8, pp. 6423–6429. ISSN 01631829. Available from: doi:10.1103/PhysRevB.43.6423.

[142] YEH, P. Optics of anisotropic layered media: A new 4 × 4 matrix algebra. *Surface Science*. 1980, vol. 96, no. 1-3, pp. 41–53. ISSN 00396028. Available from: doi:10.1016/0039-6028(80)90293-9.

[143] ZAK, J., MOOG, E. R., LIU, C., and BADER, S. D. Fundamental magneto-optics. *Journal of Applied Physics*. 1990, vol. 68, no. 8, pp. 4203. ISSN 00218979. Available from: doi:10.1063/1.346209.

[144] ZAK, J., MOOG, E. R., LIU, C., and BADER, S. D. Elementary formula for the magneto-optic Kerr effect from model superlattices. *Applied Physics Letters*. 1991, vol. 58, no. 1991, pp. 1214–1216. ISSN 00036951. Available from: doi:10.1063/1.104368.

[145] ASHIDA, K., KAJINO, T., KUTSUMA, Y., OHTANI, N., and KANEKO, T. Crystallographic orientation dependence of SEM contrast revealed by SiC polytypes. *Journal of Vacuum Science & Technology B, Nanotechnology and Microelectronics: Materials, Processing, Measurement, and Phenomena*. 2015, vol. 33, no. 4, pp. 04E104. ISSN 2166-2746. Available from: doi:10.1116/1.4927136.

[146] SCHWARTZ, A. J., KUMAR, M., ADAMS, B. L., and FIELD, D. P. *Electron Backscatter Diffraction in Materials Science*. Boston, MA: Springer US, 2009. ISBN 978-0-387-88135-5. Available from: doi:10.1007/978-0-387-88136-2.

[147] KALKI, K., CHAMBLISS, D. D., JOHNSON, K. E., WILSON, R. J., and CHIANG, S. Evidence for martensitic fcc-bcc transition of thin Fe films on Cu(100). *Physical Review B*. 1993, vol. 48, no. 24, pp. 18344–18347. ISSN 01631829. Available from: doi:10.1103/PhysRevB.48.18344.

[148] HATHAWAY, K. B., and PRINZ, G. A. First-Order Magnetic Phase Transitions in Fe. *Physical Review Letters*. 1981, vol. 47, no. 24, pp. 1761–1765. ISSN 0031-9007. Available from: doi:10.1103/PhysRevLett.47.1761.

[149] VANSTEENKISTE, A., LELIAERT, J., DVORNIK, M., GARCIA-SANCHEZ, F., and VAN WAEYENBERGE, B. The design and verification of Mumax3. 2014, vol. 107133, no. 4, pp. 0–22. ISSN 21583226. Available from: doi:10.1063/1.4899186.

[150] CHAPPERT, C. Planar Patterned Magnetic Media Obtained by Ion Irradiation. *Science*. 1998, vol. 280, no. 5371, pp. 1919–1922. ISSN 00368075. Available from: doi:10.1126/science.280.5371.1919.

[151] BIEDERMANN, A., SCHMID, M., and VARGA, P. Nucleation of bcc Iron in Ultrathin fcc Films. *Physical Review Letters*. 2001, vol. 86, no. 3, pp. 464–467. ISSN 0031-9007. Available from: doi:10.1103/PhysRevLett.86.464.

[152] HEINZ, B., BRÄCHER, T., SCHNEIDER, M., WANG, Q., LÄGEL, B., FRIEDEL, A. M., BREITBACH, D., STEINERT, S., MEYER, T., KEWENIG, M., DUBS, C., PIRRO, P., and CHUMAK, A. V. Propagation of coherent spin waves in individual nano-sized yttrium iron garnet magnonic conduits. 2019. Available from: `http://arxiv.org/abs/1910.08801`.

[153] DEMIDOV, V. E., KOSTYLEV, M. P., ROTT, K., MÜNCHENBERGER, J., REISS, G., and DEMOKRITOV, S. O. Excitation of short-wavelength spin waves in magnonic waveguides. *Applied Physics Letters*. 2011, vol. 99, no. 8, pp. 082507. ISSN 0003-6951. Available from: doi:10.1063/1.3631756.

[154] CLAUSEN, P., VOGT, K., SCHULTHEISS, H., SCHÄFER, S., OBRY, B., WOLF, G., PIRRO, P., LEVEN, B., and HILLEBRANDS, B. Mode conversion by symmetry breaking of propagating spin waves. *Applied Physics Letters*. 2011, vol. 99, no. 16, pp. 162505. ISSN 0003-6951. Available from: doi:10.1063/1.3650256.

[155] DEMIDOV, V. E., and DEMOKRITOV, S. O. Magnonic Waveguides Studied by Microfocus Brillouin Light Scattering. *IEEE Transactions on Magnetics*. 2015, vol. 51, no. 4, pp. 1–15. ISSN 0018-9464. Available from: doi:10.1109/TMAG.2014.2388196.

[156] SADOVNIKOV, A. V., DAVIES, C. S., KRUGLYAK, V. V., ROMANENKO, D. V., GRISHIN, S. V., BEGININ, E N, SHARAEVSKII, Y. P., and NIKITOV, S. A. Spin wave propagation in a uniformly biased curved magnonic waveguide. *Physical Review B*. 2017, vol. 96, no. 6, pp. 060401. ISSN 2469-9950. Available from: doi:10.1103/PhysRevB.96.060401.

[157] DEMIDOV, V. E., DEMOKRITOV, S. O., ROTT, K., KRZYSTECZKO, P., and REISS, G. Nano-optics with spin waves at microwave frequencies. *Applied Physics Letters*. 2008, vol. 92, no. 23, pp. 232503. ISSN 0003-6951. Available from: doi:10.1063/1.2945000.

[158] PARK, J. P., EAMES, P., ENGEBRETSON, D. M., BEREZOVSKY, J., and CROWELL, P. A. Spatially Resolved Dynamics of Localized Spin-Wave Modes in Ferromagnetic Wires. *Physical Review Letters*. 2002, vol. 89, no. 27, pp. 277201. ISSN 0031-9007. Available from: doi:10.1103/PhysRevLett.89.277201.

[159] SCHULTHEISS, K., VERBA, R., WEHRMANN, F., WAGNER, K., KÖRBER, L., HULA, T., HACHE, T., KÁKAY, A., AWAD, A. A., TIBERKEVICH, V., SLAVIN, A. N., FASSBENDER, J., and SCHULTHEISS, H. Excitation of Whispering Gallery Magnons in a Magnetic Vortex. *Physical Review Letters*. 2019, vol. 122, no. 9, pp. 097202. ISSN 0031-9007. Available from: doi:10.1103/PhysRevLett.122.097202.

[160] FLAJŠMAN, L., WAGNER, K., VAŇATKA, M., GLOSS, J., KŘIŽÁKOVÁ, V., SCHMID, M., SCHULTHEISS, H., and URBÁNEK, M. Zero-field propagation of spin waves in waveguides prepared by focused ion beam direct writing. *Accepted to Physical Review B*. 2019, pp. 1–12. Available from: doi:arXiv:1906.12254.

[161] DEMIDOV, V. E., JERSCH, J., DEMOKRITOV, S. O., ROTT, K., KRZYSTECZKO, P., and REISS, G. Transformation of propagating spin-wave modes in microscopic waveguides with variable width. *Physical Review B*. 2009, vol. 79, no. 5, pp. 054417. ISSN 1098-0121. Available from: doi:10.1103/PhysRevB.79.054417.

[162] GLADII, O., HALLEY, D., HENRY, Y., and BAILLEUL, M. Spin-wave propagation and spin-polarized electron transport in single-crystal iron films. *Physical Review B*. 2017, vol. 96, no. 17, pp. 174420. ISSN 2469-9950. Available from: doi:10.1103/PhysRevB.96.174420.

[163] ZAMAN, S. S., DVOŘÁK, P., RITTER, R., BUCHSBAUM, A., STICKLER, D., OEPEN, H. P., SCHMID, M., and VARGA, P. In-situ magnetic nano-patterning of Fe films grown on Cu(100). *Journal of Applied Physics*. 2011, vol. 110, no. 2, pp. 024309. ISSN 0021-8979. Available from: doi:10.1063/1.3609078.

[164] MCMICHAEL, R. D., and MARANVILLE, B. B. Edge saturation fields and dynamic edge modes in ideal and non-ideal magnetic film edges. In: *INTERMAG 2006 - IEEE International Magnetics Conference*. IEEE, 2006pp. 931–931. ISBN 1-4244-1479-2. Available from: doi:10.1109/INTMAG.2006.374962.

[165] VENKAT, G., KUMAR, D., FRANCHIN, M., DMYTRIIEV, O., MRUCZKIEWICZ, M., FANGOHR, H., BARMAN, A., KRAWCZYK, M., and PRABHAKAR, A. Proposal for a Standard Micromagnetic Problem: Spin Wave Dispersion in a Magnonic Waveguide. *IEEE Transactions on Magnetics*. 2013, vol. 49, no. 1, pp. 524–529. ISSN 0018-9464. Available from: doi:10.1109/TMAG.2012.2206820.

[166] KITTEL, C. Excitation of Spin Waves in a Ferromagnet by a Uniform rf Field. *Physical Review*. 1958, vol. 110, no. 6, pp. 1295–1297. ISSN 0031-899X. Available from: doi:10.1103/PhysRev.110.1295.

[167] VOGT, K., SCHULTHEISS, H., JAIN, S., PEARSON, J. E., HOFFMANN, A., BADER, S. D., and HILLEBRANDS, B. Spin waves turning a corner. *Applied Physics Letters*. 2012, vol. 101, no. 4, pp. 042410. ISSN 0003-6951. Available from: doi:10.1063/1.4738887.

[168] VIZMULLER, P. *RF Design Guide*. 1. edition. Artech House Publishers, 1995. ISBN 0890067546.

[169] SIMONS, R. N. Coplanar Waveguide Applications. In: *Coplanar Waveguide Circuits, Components, and Systems*. New York, USA: John Wiley & Sons, Inc., 2003pp. 384–433. ISBN 0471161217. Available from: doi:10.1002/0471224758.ch12.

[170] HÄMÄLÄINEN, S. J., MADAMI, M., QIN, H., GUBBIOTTI, G., and van DIJKEN, S. Control of spin-wave transmission by a programmable domain wall. *Nature Communications*. 2018, vol. 9, no. 1, pp. 4853. ISSN 2041-1723. Available from: doi:10.1038/s41467-018-07372-x.

[171] STIGLOHER, J., DECKER, M., KÖRNER, H. S., TANABE, K., MORIYAMA, T., TANIGUCHI, T., HATA, H., MADAMI, M., GUBBIOTTI, G., KOBAYASHI, K., ONO, T., and BACK, C. H. Snell's Law for Spin Waves. *Physical Review Letters*. 2016, vol. 117, no. 3, pp. 037204. ISSN 0031-9007. Available from: doi:10.1103/PhysRevLett.117.037204.

[172] SUN, F., and HE, S. Waveguide bends by optical surface transformations and optic-null media. *Journal of the Optical Society of America B*. 2018, vol. 35, no. 4, pp. 944. ISSN 0740-3224. Available from: doi:10.1364/JOSAB.35.000944.

[173] FEIT, M. D., and FLECK, J. A. Light propagation in graded-index optical fibers. *Applied Optics*. 1978, vol. 17, no. 24, pp. 3990. ISSN 0003-6935. Available from: doi:10.1364/AO.17.003990.

[174] DAVIES, C. S., FRANCIS, A., SADOVNIKOV, A. V., CHERTOPALOV, S. V., BRYAN, M. T., GRISHIN, S. V., ALLWOOD, D. A., SHARAEVSKII, Y. P., NIKITOV, S. A., and KRUGLYAK, V. V. Towards graded-index magnonics: Steering spin waves in magnonic networks. *Physical Review B*. 2015, vol. 92, no. 2, pp. 020408. ISSN 1098-0121. Available from: doi:10.1103/PhysRevB.92.020408.

[175] DAVIES, C. S., and KRUGLYAK, V. V. Graded-index magnonics. *Low Temperature Physics*. 2015, vol. 41, no. 10, pp. 760–766. ISSN 1063-777X. Available from: doi:10.1063/1.4932349.

[176] OBRY, B., VASYUCHKA, V. I., CHUMAK, A. V., SERGA, A. A., and HILLEBRANDS, B. Spin-wave propagation and transformation in a thermal gradient. *Applied Physics Letters*. 2012, vol. 101, no. 19, pp. 192406. ISSN 0003-6951. Available from: doi:10.1063/1.4767137.

[177] VOGEL, M., AßMANN, R., PIRRO, P., CHUMAK, A. V., HILLEBRANDS, B., and von FREYMANN, G. Control of Spin-Wave Propagation using Magnetisation Gradients. *Scientific Reports*. 2018, vol. 8, no. 1, pp. 11099. ISSN 2045-2322. Available from: doi:10.1038/s41598-018-29191-2.

[178] GRUSZECKI, P., and KRAWCZYK, M. Spin-wave beam propagation in ferromagnetic thin films with graded refractive index: Mirage effect and prospective applications. *Physical Review B*. 2018, vol. 97, no. 9, pp. 094424. ISSN 2469-9950. Available from: doi:10.1103/PhysRevB.97.094424.

[179] GLOSS, J. *Metastable Iron-Nickel Thin Films*. 2019. Doctoral thesis. TU Wien.

Own publications

[1] URBÁNEK, M., UHLÍŘ, V., LAMBERT, C.-H., KAN, J. J., EIBAGI, N., VAŇATKA, M., **FLAJŠMAN, L.**, KALOUSEK, R., IM, M.-Y., FISCHER, P., ŠIKOLA, T., and FULLERTON, E. E. Dynamics and efficiency of magnetic vortex circulation reversal. *Physical Review B*, 2015, vol. 91, no. 9, pp. 1-11. ISSN 1098-0121. doi: `10.1103/PhysRevB.91.094415`.

[2] **FLAJŠMAN, L.**, URBÁNEK, M., KŘIŽÁKOVÁ, V., VAŇATKA, M., TURČAN, I., and ŠIKOLA, T. High-resolution fully vectorial scanning Kerr magnetometer. *Review of Scientific Instruments*, 2016, vol. 87, no. 5, pp. 053704. ISSN 0034-6748. doi: `10.1063/1.4948595`.

[3] **FLAJŠMAN, L.**, URBÁNEK, M., KŘIŽÁKOVÁ, V., VAŇATKA, M., TURČAN, I., and ŠIKOLA, T. Vektorová Kerrova magnetometrie s vysokým prostorovým rozlišením. *Jemná mechanika optika*, 2016, vol. 6.

[4] BARTOŠÍK, M., KORMOŠ, L., **FLAJŠMAN, L.**, KALOUSEK, R., MACH, J., LIŠKOVÁ, Z., NEZVAL, D., ŠVARC, V., ŠAMOŘIL, T., and ŠIKOLA, T. Nanometer-Sized Water Bridge and Pull-Off Force in AFM at Different Relative Humidities: Reproducibility Measurement and Model Based on Surface Tension Change. *The Journal of Physical Chemistry B*, 2017, vol. 121, no. 3, pp. 610-619. ISSN 1520-6106. doi: `10.1103/10.1021/acs.jpcb.6b11108`.

[5] VAŇATKA, M., URBÁNEK, M., JÍRA, R., **FLAJŠMAN, L.**, DHANKHAR, M., IM, M.-Y., MICHALIČKA, J., UHLÍŘ,V., and ŠIKOLA, T. Magnetic vortex nucleation modes in static magnetic fields. *AIP Advances*. 2017, vol. 7, no. 10, pp. 105103, ISSN 21583226. doi: `10.1063/1.5006235`.

[6] URBÁNEK, M., **FLAJŠMAN, L.**, KŘIŽÁKOVÁ, V., GLOSS, J., HORKÝ, M., SCHMID, M., and VARGA, P. Research Update: Focused ion beam direct writing of magnetic patterns with controlled structural and magnetic properties. *APL Materials*. 2018, vol. 6, no. 6. ISSN 2166532X. doi: `10.1063/1.5029367`.

[7] GLOSS, J., HORKÝ, M., KŘIŽÁKOVÁ, V., **FLAJŠMAN, L.**, SCHMID, M., URBÁNEK,M., and VARGA, P. The growth of metastable fcc Fe78Ni22 thin films on H-Si (1 0 0) substrates suitable for focused ion beam direct magnetic patterning. *Applied Surface Science*. 2019, vol. 469, no. 100, pp. 747-752, ISSN 01694332. doi: `10.1016/j.apsusc.2018.10.263`.

[8] **FLAJŠMAN, L.**, WAGNER, K., VAŇATKA, M., GLOSS, J., KŘIŽÁKOVÁ, V., SCHMID,M., SCHULTHEISS, H., and VARGA, P. Zero-field propagation of spin

waves in waveguides prepared by focused ion beam direct writing. *Accepted to Physical Review B*. 2019, pp. 1-12. doi: `arXiv:1906.12254`.

[9] HACHE, T., VAŇATKA, M., **FLAJŠMAN, L.**, WEINHOLD, T., HULA, T., CIUBOTARIU, O., ALBRECHT, M., ARKOOK, B., BARSUKOV, I., FALLARINO, L., HELLWIG, O., FASSBENDER, J., URBÁNEK, M., and SCHULTHEISS, H. Free-standing and positionable microwave antenna device for magneto-optical spectroscopy experiments. 2019, pp. 1-8. doi: `arXiv:1911.11517v1`.

[10] FERREIRA, I., AYRE, M., BAVDAZ, M., GUAINAZZI, M., STEFANESCU, A., KOMÁREK, M., VALENTA, T., HYNEK, R., ZÁVODNÍK, M., SOBOTKA, P., PEJCHAL, T., BADIN, V., KALOUSEK, R., BAČOVSKÝ, J., **FLAJŠMAN, L.**, WOJEWODA, O., and ZLÁMAL, J. Minimization of the charged particle background on the ATHENA mission. To be submitted.